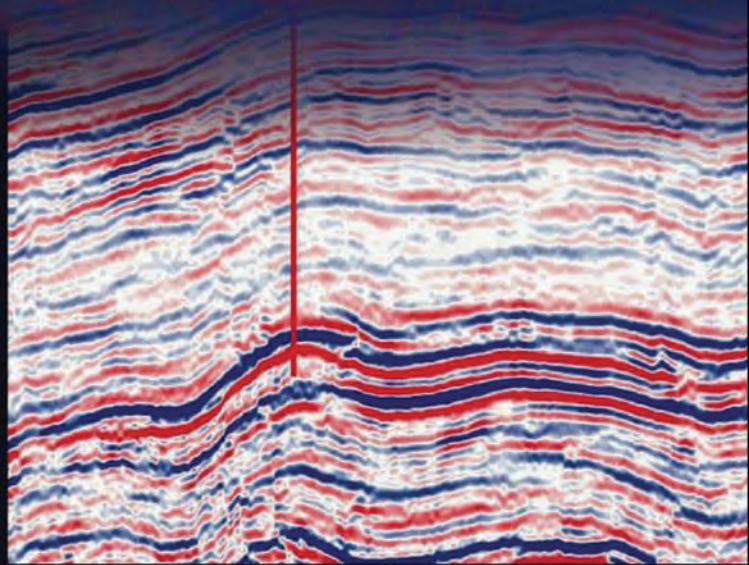


Seismic Inverse Q Filtering



YANGHUA WANG



Blackwell
Publishing

SEISMIC INVERSE Q FILTERING

*This book is dedicated to my wife Guo-ling, and
my two children Brian and Claire.*

SEISMIC INVERSE Q FILTERING

by

Yanghua Wang

Professor of Reservoir Geophysics
Imperial College London, UK

© 2008 by Yanghua Wang

BLACKWELL PUBLISHING

350 Main Street, Malden, MA 02148-5020, USA

9600 Garsington Road, Oxford OX4 2DQ, UK

550 Swanston Street, Carlton, Victoria 3053, Australia

The right of Yanghua Wang to be identified as the author of this work has been asserted in accordance with the UK Copyright, Designs, and Patents Act 1988.

All rights reserved. No part of this publication may be reproduced, stored in a retrieval system, or transmitted, in any form or by any means, electronic, mechanical, photocopying, recording or otherwise, except as permitted by the UK Copyright, Designs, and Patents Act 1988, without the prior permission of the publisher.

Designations used by companies to distinguish their products are often claimed as trademarks. All brand names and product names used in this book are trade names, service marks, trademarks, or registered trademarks of their respective owners. The publisher is not associated with any product or vendor mentioned in this book.

This publication is designed to provide accurate and authoritative information in regard to the subject matter covered. It is sold on the understanding that the publisher is not engaged in rendering professional services. If professional advice or other expert assistance is required, the services of a competent professional should be sought.

First published 2008 by Blackwell Publishing Ltd

1 2008

Library of Congress Cataloging-in-Publication Data

Wang, Yanghua.

Seismic inverse Q filtering / by Yanghua Wang.

p. cm.

Includes bibliographical references and index.

ISBN 978-1-4051-8540-0 (hardcover : alk. paper)

1. Seismic traveltimes inversion. 2. Seismic reflection method--Deconvolution. 3. Amplitude variation with offset analysis. 4. Seismic tomography. 5. Seismology--Mathematical models. I. Title.

QE539.2.S43W36 2008

551.22028'7--dc22

2008000305

A catalogue record for this title is available from the British Library.

Set in 11 Times New Roman

by Yanghua Wang

Printed and bound in Singapore

by Markono Print Media Pte Ltd

The publisher's policy is to use permanent paper from mills that operate a sustainable forestry policy, and which has been manufactured from pulp processed using acid-free and elementary chlorine-free practices. Furthermore, the publisher ensures that the text paper and cover board used have met acceptable environmental accreditation standards.

For further information on

Blackwell Publishing, visit our website at

www.blackwellpublishing.com

Contents

Preface	viii
1 Introduction to inverse Q filtering	1
1.1 The earth Q effect on seismic waves	2
1.2 Inverse Q filters	5
1.3 The effectiveness of inverse Q filtering	8
Part I Mathematical Q models	15
2 Kolsky's model for seismic attenuation and dispersion	17
2.1 Kolsky's attenuation-dispersion model	18
2.2 Modification to the Kolsky model	19
2.3 Accurate velocity dispersion correction	22
2.4 Comparison with different Q models	25
3 Mathematical definition of the earth Q models	39
3.1 Mathematical definition of Q	40
3.2 Kolsky's Q model and the complex wavenumber	44
3.3 The Strick–Azimi Q model	46
3.4 Kjartansson's constant- Q model	46
3.5 Azimi's second and third Q models	47
3.6 Müller's Q model	48
3.7 The Zener or standard linear solid model	50
3.8 The Cole–Cole Q model	52
3.9 A general linear model	54

Part II	Inverse Q filters	57
4	Stabilized inverse Q filtering algorithm	59
4.1	Basics of inverse Q filtering	60
4.2	Numerical instability of inverse Q filtering	62
4.3	Stabilized inverse Q filter	66
4.4	Comparison with gain-limited inverse Q filter	68
4.5	Comparison with a conventional inverse Q filter	74
4.6	Synthetic and real data examples	79
5	Inverse Q filtering for phase and amplitude separately	85
5.1	Phase-only inverse Q filtering	86
5.2	Amplitude-only inverse Q filtering	87
5.3	Forward Q filtering	90
5.4	Summary of inverse and forward Q filters by downward continuation	93
5.5	Different stabilization schemes	95
6	Layered implementation of inverse Q filters	99
6.1	The layered approach to inverse Q filtering	100
6.2	Inverse Q filtering within a constant- Q layer	103
6.3	Phase- or amplitude-only inverse Q filtering	107
6.4	Forward Q filtering	110
6.5	Application of layered inverse Q filtering	113
7	Inverse Q filtering in the Gabor transform domain	119
7.1	Stabilized inverse Q filter	120
7.2	The Gabor transform	122
7.3	Inverse Q filtering by Gabor transform	125
7.4	Forward Q filtering by Gabor transform	126
7.5	An empirical formula for the stabilization factor	128
8	The effectiveness of stabilized inverse Q filtering	133
8.1	Inverse Q filtering of a land seismic section	134
8.2	Flattening the amplitude spectrum and strengthening the relative amplitude	136
8.3	Increasing the spectral bandwidth	139
8.4	Improving the signal-to-noise ratio	140
8.5	Enhancing seismic resolution	141

8.6	Sensitivity of the resolution enhancement to Q values	143
9	Migration with inverse Q filtering	147
9.1	Inverse Q filtered migration in the wavenumber-frequency domain	148
9.2	Stabilized migration with lateral variation in velocity and Q models	156
9.3	The implicit finite-difference extrapolator in the space-frequency domain	159
9.4	Migration examples	162
Part III	Q estimation	167
10	Q estimation from vertical seismic profiling data	169
10.1	The attenuation effect on VSP waveform	170
10.2	Spectral ratio method for Q estimation	174
10.3	The multitaper technique for spectral estimation	176
10.4	Robust Q estimation from real VSP data	181
11	Q analysis from reflection seismic data	187
11.1	Q analysis based on amplitude attenuation	188
11.2	Q analysis based on amplitude compensation	195
11.3	Correction of spherical divergence prior to Q analysis	199
11.4	Q analyses on the P - P and P - SV wave sections	201
12	Crosshole seismic tomography for the Q model	209
12.1	Inverse theory for waveform tomography	211
12.2	Issues in real data application	215
12.3	Waveform inversion for the velocity model	218
12.4	Waveform tomography for the attenuation model	222
	References	227
	Author index	235
	Subject index	237

Preface

Seismic inverse Q filtering is a data-processing technology for enhancing the resolution of seismic images. When seismic waves propagate through the earth subsurface, the anelasticity and inhomogeneity of the subsurface media will have two effects on the seismic waves. One is the dissipation effect as the wave energy is absorbed by the media. The other is velocity dispersion, where different frequency components travel with different speeds. Consequently, it is observed in a seismic profile that the amplitude of the wavelet generally decreases with depth and the width of the wavelet gradually broadens with increased traveltime. Inverse Q filtering is a wave propagation-reversal procedure that compensates for the energy absorption and corrects the wavelet distortion in terms of the shape and timing, to produce a seismic image of very high resolution.

As seismic techniques move more from exploration to hydrocarbon development and production, the need for increased resolution becomes more acute. This monograph presents the theory of inverse Q filtering and a series of algorithms, collected with the following selection criteria in mind: robustness, effectiveness and practicality. By compensating for the amplitude attenuation, seismic data may provide true relative-amplitude information for the amplitude inversion and subsequent reservoir characterization. By correcting the phase distortion, seismic data with enhanced vertical resolution may provide correct timings for lithological identification. When applying amplitude compensation and phase correction simultaneously, real data examples show superior pictures which facilitates seismic interpretation for reservoir geophysics.

The book consists of three parts. Part I presents different mathematical Q models that can be used in designing inverse Q filters. Part II presents a variety of inverse Q filtering algorithms for amplitude compensation and

phase correction simultaneously or separately. As these inverse Q filters are model-based, Part III presents procedures for estimating Q values from borehole seismic data and from reflection seismic data recorded at the earth surface. Each chapter begins with an abstract to orient the reader as to the various topics to be discussed and their relationship to each other.

One of the highlights of this book is the stabilization of any proposed inverse Q filtering algorithm. A quantitative measurement of seismic resolution enhancement by an inverse Q filter is not only a function of the change in seismic bandwidth but also a function of the change in signal-to-noise ratio. A problem with conventional inverse Q filters is that they might increase seismic bandwidth but degrade the signal-to-noise ratio, and thus might not improve the overall resolution. Stabilized inverse Q filters can have positive changes in both the bandwidth and signal-to-noise ratio and, in turn, reinforce the improvement in seismic resolution.

This book is written for readers who do not necessarily have expert knowledge of seismic theory or the mechanics of wave propagation through anelastic media. It is written for practitioners who are attempting to improve seismic quality in terms of resolution and signal-to-noise ratio, such as processing geophysicists, and who are concerned about seismic fidelity in terms of true amplitudes, true timings and true frequencies, such as reservoir geophysicists. It is written particularly as a guide book for seasoned geophysicists who are attempting to develop seismic software for various research settings. It is also a reference work or textbook for postgraduate students in seismic and reservoir geophysics.

The author acknowledges *Geophysics*, *Geophysical Research Letters*, *Journal of Geophysics and Engineering* and *Geophysical Journal International* for their permission to reproduce in this monograph published materials from the author's research articles. The author is also grateful to the sponsors of the Centre for Reservoir Geophysics at Imperial College London.

Yanghua Wang

Professor of Reservoir Geophysics
Director, Centre for Reservoir Geophysics
Imperial College London, UK

June 2007

Chapter 1

Introduction to inverse Q filtering

Abstract When seismic waves propagate through the earth subsurface, the absorption and dispersion effects will cause attenuation of wave amplitudes and shape distortion of seismic waveforms. Inverse Q filtering is a wave propagation-reversal processing that removes these effects from recorded seismic data. After inverse Q filtering, seismic data will have improved quality with correct amplitudes and phases, which will result in better matching with the well-log information, higher resolution for thin-layer interpretation and reliable seismic inversion for reservoir characterization.

High-resolution seismic data are needed for detailed descriptions of oil and gas reservoirs; for determination of spatial heterogeneities such as the spatial variation of porosity, gas content or pore pressure; and for monitoring temporal changes within a reservoir that result from production. Although the development of new methods for high-resolution seismic data acquisition is important, maximum immediate benefit can be obtained by applying methods that can improve the resolution of existing seismic data sets and that can be used with new data sets acquired with existing systems. This book discusses one such resolution-enhancement technique, inverse Q filtering.

Anelasticity and inhomogeneity in the subsurface dissipate high-frequency seismic energy, which decreases seismic amplitudes; they also cause velocity dispersion, thus modifying, delaying and stretching seismic wavelets. Because these two effects, dissipation and dispersion, are

interrelated, they are simply referred to as the attenuation effect.

The attenuation effect is inversely proportional to the earth quality factor, or the Q factor. Quantitatively, the attenuation coefficient is approximately $27.3Q^{-1}$ dB per wavelength. That is, the attenuation is frequency-dependent. With the dissipation effect, the amplitude of a high-frequency wave component is attenuated more than that of a low-frequency component. For the dispersion effect, a high-frequency wave component travels faster than a low-frequency component, and the phase of the wavelet varies along the travel path. Thus the recorded seismic data appear to have weak amplitudes and broadened wavelets, resulting in a low signal-to-noise ratio and low resolution.

These two frequency-dependent effects, or the earth Q filtering effect, on the seismic records require suitable treatment to produce a high-resolution subsurface reflectivity image. This treatment is generally referred to as inverse Q filtering. It performs the amplitude compensation and the phase correction separately or simultaneously. The ultimate purposes of the inverse Q filtering process are to enhance the resolution and improve the signal-to-noise ratio of seismic data.

1.1 The earth Q effect on seismic waves

1.1.1 The form of seismic waves

Ricker (1953) asked the following two questions: ‘What is the form of the seismic disturbance which proceeds outward from the explosion of a charge of dynamite in the earth, and what are the laws of propagation of this disturbance?’

The classical wave equation is expressed as

$$\nabla^2 \Phi = \frac{1}{c^2} \frac{\partial^2 \Phi}{\partial t^2}, \quad (1.1)$$

where c is the speed of the wave propagation, t is the traveltime and Φ is the pressure. To properly explain seismic phenomena with dissipation, however, it is necessary to make use of Stokes’ (1845) wave equation:

$$\nabla^2 \left[\Phi + \frac{1}{\omega_0} \frac{\partial \Phi}{\partial t} \right] = \frac{1}{c^2} \frac{\partial^2 \Phi}{\partial t^2}, \quad (1.2)$$

where ω_0 is a transition frequency related to the viscoacoustic properties by

$$\frac{1}{\omega_0} = \frac{\eta_1 + \frac{4}{3}\eta_2}{\rho c^2}. \quad (1.3)$$

Here, η_1 and η_2 are the viscoacoustic coefficients, and ρ is the density. Comparing wave equations (1.1) and (1.2), the dissipation term $\omega_0^{-1}\partial/\partial t$ in the viscoacoustic wave equation (1.2) contributes towards the shaping of the wavelet form and towards determining its laws of propagation. It is never possible to neglect the dissipation term, however great the value of ω_0 .

The solution of Stokes' differential equation (1.2) may be written in the form of a series of wavelet functions, such as displacement, velocity and acceleration. These functions represent the seismic behaviour of the earth when the displacement at the shot point is a sharp impulse, and show the manner in which the shape, breadth and amplitude of the disturbance vary with the travel distance from the source (Thompson, 1933; Ricker, 1943; Kolsky, 1953).

These theoretical waveforms were confirmed to be in a good agreement with observations in an extensive number of experiments, for example, Ricker (1953), and Kolsky (1956).

1.1.2 The attenuation coefficient

The disturbance of wavelets is caused by the dissipation effect or the earth Q effect. For a plane sinusoidal stress wave travelling through a viscoelastic material, the dissipation is traditionally related to the reciprocal of the Q factor, which is the ratio of the fractional energy loss ΔW per cycle of strain harmonic motion to the maximum energy W stored in a material specimen at the beginning of the cycle, by

$$\frac{1}{Q} = \left(\frac{1}{2\pi} \right) \frac{\Delta W}{W}. \quad (1.4)$$

The Q^{-1} factor may also be defined as the tangent of the phase lag between stress and strain, which are linked by the modulus.

The attenuation coefficient, α , is a quantity which measures energy absorption, and is related to Q^{-1} by

$$\alpha = \left(\frac{\omega}{2c} \right) \frac{1}{Q}. \quad (1.5)$$

This equation shows the linear dependency of the attenuation coefficient on the frequency ω , if the quality factor Q is independent of frequency. Such a linear dependency has been observed in many laboratory experiments (Peselnick and Zietz, 1959; Peselnick and Outerbridge, 1961; Toksöz *et al.*, 1979), and in field measurements (McDonal *et al.*, 1958; Tullis and Reid, 1969; Hamilton, 1972; Harris *et al.*, 1997). [Note that there are also many observations that the attenuation coefficient cannot be assumed to be linearly dependent upon the first power of frequency; for example, Shumway (1960) and Jacobson (1987).]

Equation (1.5) may be represented in terms of wavelength λ , as

$$\alpha = \frac{\pi}{\lambda Q} \text{ (nepers/unit length)} = \frac{20 \pi}{(\ln 10) Q} \text{ (dB / } \lambda \text{)}, \quad (1.6)$$

which leads to the approximation mentioned above; that is, $27.3Q^{-1}$ dB per wavelength (Johnston and Toksöz, 1979).

1.1.3 Attenuation-dispersion relation

The presence of attenuation requires the presence of dispersion, according to the principle of causality (Aki and Richards, 1980). Lomnitz (1957) and Futterman (1962) showed that for a linear system, dispersion must always accompany absorption, and that absorption and dispersion are unambiguously related.

Let us consider a plane wave, at travel distance x and time t ,

$$U(x, t) = U_0 \exp[i (\omega t - kx)], \quad (1.7)$$

where k is the wavenumber. When it propagates in inhomogeneous media, the propagation constant k must be a complex value that includes not only an imaginary part, the frequency-dependent attenuation coefficient, but also a real part, the dispersive wavenumber:

$$k = \kappa - i \alpha. \quad (1.8)$$

Then the waveform $U(x, t)$ is given by

$$U(x, t) = U_0 \exp[-\alpha x] \exp[i(\omega t - \kappa x)]. \quad (1.9)$$

This expression clearly indicates that α is the attenuation coefficient, and $\kappa \equiv \text{Re}(k)$ is related to the phase of a plane wave. Setting the phase to be stationary, the dispersive phase velocity is

$$v(\omega) = \frac{\omega}{\kappa}. \quad (1.10)$$

For a linear theory of wave propagation, the presence of absorption is a necessary and sufficient condition for the presence of dispersion. Futterman (1962) suggested that the attenuation-dispersion relation could be of the Kramers–Krönig type (Krönig, 1926; Kramers, 1927). Using the Kramers–Krönig dispersion relation, the real part of the wavenumber can be determined from the values of the imaginary part summed over the entire range of frequencies for wave motions that are linear.

Note that the Kramers–Krönig dispersion relation yields the dispersion directly from the absorption coefficient, and yields no information about the physical mechanism that accounts for the absorption and the corresponding dispersion. But this theoretical treatment of dispersive body waves fits well with the experimental data, as shown by Wuenschel (1965), Strick (1970), Brennan and Stacey (1977), Winkler (1986) and Sams *et al.* (1997), among many others.

In the first part of this book (Chapters 2 and 3), we will review and compare different earth Q models. These different models are defined mathematically by different attenuation coefficients $\alpha(\omega)$ and associated dispersive phase velocities $v(\omega)$. Understanding the similarity and difference between these models will give us confidence about whether the inverse Q filters designed using different mathematical Q models are interchangeable and if the filtered results are comparable with each other.

1.2 Inverse Q filters

For the inverse Q filter, we should realize that there are two fundamental assumptions made in the theory of earth Q filtering: (a) the attenuation coefficient $\alpha(\omega)$ is strictly linear in the frequency, over the range of

measurement; and (b) the wave motion is linear, i.e. the principle of superposition is valid.

Based on the second assumption, we can sum all inverse Q filtered plane waves to generate a time domain seismic trace. This is called the imaging condition.

1.2.1 Inverse Q filter for dispersion

When a mechanical pulse is propagated through a viscoelastic solid it is dispersed, as the high-frequency components travel faster and are attenuated more rapidly than those of lower frequency. The dispersion effect is most pronounced at high record times corresponding to deep reflectors. When we correlate a synthetic seismic trace (derived from well logs) with a seismic trace actually recorded at the surface, we can see mismatch commonly caused by the dispersion effect.

Robinson (1979) introduced a dispersion quantity that linked the Q factor to the dispersion as

$$\mu = \frac{10^3 \ln 2}{\pi Q}. \quad (1.11)$$

This dispersion quantity μ has units of ‘mose’: ms/oct/s. That is, at a dispersion rate of one *mose*, there would accumulate 1 *ms* of time advance for each *second* of seismic traveltime for a frequency component (e.g. 20 Hz) of the propagating waveform relative to the component at one *octave* less than (one-half) that frequency (i.e. 10 Hz).

To correct for the frequency-dependent time shift caused by velocity dispersion, Robinson (1979) proposed an algorithm implemented through frequency-dependent rescaling and interpolation. Robinson (1982) improved the efficiency by introducing a phased sinc function for the interpolation in the frequency domain.

Hargreaves and Calvert (1991) pointed out that Robinson’s frequency-domain rescaling and interpolation method was analogous to the Stolt (1978) migration algorithm, and developed an inverse Q filter approach. The Stolt (1978) migration method is a frequency domain method and assumes a constant-velocity model. Hargreaves and Calvert’s (1991) phase-only inverse Q filter works also for a time-invariant Q model. With fast Fourier transforms this method is highly efficient to implement. However,

when applying this method to a variant Q model, recursion has to be employed. Therefore, the efficiency of this method is case-dependent. Bano (1996) extended Hargreaves and Calvert's (1991) constant- Q method to a multi-layered earth. Within each layer, the pre-mentioned constant- Q method is performed.

The 'similarity' principle (Bracewell, 1965) states that given a frequency spectrum $G(\omega)$ of a function $g(t)$, a frequency-scaled version $G(m\omega)$ of the spectrum can be written as a time function $m^{-1}g(m^{-1}t)$. Thus, the above frequency-domain implementation has an equivalent counterpart in the time domain. According to the 'similarity' property, the frequency scaling caused by attenuation gives rise to a time and amplitude scaling of the Q filter response. Carpenter (1966) used this property to derive a method of computing forward Q filters for varying traveltimes and Q . In the context of inverse Q filter, Robinson (1979, 1982), Hargreaves (1992), and Bickel (1993) used similarity to derive efficient algorithms to correct for dispersive phase shifts.

Although Q is seldom known to a high degree of precision, conservative inverse Q filtering almost always improves data quality. Since it is possible to perform inverse Q filtering for dispersion correction cheaply and accurately, it has become a practical routine in real seismic data processing.

1.2.2 Inverse Q filter for dispersion and absorption simultaneously

The phase-only inverse Q filter mentioned above is unconditionally stable. However, if including the accompanying amplitude compensation in the inverse Q filter, stability is a major issue of concern in the implementation.

Hale (1981, 1982) found that the inverse Q filter overcompensated the amplitudes for the later events in a seismic trace. In order to obtain reasonable amplitude, the amplitude spectrum of the computed filter has to be clipped at some maximum gain to prevent undue amplitude at later times. This gain limitation causes not only the ambiguity of amplitude but also influences the phase action of the filter since the minimum phase spectrum of this algorithm is determined by the clipped amplitude spectrum. Therefore, although Hale's approach is efficient, the result could be one that is not desired.

Bickel and Natarajan (1985) suggested that for a fixed distance between the source and receiver the effects of the propagation path can be deconvolved (removed) within the seismic band by reversing the propaga-

tion of the plane wave. As the inverse filter must be time-varying, the deconvolution is implemented by filtering the observed trace with the forward time-varying filter, in which the absorption is replaced by gain in the complex wavenumber, to realize the reversal of the propagation effects.

In Hale's (1982) deconvolution method, there is an incompatibility between the digital minimum phase which is estimated during the deconvolution process, and the phase which is computed from the theoretical dispersive models. Varela *et al.* (1993) modified Hale's algorithm in a manner such that the treatment of phase is compatible with the Futterman dispersive model.

Wang (2002, 2006) proposed a stabilized inverse Q filtering approach that is able to compensate simultaneously for both attenuation and dispersion. The proposed method is based on wave extrapolation by using downward continuation theory. The algorithm may also be implemented in a layered manner or in the Gabor transform domain, to afford greater efficiency. The theoretical background and implementation of this are covered in the second part of this book, consisting of Chapters 4–9.

The inverse Q filter algorithms presented in this book are model-based. The third part of this book covers techniques for Q estimation from borehole and surface seismic data.

1.3 The effectiveness of inverse Q filtering

What can an inverse Q filter do to the seismic data? Before we start to view the theoretical and technical details, in this opening chapter, I would like to display some applications on real seismic data, and demonstrate three important improvements made by inverse Q filtering as follows.

1.3.1 Better seismic matching with well-log data

Figure 1.1 is a comparison between seismic impedance sections and impedance synthetics from well-logging information. The impedance section displayed in Figure 1.1a is inverted from seismic data without inverse Q filtering, whereas the impedance section shown in Figure 1.1b is extracted from seismic data after applying the inverse Q filter. The inverse Q filter corrects the dispersion effect of wave propagation and results in much better matching between the seismic and the synthetic.

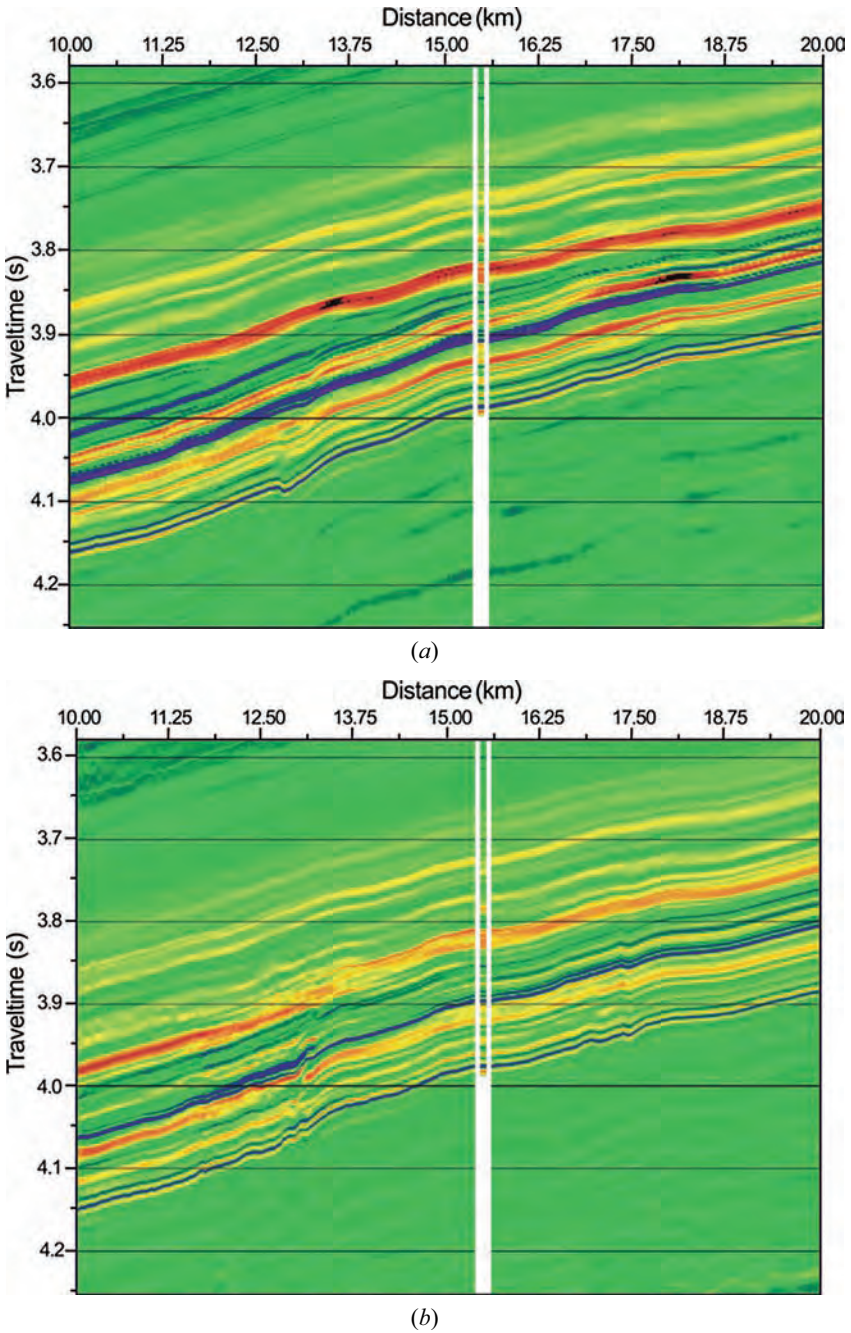


Figure 1.1 Comparison of seismic impedance sections and the impedance synthetics from well-logging information. (a) Seismic impedance section extracted from seismic data without inverse Q filtering. (b) Seismic impedance section after inverse Q filtering. The latter has much better matching between the seismic section and well-log information.

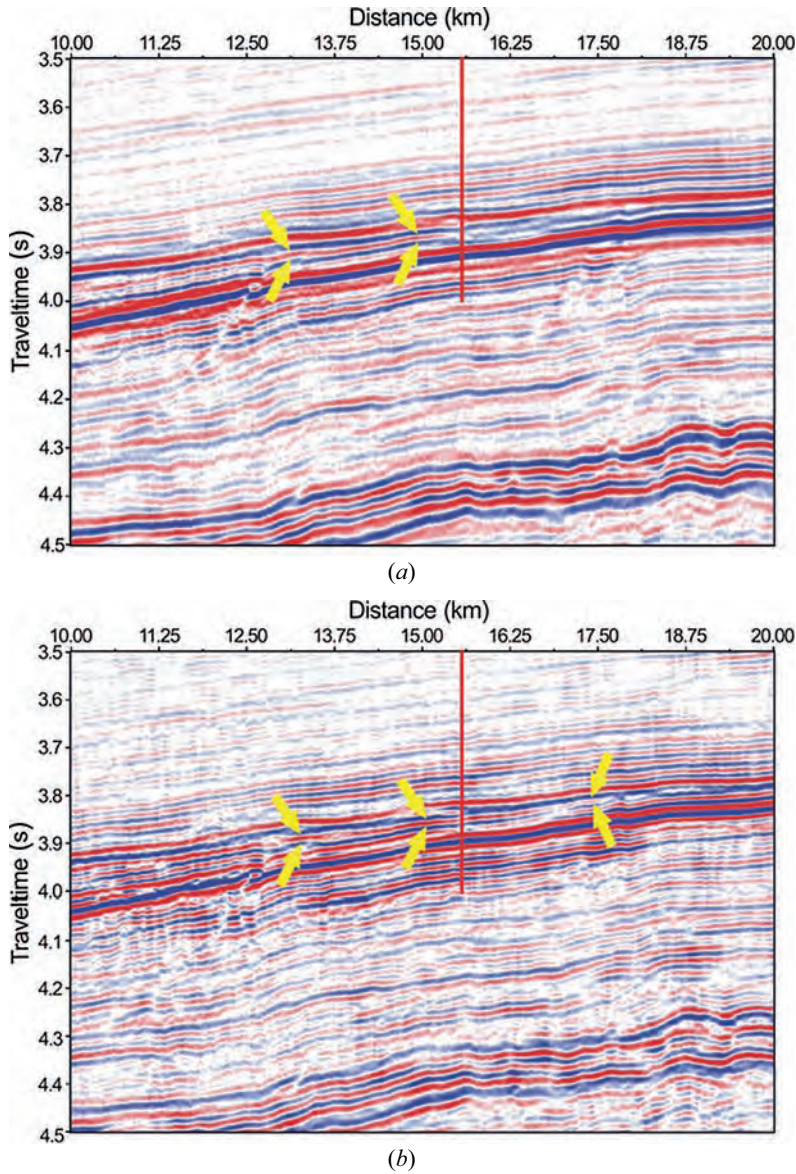


Figure 1.2 Inverse Q filtering on a real three-dimensional seismic data set: (a) and (b) are an in-line section before and after inverse Q filtering, respectively.

1.3.2 Enhanced seismic resolution

Figure 1.2 displays seismic sections extracted from a three-dimensional seismic data cube, where arrows indicate the reservoir layer and the vertical

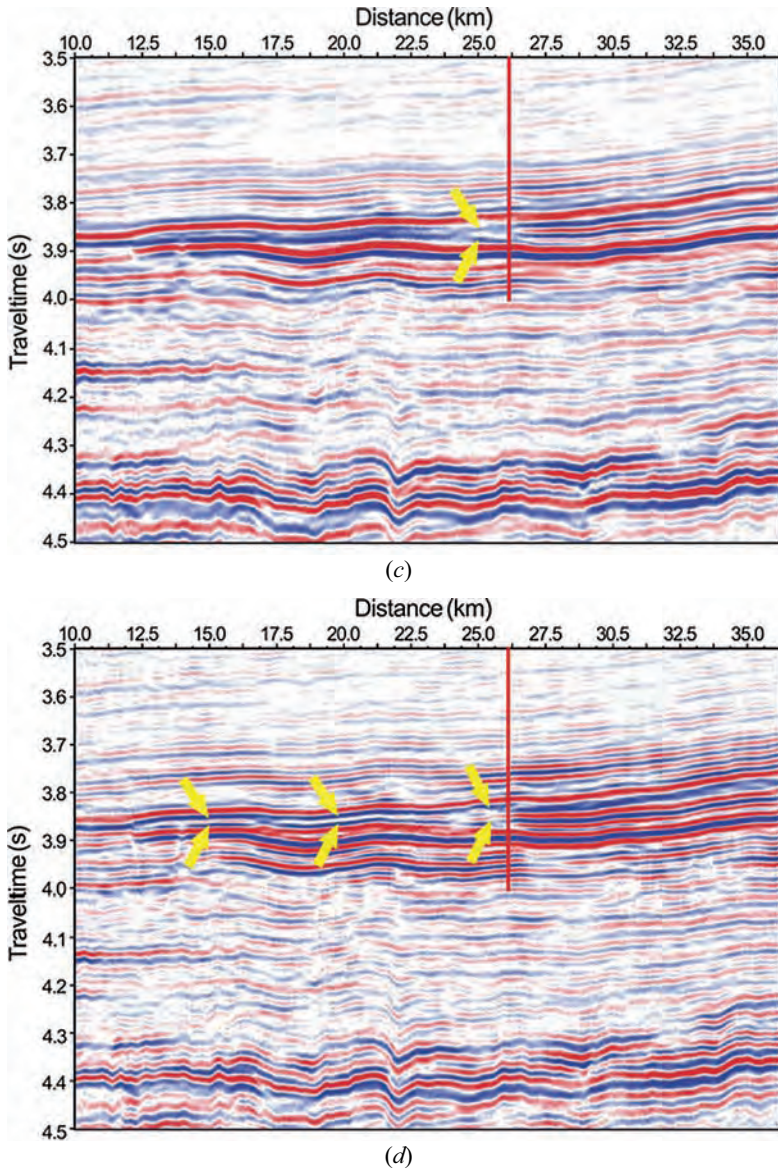


Figure 1.2 (contd) (c) and (d) are a crossline section before and after inverse Q filtering, respectively. Arrows indicate the reservoir and the vertical line is the exploration well.

line is the exploration well. The inverse Q filter will increase the frequency bandwidth and shrink the breadth of seismic waveforms. Comparing the in-line sections in panels (a) and (b), or comparing the cross-line sections (c) with (d), we can see that, after inverse Q filtering, the target thin reservoir

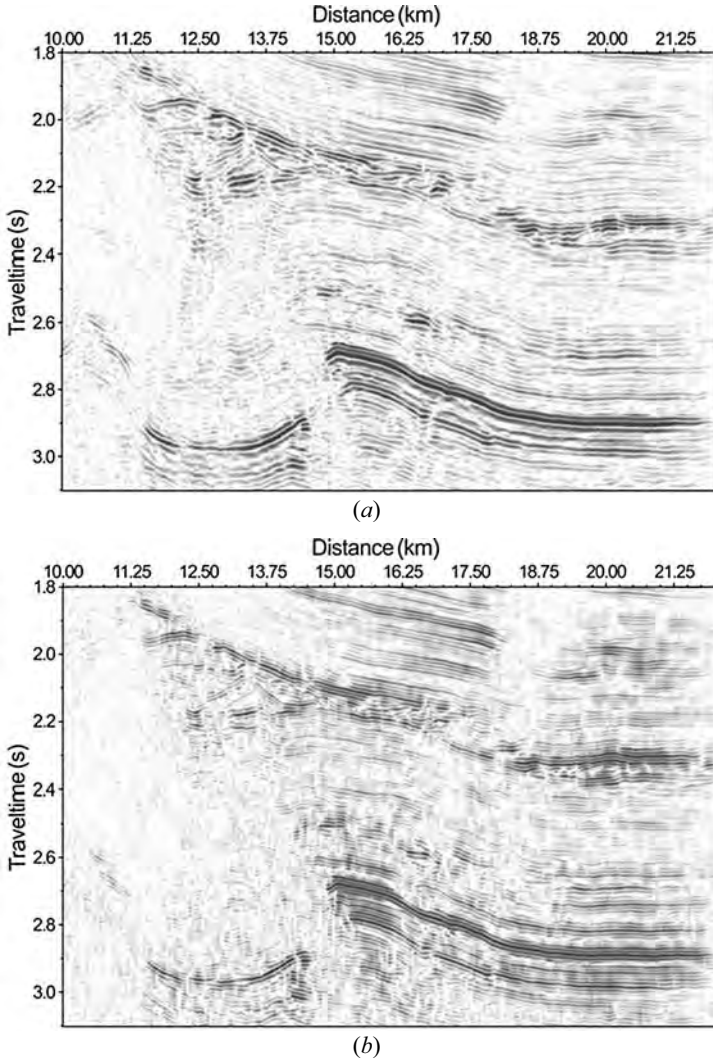


Figure 1.3 Inverse Q filtering on a real three-dimensional seismic data set: (a) and (b) are seismic sections before and after applying the inverse Q filter, respectively.

clearly stands out, with encouraging spatial extension.

1.3.3 Better reservoir characterization

Figure 1.3 compares two seismic sections before and after inverse Q filtering, whereas Figure 1.4 compares the velocity profiles inverted from these two seismic sections. Because the inverse Q filter processing

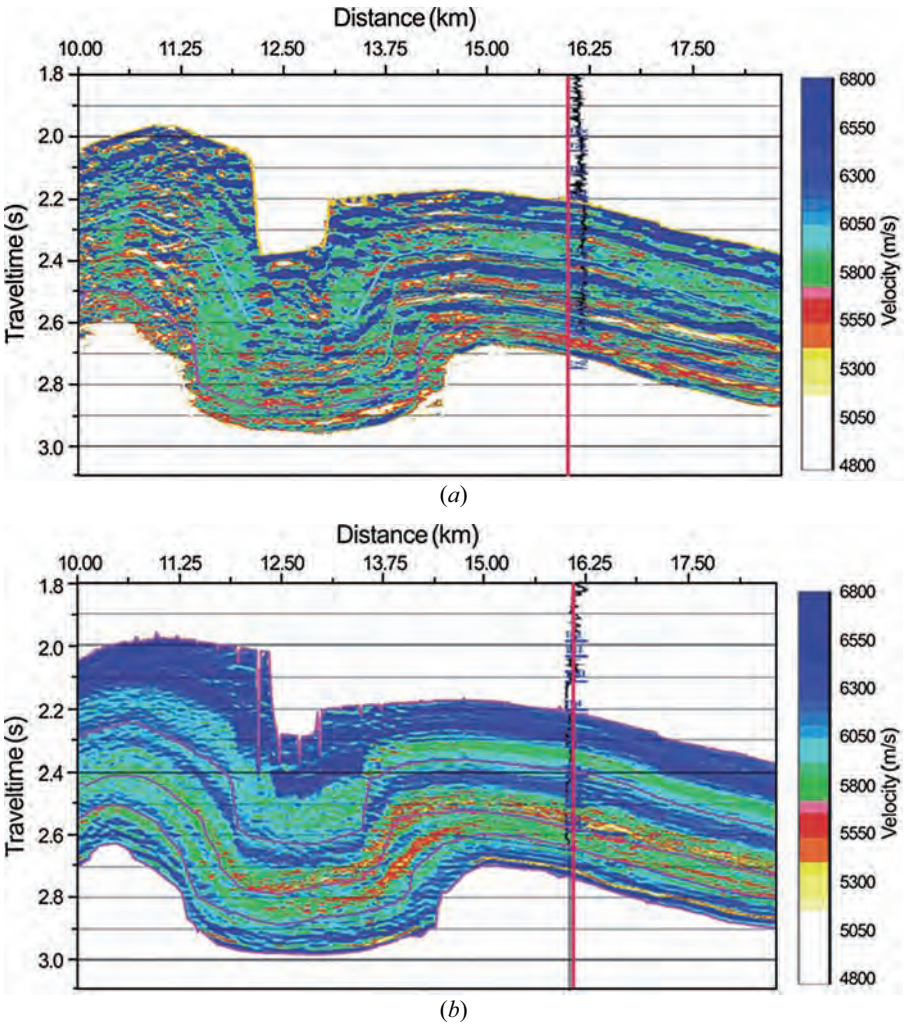


Figure 1.4 The effect of inverse Q filtering on seismic inversion: (a) and (b) are velocity profiles inverted from the sections before and after the inverse Q filter, respectively.

compensates the amplitude and corrects the phase of waveforms, the resultant inversion profile, which has much higher signal-to-noise ratio, clearly highlights the lateral heterogeneity of a carbonate gas reservoir in this case (2.5–2.6 s at the well location shown by the vertical line).

Part I

Mathematical Q models

Chapter 2

Kolsky's model for seismic attenuation and dispersion

Abstract

Frequency-dependent amplitude attenuation and velocity dispersion may be defined conveniently as the earth quality factor, or the Q factor. Kolsky's Q model is widely used for its simplicity in seismic data processing, but does not rigorously satisfy the minimum delay criterion. This chapter modifies Kolsky's basic Q model to produce an accurate representation of the velocity dispersion within the seismic frequency band. Such a modification may lead to: (1) an accurate phase correction in the inverse Q filtering that follows and (2) a good match to other, different earth Q models. The latter suggests that, when applying different mathematical earth Q models to design an inverse Q filter, filtered seismic profiles should in principle be comparable with each other.

Two fundamental properties associated with seismic wave propagation through subsurface materials are the energy dissipation of plane waves with high frequencies, and the velocity dispersion causing high-frequency plane waves to travel faster than low-frequency waves. Mathematically, these dissipation and dispersion effects of the viscoacoustic media may be represented by a specified quality factor, Q :

$$Q(\omega) = \frac{|\omega|}{2\alpha(\omega)v(\omega)}, \quad (2.1)$$

where ω is the angular frequency, $v(\omega)$ is the phase velocity and $\alpha(\omega)$ is the attenuation coefficient in units of inverse length. Equation (2.1) is a key formula for the earth Q model (Kolsky, 1953; Mason, 1958; Futterman, 1962) and is valid under a low-loss assumption, $Q \gg 1$. Such a small dissipation assumption is valid under most conditions of interest in geophysics. In geophysics literature, different earth Q models are expressed in terms of different definitions of the attenuation coefficient $\alpha(\omega)$ and different definitions of the phase velocity $v(\omega)$. Before we start discussing the design and application of an inverse Q filter, we need first to specify a mathematical Q model.

There is a wide range of mathematical definitions of the Q model presented in the literature. In this chapter, we first review the basic Kolsky (1953) model that is used extensively in seismic inverse Q filtering as the parameters involved are relatively easy to estimate from a seismic data set itself or some other seismic measurements. Then we propose to modify the Kolsky's basic attenuation-dispersion model in an attempt to accurately represent the velocity dispersion effect within the seismic frequency band. Finally, we compare the modified Kolsky model with other different Q models.

If one compares the basic Kolsky model with other different mathematical Q models, one finds that different models were not close to the basic Kolsky model. Ursin and Toverud (2002) for example tried this kind of comparison by using a set of analytically derived parameters. In this chapter, we show that, using a modified Kolsky model, we are able to derive a set of parameters analytically to match each of the different Q models fairly closely. Such a modification is initiated primarily by making Kolsky's model be comparative with a model satisfying a dispersion condition that is necessary to preserve the causality of a propagating wavelet. Such a dispersion condition is called the Kramers–Krönig dispersion relation (Krönig, 1926; Kramers, 1927) and is satisfied by different models other than the Kolsky model. Use of the modified Kolsky model will result in the following two benefits: an accurate phase correction in inverse Q filtering and a good match to other, different Q models.

2.1 Kolsky's attenuation-dispersion model

The Kolsky model (Kolsky, 1953) assumes the attenuation $\alpha(\omega)$ to be strictly linear with frequency over the range of measurement:

$$\alpha(\omega) = \frac{|\omega|}{2v_r Q_r}, \quad (2.2)$$

and defines the phase velocity as (Kolsky, 1956):

$$\frac{1}{v(\omega)} = \frac{1}{v_r} \left(1 - \frac{1}{\pi Q_r} \ln \left| \frac{\omega}{\omega_r} \right| \right), \quad (2.3)$$

where v_r and Q_r are the phase velocity and the Q value at a reference frequency, ω_r , respectively. Kolsky's model was derived from and fitted well with experimental observations (Hillier, 1949; Kolsky, 1956).

For a large value of $Q_r \gg 1$, the phase velocity can be approximated to

$$\frac{1}{v(\omega)} \approx \frac{1}{v_r} \left| \frac{\omega}{\omega_r} \right|^{-\frac{1}{\pi Q_r}}. \quad (2.4)$$

Here we usually define a γ factor as

$$\gamma = \frac{1}{\pi Q_r}. \quad (2.5)$$

A requirement in the theory for materials satisfying the linear attenuation assumption is that the reference frequency ω_r is a finite (arbitrarily small but nonzero) cut-off on the absorption. According to Kolsky (1956) and Futterman (1962), we are free to choose ω_r following the phenomenological criterion that it be small compared with the lowest measured frequency ω . However, the basic Kolsky model does not satisfy the minimum delay condition in dispersive earth media, and the latter is described rigorously by the Kramers–Krönig dispersion relation. It is necessary to modify it so that an inverse Q filter is able to fully correct the velocity dispersion.

2.2 Modification to the Kolsky model

The phase velocity formula given in the basic Kolsky model is now modified by setting an appropriate reference frequency, to minimize the

phase errors in inverse Q filtering for seismic data processing (Wang and Guo, 2004b).

Recall that in the Kolsky model, given the attenuation coefficient (2.2), the phase velocity is defined by equation (2.3). This expression, however, is merely an asymptotic formula for $\omega \gg \omega_r$ (Futterman, 1962). For exploration seismic data, which have relative low frequencies (say, ≤ 500 Hz), we propose to modify the preceding expressions (2.3) and (2.4) as follows:

$$\frac{1}{v(\omega)} = \frac{1}{v_r} \left(1 - \frac{1}{\pi Q_r} \ln \left| h \frac{\omega}{\omega_r} \right| \right) \approx \frac{1}{v_r} \left| h \frac{\omega}{\omega_r} \right|^{-\gamma}, \quad (2.6)$$

where h is a frequency-independent constant. Combining ω_r and h into a single parameter, we have the following expression:

$$\frac{1}{v(\omega)} = \frac{1}{v_r} \left(1 - \frac{1}{\pi Q_r} \ln \left| \frac{\omega}{\omega_h} \right| \right) \approx \frac{1}{v_r} \left| \frac{\omega}{\omega_h} \right|^{-\gamma}, \quad (2.7)$$

where ω_h is a new, undetermined, tuning parameter. This tuning parameter still has units of frequency, but is no longer the smallest frequency of the seismic band. We now show that for seismic exploration, the tuning constant ω_h is the highest possible seismic frequency.

The exact mechanism of seismic dispersion through the earth is unknown. If possible a generic model should be considered when designing an inverse Q filter. One such generic condition is the minimum delay described by the Kramers–Krönig dispersion relation:

$$\frac{\omega}{v(\omega)} - \frac{\omega}{v_\infty} = \mathcal{H}\{\alpha(\omega)\}, \quad (2.8)$$

where $\mathcal{H}\{\cdot\}$ denotes the Hilbert transform and v_∞ is the limit of $v(\omega)$ as $\omega \rightarrow \infty$.

Given the attenuation coefficient (2.2), we now compare the phase velocity (2.7) in the modified Kolsky model with the phase velocity estimated using the Kramers–Krönig dispersion relation (2.8). The comparison shown in Figure 2.1 (the left column) is made through the wavenumber, the real part of the complex wavenumber in equation (1.8).

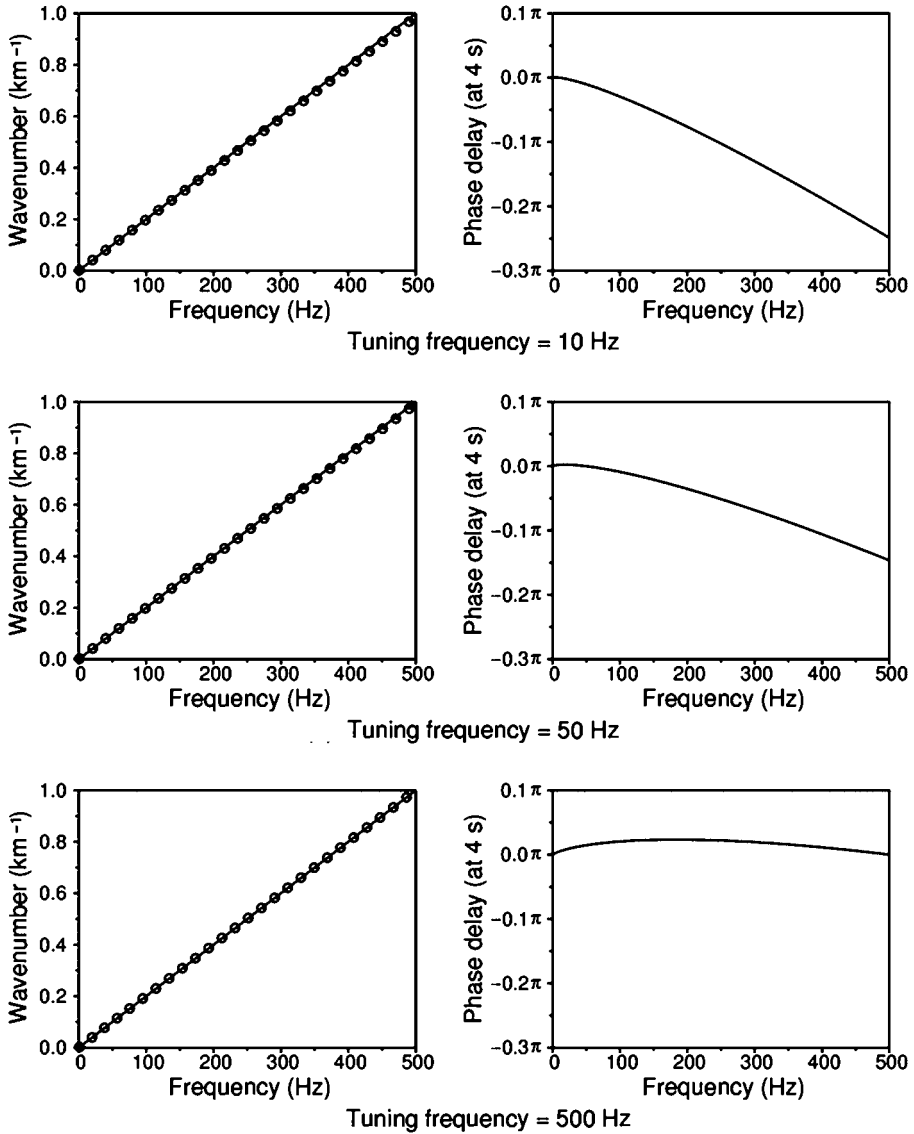


Figure 2.1 The wavenumber differences (left column) between the wavenumber numerically obtained from the Hilbert-transforming method (solid lines) and the analytical wavenumber in the Kolsky model (circled lines), and the associated phase delays (right column) caused by the wavenumber difference. In the three rows, the tuning frequencies used are 10, 50 and 500 Hz, respectively. The phase delays are estimated at a two-way time of 4 s. The conclusion drawn from this figure is that a 500 Hz tuning frequency should be used in designing the inverse Q filter to process reflection seismic data of 4 s.

The circled lines in Figure 2.1 are the real wavenumbers defined by

$$\text{Re}(k) \equiv \kappa = \frac{\omega}{v(\omega)}, \quad (2.9)$$

in which the modified phase velocity from the Kolsky model is used. The solid lines are the wavenumbers obtained numerically from the Kramers–Krönig dispersion relation:

$$\kappa \approx \mathcal{H}\{\alpha(\omega)\}. \quad (2.10)$$

Note that an approximation is made here, as the term ω/v_∞ is omitted. This wavenumber calculation is then normalized, so as to be comparable with the one obtained from equation (2.9). The wavenumber shown in Figure 2.1 (the left column) is defined as $(2\pi)^{-1}\kappa$ with units of km^{-1} , and the frequency is $(2\pi)^{-1}\omega$ with units of Hz. The tuning frequencies, $f_h = (2\pi)^{-1}\omega_h$, used in the three rows are 10, 50 and 500 Hz, respectively.

Figure 2.1 (the right column) also shows the phase delay caused by the wavenumber differences. The spatial phase delay is given by $v_r t \Delta\kappa$, where v_r is the phase velocity, t is the travelttime and $\Delta\kappa$ is the wavenumber difference. The spatial phase delays shown in Figure 2.1 are estimated at a two-way travelttime of 4 s. Although the wavenumber differences (the left column) seem quite small for all three cases with different tuning frequencies, they have a significant effect on the phase delay accumulated along a travel path (the right column). This experiment suggests that a 500 Hz tuning frequency may be used in designing the inverse Q filter to process reflection seismic data of 4 s.

In summary, the tuning frequency f_h should be the upper limit of the possible seismic band, whereas Q_r and v_r are reference values for the Q and the phase velocity, usually given at the dominant frequency of the seismic waveform.

2.3 Accurate velocity dispersion correction

Figures 2.2–2.4 demonstrate the effectiveness of the tuning frequency f_h in inverse Q filtering, using a synthetic example (Figure 2.2) provided by an oil company for benchmarking the inverse Q filtering algorithms from seismic data-processing vendors. The seismic quality factor Q values for

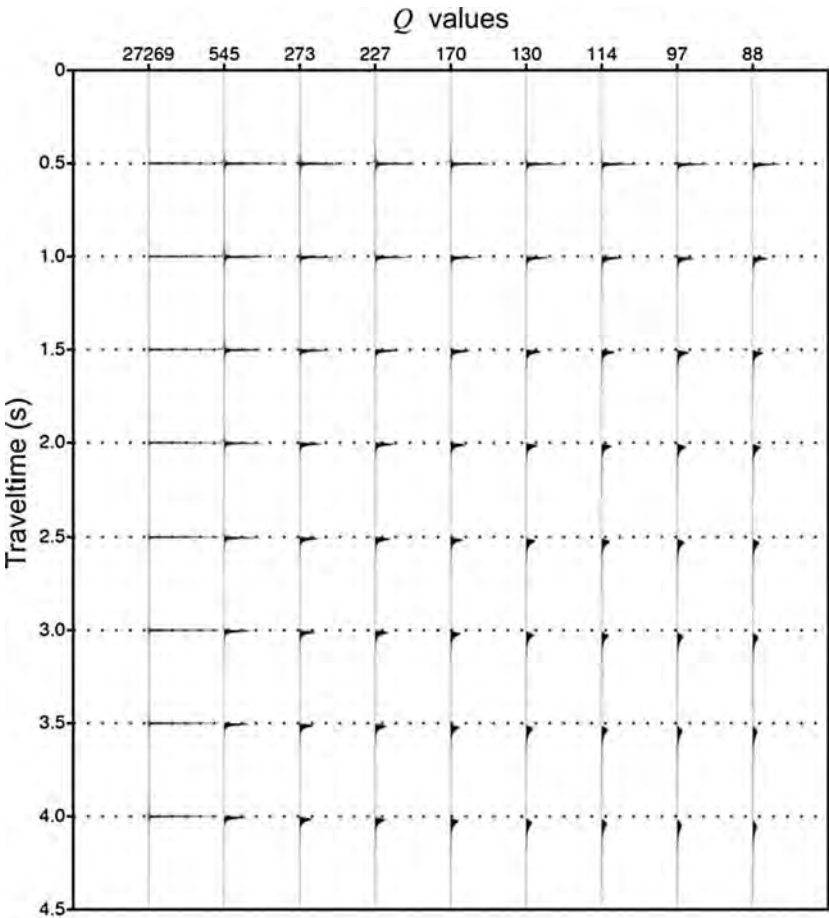


Figure 2.2 A group of synthetic seismic traces for benchmarking inverse Q filtering algorithms from seismic data-processing vendors.

each individual trace are shown on the top of the trace. The corresponding attenuation coefficients can be quantified in terms of Q by equation (1.6), or approximately $27.3Q^{-1}$ dB per wavelength. The Q and α values are listed as follows:

Q	27	269	545	273	227	170	130	114	97	88
α (dB/ λ)	0.001	0.05	0.10	0.12	0.16	0.21	0.24	0.28	0.31	

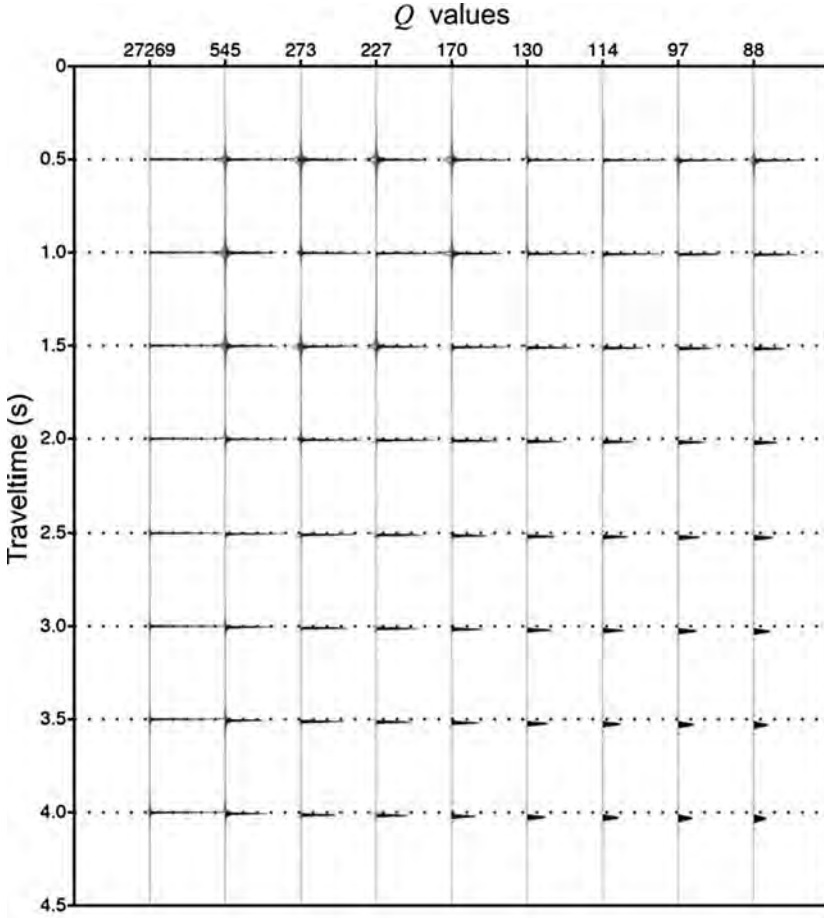


Figure 2.3 Result of inverse Q filtering when a tuning frequency $f_h = 50$ Hz is used. The misalignment (i.e. the phase error) of wavelet peaks in the horizontal direction suggests that velocity dispersion has not been fully corrected by inverse Q filtering.

Figures 2.3 and 2.4 show the inverse Q filtered results, using tuning frequencies of $f_h = 50$ and 500 Hz, respectively. The inverse Q filter used here is a stabilized inverse Q filter algorithm, which will be presented in Part II. After inverse Q filtering, changes in the event times due to dispersion correction are evident in Figures 2.3 and 2.4. The horizontal alignment of wavelet peaks in Figure 2.4 indicates that the velocity dispersion has been corrected accurately when using a tuning frequency of

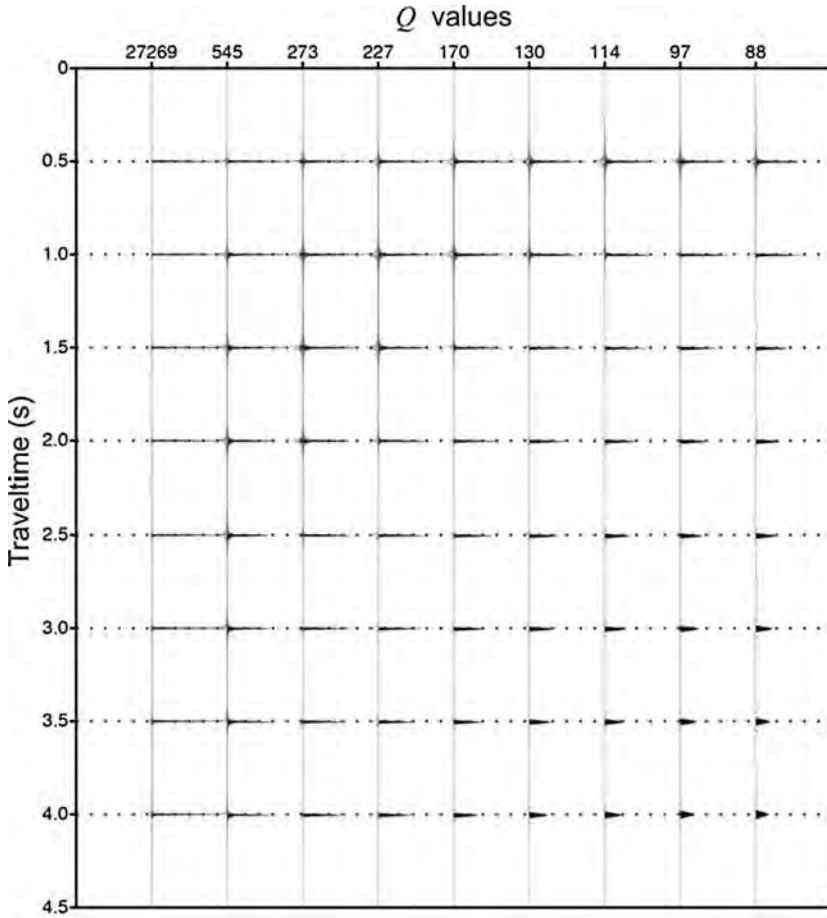


Figure 2.4 Result of inverse Q filtering when a tuning frequency $f_h = 500$ Hz is used. The horizontal alignment of wavelet peaks indicates that the velocity dispersion has been fully corrected.

$f_h = 500$ Hz. The correction of velocity dispersion is of high importance since it impacts the time-to-depth conversion of seismic reflection events from subsurface reflectors and reservoirs.

2.4 Comparison with different Q models

Although the Kolsky viscoelastic model is widely used in seismic data processing, for its simplicity, the basic Kolsky model does not rigorously

satisfy the Kramers–Krönig dispersion relation. Several other expressions that satisfy the dispersion relationship can also be found in the literature. In this section, some of these models are stated briefly with explicit expressions for both the attenuation and the phase velocity functions. Each of these models is compared with the modified Kolsky model to find out how each model can be used interchangeably in an inverse Q filter.

This section compares a total of eight earth Q models (including the modified Kolsky model) to reveal similarities and differences between them. They are:

- 1) the modified Kolsky model (linear attenuation);
- 2) the Strick–Azimi model (power-law attenuation);
- 3) the Kjartansson model (constant Q);
- 4) Azimi’s second and third models (non-linear attenuation);
- 5) Müller’s model (power-law Q);
- 6) the Zener model (the standard linear solid);
- 7) the Cole–Cole model (a general linear-solid); and
- 8) a new general linear model.

These eight models may be classified into two groups. The first group consists of models 1–5, and the other group includes models 6–8. The main difference between these two groups is the behaviour of the phase velocity when the frequency approaches zero, where the first group has a zero-valued phase velocity, and the second group has a finite, nonzero phase velocity. One exception is the Cole–Cole model, which can give either zero or non-zero phase velocity at zero frequency, depending upon an exponent that is chosen.

The linear solid model, including the standard and general versions, may be preferred in finite-difference modelling algorithms because it gives additional differential equations that can be approximated by finite differences. One of the features of linear solid models is that they have finite phase velocity and attenuation coefficient at infinite frequencies. Conversely, the Kolsky model and Kjartansson’s constant- Q model, for instance, assume $v_\infty = \infty$ and $\alpha_\infty = \infty$.

Throughout the comparison (Figures 2.5–2.12), the parameters used for the calculation of the modified Kolsky model (equations 2.2 and 2.7) are

$$Q_r = 50, \quad v_r = 2500 \text{ m s}^{-1} \quad \text{and} \quad \omega_h = 1000 \pi;$$

i.e. the highest possible seismic frequency is about 500 Hz.

2.4.1 The Strick–Azimi power-law attenuation model and Kjartansson's constant- Q model

The power-law model proposed by Strick (1967) and Azimi *et al.* (1968) has the attenuation proportional to $|\omega|^{1-\gamma}$, that is,

$$\alpha(\omega) = a_1 |\omega|^{1-\gamma}. \quad (2.11)$$

The phase velocity is written as

$$\frac{1}{v(\omega)} = \frac{1}{v_\infty} + a_1 |\omega|^{-\gamma} \cot\left(\frac{\pi}{2}\gamma\right). \quad (2.12)$$

In the above equation, if we set $v_\infty^{-1} = 0$, we can obtain Kjartansson's (1979) constant- Q model, in which the attenuation coefficient $\alpha(\omega)$ is defined in (2.11), and the phase velocity is given by

$$\frac{1}{v(\omega)} = a_1 |\omega|^{-\gamma} \cot\left(\frac{\pi}{2}\gamma\right). \quad (2.13)$$

To compare Kjartansson's constant- Q model with the Kolsky model, one may set

$$\gamma = \frac{1}{\pi Q_r} \quad \text{and} \quad a_1 = \frac{|\omega_h|^\gamma}{2 v_r Q_r}. \quad (2.14)$$

As shown in Figure 2.5, these two models fit each other perfectly. The attenuation and the phase velocity in the Kjartansson model are calculated using equations (2.11) and (2.13) with a_1 defined in equation (2.14).

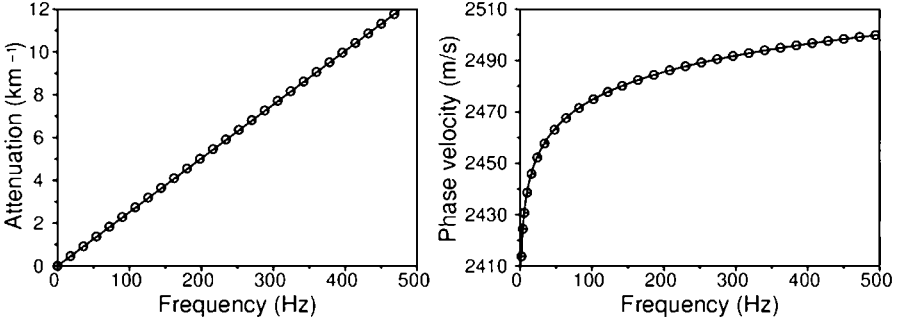


Figure 2.5 The attenuation and the phase velocity in the Kolsky model and Kjartansson's constant- Q model.

To make the Strick–Azimi power-law model similar to the Kolsky model, as shown in Figure 2.6, we may set the three ‘constants’ γ , a_1 and v_∞ as

$$\gamma = -\frac{1}{\ln \left| \frac{\omega}{\omega_h} \right|} \sim \frac{1}{\ln |\omega_h|} \quad (\text{for } \omega \ll \omega_h), \quad (2.15)$$

$$a_1 = \frac{|\omega|^\gamma}{2v_r Q_r} \sim \frac{|\omega_h|^\gamma}{2v_r Q_r} \quad (2.16)$$

and

$$\frac{1}{v_\infty} = \frac{1}{v_r} \left[1 - \frac{1}{2Q_r} \cot \left(\frac{\pi}{2} \gamma \right) \right], \quad (2.17)$$

where the term before the asymptotic expression ‘ \sim ’ is obtained by assuming the ‘constant’ to be a frequency-dependent ‘variable’ in the expression for the attenuation and for the phase velocity of an earth Q model, to match the Kolsky model. The prerequisite ‘constant’ is then derived asymptotically based on the ‘variable’ expression.

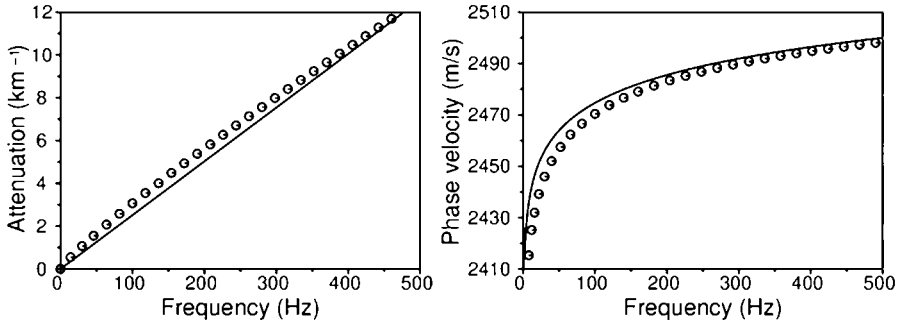


Figure 2.6 The attenuation and the phase velocity in the Strick–Azimi power-law model (circled lines) and in the Kolsky model (solid lines).

Figure 2.6 shows that the Strick–Azimi power-law model matches the Kolsky model with slight differences in the attenuation and the phase velocity. Recall that:

- 1) it is the Strick–Azimi model rather than the Kolsky model that satisfies the Kramers–Krönig dispersion relation (i.e. the minimum-phase criterion);
- 2) the requirement of causality also implies that $v(\omega)$ has an asymptotic limit so that $\omega/v(\omega) \sim O(\omega)$ (see equation 2.12). Thus, we expect that v_∞ in the subsurface earth medium should have a realistic magnitude similar to v_r .

Therefore, in principle, the Strick–Azimi power-law model with constants given by expressions (2.15), (2.16) and (2.17) should be preferable to the Kolsky model in seismic inverse Q filtering. However, when using this modified version of the Kolsky model, the difference between the Strick–Azimi model and the Kolsky model might be much less than the error caused by Q estimation from seismic data in practice.

2.4.2 Azimi's second and third models

Azimi *et al.* (1968) proposed three models that satisfy causality and are

fairly close to the Kolsky model. The first model is the power law described in the previous section. The second model is defined by

$$\alpha(\omega) = \frac{a_2 |\omega|}{1 + a_3 |\omega|}, \quad (2.18)$$

where a_2 and a_3 are constants. Using the Kramers–Krönig dispersion relation (2.8), the phase velocity is then given by

$$\frac{1}{v(\omega)} = \frac{1}{v_\infty} - \frac{2a_2 \ln(a_3 \omega)}{\pi(1 - a_3^2 \omega^2)}. \quad (2.19)$$

For all frequencies within the seismic band, it may be assumed that $a_3 \omega \ll 1$ and equation (2.19) may be approximated to

$$\frac{1}{v(\omega)} \approx \frac{1}{v_\infty} - \frac{2a_2}{\pi} \ln(a_3 \omega). \quad (2.20)$$

To make Azimi's second model similar to the Kolsky model, as shown in Figure 2.7, we may choose a_2 , a_3 and v_∞ as follows:

$$v_\infty = v_r, \quad (2.21)$$

$$a_2 = \frac{1}{2v_r Q_r} \left(1 + \frac{1}{2} \left| \frac{\omega}{\omega_h} \right| \right) \sim \frac{3}{4v_r Q_r} \quad (2.22)$$

and

$$a_3 = \frac{1}{|\omega_h|}. \quad (2.23)$$

Azimi's third model is defined as

$$\alpha(\omega) = \frac{a_4 |\omega|}{1 + a_5 \sqrt{|\omega|}}, \quad (2.24)$$

where a_4 and a_5 are constants. Following the Kramers–Krönig dispersion relation, the phase velocity is given by

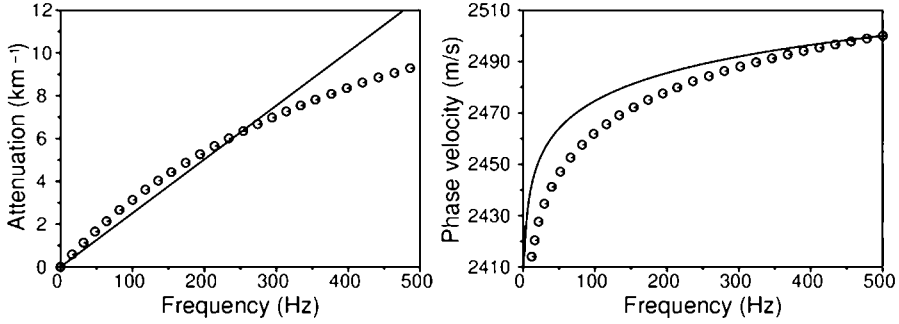


Figure 2.7 The attenuation and the phase velocity in Azimi's second model (circled lines) and in the Kolsky model (solid lines).

$$\frac{1}{v(\omega)} = \frac{1}{v_\infty} + \frac{a_4 a_5 \sqrt{|\omega|}}{1 + a_5^2 |\omega|} - \frac{2a_4 \ln(a_5^2 |\omega|)}{\pi(1 - a_5^4 \omega^2)}. \quad (2.25)$$

Assuming $a_5^2 \omega \ll 1$ for all seismic frequencies, we obtain

$$\frac{1}{v(\omega)} \approx \frac{1}{v_\infty} + a_4 a_5 \sqrt{|\omega|} - \frac{2a_4}{\pi} \ln(a_5^2 |\omega|). \quad (2.26)$$

In a similar way, we may try to match Azimi's third model to the Kolsky model by choosing the following constants:

$$\frac{1}{v_\infty} = \frac{1}{v_r} \left(1 - \frac{1 + |\omega / \omega_h|}{2Q_r} \right) \sim \frac{1}{v_r} \left(1 - \frac{1}{Q_r} \right), \quad (2.27)$$

$$a_4 = \frac{1 + \sqrt{|\omega / \omega_h|}}{2v_r Q_r} \sim \frac{1}{v_r Q_r} \quad (2.28)$$

and

$$a_5 = \frac{1}{\sqrt{|\omega_h|}}. \quad (2.29)$$

The attenuation and the phase velocity curves are plotted in Figure 2.8.

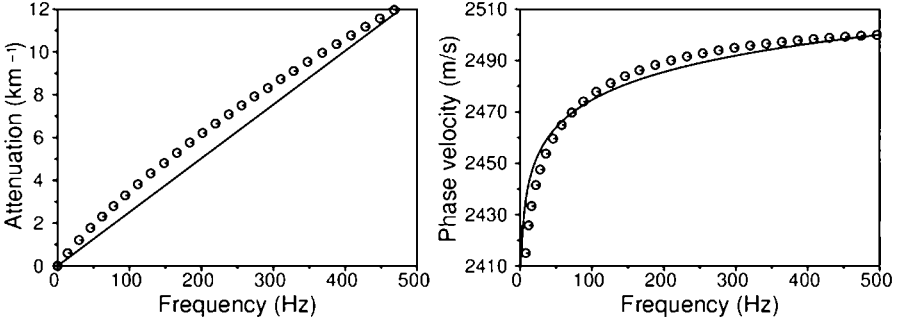


Figure 2.8 The attenuation and the phase velocity in Azimi's third model (circled lines) and in the Kolsky model (solid lines).

2.4.3 Müller's power-law model

In Müller's (1983) power-law Q model, the attenuation is defined as

$$\alpha(\omega) = \frac{|\omega|}{2v_r Q_r} \left| \frac{\omega}{\omega_r} \right|^{-\gamma}, \quad (2.30)$$

and the phase velocity is defined as

$$\frac{1}{v(\omega)} = \frac{1}{v_r} \left[1 + \frac{1}{2Q_r} \left(\left| \frac{\omega}{\omega_r} \right|^{-\gamma} - 1 \right) \cot\left(\frac{\pi}{2}\gamma\right) \right], \quad (2.31)$$

where ω_r is a reference frequency.

As shown in Figure 2.9, if we take $\gamma = (\pi Q_r)^{-1}$ and $\omega_r = \omega_h$, these two expressions (2.30) and (2.31) may give the attenuation and the phase velocity in the Kolsky model. However, recall that the two expressions here are valid for $-1 \leq \gamma \leq 1$, not just for $0 \leq \gamma \leq 1$.

2.4.4 Zener or standard linear solid model

The Zener (1948) or standard linear solid model is the most general linear

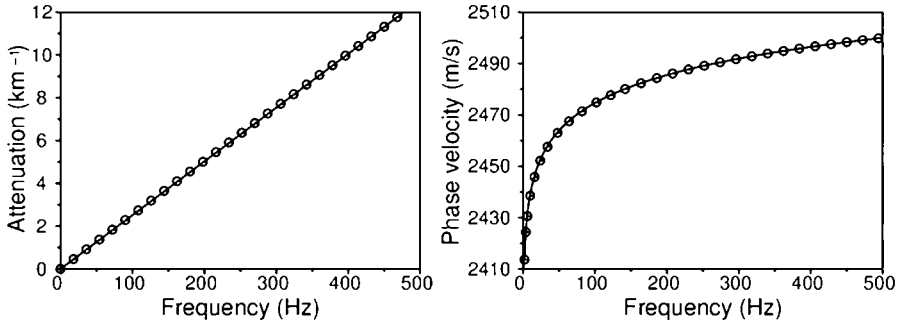


Figure 2.9 The attenuation and the phase velocity in Müller's model (circled lines) and in the Kolsky model (solid lines).

equation that links the stress and strain (Ben-Menahem and Singh, 1981). It defines the attenuation coefficient as

$$\alpha(\omega) \approx \frac{\omega^2 \tau_c}{v_0 Q_c (1 + \omega^2 \tau_c^2)}, \quad (2.32)$$

and the phase velocity as

$$\frac{1}{v(\omega)} \approx \frac{1}{v_0} \left(1 - \frac{\omega^2 \tau_c^2}{Q_c (1 + \omega^2 \tau_c^2)} \right), \quad (2.33)$$

where v_0 is the phase velocity $v(\omega)$ for $\omega \rightarrow 0$, and τ_c and Q_c are two constant parameters describing the attenuation property in the standard linear solid model: the attenuation at the peak of the attenuation function with respect to the frequency is Q_c^{-1} , and the (angular) frequency at this location is τ_c^{-1} . The mathematical treatment is given in the next chapter.

To compare this standard linear solid model with the Kolsky model, as shown in Figure 2.10, we may first set

$$\tau_c = \frac{1}{\omega_h}, \quad (2.34)$$

since the highest frequency of the seismic band has the strongest attenuation.

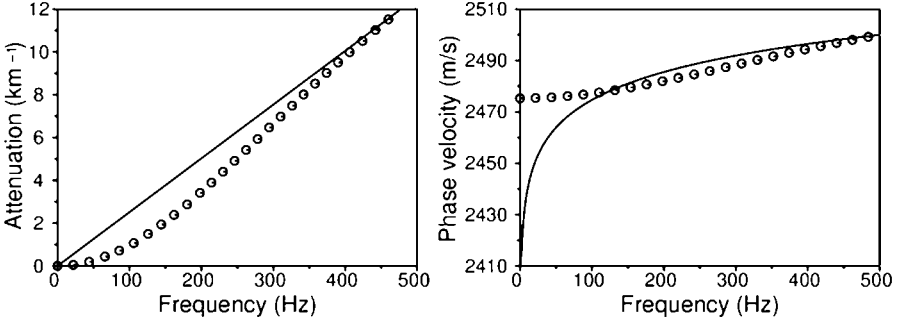


Figure 2.10 The attenuation and the phase velocity in Zener or standard linear solid model (circled lines) and in the Kolsky model (solid lines).

We then use the following two approximations:

$$\frac{1}{v_0} = \frac{1}{v_r} \left(\frac{1}{2Q_r} \left| \frac{\omega}{\omega_h} \right| + \left| \frac{\omega}{\omega_h} \right|^{-\frac{1}{\pi Q_r}} \right) \sim \frac{1}{v_r} \left(1 + \frac{1}{2Q_r} \right) \quad (2.35)$$

and

$$Q_c = \frac{1 + 2Q_r \left| \frac{\omega}{\omega_h} \right|^{-\left(1 + \frac{1}{\pi Q_r}\right)}}{1 + \left| \frac{\omega}{\omega_h} \right|^{-2}} \sim \frac{1}{2} + Q_r. \quad (2.36)$$

2.4.5 The Cole–Cole model

To generalize the standard linear solid model, the Cole and Cole (1941) model proposed for dielectrics can be used. In the Cole–Cole model, the attenuation coefficient may be expressed as

$$\alpha(\omega) \approx \frac{\gamma |\omega \tau_c|^{1+\gamma} \sin(\frac{\pi}{2} \gamma)}{v_0 \tau_c Q_c [1 + 2 |\omega \tau_c|^\gamma \cos(\frac{\pi}{2} \gamma) + |\omega \tau_c|^{2\gamma}]}, \quad (2.37)$$

and the phase velocity may be expressed as

$$\frac{1}{v(\omega)} \approx \frac{1}{v_0} \left(1 - \frac{\gamma |\omega \tau_c|^\gamma [\cos(\frac{\pi}{2}\gamma) + |\omega \tau_c|^\gamma]}{Q_c [1 + 2 |\omega \tau_c|^\gamma \cos(\frac{\pi}{2}\gamma) + |\omega \tau_c|^{2\gamma}]} \right). \quad (2.38)$$

The parameters v_0 , τ_c and Q_c are the same as those in Zener's model above. Detailed derivation is given in the next chapter.

To compare the Cole–Cole model with the Kolsky model, we set $\tau_c = \omega_h^{-1}$, as we did in the Zener model. Meanwhile, we set

$$Q_c = \frac{\gamma^2}{4} \pi Q_r \quad (2.39)$$

and

$$\frac{1}{v_0} = \frac{1}{v_r} \left(1 + \frac{2}{\gamma \pi Q_r} \right). \quad (2.40)$$

Figure 2.11 shows the attenuation and the phase velocity in the Cole–Cole model with (a) $\gamma = 1.0$ and (b) $\gamma = 0.4$. Compared with those in the Kolsky model, the Cole–Cole model with $\gamma = 0.4$ has a better fit than using $\gamma = 1.0$, which is the standard linear solid or Zener model.

2.4.6 A general linear model

Finally, an alternative to the Cole–Cole model is introduced to generalize the linear solid model (Wang and Guo, 2004b). Detailed mathematical treatment is given in the next chapter. In this general linear model, the attenuation coefficient is defined as

$$\alpha(\omega) \approx \frac{1}{v_\infty} \left[\frac{a}{2} \left(1 + \frac{1}{2} \omega^2 \tau^2 \right) + b \right] \frac{\omega^2 \tau}{1 + \omega^2 \tau^2}, \quad (2.41)$$

and the phase velocity is defined as

$$\frac{1}{v(\omega)} \approx \frac{1}{v_\infty} \left\{ 1 + \left[a \left(1 + \frac{5}{8} \omega^2 \tau^2 \right) + b \right] \frac{1}{1 + \omega^2 \tau^2} \right\}, \quad (2.42)$$

where τ is a constant denoting the relaxation time, and a and b are two constant coefficients defining the general linear solid model.

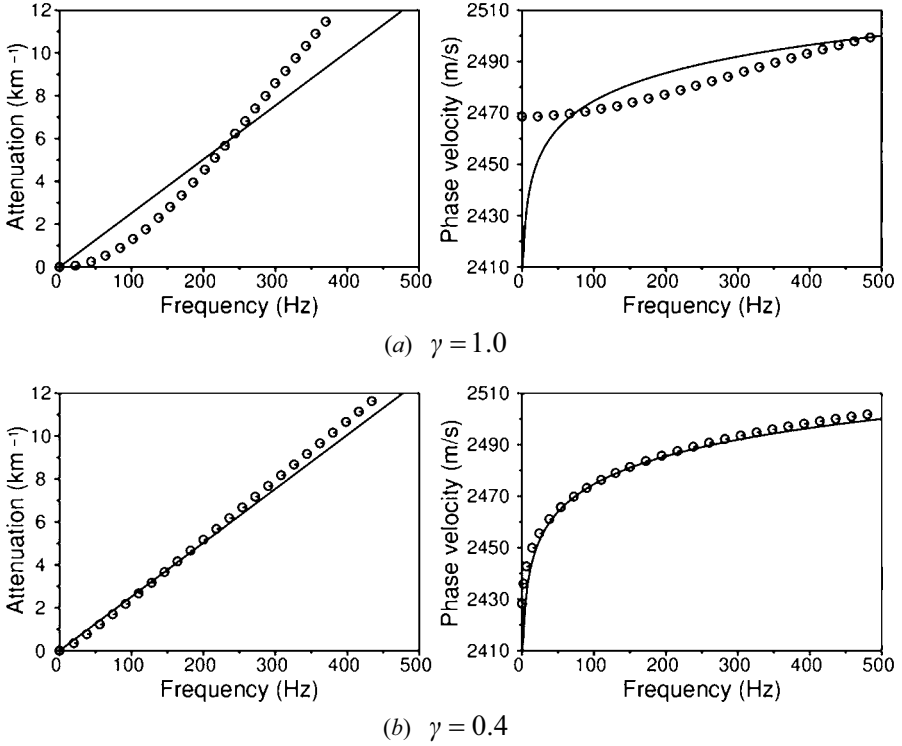


Figure 2.11 The attenuation and the phase velocity in the Cole–Cole model model (circled lines) with (a) $\gamma = 1.0$ and (b) $\gamma = 0.4$, compared with those in the Kolsky model (solid lines). The Cole–Cole model with $\gamma = 0.4$ has a better fit to the Kolsky model than using $\gamma = 1.0$, which is the standard linear solid or Zener model.

To match this general linear model to the Kolsky model, we set

$$v_{\infty} = v_r, \quad a = -\frac{8}{7Q_r} \quad \text{and} \quad b = \frac{13}{7Q_r}. \quad (2.43)$$

Figure 2.12 depicts the attenuation coefficient and the phase velocity of the general linear model, compared with the Kolsky model. In the calculation of formulae (2.41) and (2.42), $\tau = \omega_h^{-1}$ is used.

As shown above, the modified Kolsky model has a high degree of similarity to other earth Q models. In Ursin and Toverud (2002), the basic Kolsky model was compared with different models and, when using a set of analytically derived parameters, those different models were not close to the

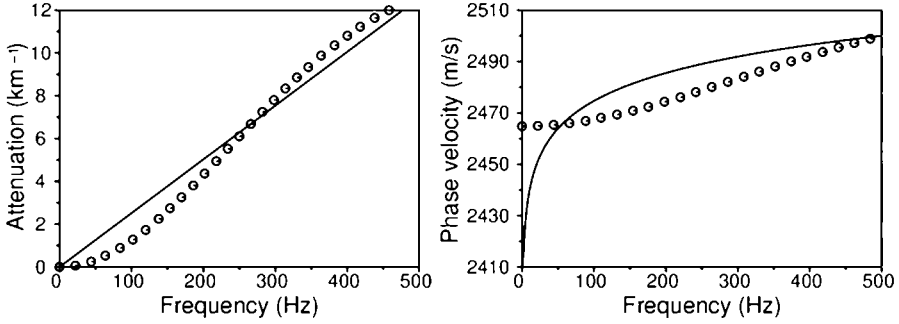


Figure 2.12 The attenuation and the phase velocity in a general linear model (circled lines), compared with those in the Kolsky model (solid lines).

basic Kolsky model. For better matching then, they numerically fitted the different earth Q models to the basic Kolsky model.

The basic Kolsky model is suitable for high-frequency waves. It is modified here by introducing a tuning parameter, which can be referred to as the highest possible frequency of the exploration and production seismic band, so that the model has an accurate representation about the velocity dispersion within the seismic frequency band. The investigation reveals that the modified Kolsky model can be fitted fairly well by any other model with a set of parameters derived analytically. Such matching exercises provide us with good confidence that when the Kolsky model is chosen for designing the inverse Q filter, the result should in principle be comparable with those using other different Q models.

Chapter 3

Mathematical definition of the earth Q models

Abstract

There are various mathematical Q models that can be used in the designing of an inverse Q filter. This chapter is a mathematical treatment showing how these Q models are theoretically related to each other, and finding out if some models have properties setting them apart from the others. Different mathematical Q models are defined in terms of different attenuation coefficients and different phase velocities. However, these attenuation coefficients and phase velocities should satisfy the Kramers–Krönig relations so as to ensure that the seismic response of the earth media is causal. The attenuation coefficient and the phase velocity in a pair are the imaginary and real part of a complex wavenumber, the basis for designing an inverse Q filter for seismic waves through viscoelastic media.

This chapter is a mathematical treatment for a variety of earth Q models, to find out how they are related to each other theoretically or if some models have properties setting them apart from the others. Practitioners may skip this chapter and go straight to the following chapters for the inverse Q filtering algorithms.

In seismic data processing, inverse Q filtering attempts to compensate recorded seismic signals for the attenuation and dispersion effects of seismic wave propagation through subsurface media. Therefore, inverse Q filtering is a reverse processing of the forward modelling of seismic wave propagation. A good understanding of the mathematical Q models is

necessary for the design and application of an inverse Q filtering algorithm. Carcione (2007) comprehensively examined not only viscoelasticity but also poroelasticity, and devoted several chapters to effects of seismic Q in forward simulation. For mechanisms of attenuation of wave propagation in dissipative media, readers may refer to the Society of Exploration Geophysicists reprint series on *Seismic Wave Attenuation*, edited by Toksöz and Johnston (1981), which reviewed various laboratory and field measurements of attenuation. But both volumes did not really address the reverse question of applying inverse Q filters to sharpen up the seismic pulse during seismic data processing.

In the previous chapter, we used the modified Kolsky model as a reference and compared it with seven different earth Q models to reveal similarities and differences between them and to find out whether the models can be used interchangeably. If the basic Kolsky model were used in comparison, the different models with a set of analytically derived parameters would not be close to the basic Kolsky model. To better match the models, Ursin and Toverud (2002) showed that they had to numerically fit the different Q models to the basic Kolsky model. Because we have modified the Kolsky attenuation-dispersion model, we are able to analytically derive a set of parameters to match each of the different models fairly close to the Kolsky model. However, the derivation of those analytical parameters also needs a good understanding of the basic mathematical background of the different Q models.

3.1 Mathematical definition of Q

When a plane wave propagates through a homogeneous viscoelastic medium, the effects of amplitude attenuation and velocity dispersion may be combined conveniently into a single dimensionless parameter, Q , the medium-quality factor. The Q parameter can be expressed as follows:

$$Q(\omega) = \frac{1}{2} \left(\frac{|\omega|}{\alpha(\omega)v(\omega)} - \frac{\alpha(\omega)v(\omega)}{|\omega|} \right). \quad (3.1)$$

As the Q value must be positive, the above equation leads to $[\alpha(\omega)v(\omega)/\omega]^2 < 1$. Assuming

$$\frac{\alpha(\omega)v(\omega)}{|\omega|} \ll 1, \quad (3.2)$$

the Q expression (3.1) is approximated to

$$Q(\omega) \approx \frac{|\omega|}{2\alpha(\omega)\nu(\omega)} . \quad (3.3)$$

The above approximate expression has been presented in the previous chapter (equation 2.1) as the definition of Q . Considering this definition, the assumption (3.2) is equivalent to $Q^{-1}(\omega) \ll 1$. With this small-dissipation assumption, $Q^{-1}(\omega)$ is often known as the dissipation factor.

Such a small-dissipation assumption is valid under most conditions of interest in geophysics; for instance, Kolsky (1953, p.106), Mason (1958, p.214) and Futterman (1962, eq.20). To intuitively understand the condition $Q^{-1}(\omega) \ll 1$, let us see two simple examples. For $Q \approx 5$, the accurate solution is $Q = 0.5 \times (10 - 0.1) = 0.495$. That is, for $Q^{-1}(\omega) \leq 0.2$, the maximum error for the Q value is 1%. For $Q \approx 10$, the accurate solution is $Q = 9.975$. That is, the maximum error is only 0.25% for $Q^{-1}(\omega) \leq 0.1$.

We now show the derivation of equation (3.1) and approximation (3.3). We start from the stress-strain relation:

$$\Sigma(\omega) = M(\omega) E(\omega) , \quad (3.4)$$

where $\Sigma(\omega)$ and $E(\omega)$ are the stress and the strain components at frequency ω , and are related by an appropriate elastic modulus $M(\omega)$. Given a sinusoidally varying stress, the strain response will also be sinusoidal. The phase lag of strain behind the stress may define the dissipation factor (White, 1965)

$$\xi(\omega) \equiv \frac{1}{Q(\omega)} = \frac{M_{\text{Im}}(\omega)}{M_{\text{Re}}(\omega)} , \quad (3.5)$$

where $M_{\text{Re}}(\omega)$ and $M_{\text{Im}}(\omega)$ are the real and imaginary part of the complex modulus $M(\omega)$. The derivation of $M_{\text{Re}}(\omega)$ and $M_{\text{Im}}(\omega)$ is given as follows.

A plane wave propagation may be expressed as

$$U(x, \omega) = U_0(\omega) \exp[i(\omega t - kx)] , \quad (3.6)$$

where $U_0(\omega)$ is the Fourier transform of the propagating pulse, and k is the wavenumber, and x and t are the travel distance and time, respectively. In viscoelastic media, wavenumber k becomes a complex function, defined as

$$k(\omega) = \frac{\omega}{c(\omega)} = \frac{\omega}{v(\omega)} - i\alpha(\omega), \quad (3.7)$$

where $c(\omega)$ is the complex velocity:

$$c(\omega) = \sqrt{\frac{M(\omega)}{\rho}}, \quad (3.8)$$

and ρ is the density. Then the wave-propagation expression (3.6) becomes

$$U(x, \omega) = U_0(\omega) \exp[-\alpha(\omega)x] \exp\left[i\omega\left(t - \frac{x}{v(\omega)}\right)\right]. \quad (3.9)$$

This shows that $\alpha(\omega)$ is related to the amplitude attenuation, and $\omega/v(\omega)$ is related to the phase change along the propagation distance x . Both $\alpha(\omega)$ and $v(\omega)$ are real, positive and even functions of frequency ω .

From equations (3.7) and (3.8), we have the equation

$$\left(\frac{1}{v(\omega)} - i\frac{\alpha(\omega)}{\omega}\right)^2 = \frac{\rho}{|M(\omega)|^2} [M_{\text{Re}}(\omega) - i M_{\text{Im}}(\omega)]. \quad (3.10)$$

This leads to

$$M_{\text{Re}}(\omega) = \left(\frac{1}{v^2(\omega)} - \frac{\alpha^2(\omega)}{\omega^2}\right) \frac{|M(\omega)|^2}{\rho} \quad (3.11)$$

and

$$M_{\text{Im}}(\omega) = \frac{2\alpha(\omega)}{\omega v(\omega)} \frac{|M(\omega)|^2}{\rho}. \quad (3.12)$$

Substitution of equations (3.11) and (3.12) into equation (3.5) will result in the Q definition of equation (3.1) straightforwardly.

Recall that in equation (3.1), the assumption of positive Q values leads to the relation $[\alpha(\omega)v(\omega)/\omega]^2 < 1$. Therefore, $M_{\text{Re}}(\omega)$ in equation (3.11) is a positive and even function of ω . The imaginary part $M_{\text{Im}}(\omega)$ in equation (3.12) is an odd function of ω and is positive for $\omega > 0$. Note also that a natural limitation on $\alpha(\omega)$ is implied by the Wiener criterion:

$$\lim_{\omega \rightarrow \infty} \frac{\alpha(\omega)}{\omega} = 0. \quad (3.13)$$

From equations (3.11) and (3.12), we obtain the attenuation coefficient (Aki and Richards, 1980)

$$\begin{aligned} \alpha(\omega) &= \frac{|\omega| M_{\text{Im}}(\omega)}{|M(\omega)|} \sqrt{\frac{\rho}{2[M_{\text{Re}}(\omega) + |M(\omega)|]}} \\ &= |\omega| \sqrt{\frac{\rho}{M_{\text{Re}}(\omega)}} \frac{\xi}{\sqrt{2(1 + \xi^2) \left(1 + \sqrt{1 + \xi^2}\right)}}, \end{aligned} \quad (3.14)$$

and the phase velocity

$$\begin{aligned} \frac{1}{v(\omega)} &= \frac{1}{|M(\omega)|} \sqrt{\frac{\rho[M_{\text{Re}}(\omega) + |M(\omega)|]}{2}} \\ &= \sqrt{\frac{\rho}{M_{\text{Re}}(\omega)}} \sqrt{\frac{1 + \sqrt{1 + \xi^2}}{2(1 + \xi^2)}}, \end{aligned} \quad (3.15)$$

where ξ is the dissipation factor defined by equation (3.5). For $\xi \equiv Q^{-1} \ll 1$, equations (3.14) and (3.15) can be approximated to

$$\alpha(\omega) \approx |\omega| \sqrt{\frac{\rho}{M_{\text{Re}}(\omega)}} \frac{\xi}{2} \quad (3.16)$$

and

$$\frac{1}{v(\omega)} \approx \sqrt{\frac{\rho}{M_{\text{Re}}(\omega)}}. \quad (3.17)$$

Combining these two approximations will also lead to the approximate formula (3.3).

For the transmission response of the medium to be causal, the attenuation and the phase velocity must satisfy the Kramers–Krönig relations. Dispersion relations of the Kramers–Krönig type (Krönig, 1926; Kramers, 1927), well known in electric circuit theory, determine, for example, the real part of the propagation constant from the values of the imaginary part summed over the entire range of frequencies for wave motions that are linear. The Kramers–Krönig dispersion relations for the attenuation and phase velocity are given by

$$\frac{\omega}{v(\omega)} - \frac{\omega}{v_\infty} = \mathcal{H}\{\alpha(\omega)\} \quad (3.18)$$

and

$$\frac{\alpha(\omega) - \alpha(0)}{\omega} = -\mathcal{H}\left\{\frac{1}{v(\omega)} - \frac{1}{v_\infty}\right\}, \quad (3.19)$$

where $\mathcal{H}\{\cdot\}$ denotes the Hilbert transform, v_∞ is the limit of $v(\omega)$ as $\omega \rightarrow \infty$,

$$v_\infty = \lim_{\omega \rightarrow \infty} v(\omega) = \lim_{\omega \rightarrow \infty} \sqrt{\frac{M_{\text{Re}}(\omega)}{\rho}} \quad (3.20)$$

and $\alpha(0)$ is the limit of $\alpha(\omega)$ as $\omega \rightarrow 0$,

$$\alpha(0) = \lim_{\omega \rightarrow 0} \alpha(\omega) = 0. \quad (3.21)$$

If the relations (3.18) and (3.19) are fulfilled, then the transmission response is minimum delay with respect to the first arrival time (e.g. Aki and Richards, 1980).

For the application of inverse Q filtering to real seismic traces, we henceforth consider the complex wavenumber only with positive frequencies.

3.2 Kolsky's Q model and the complex wavenumber

The Kolsky model is used extensively in seismic inverse Q filtering because

the parameters involved are relatively easy to estimate from a seismic data set itself or some other seismic measurements. For the Kolsky model, given the attenuation coefficient (2.2) and the phase velocity (2.3), we may use equation (3.1) to derive the quality factor Q as

$$Q(\omega) = Q_r - \frac{1}{4Q_r} - \frac{1}{\pi} \left(1 + \frac{1}{4Q_r^2} \right) \ln \left| \frac{\omega}{\omega_r} \right|, \quad (3.22)$$

or approximations

$$Q(\omega) \approx Q_r \left(1 - \frac{1}{\pi Q_r} \ln \left| \frac{\omega}{\omega_r} \right| \right) \quad (3.23)$$

$$\approx Q_r \left| \frac{\omega}{\omega_r} \right|^{-\gamma}, \quad (3.24)$$

where $\gamma = (\pi Q_r)^{-1}$.

In the previous chapter, we discussed that it is necessary to modify the basic Kolsky model so as to accurately represent the velocity dispersion effect. Given the modified phase velocity (2.7), the modified Kolsky Q model is expressed as

$$Q(\omega) \approx Q_r \left(1 - \frac{1}{\pi Q_r} \ln \left| \frac{\omega}{\omega_h} \right| \right) \approx Q_r \left| \frac{\omega}{\omega_h} \right|^{-\gamma}. \quad (3.25)$$

Using this expression, we may rewrite the attenuation coefficient as

$$\alpha(\omega) = \frac{|\omega|}{2v_r Q_r} \approx \frac{|\omega|}{2v_r Q(\omega)} \left| \frac{\omega}{\omega_h} \right|^{-\gamma}. \quad (3.26)$$

Substituting this expression and the modified phase velocity (2.7) into equation (3.7), we may obtain the complex wavenumber as

$$k(\omega) \approx \left(1 - \frac{i}{2Q(\omega)} \right) \frac{|\omega|}{v_r} \left| \frac{\omega}{\omega_h} \right|^{-\gamma}. \quad (3.27)$$

This definition of complex wavenumber $k(\omega)$ is the basis for designing an inverse Q filter throughout the rest of this book.

3.3 The Strick–Azimi Q model

The power-law model proposed by Strick (1967) and Azimi *et al.* (1968) has attenuation proportional to $|\omega|^s$:

$$\alpha(\omega) = a_1 |\omega|^s, \quad (3.28)$$

for $0 < s < 1$, where a_1 is a constant. Using the Kramers–Krönig dispersion relation (3.18) we obtain the phase velocity as

$$\frac{1}{v(\omega)} = \frac{1}{v_\infty} + a_1 |\omega|^{s-1} \tan\left(\frac{\pi}{2}s\right). \quad (3.29)$$

Then, from equation (3.1), we obtain the earth $Q(\omega)$ model as

$$Q(\omega) = \frac{1}{2} \left\{ \left[\frac{|\omega|^{1-s}}{a_1 v_\infty} + \tan\left(\frac{\pi}{2}s\right) \right] - \left[\frac{|\omega|^{1-s}}{a_1 v_\infty} + \tan\left(\frac{\pi}{2}s\right) \right]^{-1} \right\}. \quad (3.30)$$

Substituting s for $1 - \gamma$ can make the power-law attenuation model similar to the Kolsky linear attenuation model: the power-law attenuation is expressed as equation (2.11), and the phase velocity is written as (2.12). Then the earth Q model is represented as

$$Q(\omega) = \frac{1}{2} \left\{ \left[\frac{|\omega|^\gamma}{a_1 v_\infty} + \cot\left(\frac{\pi}{2}\gamma\right) \right] - \left[\frac{|\omega|^\gamma}{a_1 v_\infty} + \cot\left(\frac{\pi}{2}\gamma\right) \right]^{-1} \right\}. \quad (3.31)$$

3.4 Kjartansson's constant- Q model

Setting $v_\infty^{-1} = 0$, the Strick–Azimi Q model becomes Kjartansson's (1979) Q model, where the attenuation coefficient $\alpha(\omega)$ is defined in (2.11) and the

phase velocity is given by

$$\frac{1}{v(\omega)} = a_1 |\omega|^{-\gamma} \cot\left(\frac{\pi}{2}\gamma\right). \quad (3.32)$$

The Q model deduced from equation (3.31) is

$$Q \approx \frac{1}{2} \left[\cot\left(\frac{\pi}{2}\gamma\right) - \tan\left(\frac{\pi}{2}\gamma\right) \right]. \quad (3.33)$$

It is frequency-independent and is thus referred to as a constant- Q model. For a small γ value, the Q expression (3.33) also leads to the expression

$$\gamma \approx \frac{2}{\pi} \tan^{-1}\left(\frac{1}{2Q}\right) \approx \frac{1}{\pi Q}. \quad (3.34)$$

This is consistent with the γ factor definition (2.5) given in the previous chapter.

3.5 Azimi's second and third Q models

For Azimi's second model (Azimi *et al.*, 1968) with the attenuation coefficient defined in equation (2.18) and the phase velocity given by equation (2.20), the earth $Q(\omega)$ model is defined as

$$Q(\omega) \approx \frac{1}{2a_2 v_\infty} - \frac{1}{\pi} \ln(a_3 \omega). \quad (3.35)$$

Azimi's third model with the attenuation coefficient and phase velocity given by expressions (2.24) and (2.26) defines the earth Q model as

$$Q(\omega) \approx \frac{1}{2} \left(1 + a_5 \sqrt{|\omega|} \right) \left(\frac{1}{a_4 v_\infty} + a_5 \sqrt{|\omega|} - \frac{2}{\pi} \ln(a_5^2 |\omega|) \right). \quad (3.36)$$

3.6 Müller's Q model

Müller (1983) proposed a power-law Q model, for $-1 \leq \gamma \leq 1$, as

$$Q(\omega) = \left(\frac{\omega}{\omega_0} \right)^\gamma = Q(\omega_r) \left(\frac{\omega}{\omega_r} \right)^\gamma, \quad (3.37)$$

where ω_r is a reference frequency and ω_0 is the frequency where $Q(\omega_0) = 1$. For $\gamma = 0$, this gives Kjartansson's constant- Q model.

For $0 < \gamma \leq 1$ and large $Q(\omega)$ ($\omega \gg \omega_0$), the complex velocity $c(\omega)$ is approximated by

$$\frac{1}{c(\omega)} = \frac{1}{c_\infty} \exp \left\{ \frac{1}{2} \left| \frac{\omega}{\omega_0} \right|^{-\gamma} \left[\cot \left(\frac{\pi}{2} \gamma \right) - i \right] \right\}. \quad (3.38)$$

When the exponential function is expanded in a first-order Taylor series, we obtain

$$\alpha(\omega) = \frac{|\omega|}{2c_\infty} \left| \frac{\omega}{\omega_0} \right|^{-\gamma} \quad (3.39)$$

and

$$\frac{1}{v(\omega)} = \frac{1}{c_\infty} \left[1 + \frac{1}{2} \left| \frac{\omega}{\omega_0} \right|^{-\gamma} \cot \left(\frac{\pi}{2} \gamma \right) \right]. \quad (3.40)$$

These are exactly the power-law attenuation (2.11) and phase velocity (2.12) with parameter

$$a_1 = \frac{|\omega_0|^\gamma}{2c_\infty}. \quad (3.41)$$

For $-1 \leq \gamma < 0$ and large $Q(\omega)$ ($\omega \ll \omega_0$), Müller's model is approximately

$$\frac{1}{c(\omega)} = \frac{1}{c_0} \exp \left\{ \frac{1}{2} \left| \frac{\omega}{\omega_0} \right|^{-\gamma} \left[\cot \left(\frac{\pi}{2} \gamma \right) - i \right] \right\}. \quad (3.42)$$

This formula is similar to equation (3.38) but differs in the sign of γ . A first-order Taylor expansion may produce

$$\alpha(\omega) = \frac{|\omega|}{2c_0} \left| \frac{\omega}{\omega_0} \right|^{| \gamma |} \quad (3.43)$$

and

$$\frac{1}{v(\omega)} = \frac{1}{c_0} \left[1 - \frac{1}{2} \left| \frac{\omega}{\omega_0} \right|^{| \gamma |} \cot \left(\frac{\pi}{2} | \gamma | \right) \right]. \quad (3.44)$$

This is roughly a power law with attenuation proportional to $|\omega|^{1+|\gamma|}$, for $0 < |\gamma| \leq 1$.

The complex velocity presented in equations (3.38) and (3.42) may be presented in a unified formula as

$$\frac{1}{c(\omega)} = \frac{1}{v_r} \exp \left[\frac{1}{2Q_r} \left(\left| \frac{\omega}{\omega_r} \right|^{-\gamma} - 1 \right) \cot \left(\frac{\pi}{2} \gamma \right) - i \frac{1}{2Q_r} \left| \frac{\omega}{\omega_r} \right|^{-\gamma} \right], \quad (3.45)$$

which is expressed in terms of the phase velocity v_r at the reference frequency. It is derived as follows. Considering

$$\omega_0 = \omega_r [Q(\omega_r)]^{-1/\gamma}, \quad (3.46)$$

obtained from equation (3.37), equation (3.38) gives

$$\frac{1}{c_\infty} = \frac{1}{v_r} \exp \left[-\frac{1}{2Q_r} \cot \left(\frac{\pi}{2} \gamma \right) \right], \quad (3.47)$$

valid for $0 < \gamma \leq 1$ and $\omega \gg \omega_0$, and equation (3.42) gives

$$\frac{1}{c_0} = \frac{1}{v_r} \exp \left[-\frac{1}{2Q_r} \cot \left(\frac{\pi}{2} \gamma \right) \right], \quad (3.48)$$

valid for $-1 \leq \gamma < 0$ and $\omega \ll \omega_0$. Substituting these into equations (3.38) and (3.42) derives an identical equation to equation (3.45).

From equation (3.7), the attenuation coefficient and the phase velocity are defined as

$$\alpha(\omega) = -\text{Im}\left\{\frac{\omega}{c(\omega)}\right\} \quad \text{and} \quad \frac{1}{v(\omega)} = \text{Re}\left\{\frac{1}{c(\omega)}\right\}. \quad (3.49)$$

With a Taylor expansion, equation (3.45) gives the attenuation coefficient (2.30) and the phase velocity (2.31).

3.7 The Zener or standard linear solid model

The Zener (1948) or standard linear solid model is the most general linear equation in stress σ , strain ε and their first time derivatives $\dot{\sigma}$ and $\dot{\varepsilon}$. In the Fourier transform domain (equation 3.4), the stress $\Sigma(\omega)$ and the strain $E(\omega)$ are linked by the complex modulus defined as (Ben-Menahem and Singh, 1981):

$$M(\omega) = M_R \frac{1 + i\omega\tau_\varepsilon}{1 + i\omega\tau_\sigma}, \quad (3.50)$$

where τ_ε is the strain relaxation time, τ_σ is the stress relaxation time and M_R is a deformation modulus with sub-index R denoting the relaxed modulus.

The mechanical ‘relaxation’ means that the strain produced by the sudden application of a fixed stress to a material increases asymptotically with time. Similarly, the stress produced when the material is suddenly strained relaxes asymptotically (Kolsky, 1953). It is found that stress waves whose periods are close to the ‘relaxation times’ of such a medium are severely attenuated when passing through it.

Physically, the ‘relaxed’ elastic modulus M_R is the final value of the ratio of stress to strain after relaxation has taken place, whereas a so-called ‘unrelaxed’ elastic modulus, M_U , is the initial value of the ratio of stress to strain, before relaxation has time to occur. Mathematically, the relaxed modulus M_R is obtained from $M(\omega)$ for $\omega \rightarrow 0$ (see equation 3.50).

The unrelaxed modulus can be given by

$$M_U \equiv \lim_{\omega \rightarrow \infty} M(\omega) = M_R \frac{\tau_\varepsilon}{\tau_\sigma}. \quad (3.51)$$

Thus, M_R and M_U are also called the low- and the high-frequency moduli, respectively.

A special case of the standard linear solid model is the Kelvin-Voigt viscoelastic model obtained when $\tau_\sigma = 0$, so that

$$M(\omega) = M_R (1 + i\omega\tau_\varepsilon). \quad (3.52)$$

In the Kelvin–Voigt viscoelastic model, the stress σ in the medium for a given strain ε and strain rate $\dot{\varepsilon}$ is the superposition of linear elastic and linear viscous stresses (Thomson (Lord Kelvin), 1856; Meyer, 1874; Voigt, 1892).

The real part of the complex modulus $M(\omega)$ in equation (3.50) may be written as

$$M_{\text{Re}}(\omega) = M_R \frac{1 + \omega^2 \tau_\varepsilon \tau_\sigma}{1 + \omega^2 \tau_\varepsilon^2}, \quad (3.53)$$

and the attenuation Q^{-1} is given by

$$Q^{-1}(\omega) \equiv \xi(\omega) = \frac{|\omega|(\tau_\varepsilon - \tau_\sigma)}{1 + \omega^2 \tau_\varepsilon \tau_\sigma}, \quad (3.54)$$

which measures the lag of the strain behind the stress. We assume here $\tau_\varepsilon > \tau_\sigma$. Substituting them into equations (3.16) and (3.17), we may obtain the attenuation

$$\alpha(\omega) \approx \frac{\omega^2(\tau_\varepsilon - \tau_\sigma)}{2v_0(1 + \omega^2 \tau_\varepsilon \tau_\sigma)}, \quad (3.55)$$

and the phase velocity

$$\frac{1}{v(\omega)} \approx \frac{1}{v_0} \left(1 - \frac{\omega^2 \tau_\sigma (\tau_\varepsilon - \tau_\sigma)}{2(1 + \omega^2 \tau_\varepsilon \tau_\sigma)} \right), \quad (3.56)$$

where v_0 is the phase velocity for $\omega \rightarrow 0$,

$$v_0 = \sqrt{\frac{M_R}{\rho}} = \lim_{\omega \rightarrow 0} \sqrt{\frac{M_{\text{Re}}(\omega)}{\rho}}. \quad (3.57)$$

Attempting to use a single relaxation time, we may define two parameters as follows:

$$Q_c^{-1} = \frac{\tau_\varepsilon - \tau_\sigma}{2\sqrt{\tau_\varepsilon \tau_\sigma}} \quad \text{and} \quad \tau_c = \sqrt{\tau_\varepsilon \tau_\sigma}. \quad (3.58)$$

For the standard linear solid model, considering equation (3.51), this can be written as $Q_c^{-1} = \frac{1}{2} \Delta M$, where ΔM is the modulus defect

$$\Delta M = \frac{M_U - M_R}{\sqrt{M_U M_R}}; \quad (3.59)$$

that is, the normalized difference between the unrelaxed and relaxed moduli. For the standard linear solid model, the attenuation at the peak of the attenuation function with respect to frequency is $\frac{1}{2} \Delta M$ and the (angular) frequency at this location is $1/\tau_c$.

The parameters τ_ε and τ_σ in (3.55) and (3.56) may be expressed as (Casula and Carcione, 1992):

$$\tau_\varepsilon = \tau_c \left(\sqrt{1 + \frac{1}{Q_c^2}} + \frac{1}{Q_c} \right) \quad (3.60a)$$

and

$$\tau_\sigma = \tau_c \left(\sqrt{1 + \frac{1}{Q_c^2}} - \frac{1}{Q_c} \right), \quad (3.60b)$$

obtained from the Q_c and τ_c definition in (3.58). Therefore, we may rewrite expressions (3.55) and (3.56) as (2.32) for the attenuation and as (2.33) for the phase velocity. With these two expressions, Zener's Q model may be expressed as

$$Q^{-1}(\omega) \approx \frac{2|\omega|\tau_c}{Q_c(1 + \omega^2\tau_c^2)}. \quad (3.61)$$

3.8 The Cole–Cole Q model

To generalize the standard linear solid model, we may use the model

proposed for dielectrics by Cole and Cole (1941). Jones (1986) extended the Cole–Cole model to viscoelastic media for fitting laboratory data involving frequency-dependent absorption and dispersion, and found that it was more satisfying than the previously used dispersion-absorption relationships because of its generality and because its relaxation time was related to the petrophysical property of pore geometry (viscosity).

In the Cole–Cole model, the complex modulus may be written as

$$M(\omega) = M_R \frac{1 + (i\omega\tau_\varepsilon)^\gamma}{1 + (i\omega\tau_\sigma)^\gamma}. \quad (3.62)$$

When $\gamma = 1$, this is the standard linear solid model. The unrelaxed modulus is given by

$$M_U \equiv \lim_{\omega \rightarrow \infty} M(\omega) = M_R \left(\frac{\tau_\varepsilon}{\tau_\sigma} \right)^\gamma. \quad (3.63)$$

Therefore equation (3.62) may also be expressed as

$$M(\omega) \approx M_U + \frac{M_R - M_U}{1 + (i\omega\tau_\sigma)^\gamma}, \quad (3.64)$$

which is the original formula presented in Cole and Cole (1941, eq.5).

The real part of the complex modulus is

$$M_{\text{Re}}(\omega) = M_R \frac{1 + (\omega^2 \tau_\varepsilon \tau_\sigma)^\gamma + (|\omega\tau_\varepsilon|^\gamma + |\omega\tau_\sigma|^\gamma) \cos(\frac{\pi}{2}\gamma)}{1 + |\omega\tau_\sigma|^{2\gamma} + 2|\omega\tau_\sigma|^\gamma \cos(\frac{\pi}{2}\gamma)} \quad (3.65)$$

and the inverse Q function is given by

$$Q^{-1}(\omega) = \frac{(|\omega\tau_\varepsilon|^\gamma - |\omega\tau_\sigma|^\gamma) \sin(\frac{\pi}{2}\gamma)}{1 + (\omega^2 \tau_\varepsilon \tau_\sigma)^\gamma + (|\omega\tau_\varepsilon|^\gamma + |\omega\tau_\sigma|^\gamma) \cos(\frac{\pi}{2}\gamma)}. \quad (3.66)$$

From these two expressions we use expression (3.16) to compute the attenuation coefficient,

$$\alpha(\omega) \approx \frac{\omega(|\omega\tau_\varepsilon|^\gamma - |\omega\tau_\sigma|^\gamma) \sin(\frac{\pi}{2}\gamma)}{2v_0[1 + (\omega^2\tau_\varepsilon\tau_\sigma)^\gamma + (|\omega\tau_\varepsilon|^\gamma + |\omega\tau_\sigma|^\gamma) \cos(\frac{\pi}{2}\gamma)]}, \quad (3.67)$$

and expression (3.17) for the phase velocity,

$$\frac{1}{v(\omega)} \approx \frac{1}{v_0} \left(1 - \frac{(|\omega\tau_\varepsilon|^\gamma - |\omega\tau_\sigma|^\gamma)[|\omega\tau_\sigma|^\gamma + \cos(\frac{\pi}{2}\gamma)]}{2[1 + |\omega\tau_\sigma|^{2\gamma} + 2|\omega\tau_\sigma|^\gamma \cos(\frac{\pi}{2}\gamma)]} \right). \quad (3.68)$$

Based on the definition of τ_ε and τ_σ in equation (3.58), we have the following two approximate expressions (Ursin and Toverud, 2002):

$$\tau_\varepsilon^\gamma \approx \tau_c^\gamma \left(1 + \frac{\gamma}{Q_c} + \frac{\gamma^2}{2Q_c^2} \right) \quad (3.69a)$$

and

$$\tau_\sigma^\gamma \approx \tau_c^\gamma \left(1 - \frac{\gamma}{Q_c} + \frac{\gamma^2}{2Q_c^2} \right). \quad (3.69b)$$

The attenuation coefficient (3.67) and the phase velocity (3.68) can be approximated to expressions (2.37) and (2.38), respectively. Finally, the earth Q model may be expressed as

$$Q^{-1}(\omega) \approx \frac{2\gamma |\omega\tau_c|^\gamma \sin(\frac{\pi}{2}\gamma)}{Q_c[1 + |\omega\tau_c|^{2\gamma} + 2|\omega\tau_c|^\gamma \cos(\frac{\pi}{2}\gamma)]}. \quad (3.70)$$

3.9 A general linear model

An alternative to the Cole–Cole model to generalize the Zener or standard linear solid model can be established using products and/or sums of different attenuation-dispersion models to obtain a more complicated behaviour as a function of frequency (Ben-Menahem and Singh, 1981). For instance, Liu *et al.* (1976) used a sum of standard linear solids to obtain a model with constant Q over three orders of magnitude of frequency.

I now present an example of a general linear model, in which the complex velocity $c(\omega)$ is defined as (Wang and Guo, 2004b):

$$\frac{1}{c(\omega)} = \frac{1}{v_\infty} \left(1 + \frac{a}{\sqrt{1 + i\omega\tau}} + \frac{b}{1 + i\omega\tau} \right), \quad (3.71)$$

where τ denotes a relaxation time constant. Considering $c(\omega) = \sqrt{M(\omega)/\rho}$, equation (3.71) is a standard linear solid model in parallel with a non-rational function involving a square root, which also shows some similarity to the Cole–Cole model.

This model is similar to Hanyga and Seredyńska's (1999a, 1999b) model, which they claimed was appropriate for wave-propagation modelling in poro- and viscoelastic media. However, their model was without the factor $1/v_\infty$. Here I introduce this $1/v_\infty$ factor so that both sides of the equation have physical units of inverse velocity. When $\omega \rightarrow 0$ and $\omega \rightarrow \infty$, the phase velocities can be expressed as

$$\operatorname{Re} \left\{ \frac{1}{c_0} \right\} = \frac{1}{v_\infty} (1 + a + b) \quad (3.72)$$

and

$$\operatorname{Re} \left\{ \frac{1}{c_\infty} \right\} = \frac{1}{v_\infty}, \quad (3.73)$$

respectively.

The general linear model (3.71) defines the attenuation coefficient as

$$\alpha(\omega) \equiv -\operatorname{Im} \left\{ \frac{\omega}{c(\omega)} \right\} \approx \frac{1}{v_\infty} \left[\frac{a}{2} \left(1 + \frac{1}{2} \omega^2 \tau^2 \right) + b \right] \frac{\omega^2 \tau}{1 + \omega^2 \tau^2}, \quad (3.74)$$

and the phase velocity as

$$\frac{1}{v(\omega)} \equiv \operatorname{Re} \left\{ \frac{1}{c(\omega)} \right\} \approx \frac{1}{v_\infty} \left\{ 1 + \left[a \left(1 + \frac{5}{8} \omega^2 \tau^2 \right) + b \right] \frac{1}{1 + \omega^2 \tau^2} \right\}. \quad (3.75)$$

In the previous chapter, we have shown that this general linear model is able to match the modified Kolsky model reasonably well (Figure 2.12). Conversely, Ursin and Toverud (2002) mentioned Hanyga and Seredyńska's (1999a, 1999b) model as an example of a general linear solid model but did not compare it with other models, either analytically or numerically.

For this new general linear model, which was first presented in Wang and Guo (2004b), the earth Q model may be expressed as

$$Q^{-1}(\omega) \approx \frac{|\omega\tau| (a + 2b + \frac{1}{2}a\omega^2\tau^2)}{1 + a + b + (1 + \frac{5}{8}a)\omega^2\tau^2}. \quad (3.76)$$

Part II

Inverse Q filters

Chapter 4

Stabilized inverse Q filtering algorithm

Abstract An inverse Q filter consists of two components, for amplitude compensation and phase correction. Whereas the phase component is unconditionally stable, the amplitude compensation operator is an exponential function of the frequency and traveltime, and including it in inverse Q filtering may cause instability and generate undesirable artefacts in seismic data. This chapter presents a stable inverse Q filter algorithm. It is derived based on the theory of wavefield downward continuation. For each step of downward continuation, the extrapolated wavefield is solved as an inverse problem incorporating stabilization in the solution. This stabilized procedure can compensate for the amplitude effect and correct for the phase distortion simultaneously without boosting the ambient noise.

Inverse Q filtering is a seismic data-processing technique for enhancing the image resolution. When a seismic wave propagates through the earth media, because of the anelastic property of the subsurface material, the wave energy is partially absorbed and the wavelet is distorted. As a consequence, it is generally observed in a seismic profile that the amplitude of the wavelet decreases and the width of the wavelet gradually lengthens along a path of increasing traveltime. An inverse Q filter attempts to compensate for the energy loss, correct the wavelet distortion in terms of the shape and timing, and produce a seismic image with high resolution.

An inverse Q filter includes two components, for amplitude compensation

and phase correction. If an inverse Q filter considers phase correction only, it is unconditionally stable. When Q is constant in the medium, phase-only inverse Q filtering can be implemented efficiently as Stolt's (1978) wavenumber-frequency domain migration (Hargreaves and Calvert, 1991; Bano, 1996). This algorithm corrects the phase distortion from dispersion but neglects the amplitude effect. The amplitude-compensation operator is an exponential function of the frequency and traveltime, and including it in the inverse Q filter may cause instability and generate undesirable artefacts in the solution. Therefore, stability is the major concern in any scheme for inverse Q filtering.

It is desirable to have a stable algorithm for inverse Q filtering which can compensate for the amplitude effect and correct for the phase effect simultaneously, and does not boost the ambient noise. This chapter develops such a stable algorithm for inverse Q filtering. The implementation procedure is based on the theory of wavefield downward continuation (Claerbout, 1976). Within each step of downward continuation, the extrapolated wavefield, which is inverse Q filtered, is estimated by solving an inverse problem, and the solution is stabilized by incorporating a stabilization factor. In the implementation, the earth Q model is assumed to be a one-dimensional (1-D) function varying with depth or two-way traveltime.

4.1 Basics of inverse Q filtering

This section summarizes the basics of inverse Q filtering, to explain the new development in the following sections.

Inverse Q filtering can be introduced based on the 1-D one-way propagation wave equation

$$\frac{\partial U(r, \omega)}{\partial r} - i k(\omega) U(r, \omega) = 0, \quad (4.1)$$

where $U(r, \omega)$ is the plane wave of radial frequency ω at travel distance r , $k(\omega)$ is the wavenumber and i is the imaginary unit. Reflection seismograms record the reflection wave along the propagation path r from the source to reflector and back to the surface. Thus, in the following derivation we assume that the plane wave $U(r, \omega)$ has already been attenuated by a Q filter through travel distance r .

Equation (4.1) has an analytical solution given by

$$U(r + \Delta r, \omega) = U(r, \omega) \exp[ik(\omega)\Delta r]. \quad (4.2)$$

Considering only the positive frequencies, the complex wavenumber k defined by equation (3.27) becomes

$$k(\omega) = \left(1 - \frac{i}{2Q(\omega)}\right) \frac{\omega}{v_r} \left(\frac{\omega}{\omega_h}\right)^{-\gamma}, \quad (4.3)$$

where $\gamma = (\pi Q_r)^{-1}$, and v_r and Q_r are the phase velocity $v(\omega)$ and the $Q(\omega)$ value, respectively, at an arbitrary reference frequency. Following the investigation in Chapter 2, the tuning parameter ω_h is related to the highest possible frequency of the seismic band. Substituting this complex-valued wavenumber $k(\omega)$ into solution (4.2) produces the following expression:

$$U(r + \Delta r, \omega) = U(r, \omega) \exp \left[\left(\frac{1}{2Q(\omega)} + i \right) \left(\frac{\omega}{\omega_h} \right)^{-\gamma} \frac{\omega \Delta r}{v_r} \right]. \quad (4.4)$$

Replacing the distance increment Δr by traveltime increment $\Delta \tau = \Delta r / v_r$, equation (4.4) is expressed as

$$\begin{aligned} U(\tau + \Delta \tau, \omega) &= U(\tau, \omega) \exp \left[\left(\frac{\omega}{\omega_h} \right)^{-\gamma} \frac{\omega \Delta \tau}{2Q(\omega)} \right] \\ &\quad \times \exp \left[i \left(\frac{\omega}{\omega_h} \right)^{-\gamma} \omega \Delta \tau \right]. \end{aligned} \quad (4.5)$$

This is a basic inverse Q filter, in which the two exponential operators compensate and correct for, respectively, the amplitude effect (i.e. the energy absorption) and the phase effect (i.e. the velocity dispersion) of the earth Q filter.

Note that in derivation of equation (4.5), we assume that the reference velocity v_r approximately equals to the group velocity:

$$v_g = \left[\frac{\partial}{\partial \omega} \left(\frac{\omega}{v(\omega)} \right) \right]^{-1} = \frac{v(\omega)}{1 - \frac{\omega}{v(\omega)} \frac{\partial v(\omega)}{\partial \omega}} \approx v_r. \quad (4.6)$$

Equation (4.5) is the basis for inverse Q filtering in which downward continuation is performed in the frequency domain on all plane waves. The sum of these plane waves gives the time-domain seismic signal,

$$u(\tau + \Delta\tau) = \frac{1}{\pi} \int_0^{\infty} U(\tau + \Delta\tau, \omega) d\omega. \quad (4.7)$$

This summation is referred to as the imaging condition, as in seismic migration. Equations (4.5) and (4.7) must be applied successively to each time sample with sampling interval $\Delta\tau$, producing $u(\tau)$ at each level.

4.2 Numerical instability of inverse Q filtering

We now test the basic downward continuation scheme described above on a group of noise-free synthetic seismic traces, to show the numerical instability of inverse Q filtering.

We build a synthetic trace by

$$u(t) = \text{Re} \left\{ \frac{1}{\pi} \int_0^{\infty} S(\omega) \exp[i(\omega t - k r)] d\omega \right\}, \quad (4.8)$$

where $S(\omega)$ is the Fourier transform of a source waveform $s(t)$, defined as the real-valued Ricker wavelet,

$$s(t) = \left(1 - \frac{1}{2} \omega_0^2 t^2 \right) \exp \left(-\frac{1}{4} \omega_0^2 t^2 \right), \quad (4.9)$$

with the dominant radial frequency $\omega_0 = 100 \pi$ (i.e. 50 Hz). The Ricker wavelet is a symmetric, noncausal wavelet. We use this symmetric wavelet to conveniently examine the phase change visually after the inverse Q filter is applied, although a minimum-phase wavelet such as the Berlage wavelet

(Aldridge, 1990) would be more realistic for the source function such as in the case of an air-gun.

Given the travel distance $r = \tau v(\omega_0)$ for traveltime τ of the plane wave with dominant frequency ω_0 , the kr term used in equation (4.8) can be expressed as

$$kr = \left(1 - \frac{i}{2Q}\right) \left(\frac{\omega}{\omega_0}\right)^{-\gamma} \omega \tau, \quad (4.10)$$

so that it is independent of the velocity $v(\omega_0)$. In the example, we consider the signal to consist of a sequence of Ricker wavelets with $\tau = 100, 400, \dots, 1900$ ms (increment 300 ms). Figure 4.1a shows five synthetic traces with different Q values ($Q = 400, 200, 100, 50$ and 25) constant with depth in each case.

Figure 4.1b displays the result of applying the inverse Q filter to the synthetic signals. For traces with $Q = 400$ and 200, the process restores the Ricker wavelet with correct phase and amplitude. However, there are strong artefacts as the Q value decreases and the imaging time increases, even though the input signal is noise-free. The appearance of noise in the output signal is a natural consequence of the downward continuation procedure: a plane wave is attenuated gradually, and beyond a certain distance the signal is below the ambient noise level, but the amplification required to recover the signal amplifies the ambient noise. In the data-noise-free case here, the background noise comes from the machine errors relative to working precision. This creation of strong artefacts is referred to as the numerical instability of the inverse Q filter.

In equation (4.5), the amplitude compensation operator is

$$A(\omega) \equiv \exp \left[\frac{\omega}{2Q(\omega)} \left(\frac{\omega}{\omega_h} \right)^{-\gamma} \Delta \tau \right]. \quad (4.11)$$

If we set $A(\omega) = 1$, equation (4.5) becomes an inverse Q filter for phase correction only:

$$U(\tau + \Delta \tau, \omega) = U(\tau, \omega) \exp \left[i \left(\frac{\omega}{\omega_h} \right)^{-\gamma} \omega \Delta \tau \right]. \quad (4.12)$$

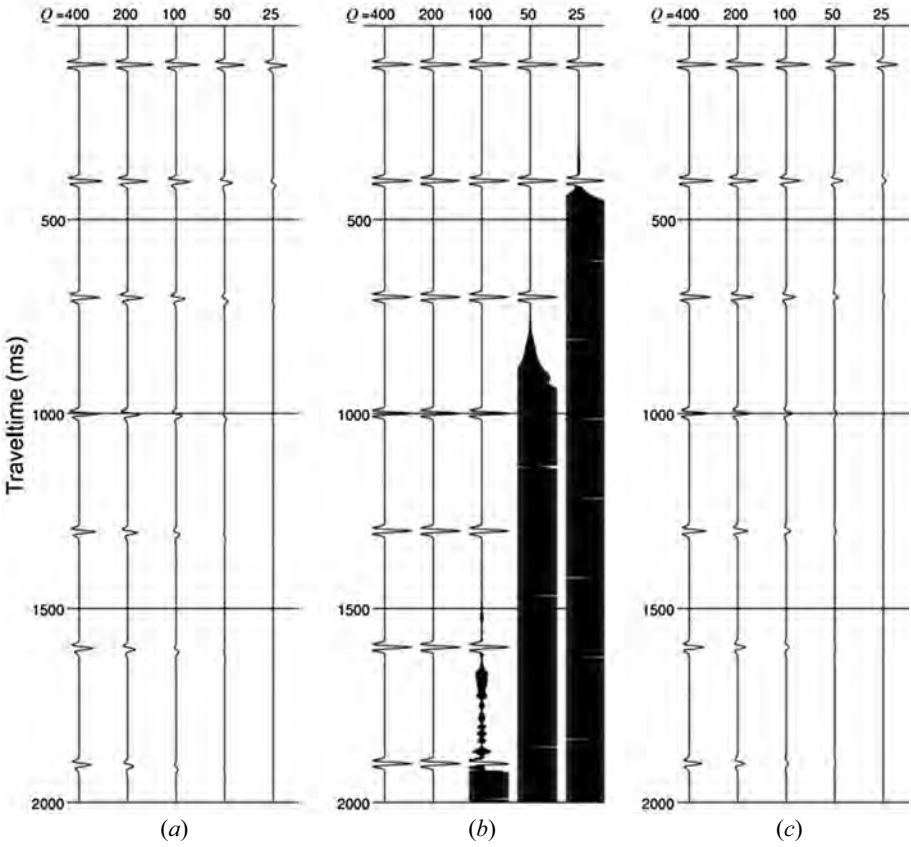


Figure 4.1 The earth Q filter and the inverse Q filter. (a) Synthetic traces show the effect of the earth Q filter with $Q = 400, 200, 100, 50$ and 25 . (b) The inverse Q filtering (compensating for both phase and amplitude) result, which clearly indicates the numerical instability. (c) The phase-only inverse Q filtered result.

This phase-only inverse Q filter is unconditionally stable, as shown in Figure 4.1c. Thus a restricted stability condition may be stated as

$$A(\omega) \approx \exp \left[\frac{\omega \Delta \tau}{2Q} \right] \leq 1, \quad (4.13)$$

required for every sample interval $\Delta \tau$.

In practice, the artefacts caused by numerical instability can be suppressed by a low-pass filter. Based on experiments, I have found the

following empirical stability condition:

$$\exp \left[\sum_{\tau} \left(\frac{\omega}{2Q(\tau)} \Delta \tau \right) \right] \leq e. \quad (4.14)$$

That is, the (accumulated) exponent of the amplitude factor is not greater than 1. Equation (4.14) thus suggests an upper limit on the frequencies that can be included in the amplitude compensation,

$$\omega \leq \frac{2Q}{\tau} \equiv \omega_q, \quad (4.15)$$

where $\tau = \sum \Delta \tau$ and ω_q is a time-varying frequency limit.

We now test this low-pass filter with the following three methods:

- 1) both phase and amplitude compensation are truncated at frequency ω_q , with cosine-square tapering;
- 2) phase compensation is performed on the full frequency band but with amplitude compensation only within the band limit $(0, \omega_q)$;
- 3) both phase and amplitude are compensated on the full frequency band with the amplitude operator defined by

$$A(\omega) = \begin{cases} \exp \left[\frac{\omega \Delta \tau}{2Q} \right], & \omega \leq \omega_q, \\ A(\omega_q), & \omega > \omega_q. \end{cases} \quad (4.16)$$

The results of these three schemes applied to the synthetic data set of Figure 4.1a are shown in Figures 4.2a–c, respectively. We can see from Figure 4.2 that (b) shows an improvement over (a), but (c) is superior to both as the amplitudes for the traces $Q \leq 200$ are better compensated. In each case the numerical instability evident in Figure 4.1b is successfully suppressed. We may consider the third test scheme (Figure 4.2c) as a type of gain-limited inverse Q filter, but just for application to a seismic data set free of acquisition noise. For practical application, a gain limit should be set also according to the noise level in the seismic data set. This aspect is discussed in the following stabilization scheme.

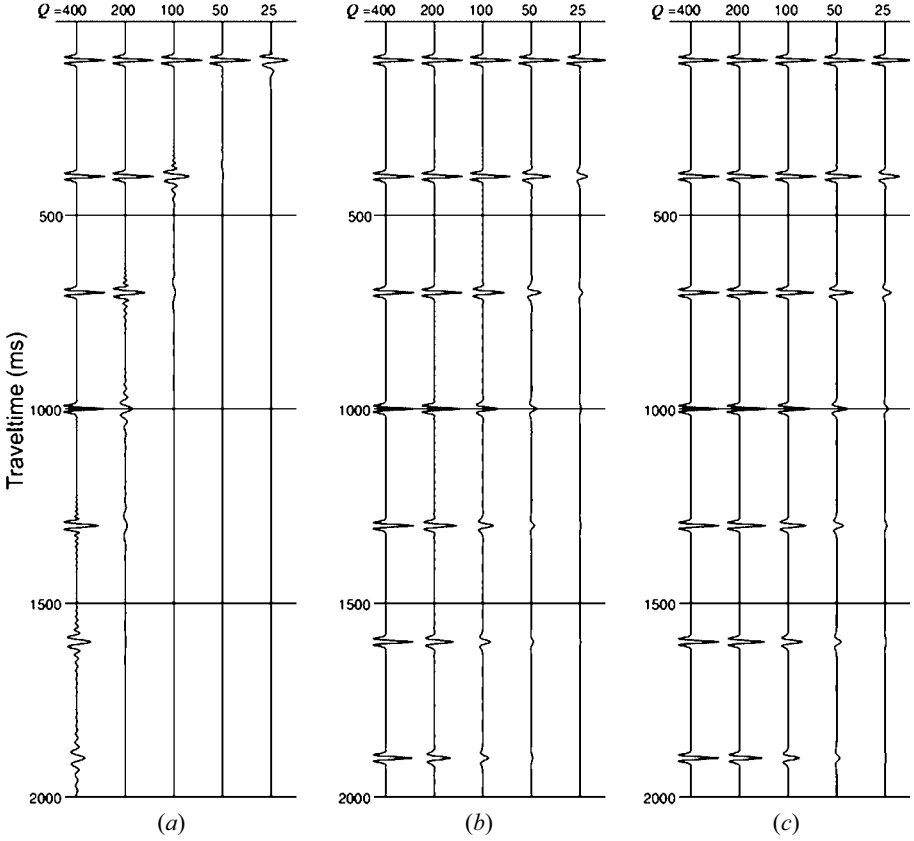


Figure 4.2 Inverse Q filters using three distinct methods: (a) with a low-pass filter, $\omega \leq \omega_q$; (b) with full-band phase compensation but band-limited amplitude compensation; (c) with full-band phase compensation and modified full-band amplitude compensation, i.e. the gain-limited inverse Q filter. The input signal in each case is as shown in Figure 4.1a.

4.3 Stabilized inverse Q filter

To further improve the performance of inverse Q filtering, we now propose a stabilized approach to the wavefield downward continuation, where Q is a 1-D function, $Q(\tau)$, varying with depth-time τ .

Considering downward continuation from the surface $\tau_0 = 0$ to the depth-time level τ using equation (4.7), we may express the wavefield $U(\tau, \omega)$ as

$$\begin{aligned}
 U(\tau, \omega) &= U(0, \omega) \exp \left[\int_0^\tau \frac{\omega}{2Q(\tau')} \left(\frac{\omega}{\omega_h} \right)^{-\gamma(\tau')} d\tau' \right] \\
 &\times \exp \left[i \int_0^\tau \left(\frac{\omega}{\omega_h} \right)^{-\gamma(\tau')} \omega d\tau' \right], \tag{4.17}
 \end{aligned}$$

where

$$\gamma(\tau) = \frac{1}{\pi Q(\tau)}. \tag{4.18}$$

To stabilize the implementation, we rewrite equation (4.17) as

$$\beta(\tau, \omega) U(\tau, \omega) = U(0, \omega) \exp \left[i \int_0^\tau \left(\frac{\omega}{\omega_h} \right)^{-\gamma(\tau')} \omega d\tau' \right], \tag{4.19}$$

where

$$\beta(\tau, \omega) = \exp \left[- \int_0^\tau \frac{\omega}{2Q(\tau')} \left(\frac{\omega}{\omega_h} \right)^{-\gamma(\tau')} d\tau' \right]. \tag{4.20}$$

Solving equation (4.19) as an inverse problem with stabilization, we derive the following amplitude-stabilized formula:

$$u(\tau) = U(0, \omega) A(\tau, \omega) \exp \left[i \int_0^\tau \left(\frac{\omega}{\omega_h} \right)^{-\gamma(\tau')} \omega d\tau' \right], \tag{4.21}$$

where

$$A(\tau, \omega) = \frac{\beta(\tau, \omega) + \sigma^2}{\beta^2(\tau, \omega) + \sigma^2}, \tag{4.22}$$

and σ^2 is a stabilization factor, a real positive constant used to stabilize the solution. Equation (4.21) is the basis for an inverse Q filter in which downward continuation is performed on all plane waves in the frequency domain. Finally, we sum these plane waves to produce the time-domain seismic signal,

$$u(\tau) = \frac{1}{\pi} \int_0^{\infty} U(0, \omega) \Lambda(\tau, \omega) \exp \left[i \int_0^{\tau} \left(\frac{\omega}{\omega_h} \right)^{-\gamma(\tau')} \omega d\tau' \right] d\omega. \quad (4.23)$$

We refer to this expression as stabilized inverse Q filtering.

Stabilized inverse Q filtering, equation (4.23), must be performed successively to each time sample τ . Therefore, we may discretize it to

$$\begin{bmatrix} u_0 \\ u_1 \\ \vdots \\ u_M \end{bmatrix} = \begin{bmatrix} a_{0,0} & a_{0,1} & \cdots & a_{0,N} \\ a_{1,0} & a_{1,1} & \cdots & a_{1,N} \\ \vdots & \vdots & & \vdots \\ a_{M,0} & a_{M,1} & \cdots & a_{M,N} \end{bmatrix} \begin{bmatrix} U_0 \\ U_1 \\ \vdots \\ U_N \end{bmatrix}, \quad (4.24)$$

or present it in a vector-matrix form as

$$\mathbf{x} = \mathbf{A}\mathbf{z}, \quad (4.25)$$

where $\mathbf{x} = \{u(\tau_i)\}$ is the time-domain output data vector, $\mathbf{z} = \{U(\omega_j)\}$ is the frequency-domain input data vector and \mathbf{A} ($M \times N$) is the inverse Q filter with elements defined as

$$a_{i,j} = \frac{1}{N} \Lambda(\tau_i, \omega_j) \exp \left[i \int_0^{\tau_i} \left(\frac{\omega_j}{\omega_h} \right)^{-\gamma(\tau')} \omega_j d\tau' \right], \quad (4.26)$$

in which $\Lambda(\tau_i, \omega_j)$ is the stabilized amplitude-compensation coefficient, and the exponential term is the phase-correction term of the inverse Q operator.

4.4 Comparison with gain-limited inverse Q filter

To demonstrate the merit of stabilized inverse Q filter, we first compare this algorithm to the gain-limited inverse Q filter presented in expression (4.17), and then compare it with a conventional inverse Q filter.

For the comparison between stabilized and gain-limited inverse Q filter algorithms, we apply them to a group of synthetic traces, first without any noise and then with noise added.

A group of noise-free synthetic traces is depicted in Figure 4.3a, the same

data set shown in Figure 4.1a. Inverse Q filtered results are displayed in Figures 4.3b and 4.3c, where (b) is the result of gain-limited inverse Q filtering, and (c) is the result of stabilized inverse Q filtering. There are two observations we can make, as follows.

- 1) Both methods have managed to overcome the instability problem in inverse Q filtering, and successfully suppressed the numerical artefacts appearing in Figure 4.1b.
- 2) Stabilized inverse Q filtering has produced a superior result, as the amplitudes of more high-frequency components have been compensated. It has recovered all the frequency components that are in principle recoverable, and intelligently limited the attempt to compensate a given high-frequency wave component when its amplitude has been attenuated to a level below the ambient noise level.

The difference between these two results seems marginal when taking into account all possible approximations involved in the seismic data processing flow. However, if we apply these two algorithms to a noisy data set, we can see a significant difference between them.

We now repeat the same exercise as in Figure 4.3 but add in some random noise to the synthetic traces. The noise added here is very weak and is hardly visible from the plot displayed in Figure 4.4a. Over all the five synthetic traces, the ratio of the maximum noise amplitude to the maximum signal amplitude is only 2%. Even with such weak noise in the input, the gain-limited inverse Q filter has boosted the noise, as shown in Figure 4.4b. The smaller the Q value, the stronger the noise is boosted by the inverse Q filter. Conversely, the stabilized inverse Q filter has produced a result with a much higher signal-to-noise ratio, as shown in Figure 4.4c.

Figure 4.5 shows a comparison of the amplitude operators for the inverse Q filters from gain-limited (dotted line) and stabilized (solid line) scheme. The operators are calculated at sample time $\tau = 1$ and 2 s for $Q = 100$. In the gain-limited scheme, $\omega_q = 2Q/\tau$, which is equivalent to a gain limit of 8.69 dB. The stabilized scheme, in which the stabilization factor $\sigma^2 = 2.66\%$ (calculated based on an empirical formula given in Chapter 7) is used, gradually reduces the compensation amount as the frequency increases.

Figure 4.5 clearly indicates that the gain-limited scheme boosts the amplitude of high frequencies and thus produces the noise in Figure 4.4b. In

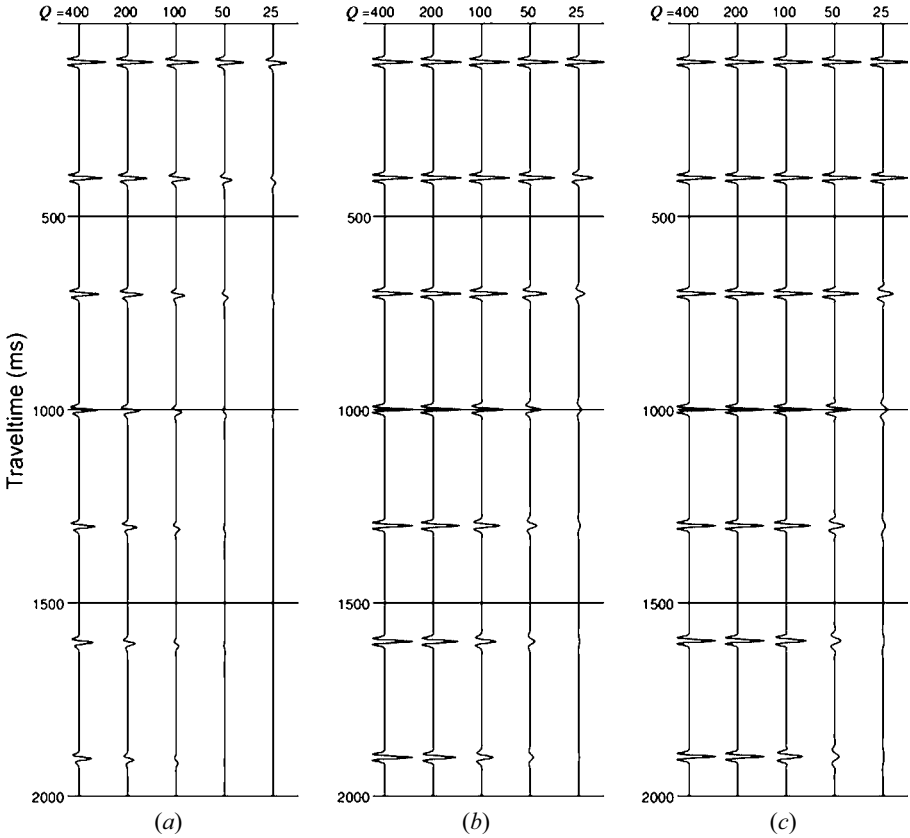


Figure 4.3 Noise-free synthetic traces and the result of two inverse Q filtering algorithms: (a) synthetic seismic traces which show the effect of earth Q filtering with different Q values (Figure 4.1a); (b) the result of the gain-limited inverse Q filtering (Figure 4.2c); (c) the result of stabilized inverse Q filtering approach, which has recovered all the frequency components that are in principle recoverable, and intelligently limited the attempt to compensate a given high-frequency wave component when its amplitude has been attenuated to a level below the ambient noise level.

the gain-limited scheme, to suppress the noise, we need to apply a low-pass filter to cut off the high-frequency noise at late time (Bickel and Natarajan, 1985). The Butterworth filter is a common form of low-pass filter. It can be defined by

$$F(\omega) = \left[1 + \left(\frac{\omega}{\omega_0} \right)^{2\eta} \right]^{-1/2}, \quad (4.27)$$

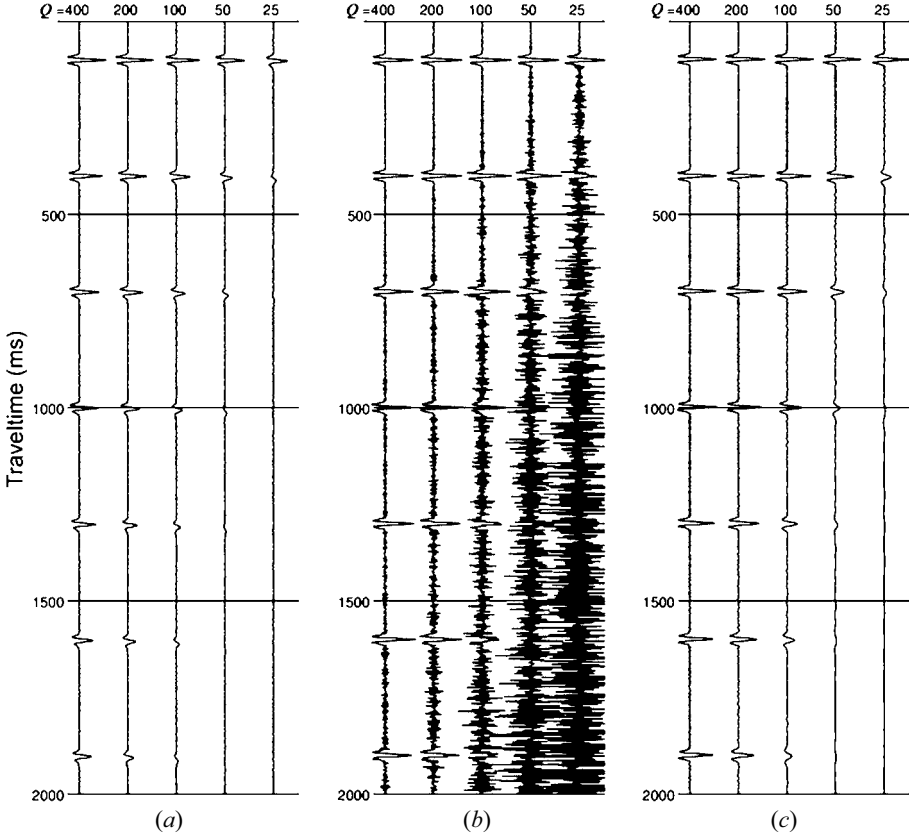


Figure 4.4 Noise-added synthetic traces and the result of two inverse Q filtering algorithms: (a) synthetic seismic traces added with a weak random noise (over all the five traces, the ratio of the maximum noise amplitude to the maximum signal amplitude is only 2%); (b) the gain-limited inverse Q filtering boosts the noise; (c) stabilized inverse Q filtering produces a result with a much higher signal-to-noise ratio, compared with the gain-limited inverse Q filtering result.

where ω_0 is the cut-off frequency and η determines the sharpness of the cut-off. The sharpness may also be measured as slope in decibels per octave, where the octave is the interval between two frequencies having a ratio of 2 and the slope may be approximated as:

$$\text{slope} \approx -10(\log_{10} 2)(2\eta - 1) \approx -6\eta \text{ (dB/oct).}$$

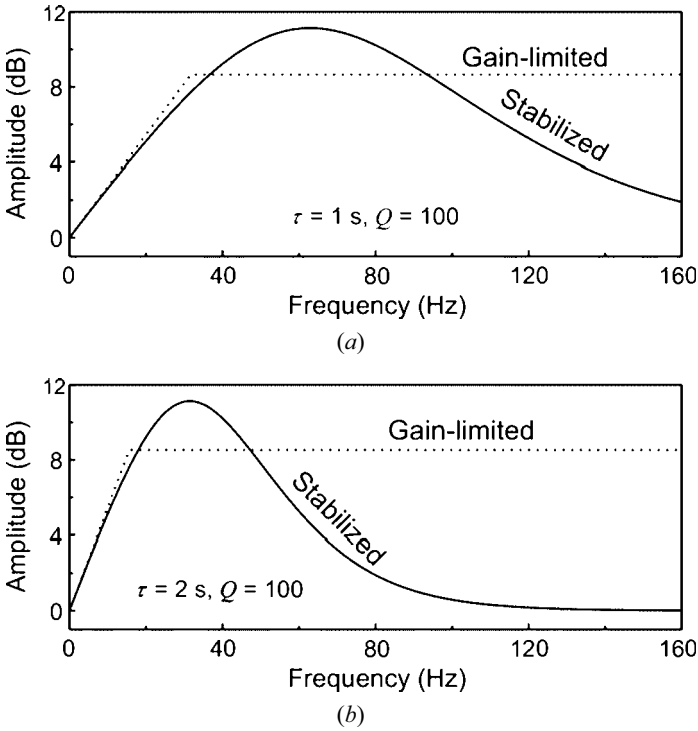


Figure 4.5 Comparison of amplitude operators for the inverse Q filters from gain-limited (dotted line) and stabilized (solid line) scheme, at sample time $\tau = 1$ and 2 s for $Q = 100$.

Figure 4.6 shows the filtered results of Figure 4.4b with a cut-off frequency of (a) 80 Hz, (b) 60 Hz and (c) 40 Hz, and the sharpness $\eta = 10$ or slope ≈ -60 dB/oct. We can make three observations from these results:

- 1) even performing high-cut filtering, traces with small Q values still have strong low-frequency noise;
- 2) the high-cut frequency should be time-variant;
- 3) however, this time-variant high-cut filter is also Q -dependent.

In fact, such a desirable high-cut filter that is time-variant and Q -dependent is naturally built in the stabilization scheme. From the stabilized gain curve shown in Figure 4.5, we can observe that (a) the stabilized gain curve is time- (and frequency-) dependent and (b) for high frequencies stabilized

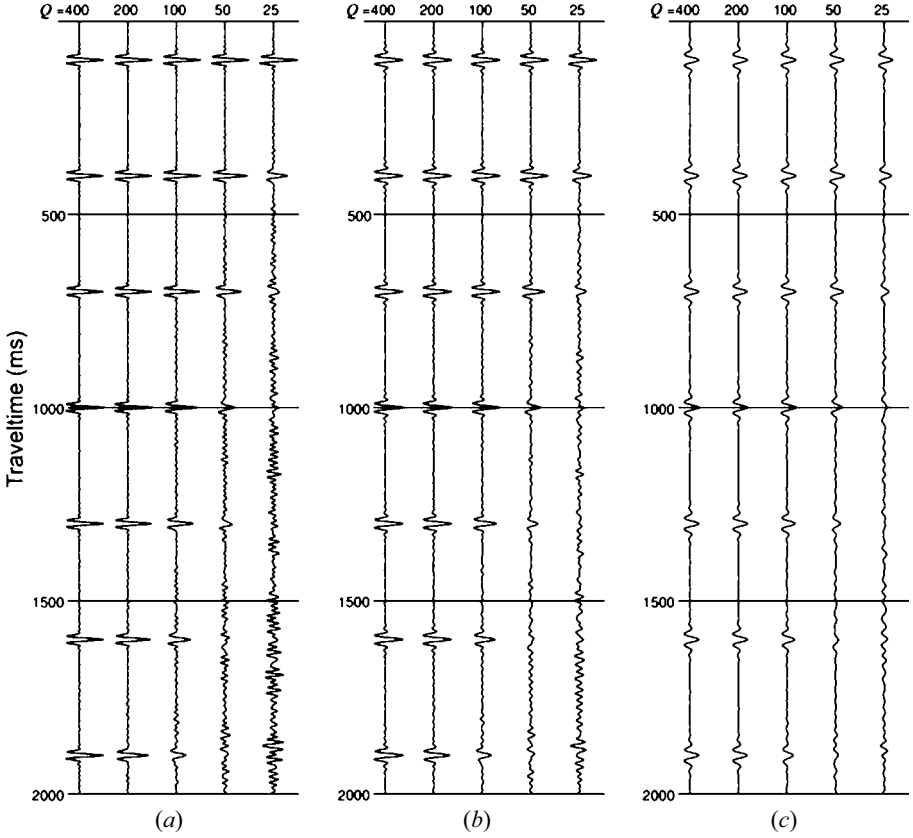


Figure 4.6 Gain-limited result (Figure 4.4b) after applying the Butterworth high-cut filter with a cut-off frequency of (a) 80 Hz, (b) 60 Hz and (c) 40 Hz. It indicates clearly that a desirable high-cut filter should be time-variant and Q -dependent. In fact, such a desirable filter is naturally built into the stabilized inverse Q filtering scheme.

gain approaches to 0 dB. The latter means that the stabilized inverse Q filter will leave those high-frequency components untouched, neither amplifying nor suppressing. This property is different from a general stabilized inversion problem which always intends to suppress the high frequencies, as presented in Wang (2002).

Note that the gain curves in Figure 4.5 are the compensation coefficients of all frequency components at a specified time, and summing all weighted frequency components will generate only the seismic sample, in this case, at time $\tau = 1$ and 2 s. But the high-cut filter was applying to the entire inverse

Q filtered trace in Figure 4.4b, not to the gain curve, and thus is not equivalent to applying a Butterworth filter to the gain-limited curve in Figure 4.5.

Certainly, the stabilized inverse Q filter is noise-level-dependent, and the stabilization factor σ^2 needs to be adjusted accordingly. In the discussion here, we assume that, in practice, the noise level in the input is very weak, as one might have applied some advanced random noise-attenuation techniques prior to the inverse Q filter. In the following examples, a forward-backward linear prediction method is used for random noise attenuation (Wang, 1999).

4.5 Comparison with a conventional inverse Q filter

We now compare the stabilized inverse Q filter with a conventional inverse Q filter. Considering the effect of earth Q filtering given by (Torey, 1962):

$$B(r, \omega) = \exp[-ik(\omega)r], \quad (4.28)$$

where r is the travelling distance, one can design an inverse Q filter as

$$A(r, \omega) \equiv \frac{1}{B(r, \omega)} = \exp[ik(\omega)r]. \quad (4.29)$$

Recall that the complex wavenumber $k(\omega)$ is given by

$$k(\omega) \equiv \frac{\omega}{v(\omega)} - i\alpha(\omega) = \mathcal{H}\{\alpha(\omega)\} - i\alpha(\omega), \quad (4.30)$$

where \mathcal{H} is the Hilbert transform to ensure the causal signal in forward Q modelling (equation 3.18), and the attenuation coefficient $\alpha(\omega)$ is given by equation (2.2) in the Kolsky model, we can then express the inverse Q filter, equation (4.29), as (Hale, 1981)

$$A(\tau, \omega) = \exp\left[\left(\omega + i\mathcal{H}\{\omega\}\right)\frac{\tau}{2Q}\right]. \quad (4.31)$$

We can also express this inverse Q filter as a Taylor series with a limited

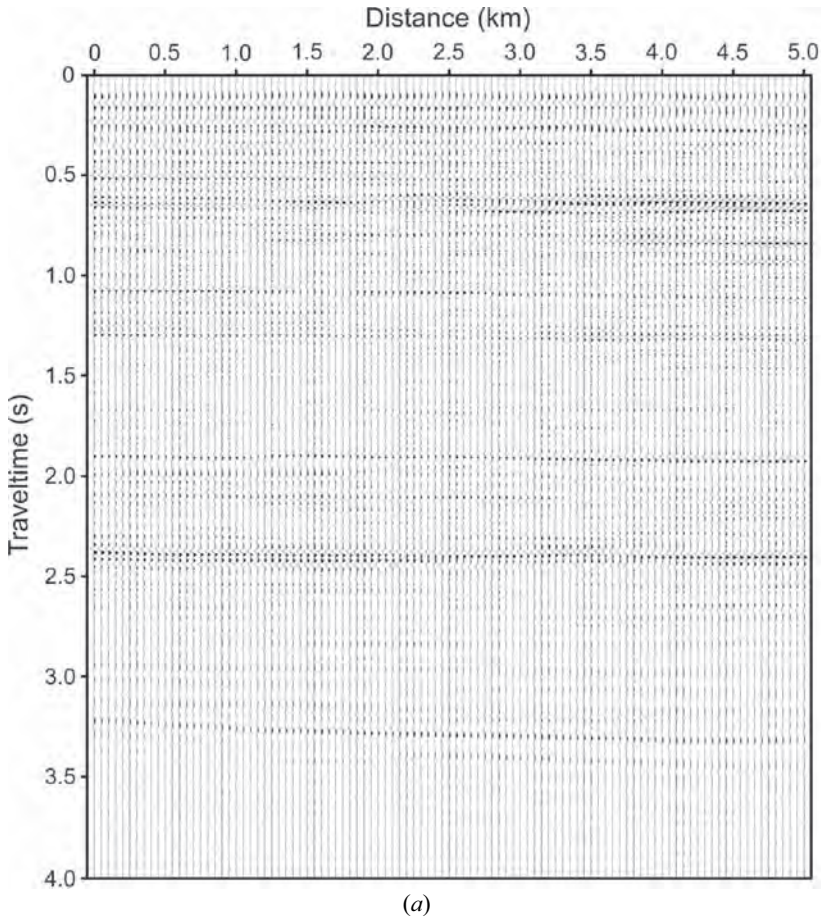


Figure 4.7 (a) A seismic section with very high signal-to-noise ratio, the input to inverse Q filtering shown in panels (b) and (c).

number of terms and treat each term separately (Hale, 1982; Gelius, 1987). To control the enthusiasm of the Q process, we then define a Butterworth spectrum in terms of a high cut-off frequency and a slope. One needs to design a series of inverse Q filters for a given time with a given Q value and given Butterworth high-cut characteristics, and then apply these filters to the seismic trace in a linear piecewise fashion, to simulate continuously varying Q compensation. We may refer to this approach as a conventional inverse Q filter.

Figure 4.7a is a marine seismic reflection, with very high signal-to-noise

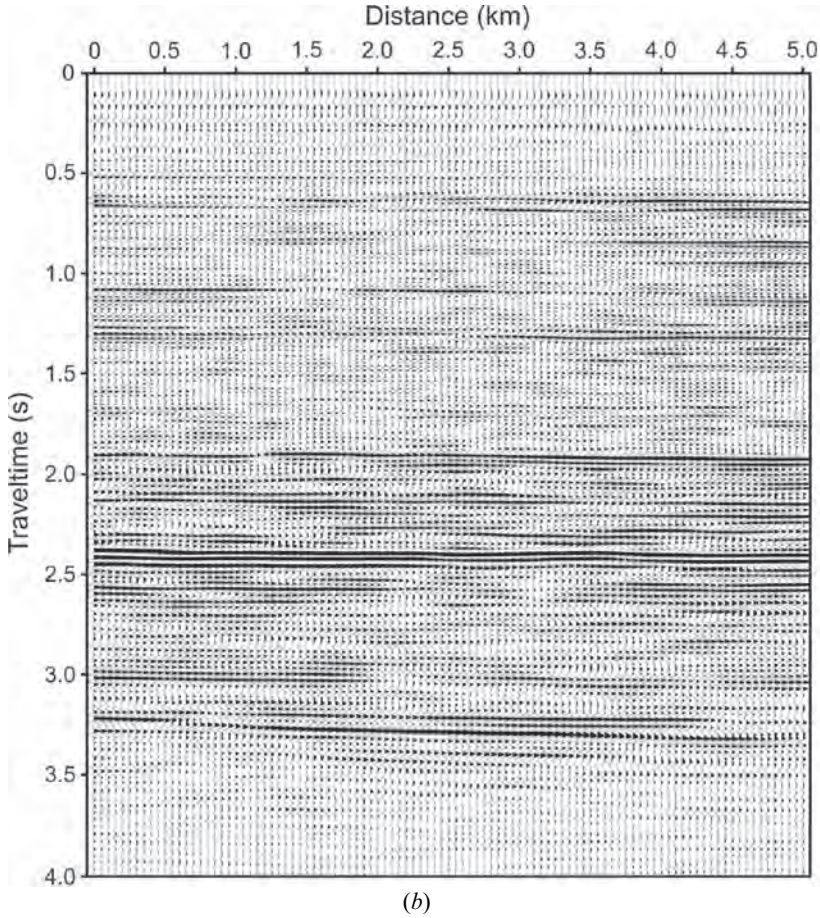


Figure 4.7 (contd) (b) Seismic section after conventional inverse Q filtering ($Q = 100$), in which a Butterworth filter is designed with a 65 Hz high cut-off frequency and a -60 dB/oct slope. Conventional inverse Q filtering boosts the ambient noise and degrades the signal-to-noise ratio of the output section.

ratio compared to a land seismic data section. Figures 4.7b and 4.7c show respectively the results of conventional and stabilized inverse Q filters. Without prior knowledge of the Q value, we set $Q = 100$ in the test. We adopt such a modest Q value here with the main purpose of minimizing the noise after the conventional inverse Q filtering. We can see that the conventional inverse Q filter boosts the ambient noise and degrades the signal-to-noise ratio of the output section. In comparison, the stabilized inverse Q filter produces a superior result by increasing the frequency

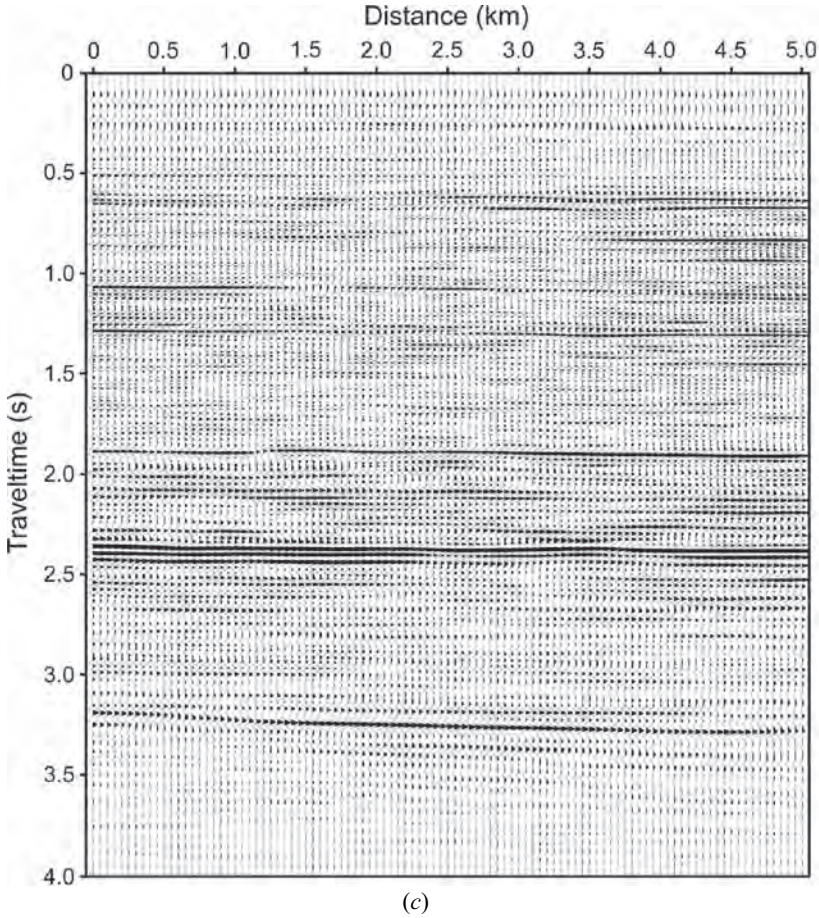


Figure 4.7 (contd) (c) Seismic section after stabilized inverse Q filtering ($Q = 100$ and $\sigma^2 = 0.5\%$). The stabilized scheme improves the interpretability of the seismic section by increasing the frequency bandwidth without degrading the signal-to-noise ratio.

bandwidth without degrading the signal-to-noise ratio, and thereby improving the interpretability of the seismic section.

A fundamental difference between the conventional and stabilized inverse Q filtering procedures is that the conventional method applies a low-pass filter, acting as a damage controller, to suppress the noise caused by inverse Q filtering, and the stabilized approach attempts to find a stable operator for inverse Q filtering. In Figure 4.7b, a Butterworth filter is designed with a high cut-off frequency of 65 Hz and a slope of -60 dB/oct. In Figure 4.7c,

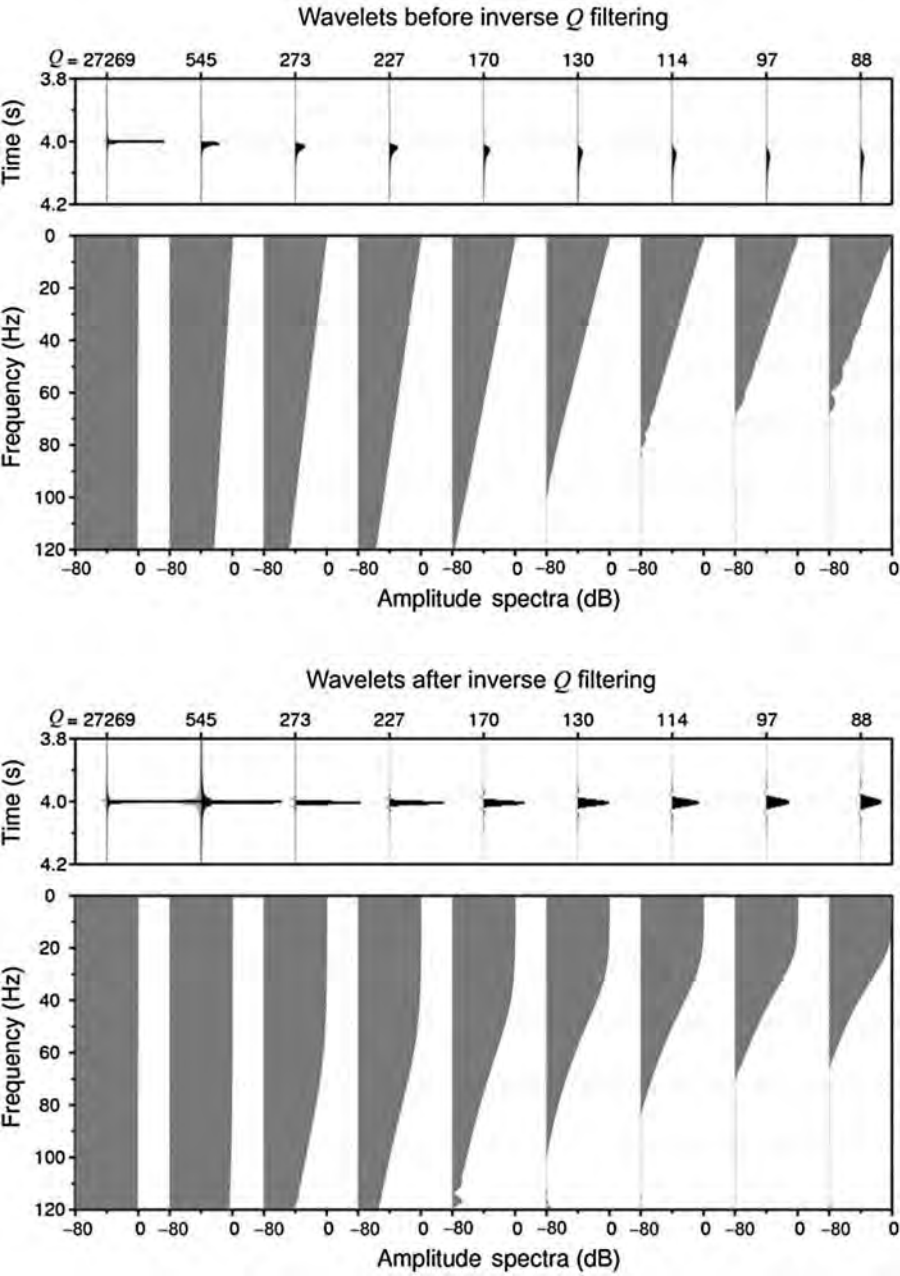


Figure 4.8 Seismic wavelets (centred at 4 s) and associated amplitude spectra before and after inverse Q filtering. The smaller the Q value, the more attenuation, and therefore the narrower the frequency bandwidth. When a plane wave with high frequency has been attenuated completely from the input seismic data, the stabilized algorithm for inverse Q filtering automatically limits the attempt to recover it.

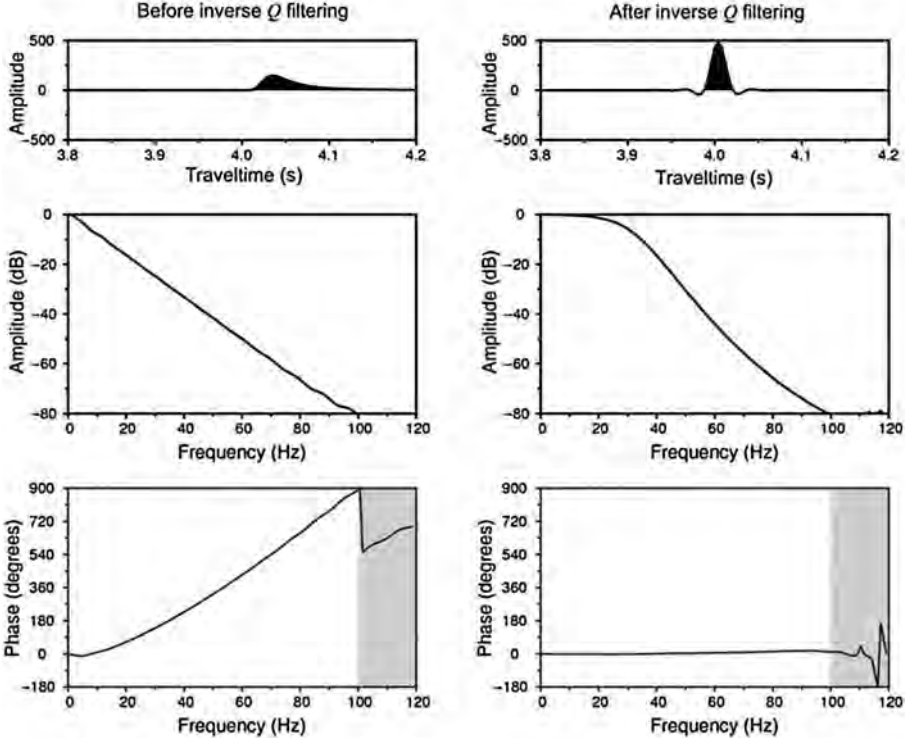


Figure 4.9 Amplitude and phase spectra of a wavelet ($Q = 130$, time = 4 s) before and after inverse Q filtering. The phase of the wavelet within the frequency range where amplitude spectra are greater than -80 dB has been fully recovered by inverse Q filtering.

a stabilization factor $\sigma^2 = 0.5\%$ is used for such a data set with high signal-to-noise ratio.

4.6 Synthetic and real data examples

First, we will take a synthetic example. In Chapter 2, Figures 2.2 and 2.4 showed a group of synthetic seismic traces and the inverse Q filtered result, respectively. Figure 4.8 shows seismic wavelets (centred at 4 s) and the associated amplitude spectra before and after inverse Q filtering for different Q values. The smaller the Q value, the greater the attenuation, and therefore the narrower the frequency bandwidth. When a plane wave with high frequency has been attenuated completely from the input seismic data,

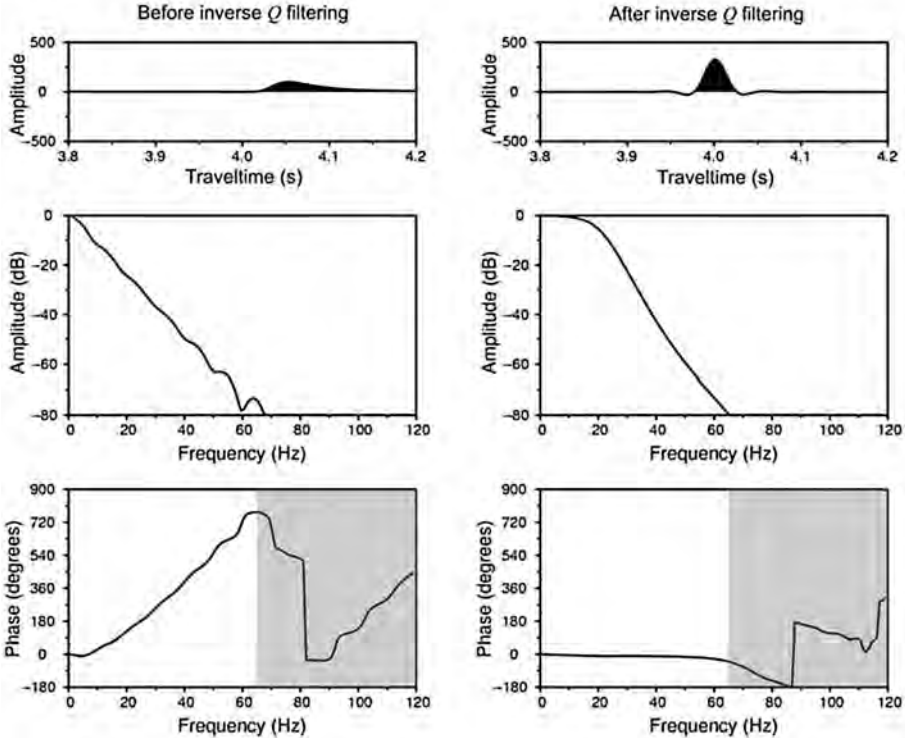


Figure 4.10 Amplitude and phase spectra of a wavelet ($Q = 88$, time = 4 s) before and after inverse Q filtering. The phase of the wavelet within the frequency range where amplitude spectra are greater than -80 dB has been fully recovered by inverse Q filtering.

the stabilized inverse Q filter algorithm automatically limits the attempt to recover it.

Figures 4.9 and 4.10 show seismic wavelets for $Q = 130$ and 88, respectively, and the associated amplitude and phase spectra before and after inverse Q filtering. In both cases, the phase of a wavelet within the frequency range where the amplitude spectra are larger than -80 dB has been fully recovered by inverse Q filtering.

Figures 4.11a and 4.11b show another example of stabilized inverse Q filtering, on land seismic data from North Africa. The Q values used in inverse Q filtering are estimated directly from the stack section (see the technical detail in Chapter 11), and listed as follows.

τ (s)	0.1–1	1–1.5	1.5–2	2–2.5	2.5–3	3–3.5	3.5–4
Q	47.5	47.5	65.8	83.0	95.8	108.0	128.0

Note that in the plot of Figure 4.11a, a time-squared gain recovery has been applied to boost the weak amplitudes for an easy visual comparison with the inverse Q filtered result shown in Figure 4.11b. Any improvement in continuity of events in Figure 4.11b should be reliable, because the inverse Q filtering algorithm works purely trace-by-trace (i.e. it is *not* a multi-channel process). We would expect that if inverse Q filtering were applied to the whole three-dimensional stack database, it would enhance the three-dimensional migration process, which would benefit from the higher bandwidth.

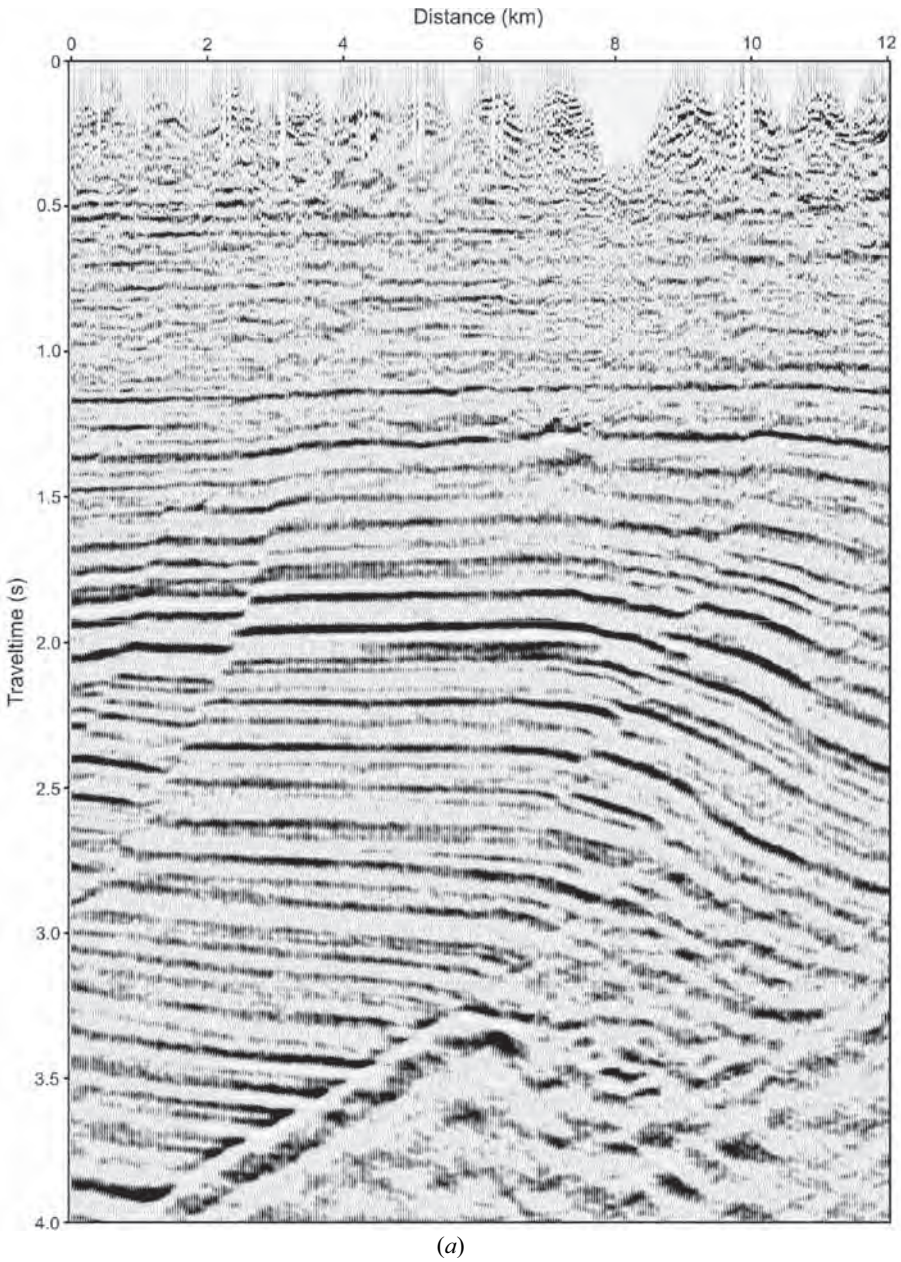


Figure 4.11 (a) A land seismic stack section for inverse Q filtering test. In this plot, a time-squared gain recovery has been applied in order to boost the weak amplitudes for an easy visual comparison to the inverse Q filtered result shown in panel (b).

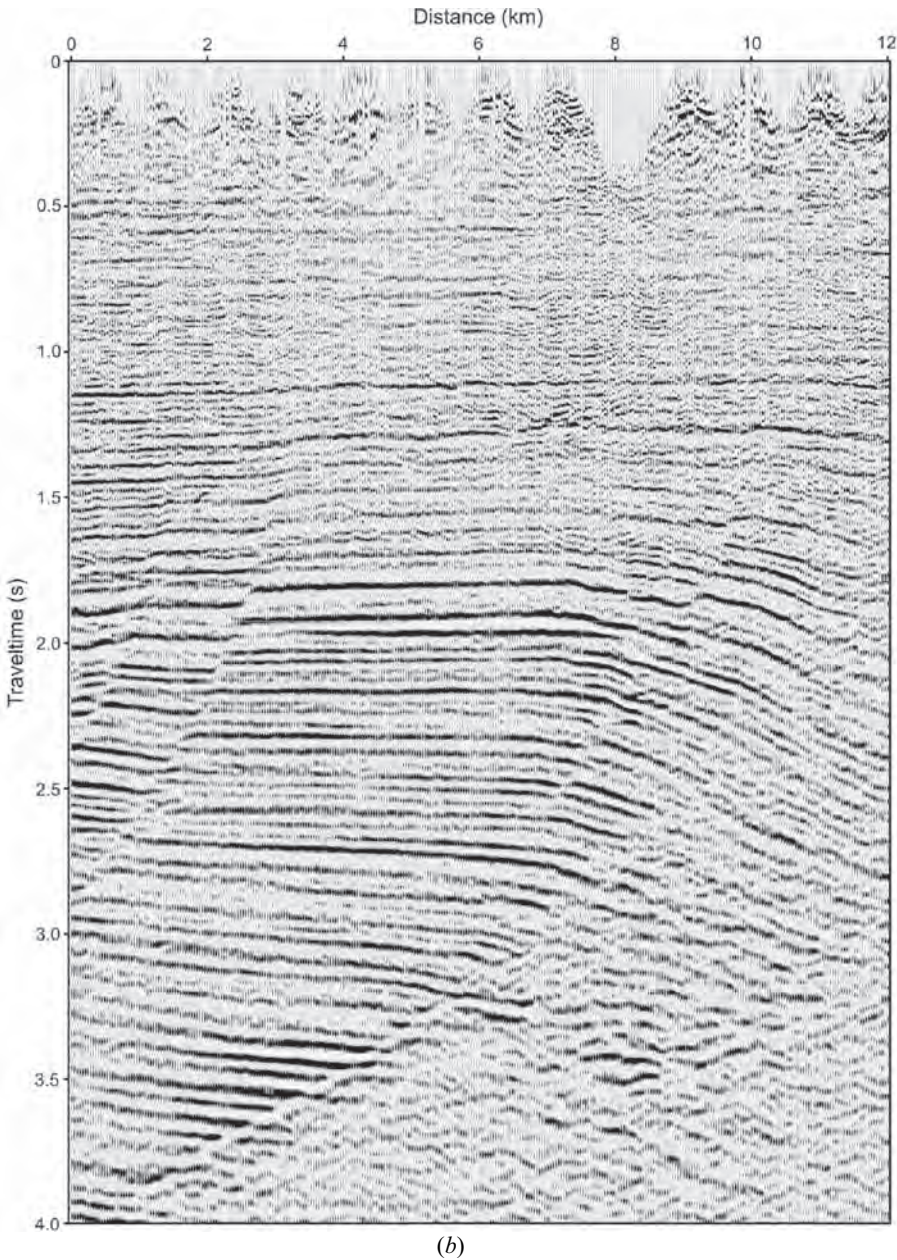


Figure 4.11 (contd) (b) The land seismic section after inverse Q filtering. Any improvement in continuity of the events in this section should be reliable, because the inverse Q filtering algorithm works purely trace-by-trace (i.e. it is not a multi-channel process).

Chapter 5

Inverse Q filtering for phase and amplitude separately

Abstract

For inverse Q filtering, if we can implement phase correction and amplitude compensation separately, we will be able to perform a reliable Q estimation or other processing steps in between. If we have applied a full inverse Q filter to the seismic data, we can also conduct phase-only or amplitude-only *forward* Q filtering to remove the phase or amplitude effect of the inverse Q filter previously applied, and then redo phase- or amplitude-only inverse Q filtering with a updated Q model. Therefore, each of these inverse and forward Q filters (phase-only, amplitude-only or both) should be fully reversible. In this chapter, we set up these different types of inverse Q filters and their counterparts of forward Q filters uniformly as wavefield downward continuation, and present them as a dual-space filter in which the input is in the frequency domain and the output in the time domain.

In this chapter, we will develop inverse Q filtering algorithms for phase correction and amplitude compensation separately. We can apply these phase-only or amplitude-only inverse Q filters in seismic data processing in different combinations as follows. (1) We can use them in sequence to produce a result from full inverse Q filtering. For example, we can apply a phase-only inverse Q filter to a pre-stack data set and defer the amplitude compensation to a late stage after stacking. In between, we can conduct a reliable Q estimation based on the phase-corrected data set without any amplitude altering. With this updated Q model, we can then perform the

amplitude compensation at a later stage. (2) Alternatively, we can remove the effect of phase correction previously applied to the seismic data, and re-apply a full inverse Q filter with a new, reliable Q function. (3) If we have applied a full inverse Q filter to the data set, we can remove either the phase-correction effect or the amplitude-compensation effect, and then re-apply a refined phase- or amplitude-only inverse Q filter to the data set.

We refer to the removal of inverse Q filtering effects previously applied to the data set as forward Q filtering. Considering inverse Q filtering for phase and amplitude separately, we can easily build the associated phase- or amplitude-only forward Q filters, which lead to a full forward Q filtering algorithm. As described in Chapter 4, we may represent a stable inverse Q filter as a linear system (equations 4.24 or 4.25). Solving this linear system as an inverse problem, we may remove the amplitude and phase effects given by inverse Q filtering and reproduce the original seismic traces. In practice, however, the tedious calculation involved in the inverse problem renders it an impractical choice for routine seismic data processing. In this chapter, we will introduce a forward Q filtering algorithm that has the same efficiency as the inverse Q filter presented in Chapter 4.

Ultimately, after the development in the previous chapter and in the current chapter, we will be able to set up all different inverse Q filters and the associated forward Q filters as wavefield downward continuation. We can represent the downward continuation as a linear system uniformly in a vector-matrix form for either inverse Q filtering or *inverse* inverse- Q filtering (i.e. forward Q filtering). In the linear system, the input is always a frequency-domain vector, the output is always a time-domain vector and the operator linking them is a dual space filter.

5.1 Phase-only inverse Q filtering

We can derive a phase-only inverse Q filter from the full inverse Q filter (equation 4.5) simply by setting $Q^{-1} = 0$ in the amplitude-compensation operator, and express it as

$$U(\tau + \Delta\tau, \omega) = U(\tau, \omega) \exp \left[i \left(\frac{\omega}{\omega_h} \right)^{-\gamma(\tau')} \omega \Delta\tau \right], \quad (5.1)$$

where $\tau' = \tau + \frac{1}{2}\Delta\tau$. Considering the downward continuation from the

recording surface $\tau_0 = 0$ down to the depth-time level τ , we rewrite equation (5.1) as

$$U(\tau, \omega) = U(0, \omega) \exp \left[i \int_0^\tau \left(\frac{\omega}{\omega_h} \right)^{-\gamma(\tau')} \omega d\tau' \right]. \quad (5.2)$$

where $\gamma(\tau)$ is the function of depth-time τ .

Applying the imaging condition (4.7), we obtain a time-domain seismic trace as

$$u(\tau) = \frac{1}{\pi} \int_0^\infty U(0, \omega) \exp \left[i \int_0^\tau \left(\frac{\omega}{\omega_h} \right)^{-\gamma(\tau')} \omega d\tau' \right] d\omega. \quad (5.3)$$

We refer to this expression as the phase-only inverse Q filter. Figure 5.1 displays the result of phase-only inverse Q filtering on the group of synthetic seismic traces shown in Figure 2.2.

5.2 Amplitude-only inverse Q filtering

In a similar way, we can derive an amplitude-only inverse Q filter from the full inverse Q filter (equation 4.5) by ignoring the Q effect (i.e. $Q^{-1} = 0$) in the phase operator. We express such an amplitude-only inverse Q filter as wavefield downward continuation:

$$U(\tau + \Delta\tau, \omega) = U(\tau, \omega) \exp \left[\frac{\omega}{2Q(\tau')} \left(\frac{\omega}{\omega_h} \right)^{-\gamma(\tau')} \Delta\tau \right] \exp[i\omega\Delta\tau]. \quad (5.4)$$

Considering the downward continuation from the recording surface $\tau_0 = 0$ to the depth-time level τ , we obtain the following expression:

$$U(\tau, \omega) = U(0, \omega) \exp \left[\int_0^\tau \frac{\omega}{2Q(\tau')} \left(\frac{\omega}{\omega_h} \right)^{-\gamma(\tau')} d\tau \right] \exp[i\omega\tau], \quad (5.5)$$

where $Q(\tau)$ and then $\gamma(\tau)$ are time- or depth-dependent.

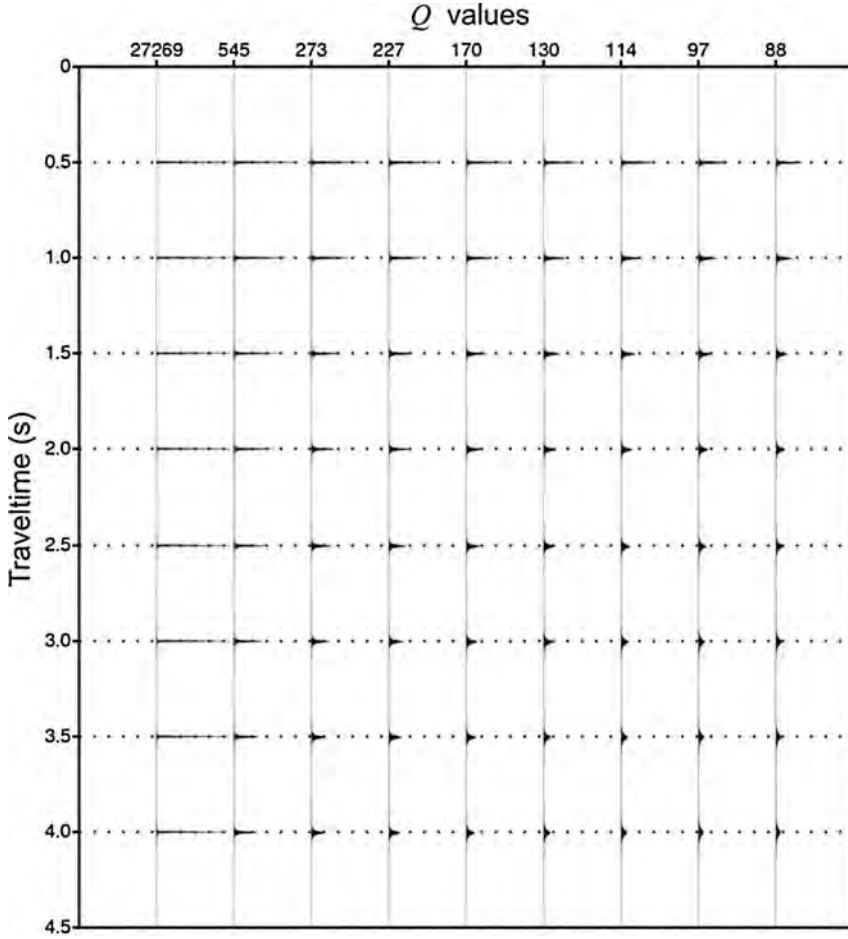


Figure 5.1 Phase-only inverse Q filter on a group of synthetic seismic traces, shown in Figure 2.2 (provided by an oil company for benchmarking inverse Q filter algorithms).

We can also express a stabilized formula as

$$U(\tau, \omega) = U(0, \omega) \Lambda(\tau, \omega) \exp[i\omega\tau], \quad (5.6)$$

where $\Lambda(\tau, \omega)$ is the stabilized amplitude-compensation coefficient, given in equation (4.22). We perform equation (5.6) on all the frequency components, and sum over all of these plane waves (i.e. applying the

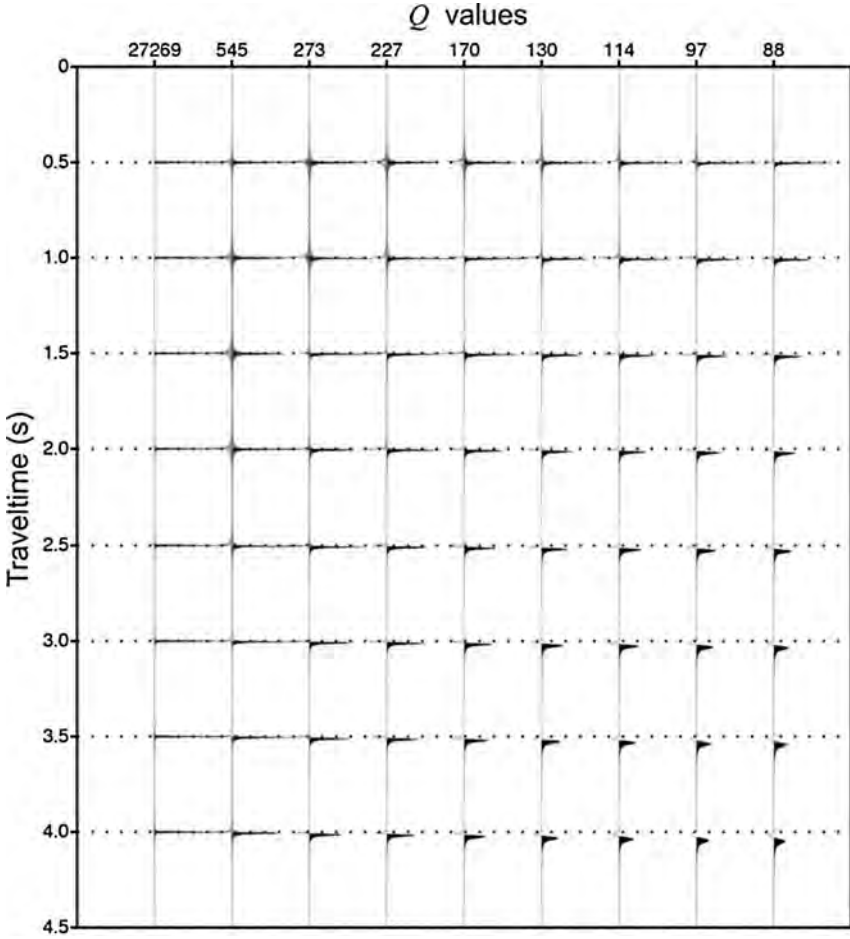


Figure 5.2 Amplitude-only inverse Q filter result.

imaging condition) to produce a sample of the seismic trace in the time domain as

$$u(\tau) = \frac{1}{\pi} \int_0^{\infty} U(0, \omega) A(\tau, \omega) \exp[i\omega\tau] d\omega. \quad (5.7)$$

Figure 5.2 shows the result of amplitude-only inverse Q filtering on the group of example synthetic traces. Note that the amplitude-only inverse Q filter has modified the shape of the wavelets.

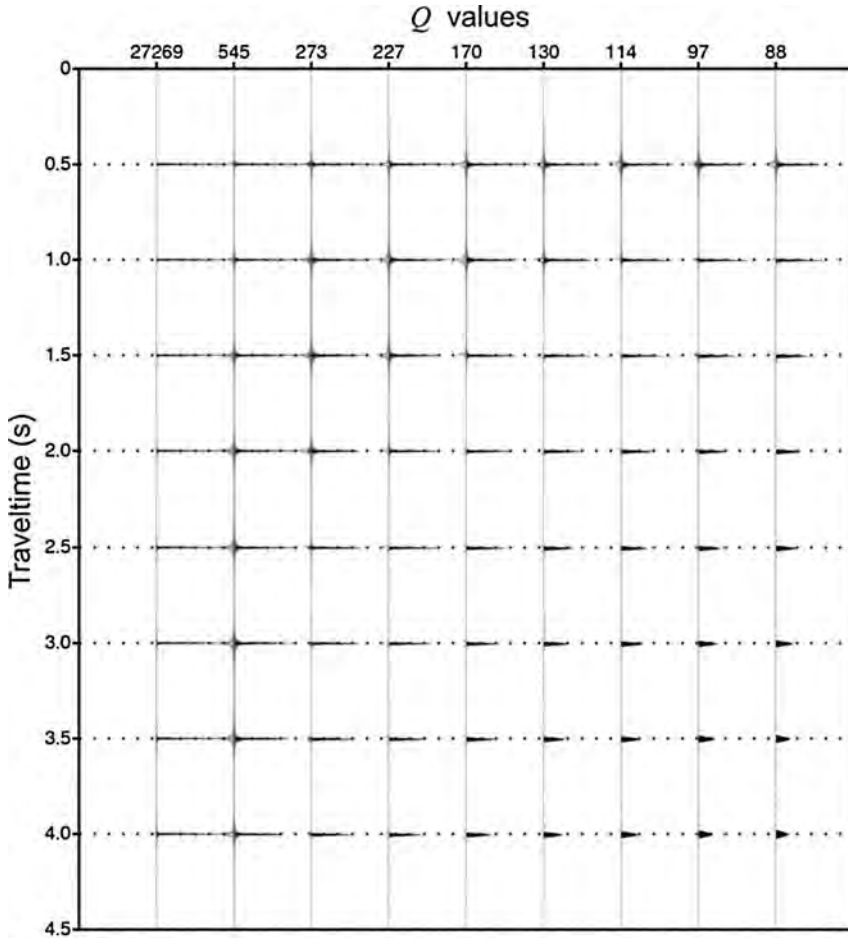


Figure 5.3 The result of two-pass inverse Q filter. It is the same as that of the one-pass inverse Q filtered result shown in Figure 2.4.

A two-pass procedure, phase-only followed by amplitude-only inverse Q filtering, produces the final result shown in Figure 5.3, which is similar to Figure 2.4, the one-pass full inverse Q filtered result.

5.3 Forward Q filtering

In practice, we often require the processing operation to be removable so that we can easily optimize the processing parameters later.

5.3.1 Phase-only forward Q filtering

We call the removal of the phase-correction effect given by a previous phase-only inverse Q filtering as phase-only forward Q filtering. It would be rather straightforward if we consider it as an inverse problem of equation (5.1) and take an inverse solution. But solving an inverse problem is often time-consuming because it involves the computation of an inverse matrix. In this section we will show that we can use the same equation as that for phase-only inverse Q filtering to represent an approximate expression for phase-only forward Q filtering by simply switching the sign of the Q value. That is, phase-only inverse Q filtering with negative Q is equivalent to phase-only forward Q filtering.

We can present the basic equation for phase-only inverse Q filtering in the time domain by applying the imaging condition to equation (5.1) as

$$u(\tau + \Delta\tau) = \frac{1}{\pi} \int_0^\infty U(\tau, \omega) \exp \left[i \left(\frac{\omega}{\omega_h} \right)^{-\gamma} \omega \Delta\tau \right] d\omega. \quad (5.8)$$

We can implement this expression as interpolation, scaling, and the fast inverse Fourier transform, following Hargreaves and Calvert (1991). To do so, we rewrite equation (5.8) as

$$u(\tau + \Delta\tau) = \frac{1}{\pi} \int_0^\infty U(\tau, \hat{\omega}) J_{\hat{\omega}} \exp[i\hat{\omega}\Delta\tau] d\hat{\omega}, \quad (5.9)$$

where $\hat{\omega}$ is a new frequency variable defined by

$$\hat{\omega} = \omega \left(\frac{\omega}{\omega_h} \right)^{-\gamma}, \quad (5.10)$$

and $J_{\hat{\omega}}$ is the Jacobian

$$J_{\hat{\omega}} \equiv \left\| \frac{d\omega}{d\hat{\omega}} \right\| = \frac{1}{1-\gamma} \left(\frac{\hat{\omega}}{\omega_h} \right)^{\frac{\gamma}{1-\gamma}} \approx (1+\gamma) \left(\frac{\hat{\omega}}{\omega_h} \right)^{\gamma}, \quad (5.11)$$

because $(1-\gamma)^{-1} \approx 1+\gamma$, for $\gamma \ll 1$. In equation (5.9), $U(\tau, \hat{\omega})$ is resampled

from $U(\tau, \omega)$, and $J_{\hat{\omega}}$ is a scaling factor. Then the integral (5.9) is an inverse Fourier transform of $J_{\hat{\omega}}U(\tau, \hat{\omega})$.

We now show that we can use the same implementation as equations (5.8) and (5.9), but with a negative $Q(\tau)$ function, to remove the phase correction made by phase-only inverse Q filtering. That is, replacing the frequency variable ω in the implementation of equation (5.9) with $\hat{\omega}$, we present phase-only forward Q filtering as

$$u(\tau + \Delta\tau) = \frac{1}{\pi} \int_0^{\infty} U(\tau, \hat{\omega}) \exp \left[i \left(\frac{\hat{\omega}}{\omega_h} \right)^{\gamma} \hat{\omega} \Delta\tau \right] d\hat{\omega}. \quad (5.12)$$

Note that we also replace $-\gamma$ in equation (5.8) with γ . Using a similar frequency-interpolation method to equation (5.10), we express equation (5.12) as

$$u(\tau + \Delta\tau) = \frac{1}{\pi} \int_0^{\infty} U(\tau, \omega) J_{\omega} \exp[i\omega\Delta\tau] d\omega, \quad (5.13)$$

where ω is the frequency after removing the inverse Q filter effect and is represented in terms of $\hat{\omega}$ as

$$\omega = \left(\frac{\hat{\omega}}{\omega_h^{\gamma}} \right)^{\frac{1}{1-\gamma}} \approx \hat{\omega} \left(\frac{\hat{\omega}}{\omega_h} \right)^{\gamma}, \quad (5.14)$$

and J_{ω} is the Jacobian given by

$$J_{\omega} \equiv \left\| \frac{d\hat{\omega}}{d\omega} \right\| = (1-\gamma) \left(\frac{\omega}{\omega_h} \right)^{-\gamma}. \quad (5.15)$$

For a seismic trace recorded as a real-time series, only the non-negative frequency components are considered above.

Notice here the sign difference in front of the γ between the group of equations (5.10) and (5.11) and the group of equations (5.14) and (5.15), apart from the swap between variables ω and $\hat{\omega}$. This analysis indicates that the implementation of equation (5.8) is its own inverse, if we simply switch the sign in front of the $\gamma(\tau)$ function.

Explicitly, we express phase-only forward Q filtering as

$$u(\tau) = \frac{1}{\pi} \int_0^{\infty} U(0, \omega) \exp \left[i \int_0^{\tau} \left(\frac{\omega}{\omega_h} \right)^{\gamma(\tau')} \omega d\tau' \right] d\omega. \quad (5.16)$$

5.3.2 Full forward Q filtering

For the removal of any amplitude-only inverse Q filter effects that are applied to the data previously, an amplitude-only forward Q filter may be built by simply replacing the amplitude operator $A(\tau, \omega)$ in equation (5.7) with the amplitude-attenuation coefficient, $A^{-1}(\tau, \omega)$, the inverse of the stabilized amplitude-compensation coefficient. We can present this as

$$u(\tau) = \frac{1}{\pi} \int_0^{\infty} U(0, \omega) A^{-1}(\tau, \omega) \exp[i\omega\tau] d\omega. \quad (5.17)$$

Combining the phase-only and the amplitude-only forward Q filters, we construct a full forward Q filter also in the form of downward continuation. We express such a full forward Q filter for removing the phase correction and the amplitude compensation simultaneously as

$$u(\tau) = \frac{1}{\pi} \int_0^{\infty} U(0, \omega) A^{-1}(\tau, \omega) \exp \left[i \int_0^{\tau} \left(\frac{\omega}{\omega_h} \right)^{\gamma(\tau')} \omega d\tau' \right] d\omega. \quad (5.18)$$

Note that the amplitude-attenuation coefficient is the inverse of the amplitude-compensation coefficient used previously, and the phase term is implemented by switching the sign of the $\gamma(\tau)$ function from the inverse Q filter.

5.4 Summary of inverse and forward Q filters by downward continuation

In Chapter 4 and the current chapter, we set up both inverse Q filtering and the associated forward Q filtering as wavefield downward continuation. We can perform such a downward continuation successively to each depth-time

sample τ , to generate a full-length seismic trace. We may present this uniformly in the vector-matrix notation as

$$\mathbf{x} = \mathbf{A} \mathbf{z}. \quad (5.19)$$

Here vector \mathbf{z} is the frequency-domain input, the Fourier transform of an original seismic trace or an inverse Q filtered trace. Vector \mathbf{x} is the time-domain output, a seismic trace after inverse Q filtering or a recovering of the original trace.

For a close comparison, we now express the operator \mathbf{A} for each case explicitly as

Inverse Q filtering

$$a_{i,j} = \frac{1}{N} \begin{cases} \exp \left[i \int_0^{\tau_i} \left(\frac{\omega_j}{\omega_h} \right)^{-\gamma(\tau')} \omega_j d\tau' \right], & \text{phase only,} \\ A(\tau_i, \omega_j), & \text{amplitude only,} \\ A(\tau_i, \omega_j) \exp \left[i \int_0^{\tau_i} \left(\frac{\omega_j}{\omega_h} \right)^{-\gamma(\tau')} \omega_j d\tau' \right], & \text{full,} \end{cases} \quad (5.20)$$

and

Forward Q filtering

$$a_{i,j} = \frac{1}{N} \begin{cases} \exp \left[i \int_0^{\tau_i} \left(\frac{\omega_j}{\omega_h} \right)^{\gamma(\tau')} \omega_j d\tau' \right], & \text{phase only,} \\ \frac{1}{A(\tau_i, \omega_j)}, & \text{amplitude only,} \\ \frac{1}{A(\tau_i, \omega_j)} \exp \left[i \int_0^{\tau_i} \left(\frac{\omega_j}{\omega_h} \right)^{\gamma(\tau')} \omega_j d\tau' \right], & \text{full.} \end{cases} \quad (5.21)$$

However, the two-pass procedure is an approximation to the one-pass full inverse Q filtering. Note also that, in the two-pass procedure, phase- and amplitude-only inverse Q filters are not rigorously commutable, even for a one-dimensional Q model.

5.5 Different stabilization schemes

In the preceding sections, we defined a stabilized amplitude-compensation operator for inverse Q filtering as

$$A(\tau, \omega) = \frac{\beta(\tau, \omega) + \sigma^2}{\beta^2(\tau, \omega) + \sigma^2}, \quad (5.22)$$

to build the associated amplitude attenuation operator, $\beta^\dagger(\tau, \omega)$, for forward Q filtering as

$$\beta^\dagger(\tau, \omega) = \frac{1}{A(\tau, \omega)}. \quad (5.23)$$

These two operators are functions of traveltime τ and frequency ω , as shown in Figure 5.4. The amplitude coefficient depends on the Q and σ^2 values. In the computation of Figure 5.4, $Q = 100$ and $\sigma^2 = 0.01$ are assumed. Although the amplitude-compensation coefficient depends on both the Q value and the stabilization factor σ^2 , its maximum value only depends on the σ^2 we chosen. This observation suggests that even if Q is a depth-dependent function, the upper boundary of the amplitude compensation is fixed, for a chosen σ^2 . The latter is related to the data signal-to-noise ratio.

Alternative stabilization formulae can be used; for example, the amplitude-compensation operator can be defined as

$$A(\tau, \omega) = \frac{\beta(\tau, \omega)}{\beta^2(\tau, \omega) + \sigma^2}. \quad (5.24)$$

This stabilization scheme is used extensively in the inverse problem. In the context of inverse Q filtering, it is used by Wang (2002) and Irving and Knight (2003).

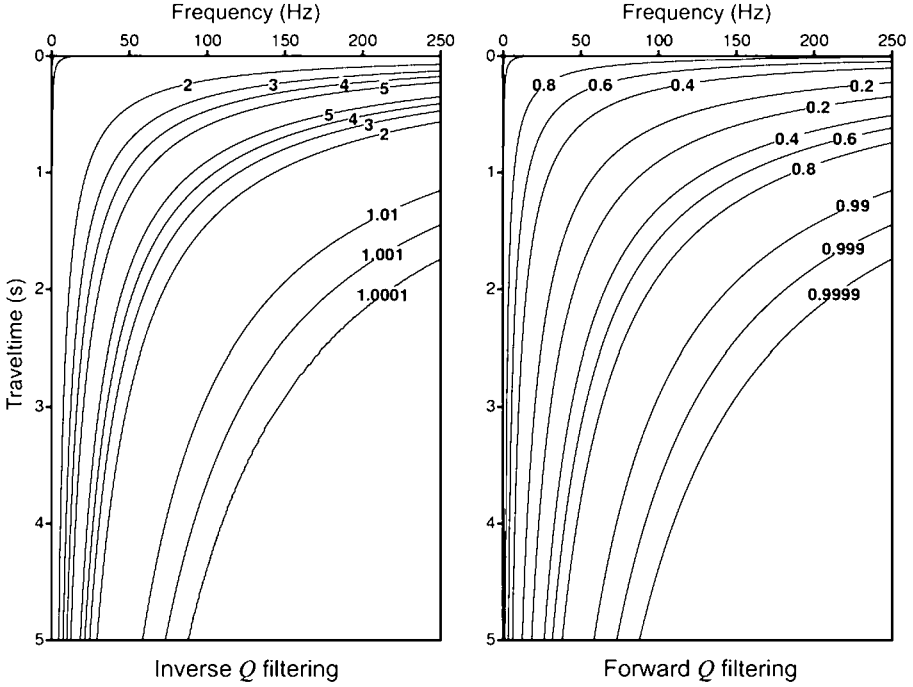


Figure 5.4 Stabilized amplitude operators in an inverse Q filter and the associated forward Q filter are the function of traveltime τ and frequency f .

For this stabilized amplitude-compensation operator, its inverse β^\dagger for the forward Q filter cannot be defined as equation (5.23), which otherwise would have an instability problem. I propose here to define the associated amplitude-attenuation operator by

$$\beta^\dagger(\tau, \omega) = \frac{A(\tau, \omega)}{A^2(\tau, \omega) + \sigma}. \quad (5.25)$$

Note that in equation (5.25) the stabilization factor is σ , instead of σ^2 .

These two operators, equation (5.24) and (5.25), act as a two-dimensional low-pass filter, as depicted in Figure 5.5, applied to the time-frequency domain seismic waveform $U(\tau, \omega)$. The cut-off edge is tapered naturally because of the use of σ^2 or σ . A justification can be given for the use of this second group of operators. When a plane wave with frequency ω propagates through subsurface media, after a certain traveltime τ , its

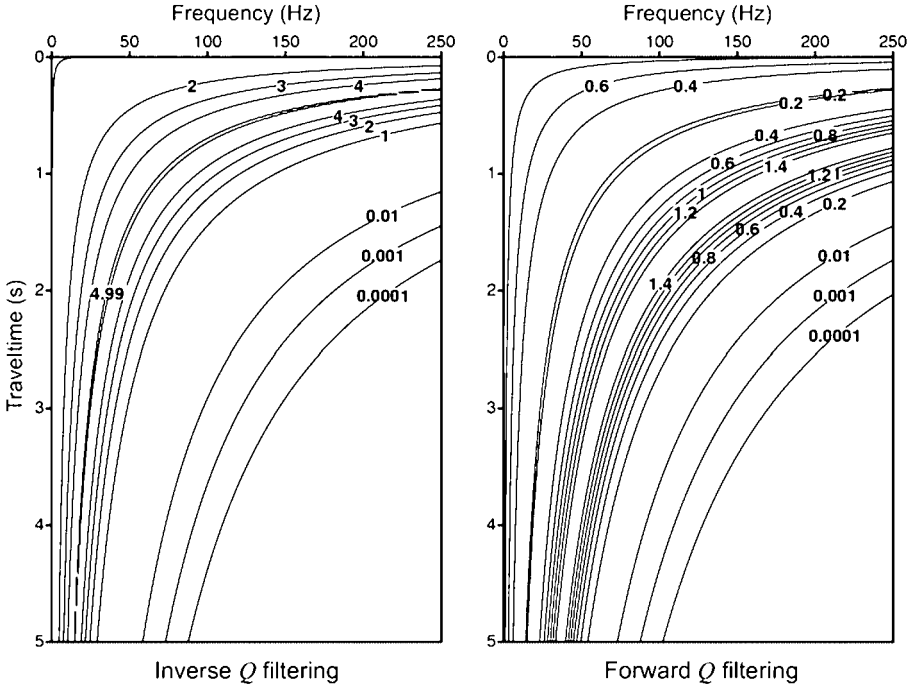


Figure 5.5 Stabilized amplitude operator with high χ ($\equiv \omega\tau$) suppression in an inverse Q filter, and the associated amplitude-attenuation operator in the forward Q filter.

energy has been absorbed completely. Inverse Q filtering and forward Q modelling with this group of operators also suppress the high-frequency noise recorded in the seismic data. Thus, we refer to this scheme as a stabilization scheme with high χ suppression, where χ is defined as the product of the frequency ω and time τ .

To closely compare these two schemes, Figure 5.6 plots the amplitude coefficients as the function of $\chi \equiv \omega\tau$, where (a) is the stabilization without high χ suppression and (b) is the stabilization with high χ suppression. Application of either of these can be justified. For the first scheme, high-frequency data components are not altered, if they are not boosted by inverse Q filtering. For the second scheme, the data have been filtered simultaneously with a time-variant low-pass filter, in conjunction with inverse Q filtering. Such a time-variant filter is designed naturally according the earth Q model, and thus has a physical basis.

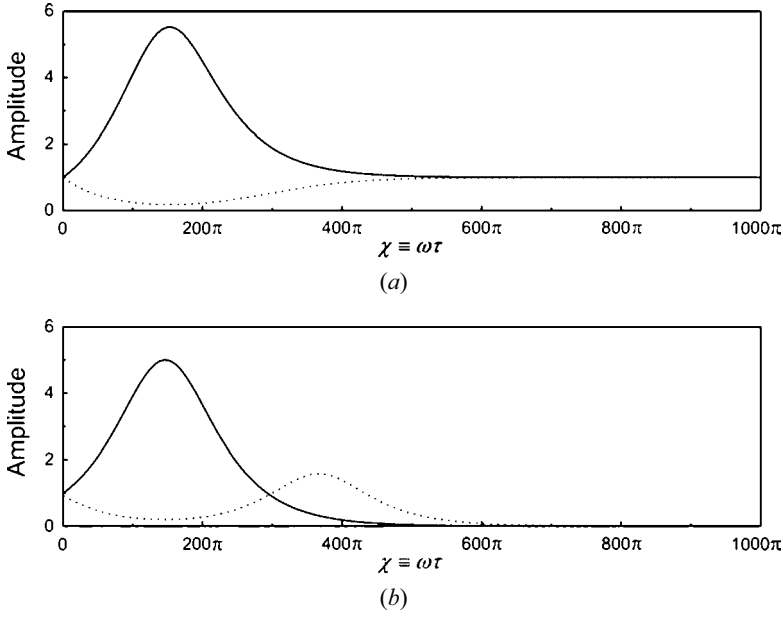


Figure 5.6 The amplitude-compensation coefficients for an inverse Q filter (solid lines) and the associated amplitude-attenuation coefficients for the forward Q filter (dotted lines) in two stabilization schemes: (a) stabilization without high χ suppression and (b) stabilization with high χ suppression.

Chapter 6

Layered implementation of inverse Q filters

Abstract

Whereas the stability issue is dealt in the previous chapters, computational efficiency is another issue of concern in inverse Q filtering. This chapter presents an efficient layered implementation of inverse Q filtering by assuming a depth-dependent, layered-earth Q model. For each individual layer, we first extrapolate the wavefield recorded at the surface downward to the top of the current layer, and then perform inverse Q filtering within the constant- Q layer. For the inverse filter with constant Q , we approximate the amplitude-compensation operator, which is a two-dimensional function of frequency and travelt ime, as an optimal product of two one-dimensional functions that depend upon the frequency and travelt ime respectively, so that we are able to implement the inverse Q filter efficiently in the Fourier transform domain.

Stability and efficiency are two general concerns in any scheme for inverse Q filtering. In the previous two chapters, we have discussed the stability issues surrounding the inverse Q filtering procedure and proposed stabilized algorithms. For a one-dimensional (1-D) earth Q model, these algorithms are sufficiently efficient, as the inverse Q filter operator (matrix \mathbf{A} defined by equations 4.26 and 5.20) is calculated only once and then applied to all the traces along an entire seismic line. For a two-dimensional (2-D) earth Q model in which Q varies in both depth and horizontal direction, the inverse Q filter operator needs to be recalculated for each of the seismic traces. For pre-stack seismic processing, even though the earth Q model is assumed to

be 1-D, the inverse Q filter operator needs to be recalculated for each individual trace corresponding to a different offset, because of the effect of source–receiver offsets. In both of these cases where the earth Q model varies with the spatial location or the source–receiver offset, computational efficiency is an important aspect that needs to be addressed.

Considering the efficiency, Hargreaves and Calvert (1991) proposed an algorithm akin to Stolt’s (1978) wavenumber-frequency domain migration. This is a phase-only inverse Q filter, valid for a constant- Q medium, which can efficiently correct for the phase distortion from velocity dispersion, but neglects the amplitude effect. Including amplitude compensation in inverse Q filtering may cause instability and generate undesirable artefacts in the solution. Stabilized schemes proposed in the previous chapters can simultaneously correct the phase effect and compensate for the amplitude without instability problems. Furthermore, it is highly desirable to have a stabilized inverse Q filter that is also computationally efficient.

In this chapter, we assume the earth Q model to have a multi-layered structure, and implement inverse Q filtering in a layered manner. For each individual layer with constant Q , we accomplish inverse Q filtering in two steps:

- 1) extrapolate the surface-recorded wavefield to the top of the current layer; and
- 2) perform constant- Q inverse filtering across the layer.

In the first step, the wavefield at the top of the current layer is the solution of downward continuation through the overburden. We stabilize this solution by incorporating a stabilization factor, as we did in the previous chapters. In the second step, we make an optimal approximation to the amplitude-compensation operator, which is a 2-D function of traveltimes and frequency, as a product of two 1-D functions depending upon time and frequency respectively. With this optimal approximation, we can implement the constant- Q inverse filter within the constant- Q layer efficiently by resampling and rescaling in the Fourier transform domain.

6.1 The layered approach to inverse Q filtering

In the downward continuation algorithm for inverse Q filtering presented in

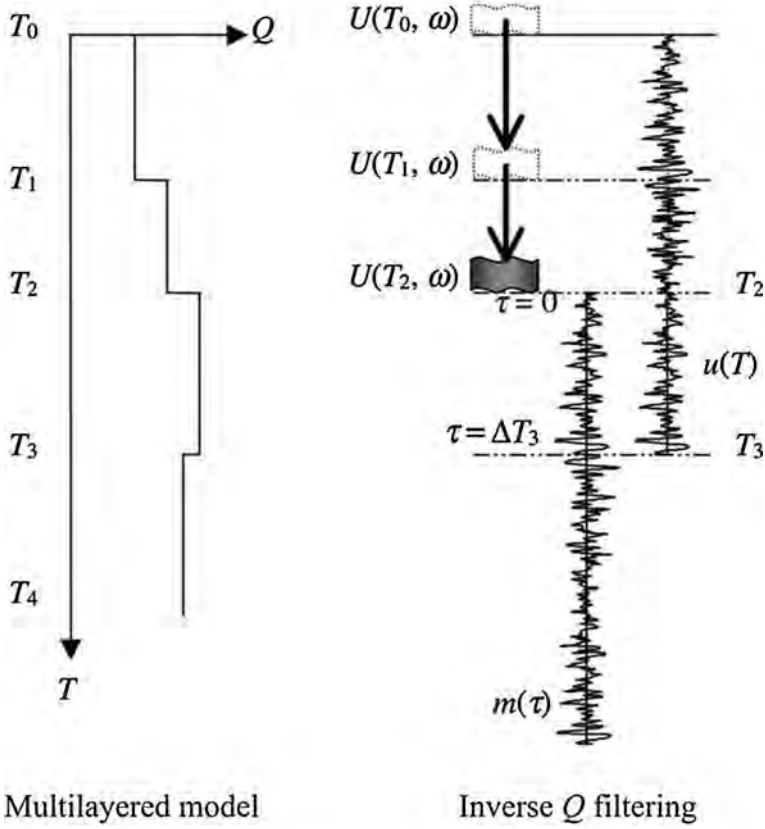


Figure 6.1 Earth Q model divided into N layers with the base of layer n at two-way time T_n . Inverse Q filtering is implemented in a layered manner. The double wave symbol represents the plane wave U ; the vertical arrows on the right indicate the downward continuation. The result of inverse Q filtering within a constant Q layer is the portion of $m(\tau)$ for $\tau \in [0, \Delta T_n]$, which is stored to the output trace $u(T)$ for $T \in [T_{n-1}, T_n]$.

the previous two chapters, the wavefield extrapolation step is the sample rate of the digitized seismic trace, and the output at each sample point is required. The computational demands of this sample-by-sample downward continuation render it impractical for routine pre-stack seismic processing, as an individual inverse Q filter is needed for each individual trace. However, since the inverse Q filter works on a single trace, it is reasonable to divide the depth-dependent earth Q model corresponding to an individual trace into a series of constant- Q layers and to implement the inverse Q filter in a layered manner. This layered procedure is shown in Figure 6.1.

The idea behind the layered model algorithm is to treat the top of the current layer as a new recording surface and thereby apply a fast algorithm of inverse Q filter to the constant Q layer. Lowering the recording surface to the level of the top of the current layer is accomplished by the downward continuation of expression (4.5). This step is very fast since equation (4.5) is applied in one step for the traveltimes across each layer in the overburden.

Suppose we divide the earth Q model into N layers defined by interfaces at two-way traveltimes T_n , for $n=1, \dots, N-1$, with $T_0=0$ and T_N being the maximum record time. The plane-wave downward continuation from the surface to the top of the n th layer can be implemented recursively:

$$U(T_0, \omega) \rightarrow U(T_1, \omega) \rightarrow \dots \rightarrow U(T_{n-1}, \omega). \quad (6.1)$$

Each step is given explicitly by

$$\begin{aligned} U(T_{n-1}, \omega) = & U(T_{n-2}, \omega) \exp \left[\frac{\omega}{2Q_{n-1}} \left(\frac{\omega}{\omega_h} \right)^{-\gamma_{n-1}} \Delta T_{n-1} \right] \\ & \times \exp \left[i \left(\frac{\omega}{\omega_h} \right)^{-\gamma_{n-1}} \omega \Delta T_{n-1} \right], \end{aligned} \quad (6.2)$$

where $\Delta T_{n-1} = T_{n-1} - T_{n-2}$ is the thickness of the $(n-1)$ th layer, in which Q_{n-1} is constant, and $\gamma_{n-1} = (\pi Q_{n-1})^{-1}$.

Downward continuation using equation (6.2), performed on all frequencies, compensates accurately for the earth Q effect between the surface $T_0 = 0$ and the top of the current layer, T_{n-1} . That is,

$$\begin{aligned} U(T_{n-1}, \omega) = & U(T_0, \omega) \exp \left[\sum_{\ell=1}^{n-1} \frac{\omega}{2Q_\ell} \left(\frac{\omega}{\omega_h} \right)^{-\gamma_\ell} \Delta T_\ell \right] \\ & \times \exp \left[i \sum_{\ell=1}^{n-1} \left(\frac{\omega}{\omega_h} \right)^{-\gamma_\ell} \omega \Delta T_\ell \right], \end{aligned} \quad (6.3)$$

where $\Delta T_\ell = T_\ell - T_{\ell-1}$ is the thickness of the ℓ th layer, in which Q_ℓ (and then γ_ℓ) is a constant. The stabilized wavefield $U(T_{n-1}, \omega)$ is estimated by

$$U(T_{n-1}, \omega) = U(T_0, \omega) \Lambda(T_{n-1}, \omega) \exp \left[i \sum_{\ell=1}^{n-1} \left(\frac{\omega}{\omega_h} \right)^{-\gamma_\ell} \omega \Delta T_\ell \right], \quad (6.4)$$

where $\Lambda(T_{n-1}, \omega)$ is the amplitude-compensation operator (equation 4.22).

6.2 Inverse Q filtering within a constant- Q layer

The extrapolated wavefield $U(T_{n-1}, \omega)$ is then used as the input of the inverse Q filter within the n th layer. Blending the downward continuation expression (4.5) and the imaging condition (4.7) into one form, the inverse Q filtered seismic trace may be presented in the time-shifted domain as

$$U(T_{n-1} + \tau) = \frac{1}{\pi} \int_0^\infty U(T_{n-1}, \omega) \exp \left[\left(\frac{\omega}{\omega_h} \right)^{-\gamma_n} \frac{\omega \tau}{2Q_n} \right] \times \exp \left[i \left(\frac{\omega}{\omega_h} \right)^{-\gamma_n} \omega \tau \right] d\omega, \quad (6.5)$$

where $\tau \in [0, \Delta T_n]$ and $\Delta T_n = T_n - T_{n-1}$ is the thickness of the n th layer.

For clarity, let us refer to T_{n-1} as the origin of a reduced time coordinate τ and denote the wavefield recorded at level T_{n-1} as

$$M(\tau = 0, \omega) \equiv U(T_{n-1}, \omega). \quad (6.6)$$

Then expression (6.5) is represented as

$$m(\tau) = \frac{1}{\pi} \int_0^\infty M(0, \omega) \exp \left[\left(\frac{\omega}{\omega_h} \right)^{-\gamma} \frac{\omega \tau}{2Q} \right] \exp \left[i \left(\frac{\omega}{\omega_h} \right)^{-\gamma} \omega \tau \right] d\omega, \quad (6.7)$$

where the layer subscript to parameters Q and γ is dropped. As depicted in Figure 6.1, only the front portion of $m(\tau)$ is stored into output $u(T)$,

$$u(T_{n-1} + \tau) = m(\tau). \quad (6.8)$$

We now describe how to implement inverse Q filtering within a constant Q layer. To obtain computational efficiency, three different approximations to the amplitude operator are tested.

Using a new variable

$$\omega' = \omega \left(\frac{\omega}{\omega_h} \right)^{-\gamma}, \quad (6.9)$$

equation (6.7) is rewritten as

$$m(\tau) = \frac{1}{\pi} \int_0^{\infty} M(0, \omega') J A(\tau, \omega') \exp[i\omega' \tau] d\omega', \quad (6.10)$$

where $M(0, \omega') \equiv M(0, \omega(\omega'))$ is resampled from $M(0, \omega)$ to $M(0, \omega')$, J is the Jacobian

$$J \equiv \left\| \frac{d\omega}{d\omega'} \right\| = \frac{1}{1-\gamma} \left(\frac{\omega'}{\omega_h} \right)^{\frac{\gamma}{1-\gamma}}, \quad (6.11)$$

and A is the amplitude-compensation operator

$$A(\tau, \omega') = \exp \left[\frac{\omega' \tau}{2Q} \right]. \quad (6.12)$$

The amplitude-compensation operator is omitted by Hargreaves and Calvert (1991), and their phase-only compensation algorithm is implemented using interpolation and scaling in the Fourier domain. Their method is fast because it is based on the fast Fourier transform. Let us now retain the amplitude operator $A(\tau, \omega')$ in equation (6.10) but use an approximation to it so that we can also use the fast Fourier transform.

Given a layer with moderate thickness indicated by two-way traveltime ΔT , we can approximate $A(\tau, \omega')$ by averaging over this time window:

$$A_1(\omega') = \frac{1}{\Delta T} \int_0^{\Delta T} \exp \left[\frac{\omega' \tau}{2Q} \right] d\tau \approx 1 + \frac{\omega' \Delta T}{4Q} + \frac{1}{6} \left(\frac{\omega' \Delta T}{2Q} \right)^2. \quad (6.13)$$

Expression (6.10) is then written as

$$m(\tau) = \frac{1}{\pi} \int_0^{\infty} M(0, \omega') J A_1(\omega') \exp[i \omega' \tau] d\omega'. \quad (6.14)$$

The evaluation of equation (6.14) thus involves the following steps:

- 1) interpolation of $M(0, \omega)$ to $M(0, \omega')$ with evenly spaced values of ω' ;
- 2) scaling with the Jacobian J ;
- 3) amplitude compensation $A_1(\omega')$; and finally
- 4) the inverse Fourier transform.

If we set $A_1(\omega') = 1$, expression (6.14) represents the phase-only inverse Q filter. Thus, the amplitude operator $A_1(\omega')$ acts as a band-pass filter applied to a phase-corrected seismic trace. The bandwidth is the useful frequency range of the seismic signal. Although there is no need for a low cut-off frequency definition, tapering is required at the high cut-off frequency edge.

Instead of averaging over the time window, we can alternatively replace the 2-D amplitude operator $A(\tau, \omega)$ (equation 6.12) by its average over the frequency band:

$$\begin{aligned} A_2(\tau) &= \frac{1}{\Delta\omega'} \int_{\omega'_c - \Delta\omega'/2}^{\omega'_c + \Delta\omega'/2} \exp\left[\frac{\omega' \tau}{2Q}\right] d\omega' \\ &\approx \left[1 + \frac{1}{6} \left(\frac{\Delta\omega' \tau}{4Q}\right)^2\right] \exp\left[\frac{\omega'_c \tau}{2Q}\right], \end{aligned} \quad (6.15)$$

where ω'_c is the centre frequency of the frequency band and $\Delta\omega'$ is the bandwidth. Both ω'_c and $\Delta\omega'$ may vary with time. Then expression (6.10) becomes

$$m(\tau) = A_2(\tau) \left[\frac{1}{\pi} \int_0^{\infty} M(0, \omega') J \exp[i \omega' \tau] d\omega' \right], \quad (6.16)$$

where the band-limited gain $A_2(\tau)$ is applied to the phase-only corrected

seismic trace. This gain compensation can be used in conjunction with the compensation of the offset-dependent spherical divergence to remove the need for any trace equalization or automatic gain control prior to, for example, an energy-preserving deconvolution.

The function $A_1(\omega')$ is a 1-D function of the frequency, whereas $A_2(\tau)$ depends on the travelttime. In a third method, we now approximate the 2-D amplitude operator $A(\tau, \omega)$ as a product of two 1-D functions

$$A_3(\tau, \omega') = A_{31}(\tau) A_{32}(\omega'). \quad (6.17)$$

Splitting the exact amplitude operator (6.12) into

$$A(\tau, \omega') = \exp\left[\frac{\omega'_c}{2Q}\tau\right] \exp\left[\frac{\omega' - \omega'_c}{2Q}\tau\right], \quad (6.18)$$

we can define the time-dependent term at the central frequency ω'_c ,

$$A_{31}(\tau) = \exp\left[\frac{\omega'_c}{2Q}\tau\right], \quad (6.19)$$

and the frequency-dependent term based on the average over the time interval ΔT ,

$$\begin{aligned} A_{32}(\omega') &= \frac{1}{\Delta T} \int_0^{\Delta T} \exp\left[\frac{\omega' - \omega'_c}{2Q}\tau\right] d\tau \\ &\approx 1 + \frac{\Delta T}{4Q}(\omega' - \omega'_c) + \frac{\Delta T^2}{24Q^2}(\omega' - \omega'_c)^2. \end{aligned} \quad (6.20)$$

The inverse Q filter (equation 6.10) is then

$$m(\tau) = A_{31}(\tau) \left[\frac{1}{\pi} \int_0^\infty M(0, \omega') J A_{32}(\omega') \exp[i\omega'\tau] d\omega' \right], \quad (6.21)$$

where the time gain function A_{31} is applied following the inverse Fourier transform.

Figure 6.2 compares numerical errors of the three approximations (A_1 , A_2 and A_3) against the exact amplitude operator A . The radius of the circles indicates the magnitude of the errors. These errors are estimated based on an example model of $Q = 50$ within a 300-ms time window and a 10–90-Hz frequency band. Errors (ε values) on the upper boundaries are given explicitly in the figure. The best alternative among these three is $A_3 = A_{31}A_{32}$, which is adopted in the following examples.

6.3 Phase- or amplitude-only inverse Q filtering

In the layered implementation for phase-only inverse Q filtering, we first extrapolate the wavefield $U(T_0 = 0, \omega)$ recorded at the surface down to the top of the n th layer. The plane-wave downward continuation can be implemented recursively as

$$U(T_{n-1}, \omega) = U(T_0, \omega) \exp \left[i \sum_{\ell=1}^{n-1} \left(\frac{\omega}{\omega_h} \right)^{-\gamma_\ell} \omega \Delta T_\ell \right]. \quad (6.22)$$

Such a downward continuation, performed on all frequencies, accurately corrects for the phase effect of earth Q filtering between the surface and the top of the current layer.

The extrapolated wavefield $U(T_{n-1}, \omega)$ is used as the input of the inverse Q filter within the n th layer. Within the n th layer, the phase-only inverse Q filtering is expressed as

$$U(T_{n-1} + \tau) = \frac{1}{\pi} \int_0^\infty U(T_{n-1}, \omega) \exp \left[i \left(\frac{\omega}{\omega_h} \right)^{-\gamma_n} \omega \tau \right] d\omega \quad (6.23)$$

$$= \frac{1}{\pi} \int_0^\infty U(T_{n-1}, \omega') J \exp [i \omega' \tau] d\omega', \quad (6.24)$$

where $\tau \in [0, \Delta T_n]$. In expression (6.24), ω' is given by equation (6.9). This phase-only inverse Q filtering expression is implemented in three steps: interpolation, scaling and inverse fast Fourier transforming (Hargreaves and Calvert, 1991; Bano, 1996).

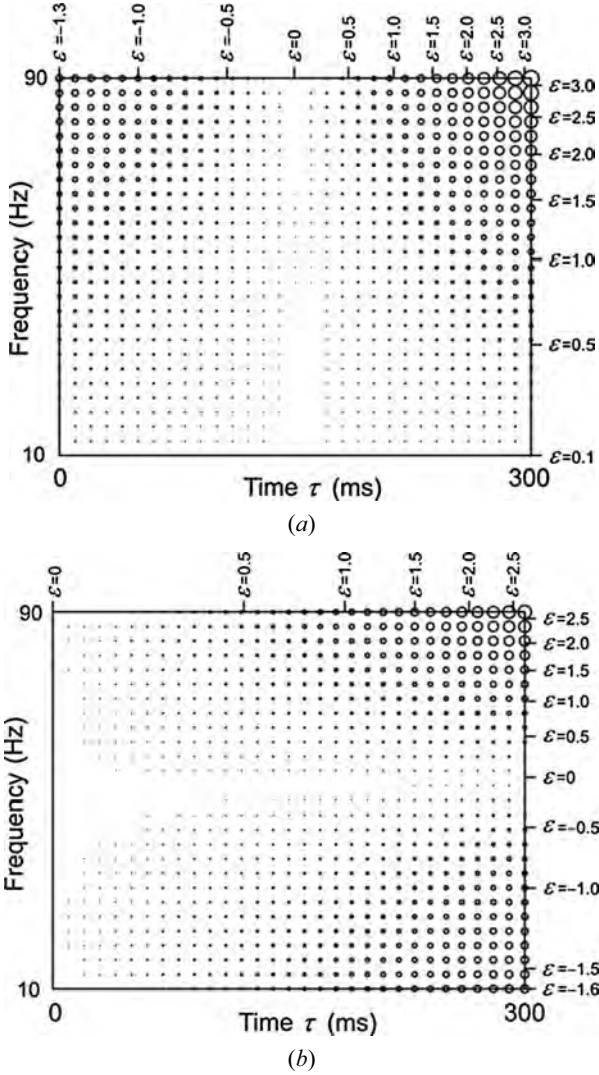


Figure 6.2 Numerical errors of three approximated amplitude operators (A_1 , A_2 and A_3) relative to the exact amplitude operator A . (a) $A - A_1$, the error of the approximated operators A_1 relative to the exact operator A . (b) $A - A_2$, the error of the approximated operators A_2 relative to the exact operator A .

Interpolation is performed between complex values in the frequency domain. For the purpose of good interpolation, we produce a densely sampled, frequency-domain seismic trace by padding with zeros on the time-domain trace, before performing FFT, the fast Fourier transform.

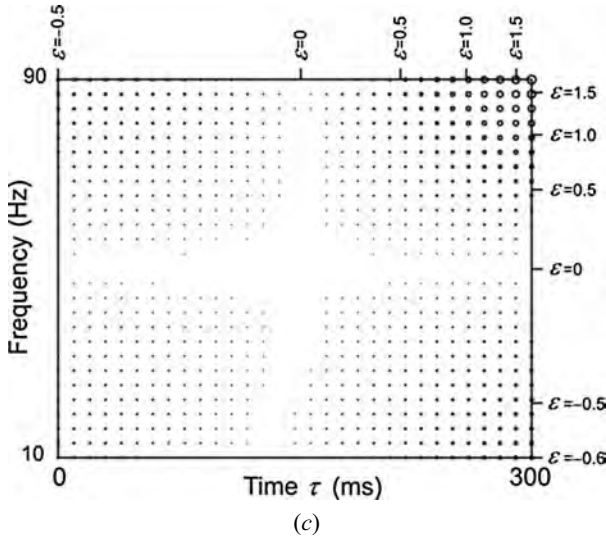


Figure 6.2 (contd) (c) $A - A_3$, the error of the approximated operator A_3 relative to the exact operator A . These errors are estimated based on an example model of $Q = 50$ within a 300-ms time window and a 10–90-Hz frequency band. The radius of each circle is proportional to the absolute value of the error, where specific error values (ϵ) indicated on the upper boundaries.

For the amplitude-only inverse Q filter, the basic equation for a layered implementation can be expressed explicitly as

$$u(T_{n-1}, \omega) = U(T_{n-2}, \omega) \exp\left[\frac{\omega \Delta T_{n-1}}{2Q_{n-1}}\right] \exp[i\omega \Delta T_{n-1}], \quad (6.25)$$

The plane-wave downward continuation from the surface to the top of the n th layer is performed recursively. A stabilized solution is given by

$$U(T_{n-1}, \omega) = U(T_0, \omega) A(T_{n-1}, \omega) \exp[i\omega T_{n-1}], \quad (6.26)$$

where the amplitude-compensation operator $A(T_{n-1}, \omega)$ is given by equation (4.22).

Within the n th layer, we can use the same expression as equation (6.25) with the corresponding layer reference. Applying the so-called imaging condition, we may represent the amplitude-only inverse Q filtering by

$$u(T_{n-1} + \tau) = \frac{1}{\pi} \int_0^{\infty} U(T_{n-1}, \omega) \exp\left[\frac{\omega\tau}{2Q}\right] \exp[i\omega\tau] d\omega, \quad (6.27)$$

where $\tau \in [0, \Delta T_n]$.

The amplitude-compensation operator

$$A(\tau, \omega) = \exp\left[\frac{\omega\tau}{2Q}\right] \quad (6.28)$$

is a 2-D function of frequency and time. Following the discussion in section 6.2, this 2-D amplitude function is approximated as a product of two 1-D functions:

$$A(\tau, \omega) = A_{31}(\tau)A_{32}(\omega), \quad (6.29)$$

and the amplitude-only inverse Q filter is then expressed as

$$u(T_{n-1} + \tau) = A_{31}(\tau) \left[\frac{1}{\pi} \int_0^{\infty} U(T_{n-1}, \omega) A_{32}(\omega) \exp[i\omega\tau] d\omega \right], \quad (6.30)$$

This can be performed by an inverse fast Fourier transform, followed by the application of a time-gain function A_{31} .

6.4 Forward Q filtering

An inverse process to inverse Q filtering is called forward Q filtering. Layered implementation of forward Q filtering is also accomplished in two stages, as in the case of inverse Q filtering.

For a phase-only forward Q filter, we may use expression (6.22) in the first stage and expression (6.23) in the second stage, the same expressions as in inverse Q filtering, but simply change the sign of γ_ℓ in equation (6.22) and γ_n in equation (6.23).

For the amplitude-only forward Q filter, the first stage of downward continuation is

$$u(T_{n-1}, \omega) = U(T_0, \omega) \frac{1}{A(T_{n-1}, \omega)} \exp[i\omega T_{n-1}], \quad (6.31)$$

where $A(T_{n-1}, \omega)$ is the amplitude-compensation operator used in equation (6.26). The second step of constant- Q layer filtering is expressed as

$$u(T_{n-1} + \tau) = A_{31}^{-1}(\tau) \left[\frac{1}{\pi} \int_0^{\infty} U(T_{n-1}, \omega) A_{32}^{-1}(\omega) \exp[i\omega\tau] d\omega \right], \quad (6.32)$$

where the $A_{31}^{-1}(\tau)$ and $A_{32}^{-1}(\omega)$ are the inverse of the amplitude-compensation operators used in equation (6.30).

For full forward Q modelling, layered implementation is also accomplished in two steps. In the first step of downward continuation,

$$u(T_{n-1}, \omega) = U(T_0, \omega) \frac{1}{A(T_{n-1}, \omega)} \exp \left[i \sum_{\ell=1}^{n-1} \left(\frac{\omega}{\omega_h} \right)^{\gamma_\ell} \omega \Delta T_\ell \right], \quad (6.33)$$

where the sign of γ_ℓ is changed from that in inverse Q filtering equation (6.4). The second step is expressed as

$$u(T_{n-1} + \tau) = \frac{1}{\pi} \int_0^{\infty} U(T_{n-1}, \omega) \exp \left[- \left(\frac{\omega}{\omega_h} \right)^\gamma \frac{\omega\tau}{2Q} \right] \exp \left[i \left(\frac{\omega}{\omega_h} \right)^\gamma \omega\tau \right] d\omega. \quad (6.34)$$

Note here the sign of γ is changed from that in equation (6.5) for inverse Q filtering (and the layer reference n is dropped).

Expression (6.34) may also be implemented through resampling, scaling and inverse Fourier transform. For resampling, equation (6.34) is expressed as

$$u(T_{n-1} + \tau) = \frac{1}{\pi} \int_0^{\infty} U(T_{n-1}, \omega') J A^{-1}(\omega') \exp[i\omega'\tau] d\omega', \quad (6.35)$$

where ω' is a new frequency variable

$$\omega' = \omega \left(\frac{\omega}{\omega_h} \right)^\gamma, \quad (6.36)$$

and J is the Jacobian defined as

$$J = \left\| \frac{d\omega}{d\omega'} \right\| = \frac{1}{1 + \gamma} \left(\frac{\omega'}{\omega_h} \right)^{-\frac{\gamma}{1+\gamma}}. \quad (6.37)$$

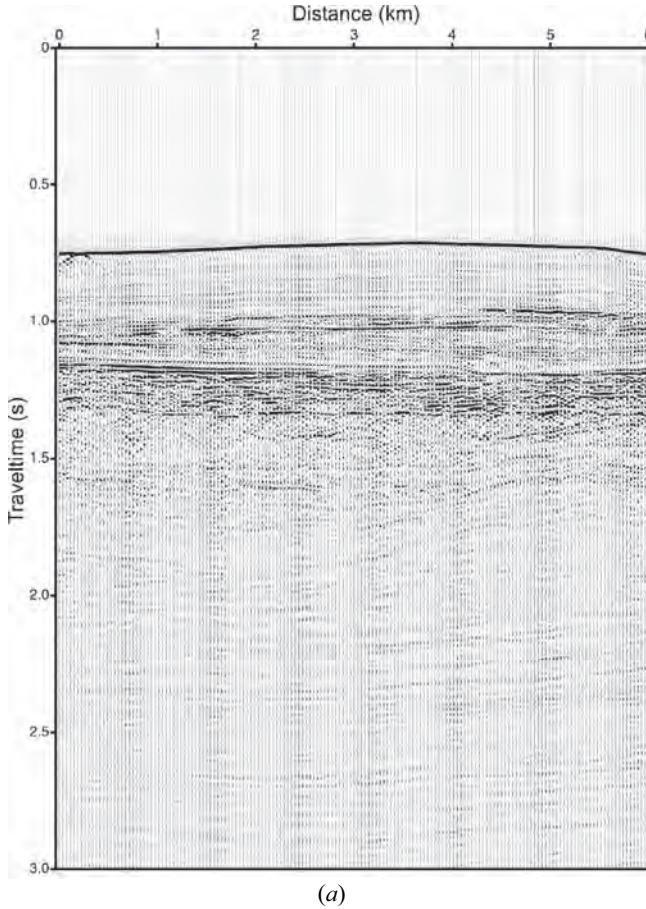


Figure 6.3 (a) A real marine seismic section, used to demonstrate the effectiveness of layered inverse Q filtering.

The amplitude-attenuation operator in equation (6.35) is given by

$$A^{-1}(\tau, \omega') = \exp\left[-\frac{\omega'\tau}{2Q}\right], \quad (6.38)$$

which can also be approximated by two 1-D functions. Finally, equation (6.35) is expressed as

$$u(T_{n-1} + \tau) = A_{31}^{-1}(\tau) \left[\frac{1}{\pi} \int_0^{\infty} U(T_{n-1}, \omega') J A_{32}^{-1}(\omega') \exp[i\omega'\tau] d\omega' \right]. \quad (6.39)$$

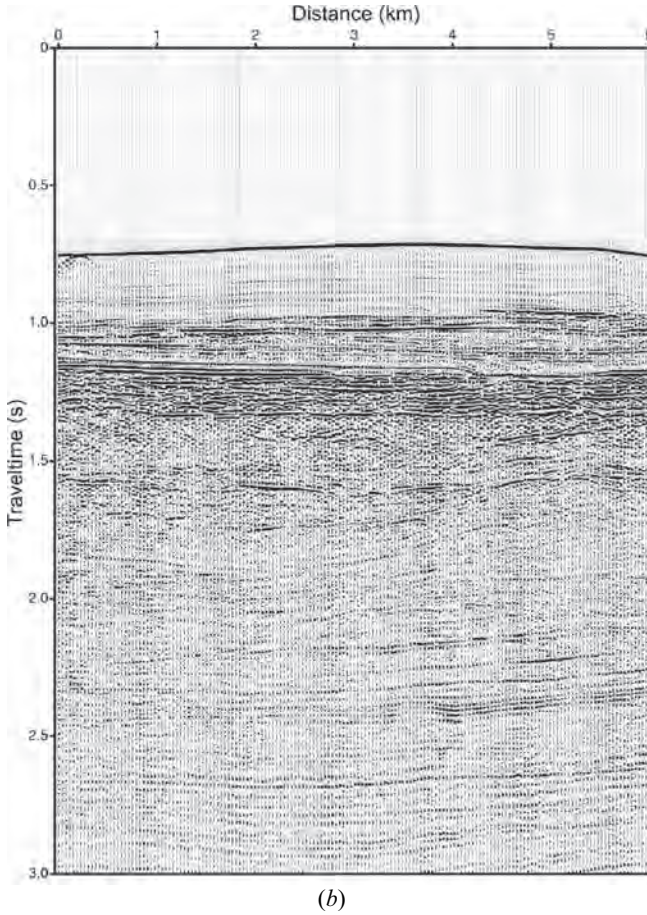


Figure 6.3 (contd) (b) The real seismic section after inverse Q filtering. These two sections are plotted to the same amplitude scale.

6.5 Application of layered inverse Q filtering

The layered, stabilized inverse Q filtering method uses equation (6.4) to extrapolate the surface-recorded wavefield to the top of current layer, and then equation (6.21) within the current constant- Q layer, to produce the inverse Q filtered output across the layer:

$$U(T_0, \omega) \rightarrow U(T_{n-1}, \omega) \rightarrow u(T_{n-1} + \tau). \quad (6.40)$$

The procedure is repeated for all constant- Q layers, $n = 1, \dots, N$.

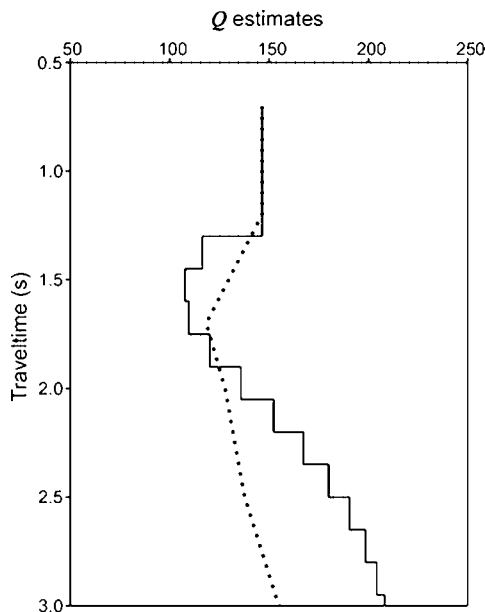


Figure 6.4 The earth Q model used to design the inverse Q filter. The average Q function (dotted line) and the interval Q values are estimated from reflection seismic data shown in Figure 6.3a, using a method described in Chapter 11. The inverse Q filtered result is shown in Figure 6.3b.

This layered implementation is akin to recursive migration, a name that emphasizes the recursive calculation of the downward continuation (Kim *et al.*, 1989). We refer to it as the layered method because the result of a specific layer is independent of the output within the overburden. This property also contrasts with a layer-stripping implementation.

Figure 6.3 displays an application example to a real marine seismic data set. The two seismic sections, before and after inverse Q filtering, are plotted to the same amplitude scale. Figure 6.4 shows the layered Q model used to design the inverse Q filter, and the average Q function (dotted line) estimated based on the stack section of Figure 6.3a. The detail of Q estimation from a reflection seismic section will be described in Chapter 11.

Inverse Q filtering for marine seismic data should start from the water bottom, which in this case is about 0.7 s. The layered implementation method presented here, starting from the recording surface, includes the water layer in which $Q^{-1} = 0$. The effective Q function below the water can be generally assumed to be proportional to the layer velocity, as suggested

by Figure 6.4. It would be better to over-estimate Q than to under-estimate Q , according to the sensitivity analysis by Duren and Trantham (1997).

The layer thickness for the interval- Q values is set arbitrarily as a constant (0.15 s). For phase-only inverse Q filtering, the layer thickness can be any size. However, for amplitude-only or full inverse Q filtering, it is better to use a small layer thickness, so that the average in the time window can closely approximate the true amplitude operator (see Figure 6.2).

Another example, shown in Figure 6.5, compares the t^2 -gain recovery and the inverse Q filtering. In Figure 6.5a, t^2 -gain recovery attempts to correct for not only the spherical divergence but also the effect of earth Q filtering, as we usually do in conventional seismic data processing. In Figure 6.5b, only divergence correction (t -gain recovery) is done, followed by inverse Q filtering. Although the inverse Q filter is performed trace by trace, it has enhanced the lateral coherence and thereby improved the data signal-to-noise ratio.

For a data gather, inverse Q filtering working on each single trace takes into account the offset effect. Suppose a given Q model is a 1-D function defined at zero offset, $Q(\tau, y = 0)$, where y is the source–receiver offset. The Q function for a nonzero offset trace is approximated by

$$Q(\tau, y) = Q\left(\sqrt{\tau^2 - \frac{y^2}{v_{\text{nmo}}^2}}, 0\right), \quad (6.41)$$

where v_{nmo} is the normal-moveout velocity.

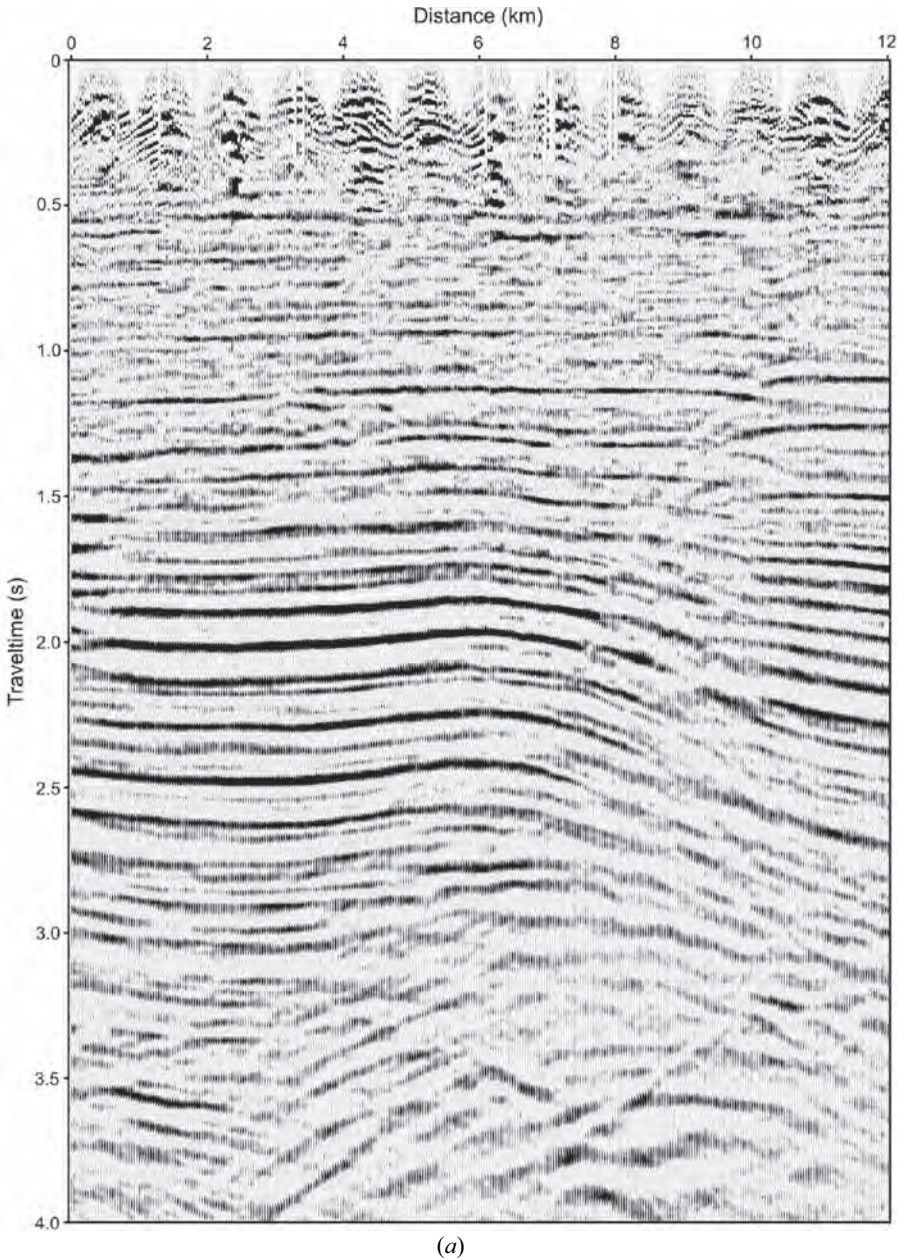


Figure 6.5 (a) A raw migration section with t^2 -gain recovery which, in conventional seismic data processing, attempts to correct for not only spherical divergence but also the effect of earth Q filtering.

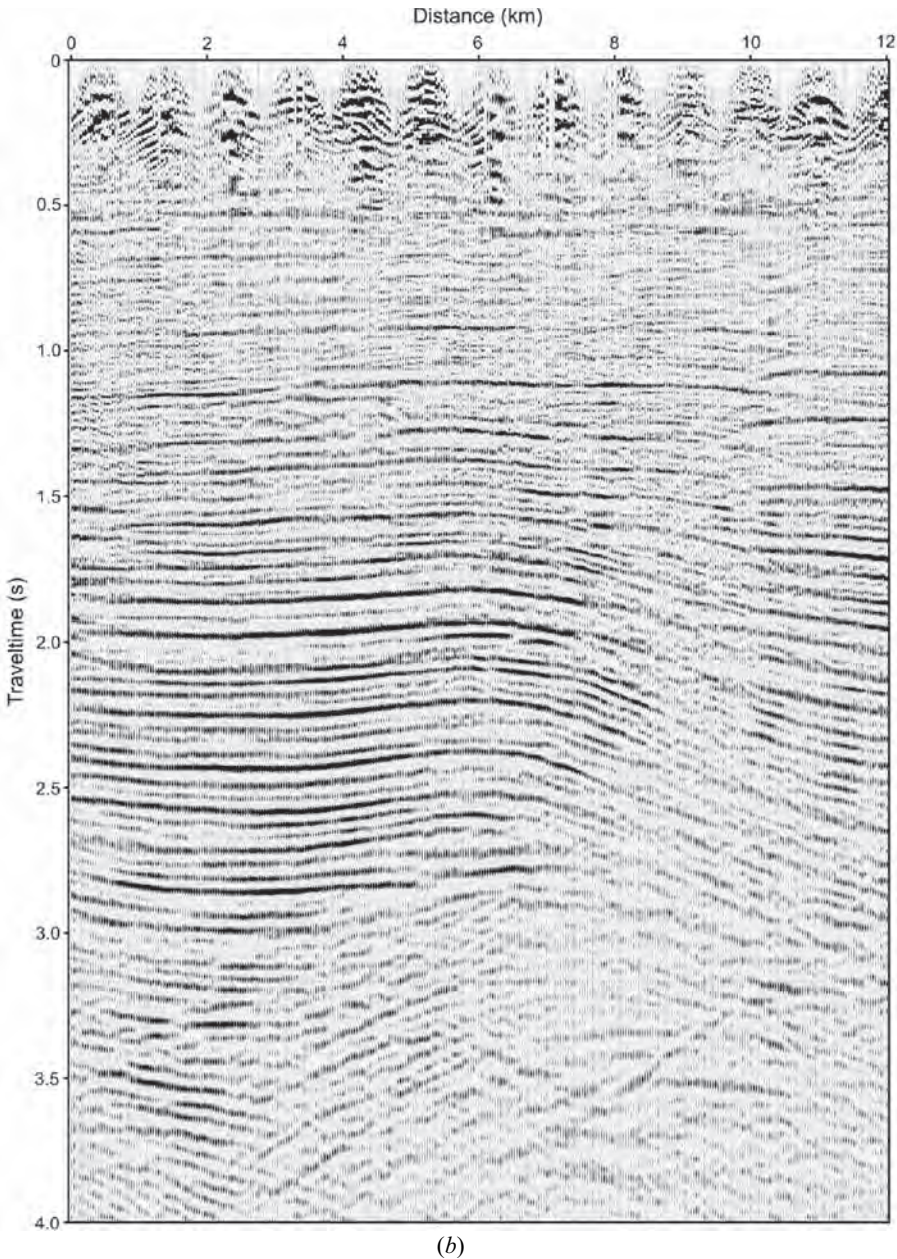


Figure 6.5 (contd) (b) The raw migration section after divergence correction (t -gain recovery) and inverse Q filtering. Although inverse Q filtering is performed trace by trace, it has improved the lateral coherence and thereby the signal-to-noise ratio of the seismic section.

Chapter 7

Inverse Q filtering in the Gabor transform domain

Abstract

This chapter presents an alternative to the layered implementation of inverse Q filtering and develops an algorithm in conjunction with the Gabor transform. For a given seismic trace, we use a forward Gabor transform to generate a time-variant frequency spectrum, the so-called Gabor spectrum, and then perform inverse Q filtering by modifying the Gabor spectrum. After that we apply an inverse Gabor transform to reproduce the time domain seismic trace. The filter between the forward and inverse Gabor transform pair can be either an inverse or forward Q filter. For the stabilization, we propose an empirical formula to express the stabilization factor in terms of gain limit (in decibels).

In the previous chapter, we described a layered implementation of the inverse Q filter based on the theory of wavefield downward continuation. In this chapter, we introduce an alternative to the layered implementation and develop an inverse Q filtering algorithm in conjunction with the Gabor transform. The differences between the layered implementation and the Gabor transform-based method are as follows.

- 1) In the layered implementation, we employ downward continuation to extrapolate the wavefield down to the top of a constant- Q layer for inverse Q filtering. In this chapter, we use the Gabor transform to generate a wavefield at that level.

- 2) In the layered implementation, just as in a general downward continuation algorithm described in the previous chapters, we apply an imaging condition to the inverse- Q filtered wavefield to produce the final seismic trace in the time domain. In the Gabor transform-based method, we perform an inverse Gabor transform on the inverse Q filtered wavefield to reproduce the time-domain seismic trace.

The Gabor transform (Gabor, 1946) decomposes a time-domain seismic trace into the time-frequency domain. Multiplying the seismic trace by a specific (Gaussian) window and then Fourier transforming produces a local Fourier spectrum. Performing such a local Fourier transform iteratively for a suite of window positions successively down the seismic trace, we obtain a time-variant spectrum called the Gabor spectrum. We can then implement a nonstationary filter such as an inverse Q filter by modifying the Gabor spectrum before the inverse Gabor transform. For any reasonable choice of window (e.g. a Gaussian or any continuous function on a finite, closed interval), an inverse Gabor transform is possible for reconstructing the time-domain series. For references devoted to Gabor transform theory, see Bastiaans (1980) and Feichtinger and Strohmer (1998).

In seismic data processing, Schoepp and Margrave (1998), Margrave *et al.* (2002) and Grossman *et al.* (2002) used the Gabor transform or the local Fourier transform for designing a nonstationary deconvolution, a natural extension of the standard Wiener deconvolution algorithm (Margrave, 1998), to recover the reflectivity from a seismic trace by simultaneously removing the source signature and the nonstationary propagation effect, i.e. the apparent Q effect.

In this chapter, we first give a derivation of the inverse Q filter formula, expressed in the time-frequency domain, and then present the implementation of Gabor-transform based inverse Q filtering. In fact, the filter between the forward and inverse Gabor transform pair can be either inverse Q filtering or forward Q modelling. For stabilization, we also propose an empirical formula for the stabilization factor, expressed in terms of gain limit (in decibels).

7.1 Stabilized inverse Q filter

In the downward continuation algorithm shown in the previous chapters, we have seen that the basic equation for inverse Q filtering is equation (4.5), expressed as

$$\begin{aligned}
 U(\tau + \Delta\tau, \omega) &= U(\tau, \omega) \exp \left[\left(\frac{\omega}{\omega_h} \right)^{-\gamma(\tau')} \frac{\omega \Delta\tau}{2Q(\tau')} \right] \\
 &\quad \times \exp \left[i \left(\frac{\omega}{\omega_h} \right)^{-\gamma(\tau')} \omega \Delta\tau \right],
 \end{aligned} \tag{7.1}$$

where $\tau' = \tau + \frac{1}{2}\Delta\tau$. For $Q \gg 1$, which is appropriate for seismic data processing, we can make the approximation:

$$\left(\frac{\omega}{\omega_h} \right)^{-\gamma(\tau)} \frac{\omega}{2Q(\tau)} \approx \frac{\omega}{2Q(\tau)}, \tag{7.2}$$

and rewrite equation (7.1) as

$$U(\tau + \Delta\tau, \omega) = U(\tau, \omega) \exp \left[\frac{\omega \Delta\tau}{2Q(\tau')} \right] \exp \left[i \left(\frac{\omega}{\omega_h} \right)^{-\gamma(\tau')} \omega \Delta\tau \right]. \tag{7.3}$$

We now use this fundamental equation as a starting point to derive the Gabor transform-based inverse Q filtering algorithm.

Considering the downward continuation from the recording surface $\tau_0 = 0$ to the depth-time level τ , equation (7.3) becomes

$$U(\tau, \omega) = U(0, \omega) \exp \left[\int_0^\tau \frac{\omega}{2Q(\tau')} d\tau' \right] \exp \left[i \int_0^\tau \left(\frac{\omega}{\omega_h} \right)^{-\gamma(\tau')} \omega d\tau' \right], \tag{7.4}$$

where $Q(\tau)$ and $\gamma(\tau)$ are depth-dependent. If we assume $Q^{-1} = 0$ in the medium, the wavefield recorded at depth level τ can be obtained from equation (7.3) as

$$\tilde{U}(\tau, \omega) = U(0, \omega) \exp[i\omega\tau]. \tag{7.5}$$

Both $U(\tau, \omega)$ in equation (7.4) and $\tilde{U}(\tau, \omega)$ in equation (7.5) are the wavefield recorded at the depth-time level τ , but the latter is without inverse

Q filtering. Using $\tilde{U}(\tau, \omega)$, we rewrite equation (7.4) as

$$U(\tau, \omega) = \tilde{U}(\tau, \omega) \exp \left[\int_0^\tau \frac{\omega}{2Q(\tau')} d\tau' \right] \\ \times \exp \left[i \int_0^\tau \left(\left(\frac{\omega}{\omega_h} \right)^{-\gamma(\tau')} - 1 \right) \omega d\tau' \right]. \quad (7.6)$$

This is the central equation for the so-called Gabor-transform based inverse Q filter. A stabilized expression for inverse Q filtering is given as

$$U(\tau, \omega) = \tilde{U}(\tau, \omega) A(\tau, \omega) \exp \left[i \int_0^\tau \left(\left(\frac{\omega}{\omega_h} \right)^{-\gamma(\tau')} - 1 \right) \omega d\tau' \right], \quad (7.7)$$

where $A(\tau, \omega)$ is a stabilized amplitude compensation coefficient.

In equation (7.7), if the amplitude compensation operator is set as $A(\tau, \omega) = 1$, it is a phase-only inverse Q filter:

$$U(\tau, \omega) = \tilde{U}(\tau, \omega) \exp \left[i \int_0^\tau \left(\left(\frac{\omega}{\omega_h} \right)^{-\gamma(\tau')} - 1 \right) \omega d\tau' \right]. \quad (7.8)$$

The problem now is, given a time-domain seismic trace $u(t)$, how to compute $\tilde{U}(\tau, \omega)$. In the derivation above, equation (7.4) offers one way to compute $\tilde{U}(\tau, \omega)$ from $U(0, \omega)$. After inverse Q filtering, the imaging condition should be applied to $U(\tau, \omega)$ to produce the time-domain seismic trace $u(\tau, 0)$. This is equivalent to what we have done in the wavefield downward continuation algorithm for inverse Q filtering. Alternatively, it can be computed using a Gabor transform pair described as follows.

7.2 The Gabor transform

7.2.1 Forward Gabor transform

The Gabor transform of a signal $u(t)$ is defined as (Gabor, 1946; Bastiaans,

1980):

$$U(\tau, \omega) = \int_{-\infty}^{\infty} u(t) w(t - \tau) \exp[-i\omega t] dt, \quad (7.9)$$

where $w(t)$ is the Gabor analysis window, τ is the location of the window centre and ω is the angular frequency. The Gabor transform can be calculated with a fast Fourier transform (FFT). Defining a Gabor slice

$$u(\tau, t) = u(t) w(t - \tau), \quad (7.10)$$

then the Gabor transform is an FFT as

$$U(\tau, \omega) = \mathcal{F}\{u(\tau, t)\}, \quad (7.11)$$

where \mathcal{F} is the Fourier transform with respect to the time t and τ is the window centre. This clearly shows that the Gabor transform of $u(t)$ is the Fourier transform of the Gabor slices $u(\tau, t)$, for all possible τ locations.

The Gabor analysis window is often chosen to be a Gaussian window

$$w(t) = \begin{cases} \frac{2}{T\sqrt{\pi}} \exp\left[-\left(\frac{2t}{T}\right)^2\right], & \text{for } -T \leq t \leq T, \\ 0, & \text{otherwise,} \end{cases} \quad (7.12)$$

where T is referred to as the (half) width of the Gaussian window. Although $w(t)$ here is set as a Gaussian function, the theory works well for quite general windows. For example, we may define a Gabor analysis window as the Hamming window, which is defined as

$$w(t) = \begin{cases} 0.54 + 0.46 \cos\left(\pi \frac{t}{T}\right), & \text{for } -T \leq t \leq T, \\ 0, & \text{otherwise.} \end{cases} \quad (7.13)$$

However, in the context of inverse Q filtering, the simple Heaviside function, defined as

$$w(t) = \begin{cases} \frac{1}{2T}, & \text{for } -T \leq t \leq T, \\ 0, & \text{otherwise,} \end{cases} \quad (7.14)$$

cannot be used as the Gabor analysis window. This is because, when a segment of digital signal is transformed into the frequency domain, it may produce side lobes in the spectrum. Such spectral errors will be severely amplified by inverse Q filtering. This side-lobe effect can be reduced by modifying the segment of digital signal by weighting, such as cosine-squared tapering.

7.2.2 Inverse Gabor transform

In order to reconstruct the time-domain signal $u(t)$ from the Gabor transform spectrum $U(\tau, \omega)$, we now define the inverse Gabor transform as

$$u(t) = h(t) \int_{-\infty}^{\infty} \int_{-\infty}^{\infty} U(\tau, \omega) \exp[i\omega t] d\omega d\tau, \quad (7.15)$$

where $h(t)$ is the Gabor synthesis window. This consists of an inverse FFT with respect to frequency,

$$u(\tau, t) = \mathcal{F}^{-1}\{U(\tau, \omega)\}, \quad (7.16)$$

which reproduces the Gabor slice, and then the data synthesis integral,

$$u(t) = h(t) \int_{-\infty}^{\infty} u(\tau, t) d\tau. \quad (7.17)$$

The Gabor synthesis window $h(t)$ can be derived by substituting equation (7.10) into equation (7.17),

$$u(t) = h(t) \int_{-\infty}^{\infty} [u(\tau) w(t - \tau)] d\tau = \left[h(t) \int_{-\infty}^{\infty} w(t - \tau) d\tau \right] u(t), \quad (7.18)$$

and obtained as

$$h(t) = \left[\int_{-\infty}^{\infty} w(t - \tau) d\tau \right]^{-1}. \quad (7.19)$$

The synthesis window is expressed here in terms of the Gabor analysis window $w(t)$. An advantage of this definition is that it can mitigate the potential numerical errors caused by digitization on the Gabor analysis window and the edge effect when moving the analysis window towards the two ends of the trace.

7.3 Inverse Q filtering by Gabor transform

The Gabor transform may be used for inverse Q filtering. Explicitly, the implementation of inverse Q filtering consists of the following five steps:

- 1) for a given seismic trace $u(t)$, constructing a set of the Gabor slices;
- 2) performing FFT on each Gabor slice to generate the Gabor transform spectrum, which is denoted as $\tilde{U}(\tau, \omega)$ in the previous section to represent the input of inverse Q filtering;
- 3) inverse Q filtering on $\tilde{U}(\tau, \omega)$ to produce $U(\tau, \omega)$;
- 4) performing inverse FFT on $U(\tau, \omega)$ or $\tilde{U}(\tau, \omega)$ to reconstruct Gabor slices $u(\tau, t)$;
- 5) integration over τ on the set of the Gabor slices $u(\tau, t)$, using equation (7.17), to reproduce the seismic trace $u(t)$ in the time domain.

Recall that the imaging condition (summing over the frequency axis) is applied in the wavefield downward continuation algorithm for inverse Q filtering. However, when using a forward Gabor transform to generate $\tilde{U}(\tau, \omega)$, after inverse Q filtering, an inverse Gabor transform should be used on $U(\tau, \omega)$ to produce a time-domain seismic trace. Therefore, we refer to this inverse Q filtering procedure as the Gabor-transform method.

Figure 7.1 compares synthetic seismic traces ($Q = 88$) before and after inverse Q filtering and the associated Gabor transform (power) spectra. The synthetic seismic trace was shown in Figure 2.2. Figure 7.1a clearly shows

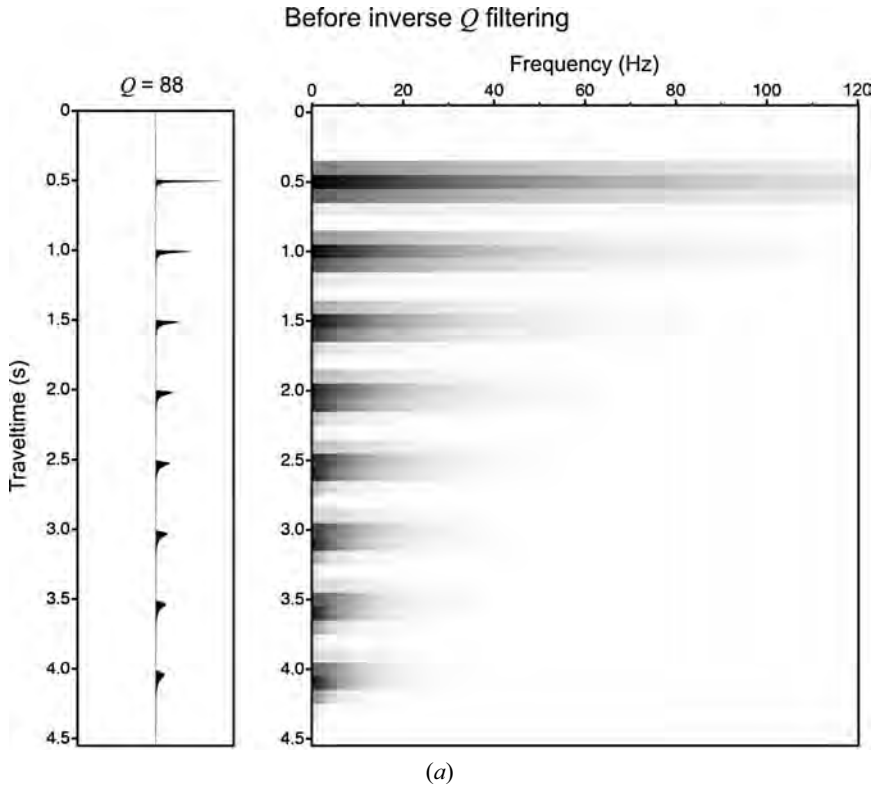


Figure 7.1 (a) A synthetic seismic trace with $Q = 88$ and the associated Gabor transform spectrum, which clearly shows that ‘frequency content’ changes with traveltime.

that ‘frequency content’ changes with time. Figure 7.1b shows that, when a plane wave with high frequency has been attenuated completely from the input seismic data, the stabilized algorithm for inverse Q filtering automatically limits the attempt to recover it.

7.4 Forward Q filtering by Gabor transform

For an inverse Q filtered seismic trace $u(t)$, an inverse process that removes previously introduced effects of inverse Q filtering is called forward Q filtering.

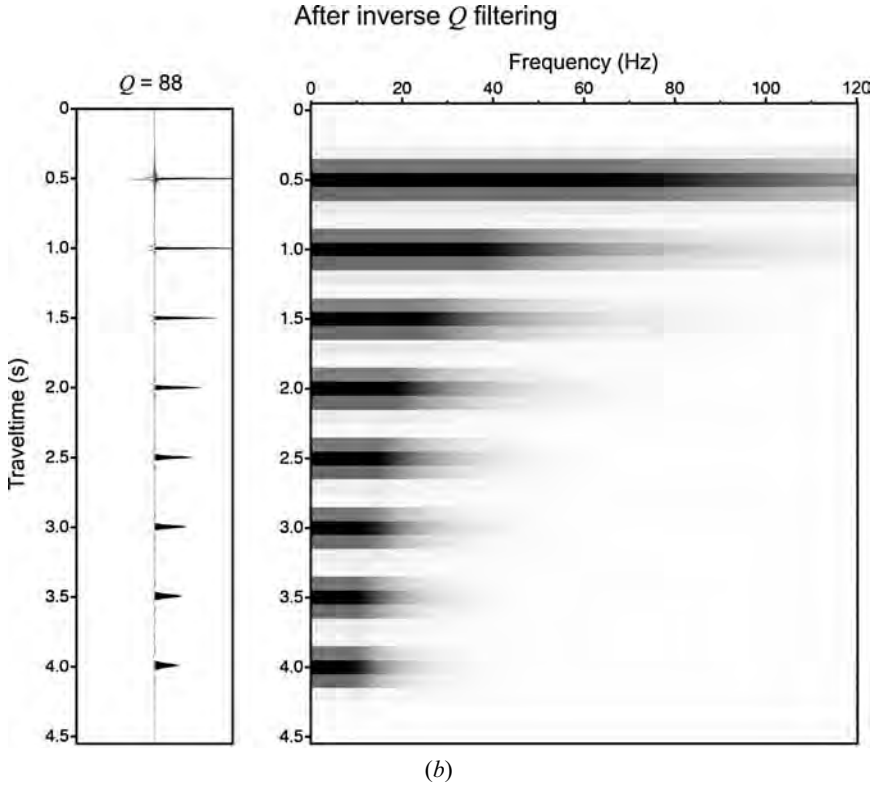


Figure 7.1 (contd) (b) Inverse Q filtered seismic trace ($Q = 88$) and the associated Gabor transform spectrum. When a plane wave with high frequency has been attenuated completely from the input seismic data, a stabilized algorithm for inverse Q filtering automatically limits the attempt to recover it.

For the phase-only inverse Q filter (7.8), the associated forward Q filter can be implemented by switching the sign of γ from negative in the inverse Q filter to positive for forward Q modelling. That is,

$$\tilde{U}(\tau, \omega) = U(\tau, \omega) \exp \left[i \int_0^\tau \left(\left(\frac{\omega}{\omega_h} \right)^{\gamma(\tau')} - 1 \right) \omega d\tau' \right]. \quad (7.20)$$

Then, the forward Q filter associated with a full inverse Q filter is expressed as

$$\tilde{U}(\tau, \omega) = U(\tau, \omega) \frac{1}{A(\tau, \omega)} \exp \left[i \int_0^\tau \left(\left(\frac{\omega}{\omega_h} \right)^{\gamma(\tau')} - 1 \right) \omega d\tau' \right], \quad (7.21)$$

where $\tilde{U}(\tau, \omega)$ is the output of forward Q filtering and $A^{-1}(\tau, \omega)$ is the amplitude-attenuation coefficient. Different amplitude-attenuation coefficients associating with various amplitude compensation coefficients were discussed in Chapter 5.

The Gabor transform may be used in the context of forward Q modelling as well. Note that Gabor transform-based forward Q modelling is implemented in exactly the same sequence as the inverse Q filter:

- 1) for a given seismic trace $u(t)$, constructing a set of the Gabor slices;
- 2) performing FFT on each Gabor slice to generate the Gabor transform spectrum, which is denoted as $U(\tau, \omega)$ to represent the inverse Q filtered wavefield;
- 3) forward Q modelling on $U(\tau, \omega)$ to produce $\tilde{U}(\tau, \omega)$;
- 4) performing inverse FFT on $\tilde{U}(\tau, \omega)$ to reconstruct the Gabor slices $u(\tau, t)$;
- 5) integration over τ on the set of the Gabor slices $u(\tau, t)$ to reproduce the seismic trace $u(t)$ in the time domain.

7.5 An empirical formula for the stabilization factor

As we have seen, the attenuation is a function of three parameters: frequency, traveltime and Q value, where the Q value can vary with two-way traveltime as well. Thus, it is not right for amplitude compensation to simply cut off at high frequency (such as in expression 4.16). The inverse Q filtering method presented in this chapter does not explicitly calculate an amplitude-compensation threshold. Instead, it uses a stabilization scheme which does the job gracefully. The stabilization factor σ^2 in equations (5.22) or (5.24) is physically linked to the signal-to-noise ratio of the seismic data.

However, some practitioners may prefer to set a gain threshold to control the amplitude boost. We derive here an empirical formula for estimating the stabilization factor σ^2 from a specific gain limit. The empirical formula is given as

$$\sigma^2 = \exp[-(0.23G_{\text{lim}} + 1.63)] \quad (7.22)$$

or

$$G_{\text{lim}} = -7.087 - 4.348 \ln \sigma^2, \quad (7.23)$$

where G_{lim} is the specified gain limit (in decibels) in an explicit gain-controlling scheme. Figure 7.2 displays the amplitude-compensation curves of an explicit gain-controlling scheme (with $G_{\text{lim}} = 20$ dB) and of the stabilized scheme using σ^2 , for various Q values.

We now show how to derive the stabilization factor σ^2 based on a specified gain limit G_{lim} . To explicitly control the amplitude boost is to define an amplitude-compensation coefficient as

$$\hat{A}(\tau, \omega) = \begin{cases} g(\tau, \omega), & \text{for } g \leq g_{\text{lim}}, \\ g_{\text{lim}}, & \text{for } g > g_{\text{lim}}, \end{cases} \quad (7.24)$$

where

$$g(\tau, \omega) = \exp \left[\int_0^\tau \frac{\omega}{2Q(\tau')} d\tau' \right], \quad (7.25)$$

and $g_{\text{lim}} = \exp[0.05G_{\text{lim}}]$. In the following derivation, we assume Q to be constant along a seismic trace, $Q(\tau) = Q$.

Defining a combined variable $\chi \equiv \omega\tau$, the stabilized amplitude-compensation operator (5.22) is represented as

$$A(\chi) = \frac{\beta(\chi) + \sigma^2}{\beta^2(\chi) + \sigma^2}, \quad (7.26)$$

and the gain-limited formula (7.24) is rewritten as

$$\hat{A}(\chi) = \begin{cases} g(\chi), & \text{for } \chi \leq \chi_q, \\ g_{\text{lim}}, & \text{for } \chi > \chi_q, \end{cases} \quad (7.27)$$

where χ_q is the critical point where the gain curve has been cut off.

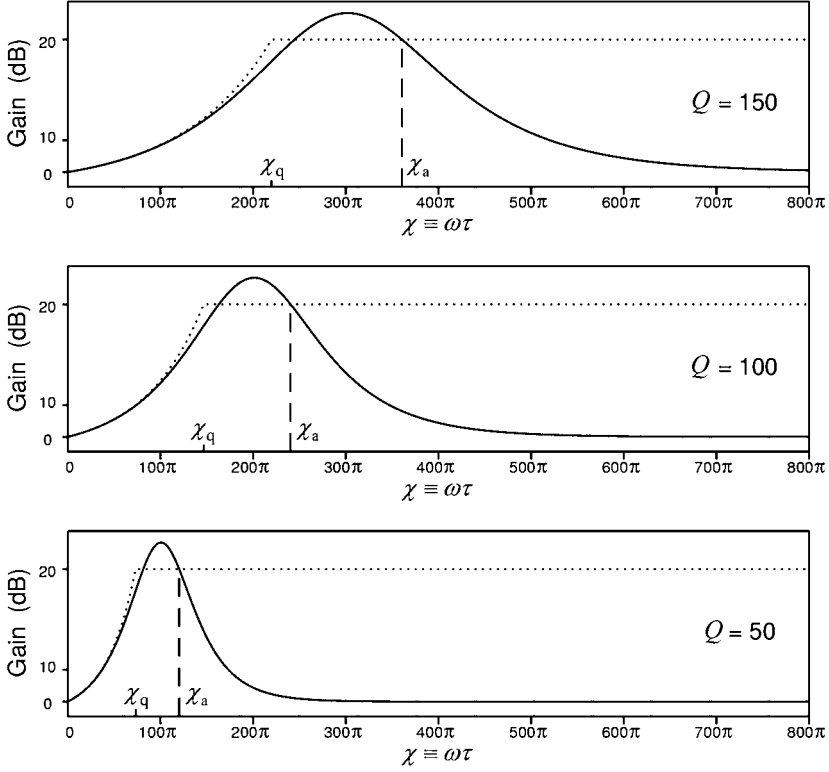


Figure 7.2 Comparison of gain curves of inverse Q filtering with an explicit gain-controlling scheme (dotted lines) and the stabilized scheme (solid lines). The horizontal axis χ is defined as $\chi \equiv \omega\tau$, where ω and τ are frequency and traveltime, respectively. The corner position χ_q corresponds the cut-off gain limit (in this case $G_{\text{lim}} = 20$ dB, for example), whereas χ_a is a point where the accumulations of two individual gain curves are equivalent.

Assuming a constant Q along a seismic trace, $\beta(\chi)$ and $g(\chi)$ functions in equations (7.26) and (7.27) respectively are given by

$$\beta(\chi) = \exp\left[-\frac{\chi}{2Q}\right] \quad (7.28)$$

and

$$g(\chi) = \exp\left[\frac{\chi}{2Q}\right]. \quad (7.29)$$

To estimate σ^2 , we now set up a criterion: the integrals up to the cross-point, χ_a (as shown in Figure 7.2), of two individual gain curves are equivalent. That is, we estimate σ^2 by solving the following two equations simultaneously:

$$\left. \begin{aligned} A(\chi_a) &= \hat{A}(\chi_a) \\ \int_0^{\chi_a} A(\xi) d\xi &= \int_0^{\chi_a} \hat{A}(\xi) d\xi \end{aligned} \right\}. \quad (7.30)$$

Using stabilization equation (7.26) and gain-limited formula (7.27), we have the following expressions:

$$A(\chi_a) = \frac{\exp\left(-\frac{\chi_a}{2Q}\right) + \sigma^2}{\exp\left(-\frac{\chi_a}{Q}\right) + \sigma^2}, \quad (7.31a)$$

$$\hat{A}(\chi_a) = g_{\lim}, \quad (7.31b)$$

$$\begin{aligned} \int_0^{\chi_a} A(\xi) d\xi &= \frac{2Q}{\sigma^2} \left[\tan^{-1}\left(\frac{1}{\sigma^2}\right) - \tan^{-1}\left(\frac{\exp\left(-\frac{\chi_a}{2Q}\right)}{\sigma^2}\right) \right. \\ &\quad \left. + \frac{\sigma^2}{2} \ln\left(\frac{1 + \sigma^2 \exp\left(\frac{\chi_a}{Q}\right)}{1 + \sigma^2}\right) \right], \end{aligned} \quad (7.31c)$$

and

$$\int_0^{\chi_a} \hat{A}(\xi) d\xi = 2Q \left[\exp\left(\frac{\chi_a}{2Q}\right) - 1 \right] + (\chi_a - \chi_q) g_{\lim}. \quad (7.31d)$$

Substituting these into equation system (7.30), the stabilization factor σ^2 may be solved numerically. Fitting a group of σ^2 for given gain limits G_{\lim} between 10 and 100 dB produces the empirical equation (7.23). Note that for a given gain limit G_{\lim} , the σ^2 conversion is independent of Q values.

The difference in terms of physical meaning between the gain-limited scheme and the stabilization scheme can be seen from Figure 7.2, where the horizontal axis is $\chi \equiv \omega\tau$, and the vertical axis is the amplitude-boost coefficient (in decibels). The dotted line is the gain curve in a gain-limited inverse Q filtering scheme and the solid line is the corresponding gain curve in a stabilized inverse Q filtering scheme. A gain-limited scheme attempts to boost amplitude all the way down to the end of the seismic trace, though the gain is controlled by the limit G_{lim} . However, a plane wave with specific frequency (ω) has been attenuated completely when it has been propagating beyond a certain travelttime (τ), and has left no information in the seismic record. The conventional gain-limited inverse Q filtering scheme will boost only the ambient noise. The stabilized inverse Q filter recognizes this fact by reducing the gain coefficient gradually.

To set a small value for the stabilization factor, σ^2 , in the inverse Q filter, random noise attenuation may be performed prior to inverse Q filtering. For the real data examples shown in this book, a random noise-attenuation method based on the two-dimensional spatial linear prediction theory (Wang, 1999) is used.

Chapter 8

The effectiveness of stabilized inverse Q filtering

Abstract

Applying an inverse Q filter to reflection seismic data may minimize the effects of dispersion and attenuation and hence improve the seismic resolution. This chapter quantitatively evaluates the effectiveness of the inverse Q filter on a land seismic data set. It shows that the inverse Q filter may flatten the amplitude spectrum, strengthen the time-variant amplitude, increase the spectral bandwidth and improve the signal-to-noise (S/N) ratio. This chapter also defines a parameter to measure the resolution enhancement as a function of changes in the bandwidth and the S/N ratio. The stabilized inverse Q filtering algorithm shows positive changes both in the bandwidth and in the S/N ratio and thereby enhances the resolution of the final processed seismic data.

Seismic attenuation is a fundamental property of wave propagation through subsurface media (Futterman, 1962; Strick, 1970; Kjartansson, 1979). It has a considerable impact on amplitude and wave shape in recorded seismic data. It is of particular importance when seismic attributes and inversion schemes are required to extract lithological information, porosity, permeability, viscosity and degree of saturation of rocks, because the attenuation parameter is more sensitive than velocity to some of these properties.

To remove the earth attenuation effect, we have developed stabilized algorithms for inverse Q filtering in Chapters 4–7, based on the theory of

wavefield downward continuation. They can recover all frequency components that in principle are recoverable, and intelligently limit the attempt to compensate the high-frequency wave component when its amplitude has been attenuated to a level below the ambient noise level. This stable feature is of significance because seismic resolution is a function of not only the frequency bandwidth but also the signal-to-noise (S/N) ratio (Widess, 1982). Later in this chapter, we shall derive a formula to measure the change of seismic resolution, which is a function of the change in bandwidth and the change in S/N ratio.

In this chapter, we apply this stabilized inverse Q filter to a two-dimensional surface seismic line, which is land seismic with a low S/N ratio relative to marine seismic data. A challenge in inverse Q filtering is whether or not the method can improve the S/N ratio without boosting the noise, when compensating for both phase and amplitude effects simultaneously. For designing the inverse Q filter, we estimate the prerequisite reliable earth Q function from a vertical seismic profile (VSP). The detail of this Q estimation from the VSP downgoing wavefield is given in Chapter 10.

In this chapter, we shall focus on the quantitative evaluation of the effectiveness of inverse Q filtering, which corrects for wavelet dispersion in a time variant manner, compensates for frequency-dependent amplitude decay along the seismic trace, and restores the attenuated frequency components within the signal pass band. These improvements in turn increase the spectral bandwidth and S/N ratio and hence the resolution of the final processed seismic data.

8.1 Inverse Q filtering of a land seismic section

Applying an inverse Q filter to surface seismic data will compensate for both phase and amplitude effects simultaneously. Let us now compare two stack sections in Figure 8.1; one stack section without inverse Q filtering and one with inverse Q filtering.

Seismic data are generally observed to lose high frequencies with increasing traveltimes. The loss of high frequencies lengthens the dominant signal wavelength and thereby degrades the seismic resolution. However, the seismic section after inverse Q filtering shows a higher dominant frequency than the original. A time-varying distortion of wavelet phase is evident in the stack section without inverse Q filtering. Inverse Q filtering has improved the lateral coherence of seismic events, even though it is processed trace by trace. For example, there is a group of linear events with

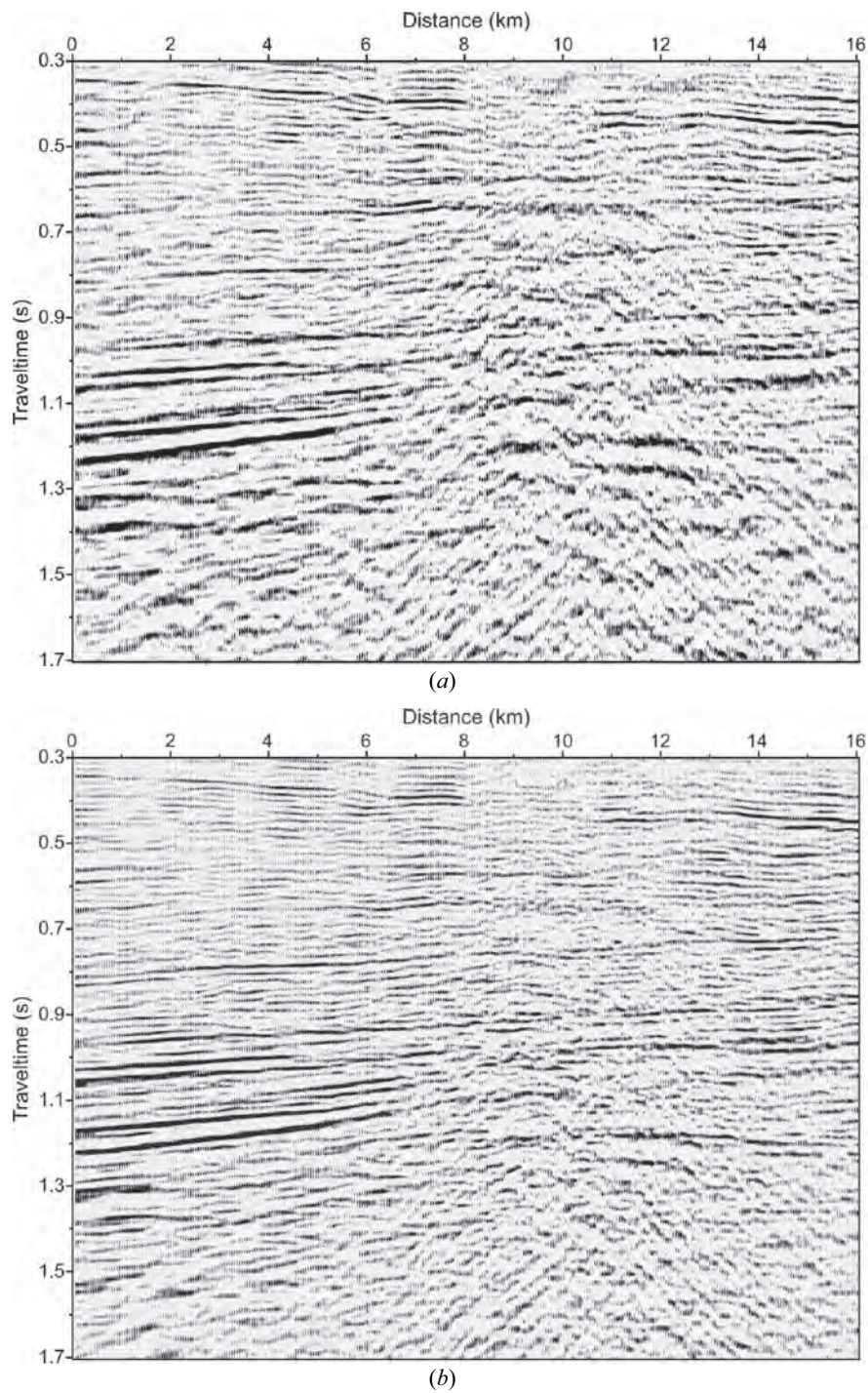


Figure 8.1 Stack sections before (a) and after (b) inverse Q filtering.

an intercept time of about 1200 ms, and a two-way time 1000 and 1200 ms at distance 16 km.

Random noise attenuation is needed before or after inverse Q filtering. A forward–backward spatial prediction-based technique (Wang, 1999) can be used. It is also necessary to apply a gap deconvolution to the data after inverse Q filtering. For a fair comparison, both sections in Figure 8.1 have been processed through these two steps with identical parameters.

Changes in event times produced by correcting for dispersion are also evident in Figure 8.1. This is of high importance since it impacts time-to-depth conversion of the seismic events. A quantitative comparison is not given here though, and readers may refer to Figures 2.2, 2.3 and 2.4 in Chapter 2 for the detail. However, any dispersion-correction-only inverse Q filtering is unconditionally stable. Difficulties occur only when inverse Q filtering includes the energy-dissipation compensation, which may cause numerical instability and generate undesirable artefacts in the solution. In the present discussion, we will focus on stabilized inverse Q filtering methods, which compensate for both velocity dispersion and energy dissipation simultaneously. In the following sections we will attempt to measure the effectiveness quantitatively.

8.2 Flattening the amplitude spectrum and strengthening the relative amplitude

The amplitude spectra shown in Figure 8.2 clearly demonstrate that inverse Q filtering has flattened the amplitude spectrum within the signal band. The amplitude spectra are computed from an arbitrarily selected trace, at distance 10 km. The flattened amplitude spectrum within the band 10–75 Hz indicates an adequate compensation for energy dissipation. It results in a compression of the dispersed wavelet and an increase in phase coherence, as seen in Figure 8.1. Although the trend of the spectrum has been flattened, the relative amplitude difference between adjacent frequency components and thereby the seismic resolution in the frequency axis were not altered.

Time-variant amplitude strength, averaged over all traces, is displayed in Figure 8.3 for different frequency components, in which the dotted and solid lines represent seismic amplitudes without inverse Q filtering and with inverse Q filtering, respectively. The difference between them reflects the amount of amplitude compensation for different frequency components at different time samples. Generally speaking, inverse Q filtering has boosted the relative amplitude strength.

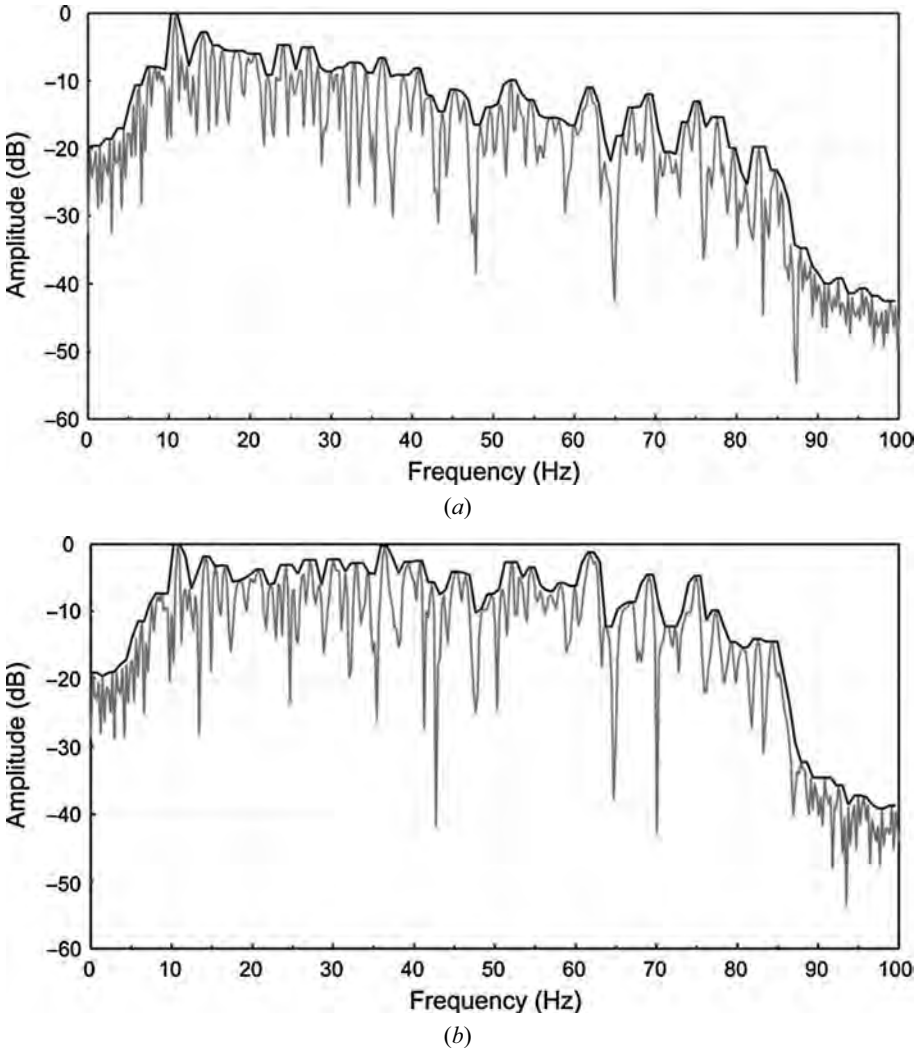


Figure 8.2 Comparison of the amplitude spectra of a stack trace (at distance 10 km) without inverse Q filtering (a) and using inverse Q filtering (b). The two lines in each spectrum plot are the DFT result (grey) and the median-filtered, smoothed spectrum (black).

The grey bar drawn as a reference mark in Figure 8.3 indicates the traveltimes within which the amplitude has been fully recovered after inverse Q filtering. The stabilized inverse Q filter systematically and implicitly determines such a traveltimes range within which a given frequency component is recoverable. Within the traveltimes range, the longer

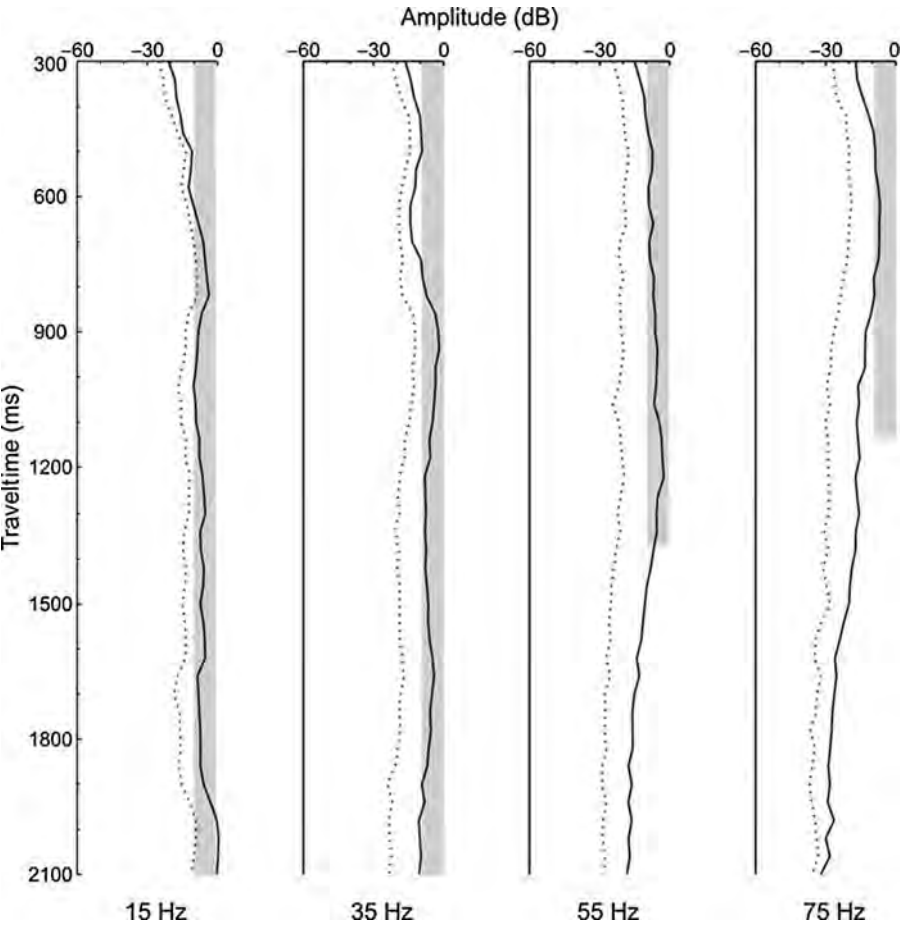


Figure 8.3 Comparison of the time-variant amplitude strength (averaged over all traces in the section) of different frequency components without inverse Q filtering (dotted lines) and using inverse Q filtering (solid lines). The grey bar drawn as a reference mark indicates the portion of the data set within which the amplitude has been fully recovered after inverse Q filtering.

the traveltime and the higher the frequency, the more the amplitude has been compensated. Beyond this range, the stabilized inverse Q filter reduces the compensation gradually and thereby we see the amplitude curves converging. These reference marks are also useful for designing a time-variant band-pass filter which is essential, especially for land seismic processing.

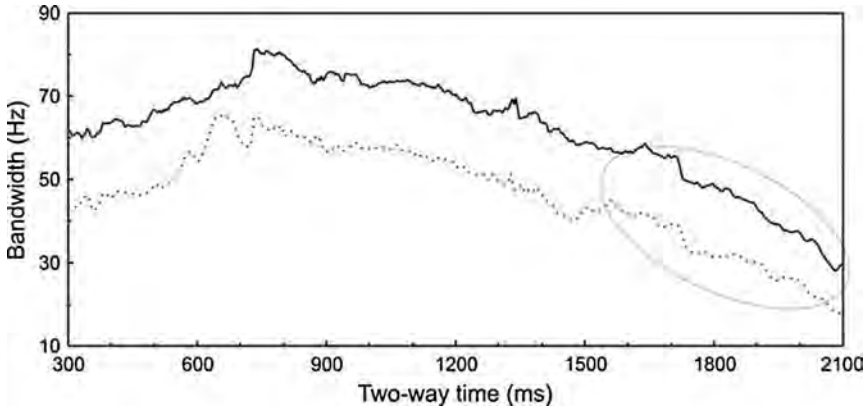


Figure 8.4 Comparison of the time-variant bandwidth estimate (averaged over all traces in the stack section) of the seismic data without inverse Q filtering (dotted line) and those with inverse Q filtering (solid line).

8.3 Increasing the spectral bandwidth

The statistical bandwidth may be estimated using the method of Walden and White (1990) as

$$\hat{B} = \frac{\phi_0^2}{2 \sum_{\tau=-(T-1)}^{T-1} \left(1 - \frac{|\tau|}{T}\right) w_\tau^2 \phi_\tau^2}, \quad (8.1)$$

where $\phi_\tau = (1/T) \sum x_t x_{t+\tau}$ is the sample autocovariance constructed from the time series $\{x_1, x_2, \dots, x_T\}$, T is the duration of the data segment and w_τ is a taper window. This is then corrected to give an approximately unbiased estimate:

$$B = \left(1 + \frac{2}{\nu}\right) \hat{B} - \frac{1}{T}, \quad (8.2)$$

where ν is the number of degrees of freedom associated with w_τ .

Figure 8.4 shows the time-variant bandwidth estimate (averaged over all the traces shown in the stack section) of the seismic data without inverse Q filtering (dotted line) and using inverse Q filtering (solid line). It indicates clearly that inverse Q filtering has increased the seismic temporal bandwidth

by 15–20 Hz. After two-way time of about 1500 ms, the bandwidth increment is gradually narrowing, because of the stabilization that prevents high-frequency, ambient noise to be boosted, as revealed by Figure 8.3.

8.4 Improving the signal-to-noise ratio

The S/N power ratio of a specific trace $x_{k,t}$, among a set of $q+1$ traces, may be estimated by (White, 1980, 1984; Walden and White, 1984):

$$\hat{\rho}_k(\omega) = \frac{\left| \underline{\Phi}_{qk}^H(\omega) \underline{\Phi}_{qq}^{-1}(\omega) \underline{\Phi}_{qk}(\omega) \right|}{\left| \Phi_{kk|q}(\omega) \right|}, \quad (8.3)$$

where $\underline{\Phi}_{qq}^{-1}$ is the inverse of the spectral matrix of the q traces, $\underline{\Phi}_{qk}$ is the column vector of their cross spectra with the trace $x_{k,t}$, $\underline{\Phi}_{qk}^H$ is its conjugate transpose and $\Phi_{kk|q}$ is the estimated noise power on $x_{k,t}$, defined as the spatially unpredictable energy:

$$\Phi_{kk|q}(\omega) = \Phi_{kk}(\omega) - \underline{\Phi}_{qk}^H(\omega) \underline{\Phi}_{qq}^{-1}(\omega) \underline{\Phi}_{qk}(\omega). \quad (8.4)$$

For each specific trace $x_{k,t}$, we have $q+1$ estimates $\hat{\rho}_k^{(j)}$, for $j = 1, 2, \dots, q+1$. Each individual $\hat{\rho}_k^{(j)}$ is estimated from one of the following trace groups,

$$\{x_{k-q,t}, \dots, x_{k,t}\}, \{x_{k-q+1,t}, \dots, x_{k+1,t}\}, \dots, \{x_{k,t}, \dots, x_{k+q,t}\},$$

each consisting of $q+1$ traces. The final measurement $\hat{\rho}_k$ is the average of these $q+1$ estimates $\{\hat{\rho}_k^{(j)}\}$. In the example, $q=3$ is used.

Figure 8.5 displays the S/N ratios (in decibels) of a seismic trace (at distance 10 km) within four different time windows. The S/N ratio improvement varies within different time windows, with significant improvement on the shallow portion. In the shallow portion the S/N ratio improvement is up to 75 Hz. In the middle and deep portions this upper limit decreases gradually. This phenomenon is consistent with the experiment we did before, showing that the stabilized inverse Q filtering method automatically determines recoverable frequency components according to the travel distance or time.

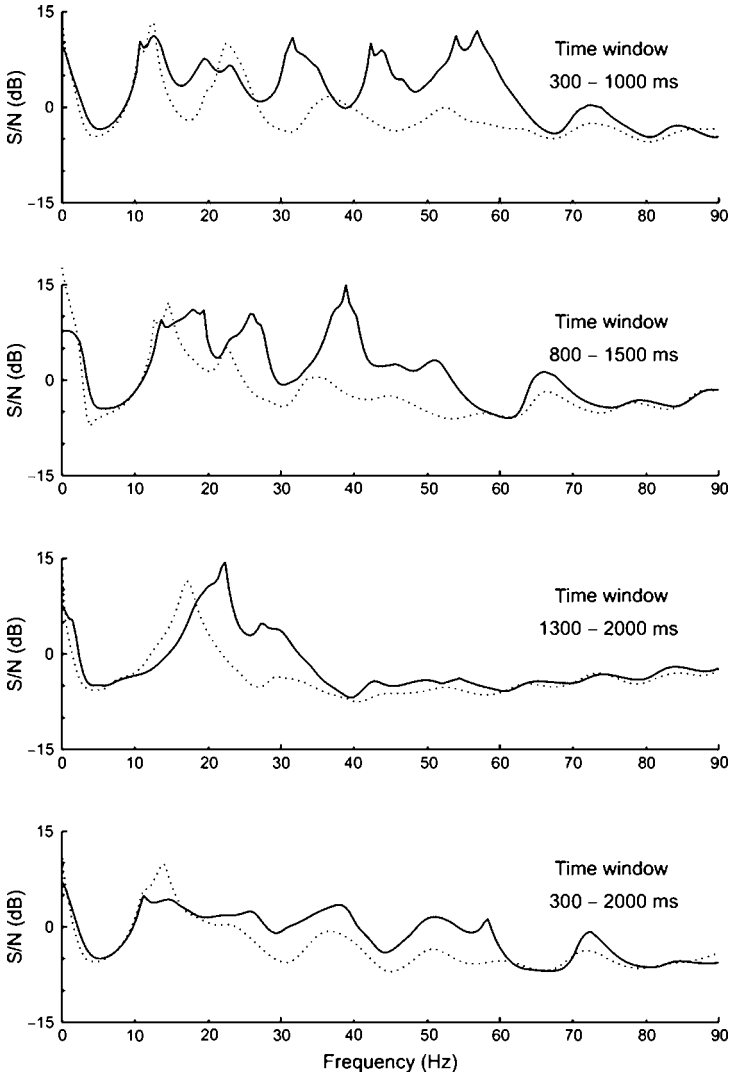


Figure 8.5 Comparison of the S/N ratios of a seismic trace (at distance 10 km) without inverse Q filtering (dotted lines) and after inverse Q filtering (solid lines). The S/N improvement varies within different time windows.

8.5 Enhancing seismic resolution

The spectral bandwidth and the S/N ratio are related to the seismic resolution. Let us now define an empirical formula to quantitatively measure the resolution enhancement.

The standard deviation of the time-shift estimate τ , on which our formula is based, may be evaluated as (White and Harris, 1993):

$$\text{var}\{\tau\} = \frac{3}{2\pi^2(B^2 - b^2)BT} \left(\frac{1}{\psi^2} - 1 \right), \quad (8.5)$$

where b is the bandwidth of the spectral window employed in the analysis, and ψ^2 is the spectral coherence. The spectral coherence measures the predictability of one trace from the other (White, 1973, 1984) and is frequency-dependent. It is estimated here approximately by

$$\hat{\psi}^2(\omega) = \frac{\hat{\rho}^2(\omega)}{[1 + \hat{\rho}(\omega)]^2}, \quad (8.6)$$

where $\hat{\rho}(\omega)$ is the average of the S/N ratio $\hat{\rho}_k(\omega)$ over all the traces. The ψ^2 value in equation (8.5) is the average of $\hat{\psi}^2(\omega)$ over the frequency band.

Defining a parameter δ to measure the resolution enhancement as

$$\delta = -\frac{\Delta(\text{var}\{\tau\})}{\text{var}\{\tau\}}, \quad (8.7)$$

represented in terms of the (negative) change of the standard deviation of the time shift, we obtain the following expression:

$$\delta = \left(3 + \frac{2b^2}{B^2 - b^2} \right) \frac{\Delta B}{B} + \left(1 + \frac{1}{1 + 2\rho} \right) \frac{\Delta\rho}{\rho}, \quad (8.8)$$

and its approximation

$$\delta \approx 3 \frac{\Delta B}{B} + 2 \frac{\Delta\rho}{\rho}. \quad (8.9)$$

Here, the relative increment of the spectral bandwidth, $\Delta B/B$, is the average value over the time window, and the relative increment in the S/N ratio, $\Delta\rho/\rho$, is the average value over the frequency band.

The parameter δ is defined as a function of changes in the bandwidth and the S/N ratio. A problem with the conventional inverse Q filtering

method is that it may increase the bandwidth but degrades the S/N ratio, and thus may not improve the resolution. However, the stabilized inverse Q filtering algorithm can have positive changes in both the bandwidth and S/N ratio, and in turn enforce a seismic resolution improvement.

The relative improvements (as a percentage) on spectral bandwidth, S/N ratio and the temporal resolution within different time windows are summarized in Table 8.1. It is worthwhile noticing that over the time range 300–2000 ms, we have a 36% increment in spectral bandwidth, a 27% increment in the S/N ratio and, finally, a 162% enhancement in temporal resolution.

Table 8.1 Relative improvements (as a percentage) on spectral bandwidth ($\Delta B/B$), S/N ratio ($\Delta \rho/\rho$) and the temporal resolution (δ).

Time (ms)	$\Delta B/B$ (%)	$\Delta \rho/\rho$ (%)	δ (%)
300–1000	30	82	254
800–1500	32	56	208
1300–2000	42	16	158
300–2000	36	27	162

8.6 Sensitivity of the resolution enhancement to Q values

In the previous section, we have seen that the resolution enhancement, denoted as δ , is a function of the change in frequency bandwidth and the change in the S/N ratio. Naturally, we would like to know the sensitivity of the resolution enhancement with respect to the Q parameter used in stabilized inverse Q filtering; in other words, whether we can set an inverse problem to invert for Q values by optimizing $\delta(Q)$.

We have seen that stabilized inverse Q filtering can improve the S/N ratio, when the input data set has a relatively poor S/N ratio. We now see what the degree of modification will be in S/N ratio, if the input data set has an extremely high S/N ratio, using the example data set shown in Figure 4.7a. Figure 8.6 shows the comparison of the S/N ratios before and after the stabilized inverse Q filtering with different Q values. From the top to the bottom, the Q value for each case decreases gradually by 20. The horizontal

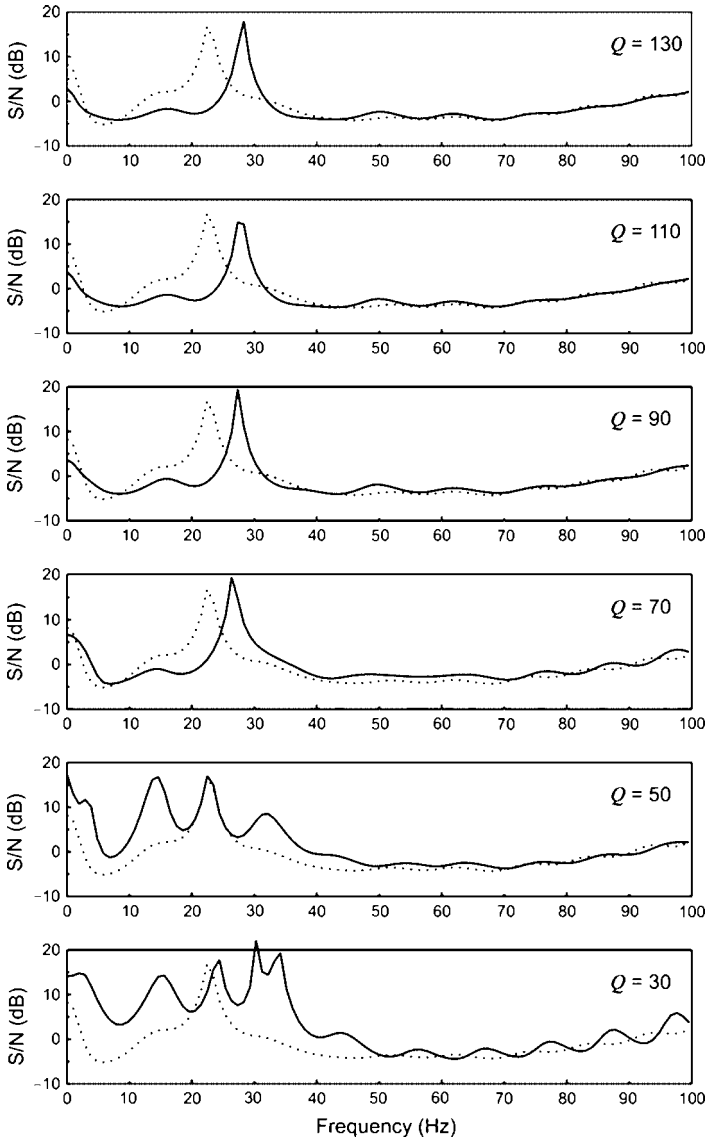


Figure 8.6 Comparison of the S/N ratios before (dotted lines) and after (solid lines) stabilized inverse Q filtering.

axis is the frequency axis. There are four observations we can make as follows.

- 1) The average S/N ratio across the whole of the frequency axis seems not to change much, as the input data set has an extremely high S/N ratio.

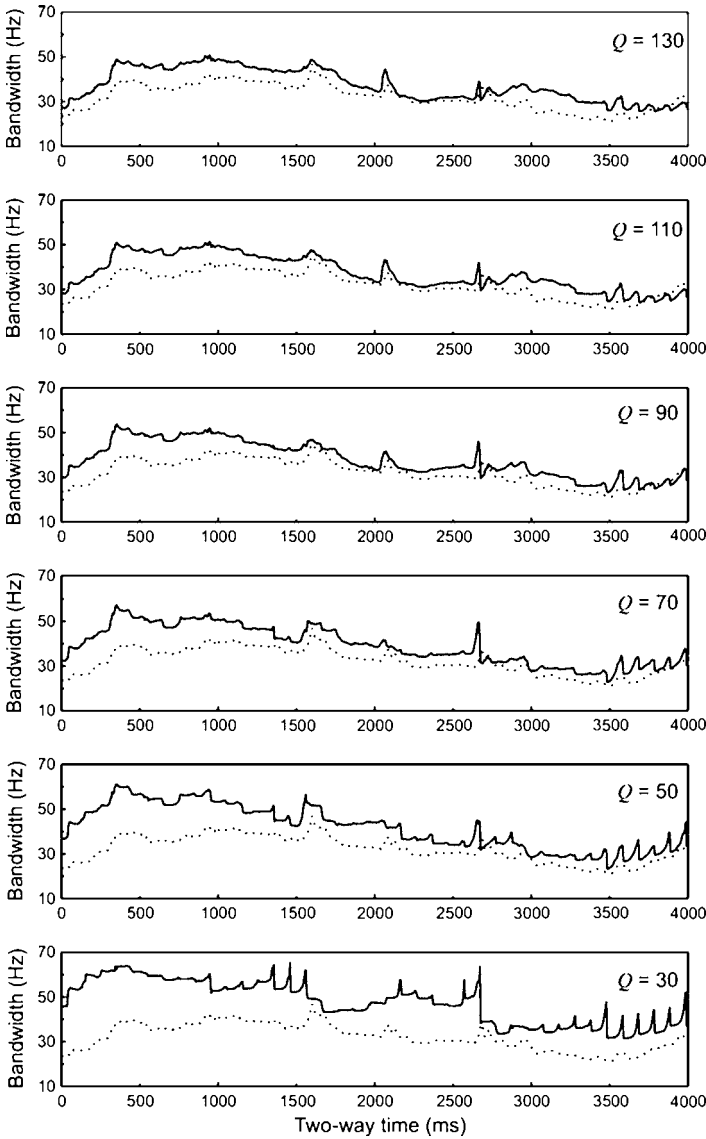


Figure 8.7 Comparison of the frequency bandwidths before (dotted lines) and after (solid lines) stabilized inverse Q filtering.

- 2) The peak of the S/N ratio has been shifted to higher frequency, because the dominant frequency of the seismic signal has been shifted after the stabilized inverse Q filtering procedure.
- 3) Generally speaking, the difference between the two S/N ratio peaks

before and after inverse Q filtering decreases when the Q value increases, as the stabilized inverse Q filtering algorithm automatically determines the recoverable frequency range implicitly based on the Q value.

- 4) However, when the Q value is equal to or smaller than 50, the S/N ratio after inverse Q filtering is no longer the simple shifted copy of the S/N ratio before inverse Q filtering, and we should see in the seismic profile that more coherent events within a certain frequency range have been boosted.

A point we can draw here is that, once the stabilized inverse Q filtering algorithm is chosen, the Q value is an insensitive variable in the measurement of S/N ratio from the result of inverse Q filtering. It can undergo very large changes without significant change in the S/N ratio after the stabilized inverse Q filtering procedure.

We now consider the change in frequency bandwidth after stabilized inverse Q filtering. A comparison of the frequency bandwidths (in hertz) before and after inverse Q filtering is shown in Figure 8.7. The horizontal axis shows the two-way traveltime in millisecond. From the top to the bottom, the Q value for each case decreases gradually by 20, and the bandwidth is gradually increased.

Figures 8.6 and 8.7 clearly show that when Q^{-1} increases, both $\Delta B/B$ and $\Delta\rho/\rho$ increase positively, and thus δ increases. The bad news is, however, that because δ increases monotonically along with Q^{-1} , it cannot be used to set up a maximization problem to invert for Q values directly from seismic data.

Chapter 9

Migration with inverse Q filtering

Abstract

Migration is a reversal process of seismic wave propagation, by which surface-recorded seismic waves are propagated back to the subsurface reflector locations. Thus, a migration process should also remove the earth Q effect, so as to produce an image with true amplitude and correct timing. This chapter first presents a wavenumber-frequency domain algorithm that is applicable to subsurface media with vertical variations in velocity and Q functions, and then proposes a space-frequency domain method for models with lateral variations. The essential element of the proposed strategy is to construct supersedent of attenuation coefficients, for given velocity and Q models, before performing wavefield extrapolation in the (x, z, ω) space.

Seismic migration is an inverse process of wave propagation, as is inverse Q filtering, in which the surface-recorded seismic waves are propagated back through the subsurface medium. Therefore, during the migration process, the earth attenuation effects including amplitude absorption and velocity dispersion should also be removed. By performing inverse Q filtering and migration process simultaneously, we are able to restore the high frequencies to balance the spectrum of the seismic image, and correct the phases and thus the associated timings of reflections. We refer to this procedure as inverse Q filtered migration.

In a viscoacoustic medium, seismic wave amplitudes and arrival times are altered because of the energy absorption and velocity dispersion, respectively. Consequently, migration processing without compensating for these earth attenuation effects would produce a result with a diffused image

and incorrectly positioned reflectors. Including an inverse Q filter in migration by wavefield extrapolation, however, raises the problem of numerical instability. Because the amplitudes of high-frequency components grow rapidly in wavefield extrapolation, the errors from observed noise, numerical approximation and round-off tend to be amplified drastically with increasing depth (Dai and West, 1994; Mittet *et al.*, 1995; Cui and He, 2004). Therefore, one has to put a limit on the number of extrapolation steps and on the maximum angle of migration dip to derive a conditionally stable extrapolation operator (Zhang and Wapenaar, 2002). As expressions (8.8) and (8.9) in Chapter 8 indicate, the improvement of seismic resolution by inverse Q filtering not only depends upon the frequency bandwidth but also the signal-to-noise ratio. The seismic resolution can be improved only when both factors enforce each other. Thus, stabilization of the inverse Q filtered migration procedure is one of the focus points in this chapter.

In this chapter, I first present a stabilized algorithm for inverse- Q filtered migration in the wavenumber-frequency domain that is applicable to a subsurface medium with a vertically variable velocity function and vertically variable Q function (Wang and Guo, 2004a). This preliminary investigation will offer us some insights into the stabilization issues in wavefield extrapolation for general downward continuation. I then propose a stabilization strategy for migration in the case with lateral variations in velocity and Q functions (Wang, 2008). The essential element of the proposed strategy is to construct ‘supersedents’ to supersede attenuation coefficients, based on the given velocity and Q models, before performing the wavefield extrapolation in the space-frequency domain.

9.1 Inverse Q filtered migration in the wavenumber-frequency domain

9.1.1 Algorithm

For an inverse Q filtered migration scheme, we start the derivation with a one-way wave equation in the Fourier transform domain:

$$\frac{\partial U(k_x, z, \omega)}{\partial z} = i k_z U(k_x, z, \omega), \quad (9.1)$$

where U is the plane wave of angular frequency ω , k_x is the horizontal

wavenumber and k_z is the vertical wavenumber. The two-dimensional (2-D) Fourier transform $U(k_x, z, \omega)$ of a wavefield $u(x, z, t)$ is defined through

$$U(k_x, z, \omega) = \int_{-\infty}^{\infty} \int_{-\infty}^{\infty} u(x, z, t) \exp[i(k_x x - \omega t)] dx dt. \quad (9.2)$$

The phase-shift solution to wave equation (9.1) is

$$U(k_x, z + \Delta z, \omega) = U(k_x, z, \omega) \exp[i k_z \Delta z], \quad (9.3)$$

where Δz is the step length of wavefield downward extrapolation. The vertical wavenumber k_z is defined as

$$k_z = \frac{\omega}{\bar{v}} \sqrt{1 - \frac{k_x^2}{k^2}}, \quad (9.4)$$

where $\bar{v} \equiv \bar{v}(z)$ is half of the wave propagation speed (Loewenthal *et al.*, 1976).

To take into account the earth Q effect, the real velocity \bar{v} is replaced by a frequency-dependent, complex-valued velocity, \bar{c} , defined as

$$\frac{1}{\bar{c}} = \frac{1}{\bar{v}} \left(\frac{\omega}{\omega_h} \right)^{-\gamma} - i \frac{1}{2 \bar{v} Q}, \quad (9.5)$$

where $\bar{c} \equiv \bar{c}(z, \omega)$, $Q \equiv Q(z)$, $\gamma \equiv \gamma(z) = (\pi Q)^{-1}$ and ω_h is a reference frequency with $\omega < \omega_h$. The vertical wavenumber (9.4) becomes

$$k_z = \left[\frac{\omega}{\bar{v}} \left(\frac{\omega}{\omega_h} \right)^{-\gamma} - i \frac{\omega}{2 \bar{v} Q} \right] \sqrt{1 - \frac{k_x^2}{k^2}}. \quad (9.6)$$

In the migration calculation, the wavenumber-square k^2 inside the square-root may be evaluated by using the real-valued velocity, $k^2 = \omega^2 / \bar{v}^2$. Both \bar{v} and Q here are variable with the depth z .

A time-domain migrated sample is obtained by replacing depth z in equation (9.3) with migration time $\tau = \sum \Delta z / \bar{v}(z)$. Considering the wavefield downward continuation starting from the recording surface $\tau = 0$,

the migrated wavefield $U(k_x, \tau, \omega)$ at time level τ may be expressed as

$$U(k_x, \tau, \omega) = U(k_x, 0, \omega) M(k_x, \tau, \omega), \quad (9.7)$$

where $U(k_x, 0, \omega)$ is the wavefield at recording surface, and $M(k_x, \tau, \omega)$ is the migration operator, given by

$$M(k_x, \tau, \omega) = \exp \left[\int_0^\tau \frac{\omega}{2Q(\tau')} \sqrt{1 - \frac{k_x^2}{k^2(\tau', \omega)}} d\tau' \right] \\ \times \exp \left[i \omega \int_0^\tau \left(\frac{\omega}{\omega_h} \right)^{-\gamma(\tau')} \sqrt{1 - \frac{k_x^2}{k^2(\tau', \omega)}} d\tau' \right], \quad (9.8)$$

which takes into account the vertical variations in the velocity and Q functions. Thus, equations (9.7) and (9.8) are the basic time-migration formulae.

By using the complex velocity \bar{c} in equation (9.5), the migration process also compensates the amplitude attenuation and corrects the phase distortion due to the earth Q filter. However, as discussed in Chapter 4, a key problem with an inverse Q filter is the numerical instability, because of the exponential growth of the amplitude-compensation operator with respect to the frequency and the traveltime. To stabilize the migration operation, we rewrite the basic migration expression (9.7) as

$$W(k_x, \tau, \omega) U(k_x, \tau, \omega) = U(k_x, 0, \omega) P(k_x, \tau, \omega), \quad (9.9)$$

where

$$W(k_x, \tau, \omega) = \exp \left[- \int_0^\tau \frac{\omega}{2Q(\tau')} \sqrt{1 - \frac{k_x^2}{k^2(\tau', \omega)}} d\tau' \right] \quad (9.10)$$

and

$$P(k_x, \tau, \omega) = \exp \left[i \omega \int_0^\tau \left(\frac{\omega}{\omega_h} \right)^{-\gamma(\tau')} \sqrt{1 - \frac{k_x^2}{k^2(\tau', \omega)}} d\tau' \right]. \quad (9.11)$$

Then we construct a stabilized migration operator by

$$M(k_x, \tau, \omega) = A(k_x, \tau, \omega) P(k_x, \tau, \omega), \quad (9.12)$$

with

$$A(k_x, \tau, \omega) = \frac{W(k_x, \tau, \omega) + \sigma^2}{W^2(k_x, \tau, \omega) + \sigma^2}, \quad (9.13)$$

where σ^2 is the small positive definite stabilization factor. That is, in the stabilized migration scheme, instead of applying the migration operator (9.8) directly, we use the stabilized migration operator (9.12) evaluated in terms of the inverse amplitude operator W . Note that stabilization here treats the amplitude operator separately; therefore, it does not affect the phase operator. This is an improvement over Wang and Guo's (2004a) paper.

We obtain the time-domain migrated sample at τ by an inverse Fourier transform with respect to ω and taking the value at $t = 0$:

$$u(k_x, \tau, t = 0) = \frac{1}{\pi} \int_0^\infty U(k_x, 0, \omega) M(k_x, \tau, \omega) d\omega. \quad (9.14)$$

This migrated wavefield $u(k_x, \tau, 0)$ is presented in the k_x domain, as we assume that the migration model (i.e. the velocity and Q functions) is laterally invariant. Finally, we may perform an inverse Fourier transform with respect to k_x to produce the desired seismic section in the space-time domain.

9.1.2 Implementation

The migration formula (9.14) can be understood as a nonstationary filter, implemented on each individual k_x trace separately.

For a given k_x component, the input to the migration is a frequency domain seismic trace $U(\omega)$, recorded at the surface $\tau = 0$, and the output is a migrated trace $u(\tau)$ presented in the time domain. Suppressing the dependency on wavenumber k_x , equation (9.14) can be discretized as

$$u_m = \frac{1}{N} \sum_{n=0}^N M_{m,n} U_n, \quad (9.15)$$

where m is the time sample index of the migrated trace and n is the frequency sample index of the input trace.

Equation (9.15) can be represented in a matrix-vector form as

$$\begin{bmatrix} u_0 \\ u_1 \\ \vdots \\ u_M \end{bmatrix} = \frac{1}{N} \begin{bmatrix} M_{0,0} & M_{0,1} & \cdots & M_{0,N} \\ M_{1,0} & M_{1,1} & \cdots & M_{1,N} \\ \vdots & \vdots & \vdots & \vdots \\ M_{M,0} & M_{M,1} & \cdots & M_{M,N} \end{bmatrix} \begin{bmatrix} U_0 \\ U_1 \\ \vdots \\ U_N \end{bmatrix}. \quad (9.16)$$

Considering each row of the matrix as a vector of the migration operator, each output sample u_m is the inner product of the row vector of the migration operator and the data vector in the frequency domain. Such a row vector is time-variant, depending on the migration time τ .

Alternatively, equation (9.16) can be implemented as a matrix multiplication ‘by columns’ as (Margrave, 2001):

$$\begin{bmatrix} u_0 \\ u_1 \\ \vdots \\ u_M \end{bmatrix} = \frac{1}{N} \left\{ \begin{bmatrix} M_{0,0} \\ M_{1,0} \\ \vdots \\ M_{M,0} \end{bmatrix} U_0 + \begin{bmatrix} M_{0,1} \\ M_{1,1} \\ \vdots \\ M_{M,1} \end{bmatrix} U_1 + \cdots + \begin{bmatrix} M_{0,N} \\ M_{1,N} \\ \vdots \\ M_{M,N} \end{bmatrix} U_N \right\}. \quad (9.17)$$

Each column vector of the migration operator can be considered as a migration response which is a function of the earth model and is data-independent. Such a migration response is frequency-dependent and thus can be referred to as the plane-wave migration response. A migration image is constructed by scaled superposition of the plane-wave migration responses.

Each of these plane-wave migration responses is a one-dimensional (1-D) function of time τ with fixed k_x and ω . That is, for a specific k_x trace, stabilized equation (9.12) gives a traveltimes range implicitly, within which a given frequency component may be fully recovered by inverse Q filtering and then migrated to the right time. Beyond such a range, the amount of compensation decreases gradually. When a given high-frequency component is fully attenuated through wave propagation, this method automatically limits the attempt to amplify it and to migrate it. Otherwise, it will boost the ambient noise.

Equation (9.16) is akin to the inverse Q filter formula (4.24). The matrix operator in equation (9.16) depends on the horizontal wavenumber k_x and

needs to be re-calculated for each k_x trace. In equation (4.24), the matrix operator depends on the lateral position x , if Q is spatially variant, and needs to be re-calculated for each x trace. But if Q is spatially invariant, the operator in equation (4.24) can be used for an entire line. The difference between equation (4.24) and equation (9.16) is that the former can work for a 2-D earth model with Q varying horizontally and vertically, but the latter only works for a 1-D earth model with vertically varying velocity and Q functions, as the seismic traces are presented in the k_x domain.

9.1.3 A real data example

We now show a real data example of applying the inverse Q filtered migration algorithm to improve the vertical resolution in a seismic section, to recover a weak reflection of the target gas-layer underneath strong coal-seam reflections.

Figure 9.1a is the sample section of land seismic data (Guo and Wang, 2004). In the study area, reflection seismic surveys are often complicated by high-velocity layers that lie above deeper interfaces of interest. High-velocity hard layers sandwiching softer coal seams form a group of strong reflections that prevents the energy from penetrating to the deeper layers. Thus, deeper reflections are commonly very weak in this area. In addition, seismic data are generally observed to lose high frequencies with increasing traveltime. The loss of high frequencies lengthens the dominant signal wavelength and thereby generally degrades the seismic resolution. In this particular area, the weak reflection of interest, a potential gas-reservoir formation, is so close to the strong reflections that it is completely buried by the lengthened wavelet of strong reflections on top. To recover the target reflection underneath the group of coal seams, we now try the algorithm of migration with inverse Q filtering described above.

Figures 9.1b and 9.1c are the migrated seismic sections without considering the anelastic property of the medium and with inverse Q filtering, respectively. In this case study, the interval Q values, estimated from the stack section (Figure 9.1a), are listed as follows:

Time (s)	0.1–1.0	1.0–1.3	1.3–1.6	1.6–2.0
Q	39.5	48.9	98.9	163.8

From Figure 9.1c, in comparison with Figure 9.1b, we can clearly see the following.

- 1) The vertical resolution has been improved because of higher-frequency bandwidth, typically in the deep portion.
- 2) More coherent events have appeared underneath the group of strong reflections at 1.5 s.
- 3) The target reflection A–A' (at time 1.52–1.56 s), immediately underneath the group of strong reflections, has been recovered. It was destroyed because of the phase distortion of the group of strong reflections, and now stands clearly after a proper phase correction.

In summary, by implementing the migration process and the inverse Q filter simultaneously, the migration image is expected to have true amplitudes and correct timings. We have illustrated this scheme with a real data example in which, because of the enhancement in seismic resolution, the target potential gas-layer underneath a group of strong coal-seam reflections has been successfully recovered.

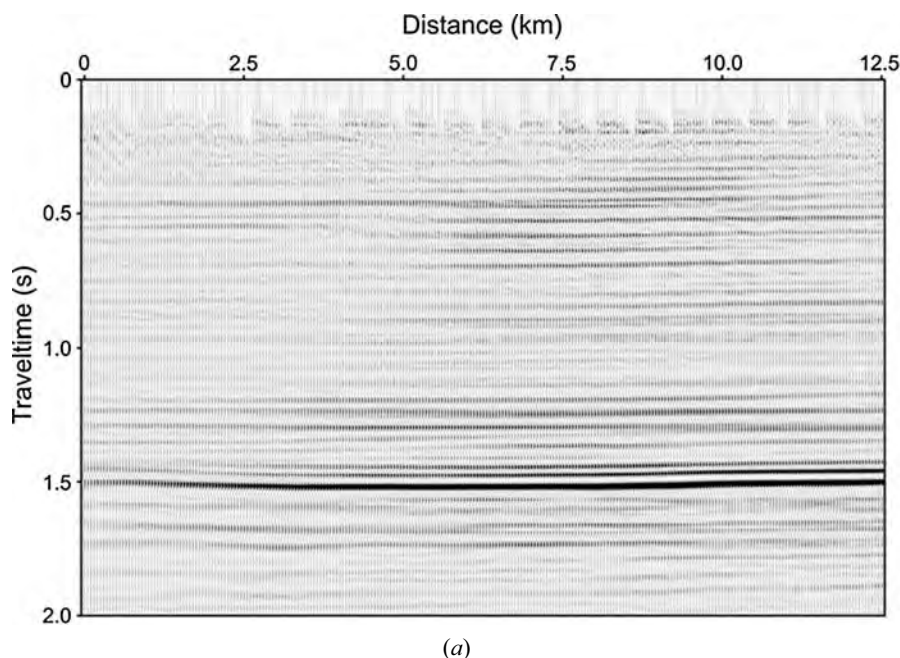


Figure 9.1 (a) Seismic stack section, used for testing the algorithm of migration with inverse Q filtering. The aim is to recover the target reflection (of a potential gas-reservoir formation) immediately underneath the group of strong (coal-seam) reflections.

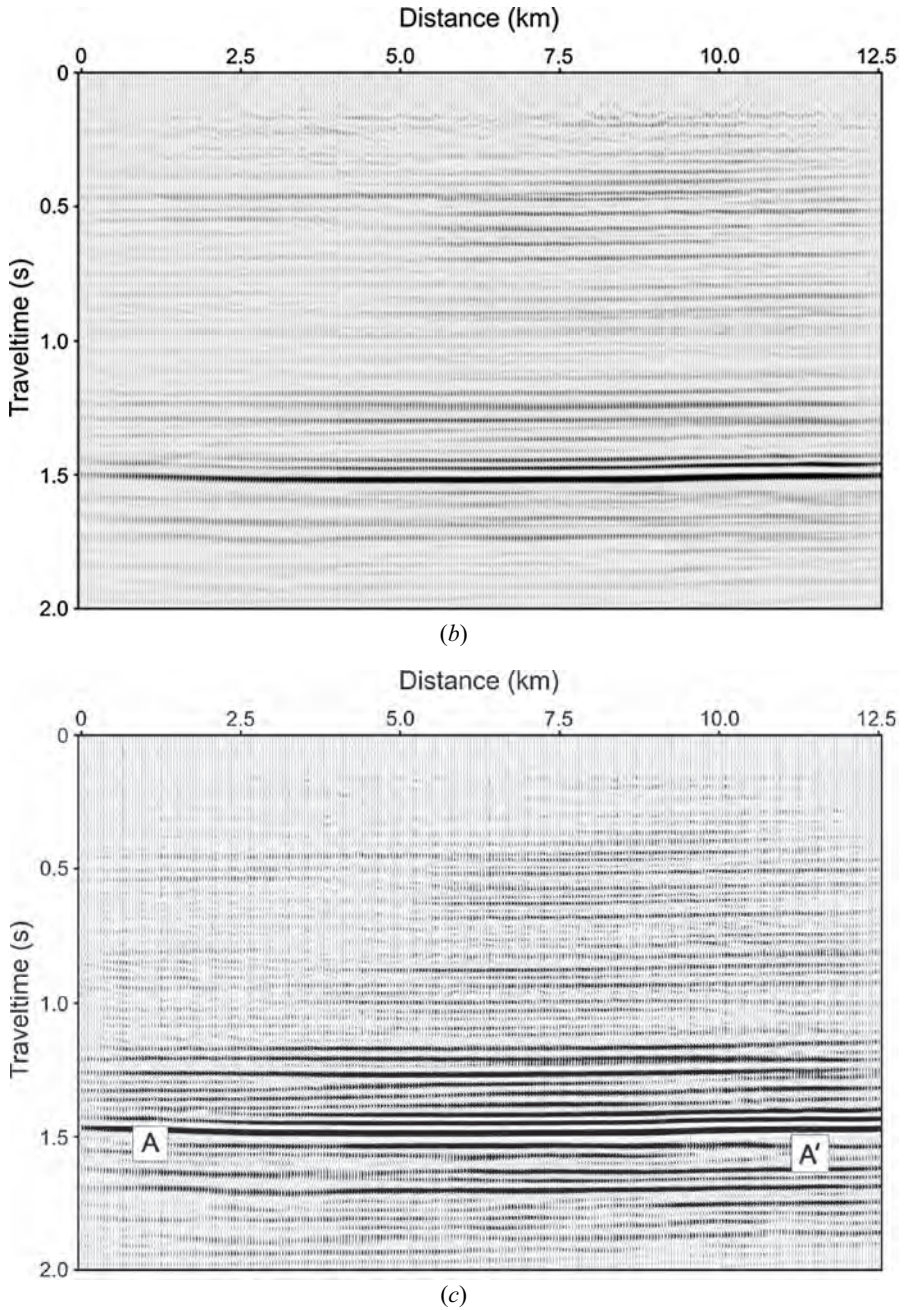


Figure 9.1 (contd) (b) Seismic section after migration, without consideration of the earth attenuation and dispersion properties. (c) Seismic section after migration with inverse Q filtering, which has enhanced the vertical resolution and recovered the target reflection A–A' (at time 1.52–1.56 s) underneath coal-seam reflections.

9.2 Stabilized migration with lateral variation in velocity and Q models

For cases with lateral variations in velocity and Q functions, the challenge is how to create a stabilized migration operator for each extrapolation step. In the previous sections, we have demonstrated the concept of migration with inverse Q filtering, and presented a stabilized algorithm that is applicable to subsurface models with vertical velocity variation and vertical Q variation. From this demonstration and stabilized inverse Q filters in the previous chapters, we may draw the following three conclusions for the stabilization.

- 1) In order to stabilize the problem, one needs to evaluate the effect accumulated from the recording surface down to the current depth, not just the effect within the current extrapolation step.
- 2) The stabilization for each frequency ω is data-independent, and only depends upon the velocity and Q models. Therefore, one can implement the stabilization treatment separately from any typical migration scheme for the wavefield extrapolation.
- 3) For the stabilization, we consider only the amplitude operator in the extrapolation operator, and keep the phase operator unaffected, as the phase operator is unconditionally stable.

To derive the stabilized extrapolation operator for migration with lateral variations in velocity and Q functions, we use a 1-D equation, variable only in the z -direction, as follows:

$$\frac{\partial U(z, \omega)}{\partial z} = i \frac{\omega}{\bar{c}} U(z, \omega). \quad (9.18)$$

Its phase shift solution is (Gazdag, 1978),

$$U(z + \Delta z, \omega) = U(z, \omega) \exp \left[i \frac{\omega}{\bar{c}} \Delta z \right]. \quad (9.19)$$

The wave equation for migration can be divided into a series of extrapolation equations, applied to the seismic data successively. Among this series of equations, the 1-D wave equation (9.18) is a key equation that also gives the maximum value of amplitude compensation, as shown in the

next section, in the $x - \omega$ domain finite-difference migration method. If we can stabilize its solution (9.19), that is, stabilize the calculation of the frequency-dependent complex-valued wavenumber $k \equiv \omega / \bar{c}$, we also can stabilize the other extrapolation equations in the series.

The complex velocity \bar{c} is defined by (9.5), to take into account the earth attenuation effect. The extrapolation operator accumulated from the recording surface down to the current extrapolation step n is

$$\begin{aligned} \exp \left[i \sum_{\ell=1}^n \frac{\omega}{\bar{c}(z^{(\ell)}, \omega)} \Delta z \right] &\approx \exp \left[\sum_{\ell=1}^n \frac{\omega}{2 \bar{v}(z^{(\ell)}) Q(z^{(\ell)})} \Delta z \right] \\ &\times \exp \left[i \sum_{\ell=1}^n \frac{\omega}{\bar{v}(z^{(\ell)})} \left(\frac{\omega}{\omega_h} \right)^{-\gamma} \Delta z \right], \quad (9.20) \end{aligned}$$

where $\bar{v}(z^{(\ell)}) \equiv \bar{v}(\ell \Delta z)$ and $Q(z^{(\ell)}) \equiv Q(\ell \Delta z)$ are the migration velocity and Q values at the ℓ th layer. The first exponential factor on the right-hand side is the amplitude operator, in which the approximation

$$\frac{1}{2Q} \left(\frac{\omega}{\omega_h} \right)^{-\gamma} \approx \frac{1}{2Q}, \quad (9.21)$$

is made because $(\omega / \omega_h)^{-\gamma} \rightarrow 1 \ll 2Q$, when $\gamma \equiv (\pi Q)^{-1} \rightarrow 0$.

The second exponential factor in equation (9.20) is the phase operator, in which the factor $(\omega / \omega_h)^{-\gamma}$ with a minor discrepancy from the unity modifies the real wavenumber ω / \bar{v} to correct the phase distortion. For stabilization, according to the investigation in the previous chapters for inverse- Q filtering, we consider only the amplitude operator in the extrapolation operator because the phase operator is unconditionally stable.

To stabilize the extrapolation, we define an amplitude-attenuation operator as

$$W(n, \omega) = \exp \left[- \sum_{\ell=1}^n \frac{\omega}{2 \bar{v}(z^{(\ell)}) Q(z^{(\ell)})} \Delta z \right], \quad (9.22)$$

and calculate a stabilized amplitude-compensation operator by

$$W^{-1}(n, \omega) = \frac{W(n, \omega) + \sigma^2}{W^2(n, \omega) + \sigma^2}. \quad (9.23)$$

We now define a stabilized attenuation coefficient $\alpha_{\text{st}}(z^{(\ell)}, \omega)$ as

$$\exp \left[\sum_{\ell=1}^n \alpha_{\text{st}}(z^{(\ell)}, \omega) \Delta z \right] = W^{-1}(n, \omega). \quad (9.24)$$

This coefficient is a supersedent to the actual attenuation coefficient and will be used for the amplitude compensation within the ℓ th step extrapolation. For the first layer, $\ell = 1$, the stabilized attenuation coefficient is

$$\alpha_{\text{st}}(z^{(1)}, \omega) = \frac{\omega}{2 \bar{v}(z^{(1)}) Q(z^{(1)})}. \quad (9.25)$$

For the current n th layer, it is given by

$$\alpha_{\text{st}}(z^{(n)}, \omega) = \frac{1}{\Delta z} \ln [W^{-1}(n, \omega)] - \sum_{\ell=0}^{n-1} \alpha_{\text{st}}(z^{(\ell)}, \omega). \quad (9.26)$$

Note that we generate an operator for the current layer by constructing an operator from the surface to the current layer and subtracting the previous steps. Therefore, as stated in the previous subsection, the operator depends on the full subsurface above the current layer.

Stabilizing the extrapolation operator means generating a stabilized complex wavenumber ω/\bar{c} . Given the stabilized attenuation coefficients above, the complex wavenumber in equations (9.18) and (9.19) is stabilized also as

$$\frac{\omega}{\bar{c}(z^{(n)}, \omega)} = \frac{\omega}{\bar{v}(z^{(n)})} \left(\frac{\omega}{\omega_h} \right)^{-\gamma} - i \alpha_{\text{st}}(z^{(n)}, \omega). \quad (9.27)$$

For wavefield extrapolation at depth $z^{(n)}$ with lateral variations in velocity and Q functions, we first construct the frequency-dependent, stabilized attenuation function $\alpha_{\text{st}}(z^{(n)}, \omega)$ separately at each x -position,

because one often assumes that the migration model has smooth lateral variations in velocity and Q functions. Once this laterally variant, 2-D slice in the $x - \omega$ space is built, we can build a stabilized extrapolation operator at depth $z^{(n)}$ in the space-frequency domain.

9.3 The implicit finite-difference extrapolator in the space-frequency domain

Using the stabilization scheme presented in the previous section, we find in this section an example of a stabilized finite-difference migration method. The derivation closely follows Gazdag and Sguazzero (1984) by replacing a real velocity with the frequency-dependent, complex-valued velocity \bar{c} .

The square root of the Helmholtz operator for the viscoacoustic wave equation, or the vertical wavenumber, may be approximated to the second order by a continued fraction as

$$k_z = \sqrt{\frac{\omega^2}{\bar{c}^2} - k_x^2} \approx \frac{\omega}{\bar{c}} \sqrt{1 - \frac{k_x^2}{|k|^2}} \approx \frac{\omega}{\bar{c}} \left(1 - \frac{s_2 \frac{k_x^2}{|k|^2}}{1 - s_1 \frac{k_x^2}{|k|^2}} \right), \quad (9.28)$$

where $\bar{c} \equiv \bar{c}(x, z, \omega)$ in this case, and

$$|k|^2 = \left(\frac{\omega}{\bar{c}} \right)^* \left(\frac{\omega}{\bar{c}} \right), \quad (9.29)$$

for stabilization. In the nonlinear approximation (9.28), s_1 and s_2 are constants that have been chosen to maximize the accuracy of the approximation. For example, the approximation with $s_1 = 0.37637$ and $s_2 = 0.47824$ is accurate for $\theta \equiv \sin^{-1}(k_x / |k|)$ less than about 65° (Lee and Suh, 1985; Halpern and Trefethen, 1988). The one-way wave equation (9.1) becomes

$$\frac{\partial U(k_x, z, \omega)}{\partial z} = i \frac{\omega}{\bar{c}} \left(1 - \frac{s_2 \frac{k_x^2}{|k|^2}}{1 - s_1 \frac{k_x^2}{|k|^2}} \right) U(k_x, z, \omega). \quad (9.30)$$

This extrapolation equation is solved by splitting it into two extrapolations (Gazdag and Sguazzero, 1984):

$$\frac{\partial U(k_x, z, \omega)}{\partial z} = i \frac{\omega}{\bar{c}} U(k_x, z, \omega) \quad (9.31)$$

and

$$\frac{\partial U(k_x, z, \omega)}{\partial z} = i \frac{\omega}{\bar{c}} \left(\frac{-s_2 \frac{k_x^2}{|k|^2}}{1 - s_1 \frac{k_x^2}{|k|^2}} \right) U(k_x, z, \omega). \quad (9.32)$$

These two extrapolations may be applied alternately in small Δz steps.

Extrapolation equation (9.31) can be presented in the $x - \omega$ domain as equation (9.18) with a phase-shift solution (9.19). From this is derived stabilization formula (9.27) for ω/\bar{c} in the previous section. Once we calculate the stabilized wavenumber ω/\bar{c} , we apply it to both migration steps (9.31) and (9.32). Comparing equations (9.31) and (9.32), we see that they differ in a factor that has an absolute magnitude less than one. Thus, stabilization formula (9.27) stabilizes both extrapolation equation (9.31) and (9.32).

To express equation (9.32) in the (x, ω) domain, we multiply it by the denominator of its right-hand side, and then apply an inverse Fourier transformation with respect to k_x to both sides. The result is

$$\left(1 + \frac{s_1}{|k|^2} \frac{\partial^2}{\partial x^2} \right) \frac{\partial}{\partial z} U(x, z, \omega) = i \frac{\omega}{\bar{c}} \frac{s_2}{|k|^2} \frac{\partial^2}{\partial x^2} U(x, z, \omega). \quad (9.33)$$

This is solved numerically by a finite-difference scheme. If Δx is the grid spacing and Δz is the extrapolation step, the wavefield at grid point (m, n) is denoted by $U_m^{(n)} = U(m\Delta x, n\Delta z, \omega)$, then equation (9.33) is discretized by using the following approximations:

$$U_m^{(n+1/2)} \approx \frac{1}{2} (U_m^{(n+1)} + U_m^{(n)}), \quad (9.34)$$

$$\frac{\partial}{\partial z} U_m^{(n+1/2)} \approx \frac{1}{\Delta z} (U_m^{(n+1)} - U_m^{(n)}) \quad (9.35)$$

and

$$\frac{\partial^2}{\partial x^2} \approx \frac{\delta_{xx}}{1 + \eta \Delta x^2 \delta_{xx}}, \quad (9.36)$$

where $\delta_{xx} = (1, -2, 1)/\Delta x^2$ is the second-order finite-difference operator, and η is an adjustable constant included to increase the accuracy of the second-order spatial derivative. Following Claerbout (1985), we set the value $\eta = (1/4) - (1/\pi^2) \approx 0.15$, instead of $\eta = 1/12$ in the Taylor expansion, to restore accuracy artificially at the higher wavenumbers up to the Nyquist component at the cost of diminished accuracy for the lower wavenumbers. The finite-difference formula of equation (9.33) is

$$\begin{aligned} U_m^{(n+1)} + (a - i b)(U_{m-1}^{(n+1)} - 2U_m^{(n+1)} + U_{m+1}^{(n+1)}) \\ = U_m^{(n)} + (a + i b)(U_{m-1}^{(n)} - 2U_m^{(n)} + U_{m+1}^{(n)}), \end{aligned} \quad (9.37)$$

where

$$a = \frac{s_1}{|k|^2 \Delta x^2} + \eta \quad \text{and} \quad b = \left(\frac{\omega}{\bar{c}} \right) \frac{s_2 \Delta z}{2 |k|^2 \Delta x^2}, \quad (9.38)$$

with ω/\bar{c} evaluated by the stabilized formula (9.27).

Equation (9.37), for all values of m , represents a system of linear equations. This system of equations is solved for each ω value; then an image at $z + \Delta z$ is formed by applying the imaging condition:

$$U(x, z + \Delta z, t = 0) = \sum_{\omega} U(x, z + \Delta z, \omega). \quad (9.39)$$

In general, we always can extract a 1-D wave equation from a high-dimensional wave equation, no matter whether we actually implement the migration in a sequence consisting of a 1-D wave-equation-based phase-shift-type step, and always can construct the supersedent of attenuation coefficients in advance. Therefore, the proposed strategy presented in these two sections is a general solution to stabilize a wave-equation-based, inverse Q filtered migration.

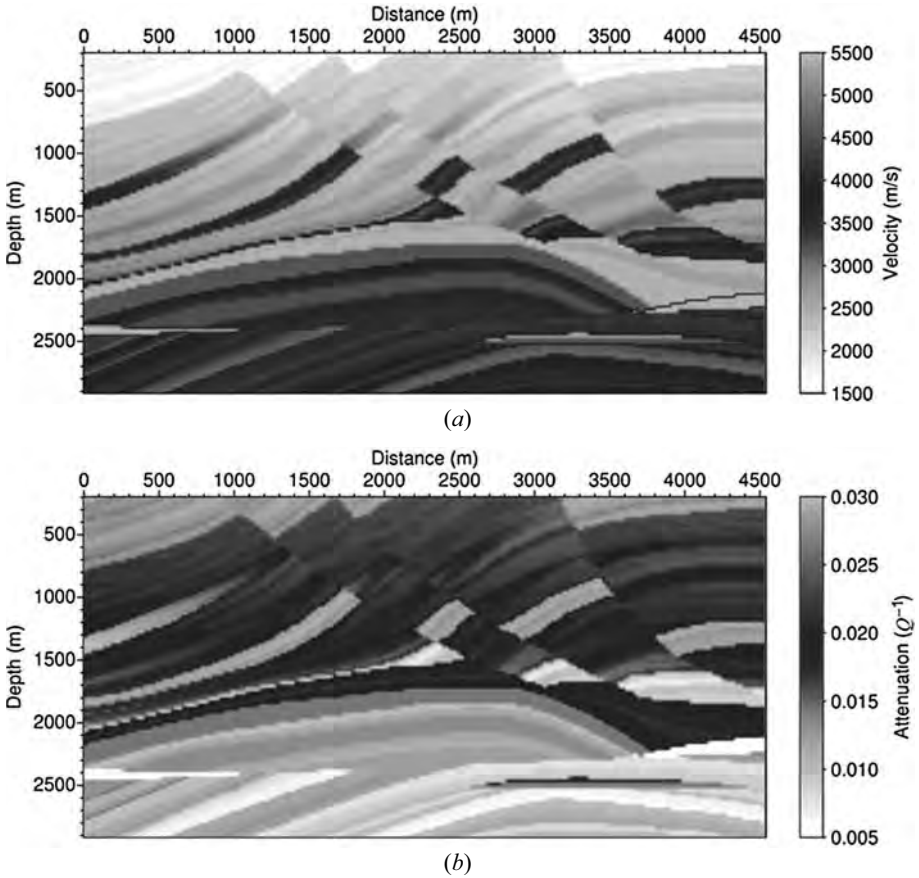
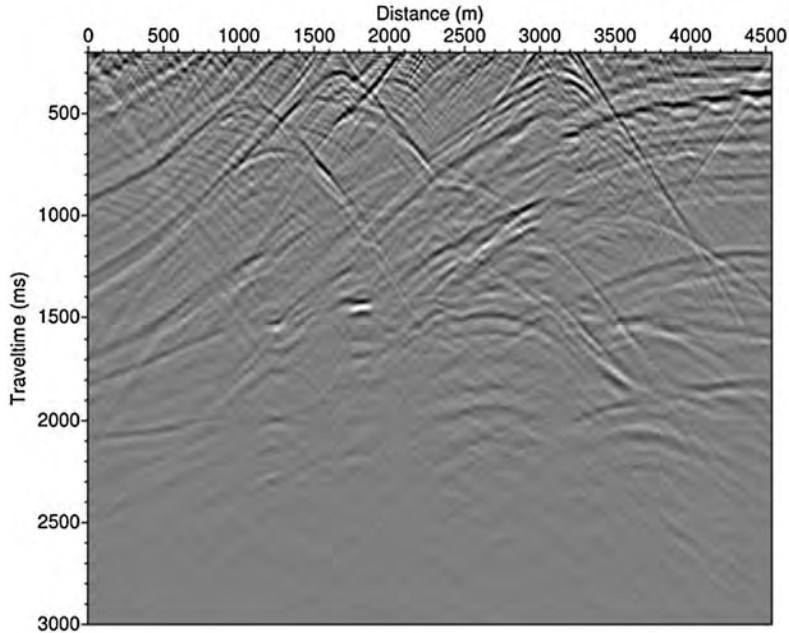


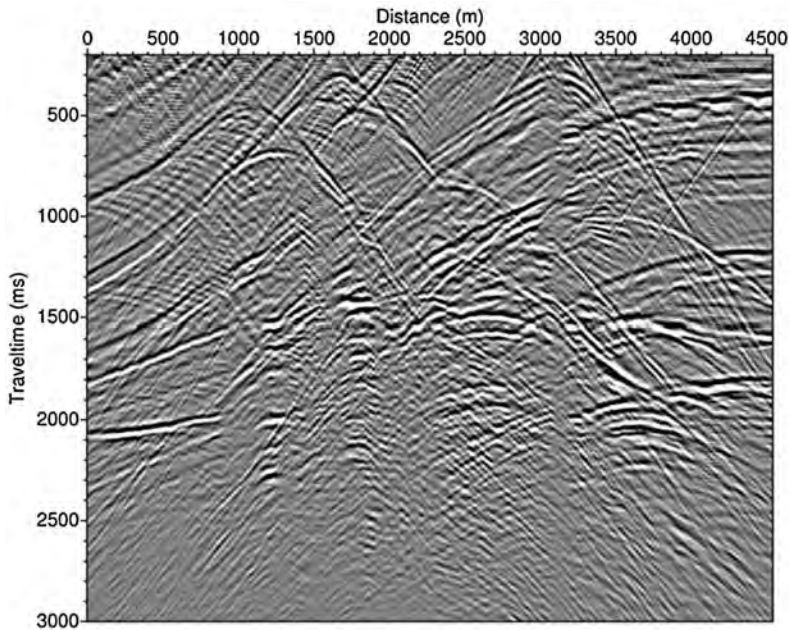
Figure 9.2 A velocity model (a) and associated attenuation model (b) for synthetic seismic modelling.

9.4 Migration examples

Figure 9.2 shows the Marmousi velocity model, and the corresponding attenuation (Q^{-1}) model we designed. Figure 9.3 displays two zero-offset sections of synthetic seismic data, where Figure 9.3a is generated by using a finite-difference viscoacoustic wave-equation method, based on the velocity and attenuation models in Figure 9.2, and Figure 9.3b is generated by using the wave equation without attenuation. The finite-difference modelling used here is a frequency-domain implementation that incorporates the effects of attenuation through the complex velocity definition (Pratt, 1990).



(a)



(b)

Figure 9.3 (a) Synthetic seismic profile generated based on the velocity and Q models shown in Figure 9.2. (b) Synthetic seismic profile generated based on the velocity model in Figure 9.2a, but without considering the attenuation effect.

Comparing these two synthetic seismic sections, we can see the amplitude absorption and phase distortion in the section including the earth attenuation effect. We now use these synthetic seismic sections to demonstrate the effectiveness of the proposed inverse Q filtered migration algorithm.

Figures 9.4a and 9.4b compare the two migration results of the synthetic data set shown in Figure 9.3a, where Figure 9.4a uses a conventional migration without inverse Q filtering and Figure 9.4b uses the proposed migration with inverse Q filtering algorithm. The inverse Q filtered migration result in Figure 9.4b shows that the amplitudes of reflections been strengthened and the resolution has been enhanced. Mittet *et al.* (1995) demonstrated that even when migrating with a Q model deviating by 10% from the correct one, the images still would be better focused and of higher quality than when no compensation was performed.

To verify the result of proposed inverse Q filtered migration further, a conventional migration without the Q compensation (Figure 9.4c) is performed on the synthetic data set without the earth attenuation effect (Figure 9.3b). When we take into account the attenuation effect in the migration of a realistic synthetic data set, we produce the image (Figure 9.4b) comparable with an ideal image as if there were no attenuation effect at all (Figure 9.4c). All the migration results in Figure 9.4 are plotted to the same scale.

Figure 9.5 compares migrated seismic traces, selected arbitrarily at distance 750 m, from the three migration results shown in Figure 9.4. The top trace (corresponding to Figure 9.4a) is the conventional migration result without inverse Q filtering. The middle trace, with the boosted amplitude of later wavelets, is the result of inverse Q filtered migration (Figure 9.4b), and is very close to the ideal situation of pure acoustic media (Figure 9.4c).

In comparison with the top trace without inverse Q filtering, the inverse Q filtered migration has moved wavelets in the middle trace leftwards, and has made them match the interface depth in the true model (the bottom trace). For example, the weak peak at 2500 m has been shifted to 2475 m and now matches the ideal trace. The amplitude of this wavelet at 2475 m is not as high as the ideal wavelet because the stabilization scheme automatically limits the compensation when a high-frequency component is attenuated completely from the original data. In this way, the stabilization scheme avoids boosting the ambient noise.

Figure 9.5b compares the amplitude spectra of three migration results. The dashed line represents the amplitude spectrum of migration without inverse Q filtering (Figure 9.4a). The solid line shows the amplitude

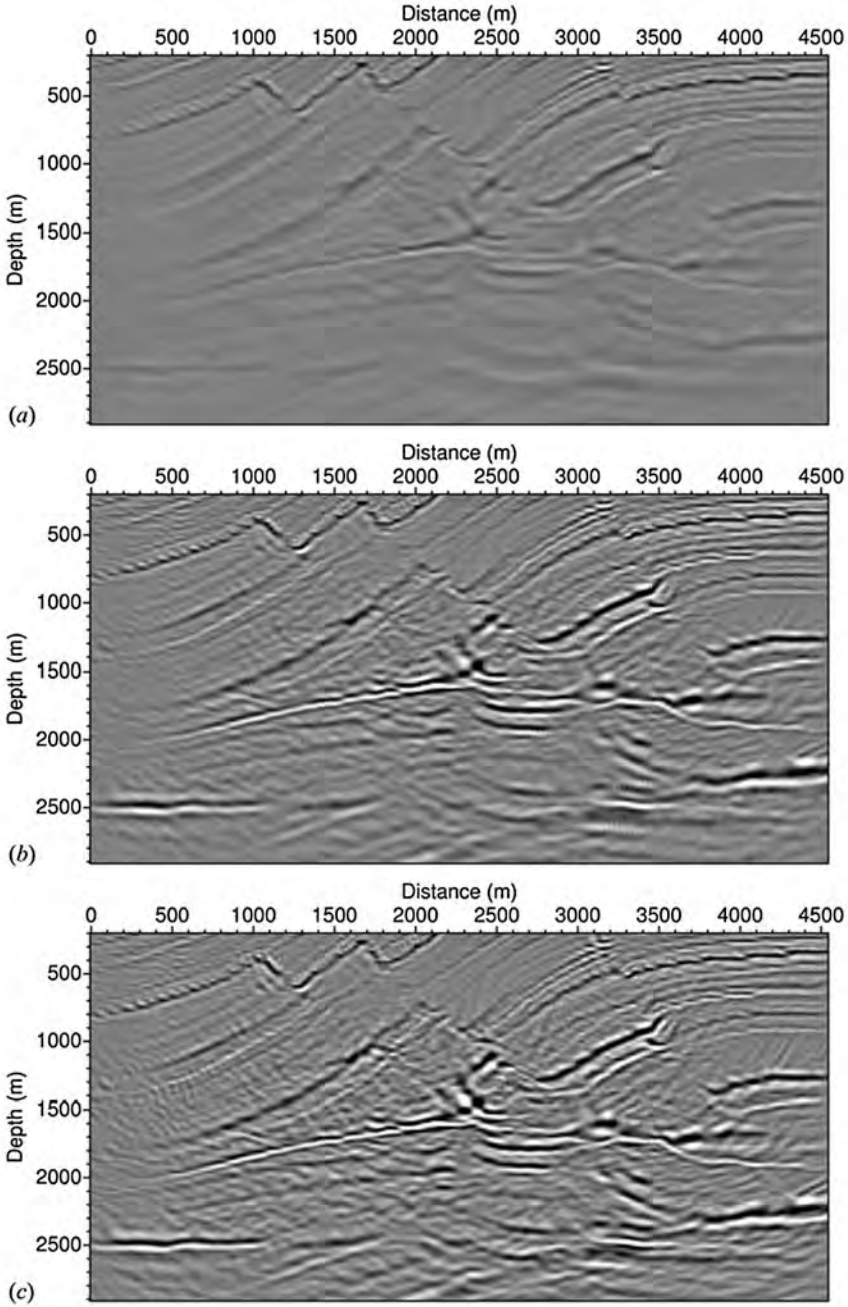


Figure 9.4 (a) Migration result of Figure 9.3a, using conventional migration without the inverse Q filter. (b) Migration result of Figure 9.3a, using the proposed inverse Q filtered migration method. (c) Migration result of Figure 9.3b; in this case both the synthetic data and the migration do not consider the earth attenuation effect.

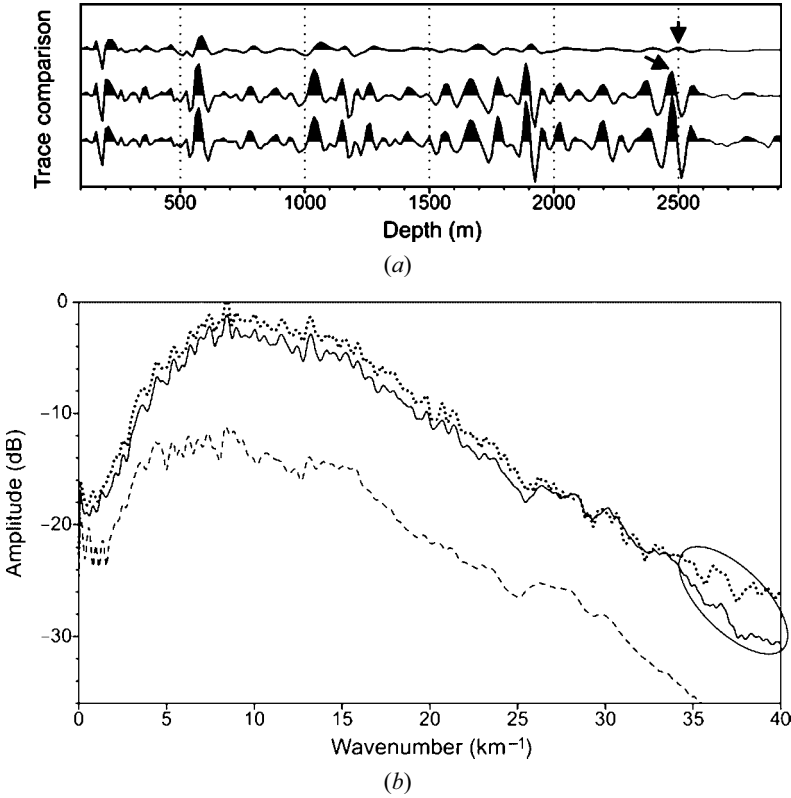


Figure 9.5 (a) Comparison of migrated seismic traces, selected arbitrarily at distance 750 m from the three migration results shown in Figure 9.4. The three traces from the top to bottom correspond to Figures 9.4a–c, respectively. (b) Comparison of spectra. The dashed line is the amplitude spectrum of Figure 9.4a, the solid line is the amplitude spectrum of Figure 9.4b and the dotted line is the amplitude spectrum of Figure 9.4c. The solid and dotted lines are close to each other, and the discrepancy at high wavenumber ($35\text{--}40 \text{ km}^{-1}$) can be attributed to the stabilization.

spectrum of inverse Q filtered migration (Figure 9.4b), and is close to the dotted line, the amplitude spectrum of Figure 9.4c. The discrepancy between the solid and dotted lines at high wavenumbers ($35\text{--}40 \text{ km}^{-1}$) can be attributed to the stabilization. Each of these three curves is an averaged spectrum, averaging the amplitude spectra of individual traces over the whole seismic section.

For real data applications, a reliable Q model with lateral variation is needed. In the following chapters, we will discuss Q analysis methods using either borehole or surface seismic data.

Part III

Q estimation

Chapter 10

Q estimation from vertical seismic profiling data

Abstract

For model-based inverse Q filtering, a reliable earth Q model is needed. This can be estimated from the spectral ratio of downgoing wavelets of vertical seismic profiling (VSP) data. To calculate the spectral ratio and the logarithm of this ratio, it is necessary to have a smooth spectral estimate for each individual waveform, because any notch in the amplitude spectrum would cause problems in the spectral division and in the logarithmic calculation. A multiple tapering technique is used to calculate the smooth spectral estimate. The tapers are mutually orthogonal, and each taper is used to generate an orthogonal sample of the original waveform. The average of the Fourier transform spectra of windowed waveforms with different tapers produces the smooth, high-resolution spectrum we need for Q estimation.

To apply an inverse Q filter to seismic data, a reliable estimate of the earth Q function is prerequisite. It has been widely accepted that in-situ borehole experiments are best suited for such a reliable Q estimation (Raikes and White, 1984; Stainsby and Worthington, 1985; Tonn, 1991; Pujol *et al.*, 1998). Dasgupta and Clark (1998) described a method for determining Q directly from surface seismic reflection data. Clark *et al.* (2001) further found that the method worked well in ‘comparative’ circumstances (e.g. time-lapse). But most of the time, surface seismic data cannot provide reliable Q values due to contamination of the seismic signal by various factors related to data acquisition, such as use of an inadequate source

spectrum, offset-dependent tuning of reflections, and poor signal-to-noise (S/N) ratio due to multiples and mode conversions. The accuracy of the Q value estimated from downhole seismic is generally higher than that from surface reflection seismic (White, 1992). One method of downhole seismic measurement is to position a source at the surface and spread a series of receivers vertically down the borehole. The seismic record is called vertical seismic profiling, or VSP. In this chapter we shall estimate Q values from the direct downgoing wavefield of VSP data.

We shall estimate the Q values using the spectral ratio method. Theoretically, the spectral ratio method will work well with the VSP downgoing wavefield, provided that the following conditions are satisfied: a constant-source waveform between upper and lower levels; no interference from reflected waves; the same receiver coupling at upper and lower levels; no variation in stratigraphic filtering between upper and lower levels; and negligible noise in the waveform. In practice, however, the spectral ratios can vary wildly, and the direct application of the spectral ratio technique to VSP data can be problematic. The VSP data quality in this study is even lower than an average level, because of poor receiver coupling within some depth ranges. This is obviously a challenge to Q estimation in terms of the robustness of the method.

10.1 The attenuation effect on VSP waveform

In practice, seismic data are always subject to the frequency-dependent attenuation effect. In seismic waveform modelling, the attenuation effect can easily be included in a frequency-domain finite-difference modelling method, by simply replacing the real-valued velocity with a complex-valued velocity. The complex-valued velocity can be expressed as

$$c(x) = c_{\text{Re}}(x) + i c_{\text{Im}}(x), \quad (10.1)$$

where $c_{\text{Re}}(x)$ and $c_{\text{Im}}(x)$ are respectively the real and the imaginary parts of the complex velocity $c(x)$, and x is the spatial position. The corresponding wavenumber is also complex-valued:

$$k = k_{\text{Re}} + i k_{\text{Im}} = \frac{\omega}{c_{\text{Re}} + i c_{\text{Im}}} = \frac{\omega c_{\text{Re}}}{c_{\text{Re}}^2 + c_{\text{Im}}^2} - i \frac{\omega c_{\text{Im}}}{c_{\text{Re}}^2 + c_{\text{Im}}^2}. \quad (10.2)$$

Then the frequency component of a plane wave at distance x is expressed

as

$$\exp(i k x) = \exp\left(\frac{\omega c_{\text{Im}} x}{c_{\text{Re}}^2 + c_{\text{Im}}^2}\right) \exp\left(i \frac{\omega c_{\text{Re}} x}{c_{\text{Re}}^2 + c_{\text{Im}}^2}\right), \quad (10.3)$$

where the second exponential term in the right-hand side represents the attenuation along distance x . In Chapter 3, we expressed the wave propagation in equation (3.9) as

$$U(x, \omega) = U_0(\omega) \exp[-\alpha(\omega)x] \exp\left[i\omega\left(t - \frac{x}{v(\omega)}\right)\right], \quad (10.4)$$

where $U_0(\omega)$ is the initial amplitude of the plane wave ω , and $U(x, \omega)$ is the amplitude at distance x .

Following equations (10.3) and (10.4), we can obtain the attenuation coefficient as

$$\alpha(\omega) = -\frac{\omega c_{\text{Im}}}{c_{\text{Re}}^2 + c_{\text{Im}}^2}, \quad (10.5)$$

expressed in terms of complex-valued velocity. Recall that the relationship between the quality factor Q and the attenuation coefficient is described as

$$Q(\omega) = \frac{1}{2} \left(\frac{\omega}{\alpha(\omega)v(\omega)} - \frac{\alpha(\omega)v(\omega)}{\omega} \right), \quad (10.6)$$

where $v = c_{\text{Re}}$, and only positive frequency is considered here. Then the Q value can be recovered from the complex velocity by

$$Q = -\frac{1}{2} \left[\frac{c_{\text{Re}}}{c_{\text{Im}}} + \frac{c_{\text{Im}}}{c_{\text{Re}}} \left(1 - \frac{1}{1 + c_{\text{Im}}^2 / c_{\text{Re}}^2} \right) \right] \approx -\frac{c_{\text{Re}}}{2 c_{\text{Im}}}. \quad (10.7)$$

A frequency-domain finite difference method may be used to model the waveform with or without the attenuation effect. Figure 10.1a shows a velocity model, and Figure 10.1b is the corresponding Q model. Given the real velocity c_{Re} and the Q value, the imaginary part of the complex velocity is calculated by $c_{\text{Im}} = -c_{\text{Re}}/(2Q)$. For VSP modelling, a line of

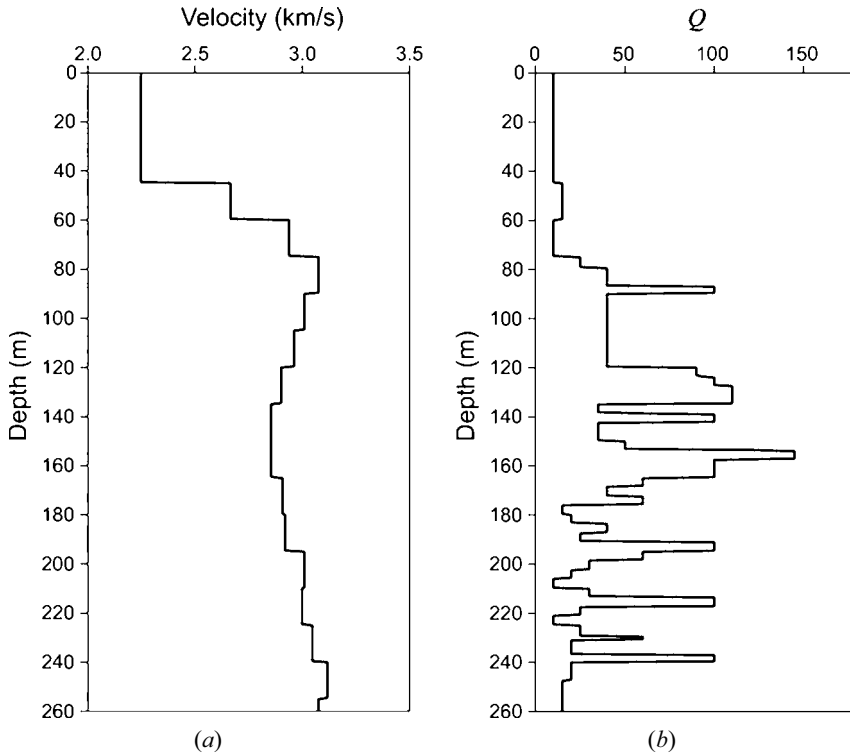


Figure 10.1 A velocity model (a) and the inverse Q model (b) for synthetic VSP modelling.

receivers is placed at $x = 50$ m, spreading in the z direction from 0 to 255 m. A point source is placed at $(0, 0)$; this gives a VSP offset of 50 m, the horizontal distance between the source point and the borehole position. For the seismic simulation, the model cell size is 0.5 m, and the time sample interval used is 0.5 ms. The source function is a first derivative of the Gauss function with a dominant frequency of 250 Hz.

Figure 10.2a shows the synthetic VSP data, generated using the velocity and the Q model shown in Figure 10.1. For comparison, Figure 10.2b displays a synthetic VSP profile without considering the attenuation effect, i.e. real-valued velocity values are used in the wave equation. Because of the attenuation effect, the amplitude of the VSP waveform is much weaker.

Figure 10.3 compares two traces at depth 140 m, selected from the two VSP gathers in Figure 10.2. These two traces at the same depth have the same geometrical spreading effect. The comparison shows clearly that the attenuation has a strong effect on the VSP waveform, both on the amplitude

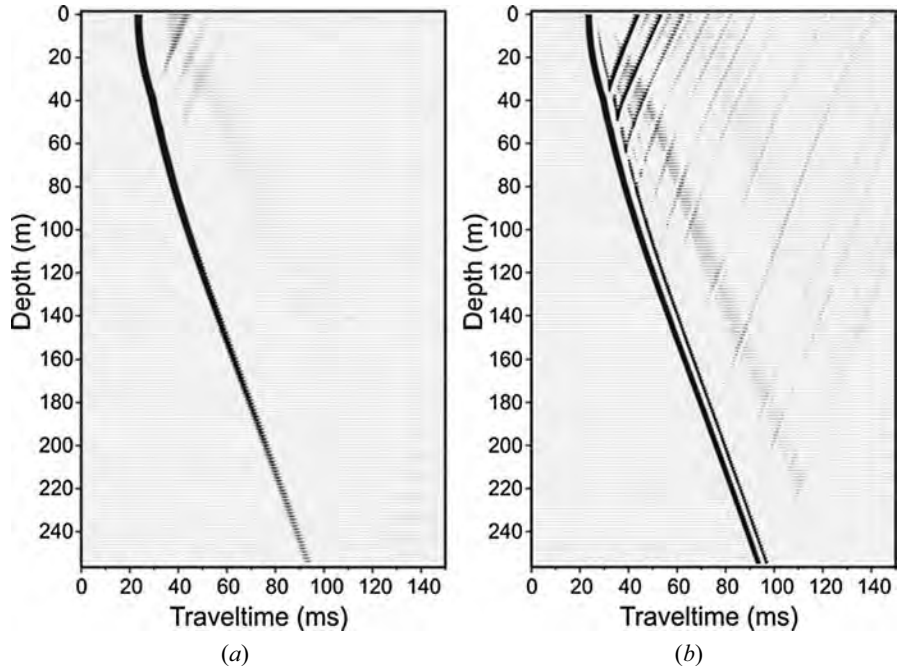


Figure 10.2 (a) Vertical seismic profiling with the attenuation effect. (b) Vertical seismic profiling without the attenuation effect.

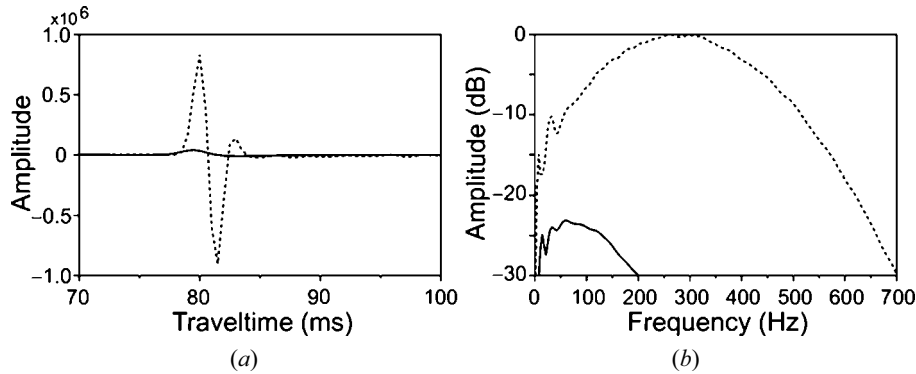


Figure 10.3 Comparison between seismic traces (a) and their spectra (b). The solid curves are the waveform and spectrum with the attenuation effect, and the dotted lines are that without the attenuation effect.

and on the frequency spectrum. Note that even if using different mathematical definitions for the attenuation in the zero-offset VSP modelling, the synthetic VSP data can be quite similar and have the same normalized misfit to real VSP data (Toverud and Ursin, 2005).

In the above example, we use a frequency-domain finite-difference method (Pratt, 1990; Song and Williamson, 1995; Štekl and Pratt, 1998). For zero-offset VSP modelling, communication theory-based method can be a good alternative to produce normal incidence, plane-wave seismograms (Treitel and Robinson, 1966). For example, Ganley (1981) considered the linear absorption, and Aminzadeh and Mendel (1983) considered the Gaussian and exponential absorption operators, in the forward modelling of one-dimensional theoretical seismograms to demonstrate the effect of attenuation in seismic data. The formulae for the reflection and transmission coefficients are the same as in the elastic case except that the phase velocity is replaced with the complex velocity. Note that the reflection and transmission coefficients are also complex functions of frequency.

10.2 Spectral ratio method for Q estimation

Figure 10.4 displays a real VSP data example, recorded at a depth range of 300–1790 m with an irregular depth interval. For the Q estimation, we use the downgoing wavefield of the VSP data because it is contaminated the least by other waves and has a relatively high S/N ratio.

Considering only amplitude attenuation in equation (10.4), we have an expression as follows (Aki and Richards, 1980):

$$A(\omega) = A_0(\omega) \exp[-\alpha(\omega)x] = A_0(\omega) \exp\left[-\frac{\omega(t-t_0)}{2Q}\right], \quad (10.8)$$

where $A(\omega)$ is the amplitude spectrum of the trace at receiver depth z , and $A_0(\omega)$ at a shallower depth z_0 . The amplitude $A(\omega)$ is decayed exponentially from a reference amplitude $A_0(\omega)$. The decay is measured using the spectral ratio method:

$$\ln\left[\frac{A(\omega)}{A_0(\omega)}\right] = -\frac{\omega(t-t_0)}{2Q}, \quad (10.9)$$

where t and t_0 are the P -wave direct arrival times at depth levels z and z_0 ,

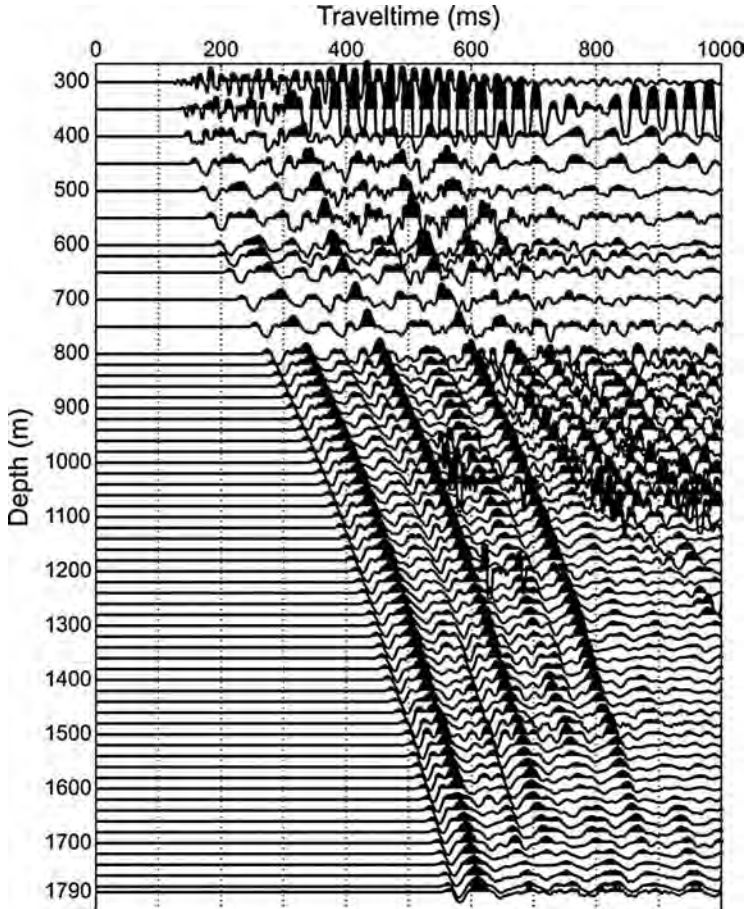


Figure 10.4 A vertical seismic profile recorded at a depth range of 300–1790 m with an irregular depth interval.

respectively. Measuring the slope of the spectral ratio

$$k = \frac{1}{\omega} \ln \left[\frac{A(\omega)}{A_0(\omega)} \right], \quad (10.10)$$

and the time delay

$$\tau = t - t_0, \quad (10.11)$$

the Q value between z_0 and z is then estimated as

$$Q^{-1}[z_0, z] = -\frac{2k}{\tau}. \quad (10.12)$$

In the following sections, we attempt to improve the Q estimation by means of a smooth high-resolution calculation of the spectra, an accurate determination of the time delay, and finally a robust estimation of Q values.

10.3 The multitaper technique for spectral estimation

To calculate the spectral ratio and its logarithm in equation (10.10), it is necessary to have a smoothed spectral estimate for each individual waveform, because any notch in the amplitude spectrum would cause problems in the spectral division and in the logarithm computation. A multitaper technique can be used to calculate a smooth, high-resolution spectral estimate (Thomson, 1982; Park *et al.*, 1987; Neep, 1995; Riedel and Sidorenko, 1995; Neep *et al.*, 1996; Wang, 2003a; Gubbins, 2004). It applies a set of orthogonal tapering windows to the data series, before Fourier transforming. An unbiased spectrum can be produced by averaging these windowed Fourier transform spectra, because each of these tapering windows is uncorrelated. For the sake of completeness, I summarize here the derivation of the multiple tapers, devised originally by Thomson (1982).

In the Fourier transform, spectral leakage occurs when a harmonic signal is recorded for a finite length of time and energy spreads to neighbouring frequencies. The original time sequence, a VSP downgoing wavelet for example, may be viewed as an infinite sequence multiplied by a boxcar taper with vertical cut-offs. Such a simple cut-off spreads the energy into side lobes of the Fourier transform of the boxcar function. This is the spectral leakage. The problem can be alleviated by tapering the data, multiplying the original time sequence by a function of time that decreases to zero at both ends. Tapers with smoother cut-offs, such as the cosine or Gaussian tapers, have smaller or no side lobes and therefore less spectral leakage. However, a conventional tapering procedure leads to loss of information as it effectively throws away perfectly good data at the ends of the sequence by multiplying it by less than unity. The multiple tapering technique, described below, can largely eliminate the loss of data problem.

A time series, u_k , can be represented by the inverse discrete Fourier transform

$$u_k = \sum_n a_n \exp \left[\frac{i 2 \pi n k}{N} \right], \quad (10.13)$$

where k is the time sample, N is the total number of samples of the record, n is the frequency index and a_n are the complex amplitudes over a range of frequencies. If we multiply this time series by an arbitrary taper function w_k , we form a new series \tilde{u}_k :

$$\tilde{u}_k = w_k \sum_n a_n \exp \left[\frac{i 2 \pi n k}{N} \right]. \quad (10.14)$$

Considering any single frequency M ,

$$y_k = w_k a_M \exp \left[\frac{i 2 \pi M k}{N} \right], \quad (10.15)$$

we take the discrete Fourier transform:

$$Y_n = \frac{1}{N} \sum_{k=0}^{N-1} w_k a_M \exp \left[\frac{i 2 \pi (M - n) k}{N} \right]. \quad (10.16)$$

Our problem is to seek the optimal taper w_k that maximizes the energy in a frequency band centred at M . Defining the frequency bandwidth as $2P$, the normalized energy inside the spectral band $[M - P, M + P]$ is

$$\lambda = \frac{\sum_{n=M-P}^{M+P} |Y_n|^2}{\sum_{n=0}^{N-1} |Y_n|^2}. \quad (10.17)$$

As λ is always less than unity, we call it the bandwidth retention factor (Park *et al.*, 1987).

The denominator in formula (10.17) is the energy of the entire time series, and can be evaluated by using Parseval's theorem:

$$\sum_{n=0}^{N-1} |Y_n|^2 = \frac{|a_M|^2}{N^2} \sum_{k=0}^{N-1} |w_k|^2. \quad (10.18)$$

The numerator in equation (10.17) can be expanded to

$$\sum_{n=M-P}^{M+P} |Y_n|^2 = \frac{|a_M|^2}{N^2} \sum_{k=0}^{N-1} \sum_{\ell=0}^{N-1} w_k^* w_\ell \sum_{n=-P}^P \exp\left[\frac{i2\pi(k-\ell)n}{N}\right], \quad (10.19)$$

where w_k^* is the complex conjugate of w_k . The sum over n is a geometric progression and sums to the ratio of sines:

$$T_{k\ell} = \frac{\sin[\pi(k-\ell)(2P+1)/N]}{\sin[\pi(k-\ell)/N]}. \quad (10.20)$$

Equations (10.18) and (10.19) can be presented in matrix form respectively as

$$\sum_{n=0}^{N-1} |Y_n|^2 = \frac{|a_M|^2}{N^2} \mathbf{w}^H \mathbf{w}, \quad (10.21)$$

and

$$\sum_{n=M-P}^{M+P} |Y_n|^2 = \frac{|a_M|^2}{N^2} \mathbf{w}^H \mathbf{T} \mathbf{w}, \quad (10.22)$$

where \mathbf{w} defines the taper values, \mathbf{w}^H is the Hermitian transpose of vector \mathbf{w} and \mathbf{T} is the matrix with elements defined by equation (10.20). The maximization problem (10.17) then reduces to finding the maximum of

$$\lambda = \frac{\mathbf{w}^H \mathbf{T} \mathbf{w}}{\mathbf{w}^H \mathbf{w}}. \quad (10.23)$$

Note that the matrix \mathbf{T} is Hermitian. Then equation (10.23) becomes an

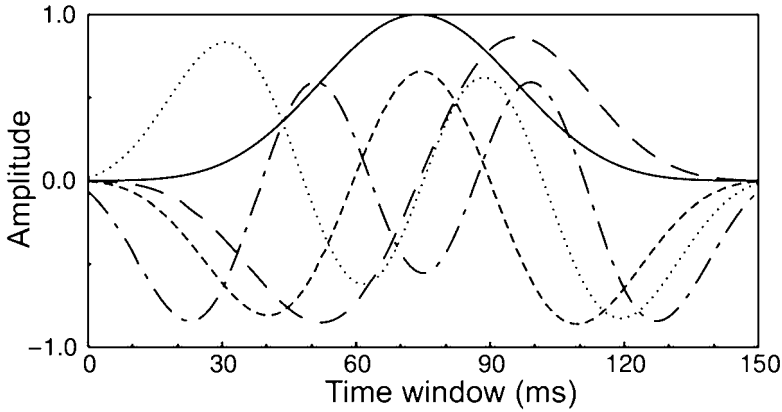


Figure 10.5 The first five optimal tapers, i.e. the eigenvectors corresponding to the first five highest eigenvalues of matrix \mathbf{T} .

eigenvalue problem:

$$\mathbf{T}\mathbf{w}^{(p)} = \lambda^{(p)}\mathbf{w}^{(p)}, \quad (10.24)$$

where p is the order of the eigenvalues according to the size. All the eigenvalues are real and positive and may be ordered according to size: $\lambda_0 > \lambda_1 > \lambda_2 > \dots$. The corresponding eigenvectors are the optimal tapers we needed.

Figure 10.5 displays five tapers corresponding to the five largest eigenvalues. Clearly the largest eigenvalue corresponds to the simplest taper function, but the remaining tapers correspond to only slightly smaller eigenvalues and therefore only slightly more spectral leakage. Each taper has energy concentrated in different part of the time series, with the zero-order ($p = 0$) taper concentrated in the central part. The zero-order taper and those with even p are symmetrical about the centre. Tapers with odd p are asymmetric.

A comparison between the amplitude spectra estimated from the Fourier transform directly and from the multitaper technique is shown in Figure 10.6, where (a) is a seismic waveform taken from a real VSP downgoing wavefield, (b) is the amplitude spectrum estimated directly from the Fourier transform and (c) is the smooth spectrum estimated by the multitaper method.

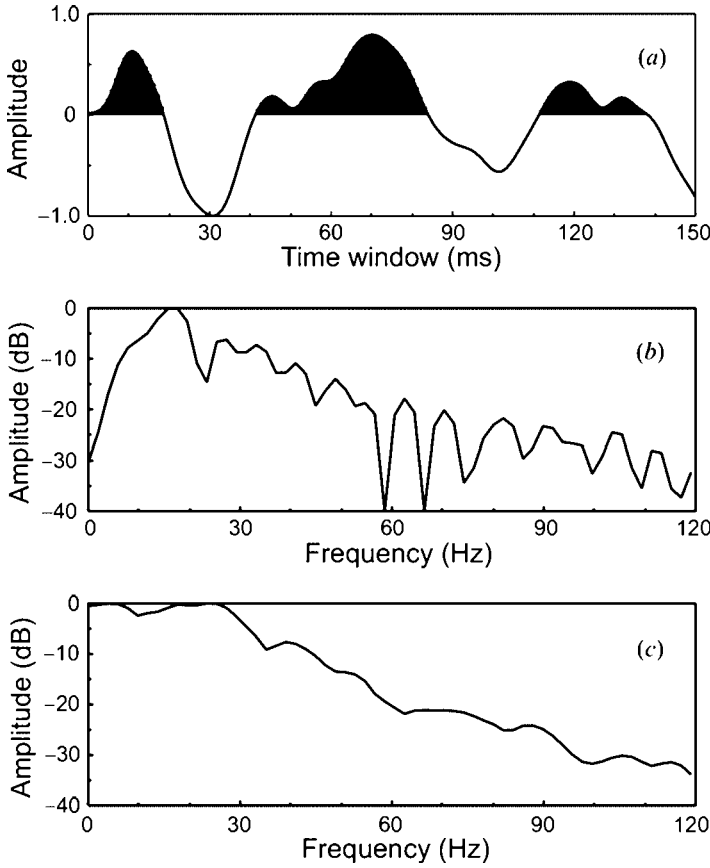


Figure 10.6 (a) A first arrival from the VSP data set. (b) The amplitude spectrum estimated directly from the Fourier transform. (c) The smooth amplitude spectrum estimated using the multitaper technique.

The tapers are mutually orthogonal because they are the eigenvectors of a Hermitian matrix. Each of them is used to provide an orthogonal sample of the original waveform. Fourier transforming these five tapered waveforms generates five spectra correspondingly, as shown in Figure 10.7. Finally, a weighted sum of these spectra produces the smooth spectral estimate shown in Figure 10.6c. Applying the multitaper technique to seismic data will produce less spectral leakage than a conventional single-taper estimate (Park *et al.*, 1987).

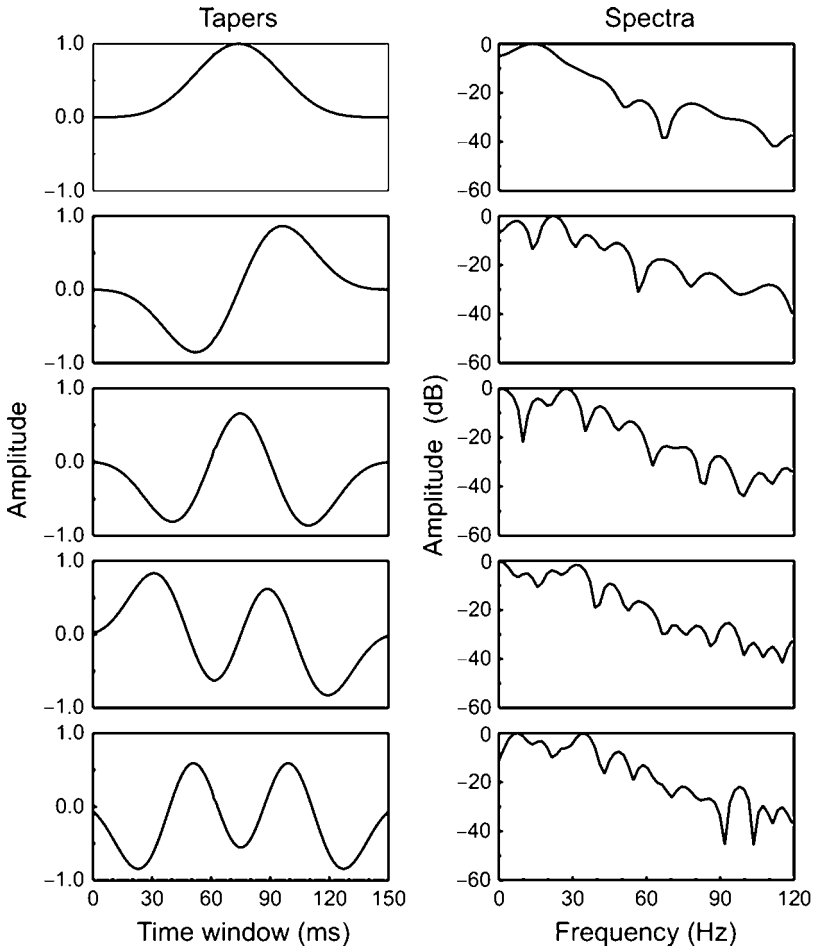


Figure 10.7 The left-hand column shows five tapers that are applied to the wavelet shown in Figure 10.6a, and the right-hand column shows the corresponding spectra. Summing these five spectra produces the smooth spectrum shown in Figure 10.6c.

10.4 Robust Q estimation from real VSP data

For the Q estimation from the real VSP data example shown in Figure 10.4, the slope k (equation 10.10) is estimated by minimizing the absolute deviation between a straight line and the spectral ratio. This algorithm is less affected by large spikes in the spectral ratio than a least-squares algorithm, as the distribution of errors contaminating the data is far from Gaussian.

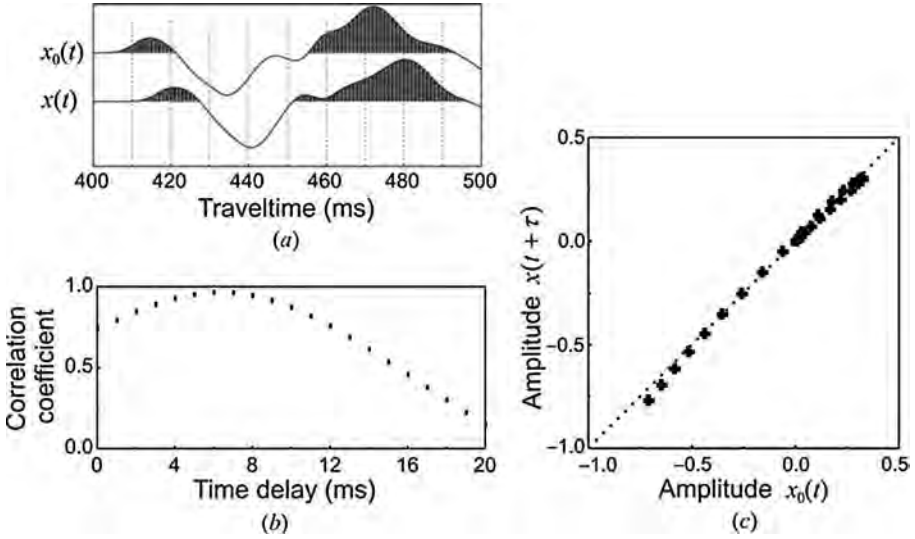


Figure 10.8 Time-delay estimation. (a) Two waveforms, $x_0(t)$ and $x(t)$, at depths of 1200 and 1220 m, respectively. (b) Pearson's correlation coefficient versus the discrete time shift. The time shift $\tau = 5$ ms at which the correlation coefficient is maximal indicates the most appropriate time delay between the two waveforms. (c) At this time delay τ , the cross-plot of the two segments $x_0(t)$ and $x(t + \tau)$ appears linear.

The time delay τ is estimated by means of Pearson's correlation coefficient (Molyneux and Schmitt, 1999). Given two waveforms $x_0(t)$ and $x(t)$ (Figure 10.8a), Pearson's correlation coefficient $r(\tau)$ is measured by

$$r(\tau) = \frac{n \sum_{t=0}^{t=n} x_0(t)x(t+\tau) - \sum_{t=0}^{t=n} x_0(t) \sum_{t=0}^{t=n} x(t+\tau)}{\sqrt{\left[n \sum_{t=0}^{t=n} x_0^2(t) - \left(\sum_{t=0}^{t=n} x_0(t) \right)^2 \right] \left[n \sum_{t=0}^{t=n} x^2(t+\tau) - \left(\sum_{t=0}^{t=n} x(t+\tau) \right)^2 \right]}}. \quad (10.25)$$

This coefficient is calculated along a series of discrete time shifts (Figure 10.8b). The τ value at which $r(\tau)$ is maximum indicates the most appropriate time shift. At this time shift, the proximity of $r(\tau)$ to unity suggests a good correlation of shapes between the waveforms $x_0(t)$ and $x(t + \tau)$, and their cross-plot appears linear (Figure 10.8c).

There are many factors affecting the measurement of Q , such as layering

effects, reflections and mode conversions, transmission effects, source and receiver coupling effects, spherical divergence and windowing, as summarized by Pujol and Smithson (1991). Above all, one of the fundamental assumptions in Q estimation is source repeatability. In standard VSP surveys, the source is fired a number of times as the receiver is moved up the well. Changes in the source signature can give rise to apparent changes in frequency content with depth, and thus can cause errors in Q estimates. Such changes should be compensated for whenever possible. If the source signature is recorded, its spectrum can be used to correct the spectra of the downhole recordings by signature deconvolution (Stainsby and Worthington, 1985).

In the case study here, however, such a record of source signature is not available. To overcome the problem associated with variation of source signature between individual shots, we select a reliable Q value from a group of Q estimates calculated for the specific depth. For each depth level z_i , we can make several estimates based on the spectral ratios from different depth pairs centred at z_i :

$$\begin{aligned}
 Q^{(1)} &= Q[\quad \quad \quad z_{i-1}, z_i \quad \quad \quad], \\
 Q^{(2)} &= Q[\quad \quad \quad z_{i-1}, \quad \quad z_{i+1} \quad \quad \quad], \\
 Q^{(3)} &= Q[\quad \quad z_{i-2}, \quad \quad \quad z_{i+1} \quad \quad \quad], \\
 Q^{(4)} &= Q[\quad \quad z_{i-2}, \quad \quad \quad \quad \quad z_{i+2} \quad \quad \quad], \\
 Q^{(5)} &= Q[\quad z_{i-3}, \quad \quad \quad \quad \quad z_{i+2} \quad \quad \quad], \\
 Q^{(6)} &= Q[\quad z_{i-3}, \quad \quad \quad \quad \quad \quad \quad z_{i+3} \quad \quad \quad].
 \end{aligned}$$

The final Q estimate is given by the following median:

$$\frac{1}{Q(z_i)} = \text{median} \left\{ \frac{1}{Q^{(1)}}, \frac{1}{Q^{(2)}}, \dots, \frac{1}{Q^{(6)}} \right\}. \quad (10.26)$$

Applying such statistics here, because of scattering in Q estimates due to the non-repeatable source, produces an average Q estimate over a large depth interval. Normally at least one wavelength separation between two receiver depths is needed to be able to measure Q (Raikes and White, 1984; White, 1992).

The estimated Q function is shown in Figure 10.9 in which the Q function is plotted against the depth and the two-way traveltime. It is interesting to

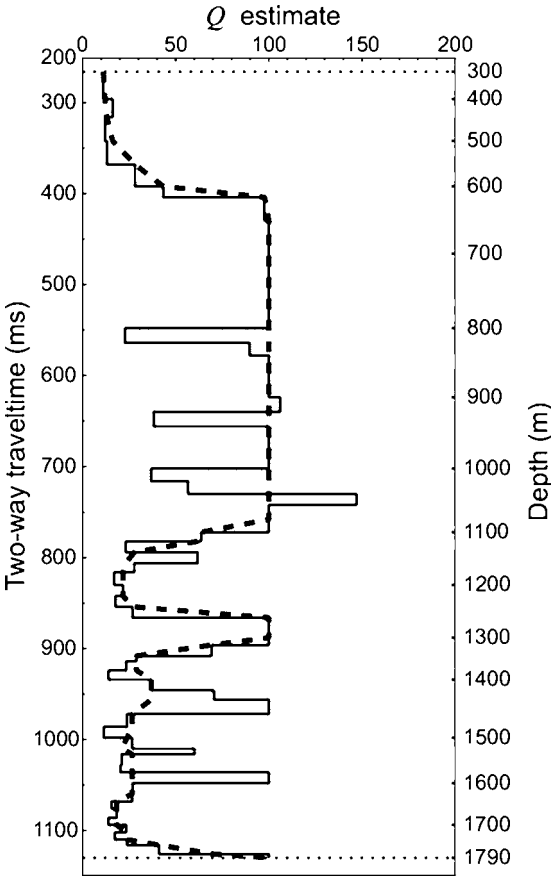


Figure 10.9 The Q function, estimated from the VSP data, is plotted against depth and two-way traveltime. The smoothed function (dashed line), after five-point median filtering, is then used in inverse Q filtering of the surface seismic data.

see that the Q function falls considerably as depth increases, typically in the depth range 1700-1790 m. This Q anomaly could be caused by a cracking and faulting zone, which acts as a low-pass filter to seismic waves passing through it (Worthington and Hudson, 2000). This Q anomaly can be used in conjunction with other petrophysics attributes as a lithological indicator for seismic interpretation (Klimentos, 1995; McCann *et al.*, 1997).

Amundsen and Mittet (1994) showed that by using zero-offset VSP data, the phase velocities could be estimated satisfactorily as the phase velocities are contained in the arrival times of the downgoing wave. But high Q values

($Q \geq 50$) were difficult to recover, since high intrinsic Q values only have a very small physical influence on waves propagating over a relatively short distance (typically 100 m). This produces an oscillating behaviour in the estimated Q function. Therefore, we should smooth the estimated Q function before we use it to design an inverse Q filter.

The smoothed Q function (the dashed line in Figure 10.9) is obtained after applying an arbitrarily chosen five-point median filter. We have used this smooth Q function to design an inverse Q filter which was applied to the two-dimensional surface seismic line shown in Figure 8.1. In practice, this zero-offset VSP Q measurements with limited depth interval can be combined with the Q measurements from either surface seismic data or walkaway VSP surveys, to build a $Q(z)$ model from the surface down to the total depth we needed (Guerra and Leaney, 2006). In this example here, below the two-way time 1160 ms (the bottom of the VSP data set), we have used $Q = 100$. The surface seismic line is an example of land seismic data with low S/N ratio relative to marine seismic data. A challenge in inverse Q filtering is whether or not the method can improve the S/N ratio without boosting the noise, when compensating for both phase and amplitude effects simultaneously. A quantitative evaluation of the effectiveness of inverse Q filtering is also shown in Chapter 8.

In addition to the spectral ratio method, there are other methods which can be used. Badri and Mooney (1987) reported that different computational techniques can result in different Q values for the same type of materials. They also tested the following four different methods.

- 1) The spectral ratio method that we have discussed in this chapter.
- 2) A rise-time-based method. The rise time is defined as the ratio of the maximum peak amplitude to the maximum slope of the initial portion of the signal after the first arrival (Gladwin and Stacey, 1974).
- 3) A pulse-broadening method. It is based on the assumptions that pulse broadening is due to anelastic attenuation in the medium and that Q is approximately independent of frequency (Gladwin and Stacey, 1974; Kjartansson, 1979).
- 4) The Futterman causal attenuation operator of an attenuating signal. This method is based on simulating a synthetic seismogram through an attenuating medium by propagating an observed signal through a perfectly elastic medium and modifying it with a filter. The filter is

based on an operator proposed by Futterman (1962). It has the important characteristic of satisfying the physical condition of causality.

Badri and Mooney (1987) concluded that the Q value computed from the spectral ratio method is probably more reliable than values computed by other techniques. But Sams and Goldberg (1990) have proven that the direct application of the spectral-ratio technique to compressional arrivals in full-waveform borehole sonic data is problematic.

Dasios *et al.* (2001) suggested an instantaneous frequency method is more stable than the spectral ratio method. The instantaneous frequency is representative of the centre frequency of the pulse. Tracking its variations with time may detect the attenuation. Barnes (1991, 1993) derived a relationship between attenuation and instantaneous frequency. Instantaneous frequency values provide maximum stability when the amplitude envelope is large (White, 1992). Using the envelope amplitude to weight the instantaneous frequency can further stabilize the estimates.

In the following chapter, we will present a stable method by fitting the amplitude compensation curve to obtain a robust Q estimate from reflection seismic data recorded at the surface.

Chapter 11

Q analysis from reflection seismic data

Abstract Q analysis refers to a method or procedure for estimating Q values directly from a reflection seismic trace. It is akin to velocity analysis in seismic data processing. Since it is difficult to pick a clean wavelet from a real reflection seismic trace without interference from other wavelets and noise, the Q analysis method does not make a direct comparison between individual wavelets, and instead is based on the Gabor transform spectrum of a reflection seismic trace. The Gabor transform, which simultaneously models localized time and frequency characteristics of a signal, can reveal the changes in frequency content with time. In this chapter we develop two Q analysis methods based on the attenuation and compensation functions respectively. The latter, based on the stabilized amplitude compensation function, is more robust for Q estimation.

In this chapter, I present methods or procedures for estimating Q values directly from a reflection seismic trace recorded at the earth surface. These methods or procedures are akin to the velocity analysis in seismic data processing. Thus we may refer to them as Q analysis.

In the previous chapter, we have demonstrated a Q -estimation procedure from downgoing wavelets of a vertical seismic profile, by directly comparing two seismic wavelets selected from different depth levels in a borehole. For a reflection seismic trace, however, it is difficult to pick a ‘clean’ wavelet without interference from other wavelets and noise (White,

1992; Dasgupta and Clark, 1998).

Instead of analysing individual wavelets, we develop a Q analysis method in this chapter based on the Gabor transform spectrum of a reflection seismic trace. The Gabor transform simultaneously models the localized time and frequency characteristics of a signal, and can reveal the changes in frequency content with time. This is in contrast to the Fourier transform, which ‘considers phenomena in an infinite interval and this is very far from our everyday point of view’ (Gabor, 1946). Thus the Gabor transform spectrum is an appropriate measurement for our seismic attenuation analysis.

In this chapter we will find two Q analysis methods, based on the amplitude-attenuation and -compensation functions (Wang, 2004a). The first method, based on the amplitude-attenuation function, will cause large errors in the Q estimation when a plane wave travels beyond a certain distance where the wave amplitude has been attenuated and may be weaker than the ambient noise. The second method, based on a stabilized amplitude-compensation function, is a robust Q analysis method.

11.1 Q analysis based on amplitude attenuation

11.1.1 Constant- Q analysis

For a given seismic trace $u(t)$, we can use Gabor transform to generate a time-variant frequency spectrum $U(\tau, \omega)$, where τ is the travelttime and ω is the angular frequency. In $U(\tau, \omega)$, considering only attenuation, we may express the amplitude of a plane wave explicitly as

$$A(\tau, \omega) = A_0 \exp\left[-\frac{\omega \tau}{2Q}\right], \quad (11.1)$$

where A_0 is the amplitude at $\tau = 0$. In the exponential attenuation function, constant Q^{-1} is an average value between $\tau = 0$ and the current time τ .

We rewrite equation (11.1) as a linear equation:

$$\ln A^2(\omega) = \ln A_0^2 - \frac{1}{Q} \omega \tau. \quad (11.2)$$

Defining the product of frequency and time as a single parameter $\chi \equiv \omega \tau$,

and considering real data from reflection seismic which is usually band-limited, we set the linear equation (11.2) as

$$y(\chi) = -\frac{1}{Q}(\chi - \chi_a), \quad (11.3)$$

where

$$y(\chi) = \ln \left(\frac{A^2(\chi)}{A^2(\chi_a)} \right). \quad (11.4)$$

In practice, we set $A^2(\chi_a)$ to be the maximum power, at the coordinate χ_a , and fit data samples for $\chi \geq \chi_a$ using the linear equation (11.3).

To fit data with equation (11.3), i.e. to estimate the slope Q^{-1} , we set up a least-squares problem as follows:

$$J = \left\| \mathbf{y} + \frac{1}{Q} \mathbf{x} \right\|^2 \rightarrow \min, \quad (11.5)$$

where \mathbf{x} is digitized variable $\chi - \chi_a$ and \mathbf{y} is the discrete data set $y(\chi - \chi_a)$. Taking derivative

$$\frac{dJ}{dQ} = 0, \quad (11.6)$$

leads to

$$\frac{1}{Q} = -\frac{\mathbf{x}^T \mathbf{y}}{\mathbf{x}^T \mathbf{x}}. \quad (11.7)$$

Only the numerically significant part of $y(\chi)$ should be considered in \mathbf{y} . Thus, data fitting (equation 11.7) is performed only within the range $[\chi_a, \chi_b]$, where the upper limit χ_b corresponds to the threshold for cutting off the small values of the one-dimensional (1-D) spectrum $y(\chi)$. Including excessively small values of $y(\chi)$, which are smaller than the ambient noise, will cause large errors in Q estimation. The threshold is given as

$$y(\chi) > -0.23 |G| = -|\ln \sigma^2|, \quad (11.8)$$

where G is a user-defined threshold, a negative value in decibels (say,

–50 dB). The threshold is set naturally by the stabilization factor σ^2 used in inverse Q filtering and thus is linked to the signal-to-noise (S/N) ratio of the data set.

The physical meaning of such a threshold is that, in the minimization problem (11.5), the support region for $\chi \equiv \omega\tau$ is finite, as seismic signals are band-limited and have finite duration, due to the attenuation effect. The support region can be defined by

$$\chi < \chi_b \equiv 0.23 |G| Q = |\ln \sigma^2| Q. \quad (11.9)$$

Note that the support region is strictly the function of Q , and is a function of the data S/N ratio as well.

Figure 11.1 demonstrates the implementation of the Q analysis, which consists of the following three steps:

- 1) performing a Gabor transform on the seismic trace and producing a time-variant (amplitude) spectrum $|A(\tau, \omega)|$;
- 2) transforming the two-dimensional (2-D) spectrum $|A(\tau, \omega)|$ into the 1-D spectrum $|A(\chi)|$;
- 3) using expression (11.7) to estimate Q^{-1} , utilizing the spectral data $y(\chi)$ within the support region.

The advantage of transforming the Gabor spectrum from 2-D to 1-D is that, after the transformation, the spectrum decreases monotonically along the axis χ . This overcomes the difficulties when using the 2-D Gabor spectrum to estimate Q vertically along the time (τ) direction, as shown in Figure 11.1b.

For comparison, the synthetic seismic trace after inverse Q filtering and its spectrum is shown in Figure 11.2, in which the spectrum is also plotted in three different ways: 2-D amplitude spectrum, 1-D amplitude spectrum and 1-D logarithmic, normalized, power spectrum.

11.1.2 Layered- Q analysis

Suppose the subsurface medium is divided into layers, separated at two-way times $T_1, T_2, \dots, T_n, \dots$, and the seismic trace is recorded at $T_0 = 0$. We now describe the method and the difficulties for a layered- Q analysis.

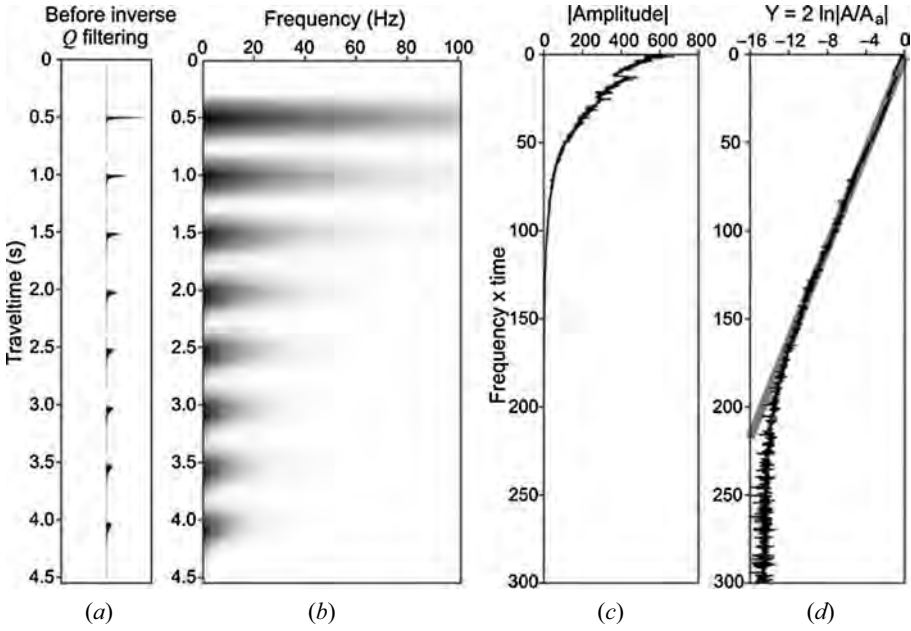


Figure 11.1 Constant- Q analysis based on amplitude attenuation. (a) A synthetic seismic trace with known Q value, $Q = 88$. (b) The Gabor-transform (amplitude) spectrum, which shows the time-variant frequency content of the seismic trace. (c) Transforming the 2-D Gabor spectrum into the 1-D spectrum with respect to the variable χ , defined as the product of frequency and time. (d) Estimating Q from the 1-D logarithmic spectrum, where the thick grey straight line corresponds to the estimated value $Q = 84.9$.

For the n th layer, which has the thickness $\Delta T_n = T_n - T_{n-1}$, the amplitude spectrum is

$$A(\tau, \omega) = A_0 \beta(\omega) \exp \left[-\frac{\omega \tau}{2 Q_n} \right], \quad (11.10)$$

where $\beta(\omega)$ is the attenuation between $T_0 = 0$ and T_{n-1} ,

$$\beta(\omega) = \exp \left[-\frac{\omega}{2} \sum_{i=1}^{n-1} \frac{\Delta T_i}{Q_i} \right], \quad (11.11)$$

and $\tau = T - T_{n-1} \geq 0$ with $\tau = 0$ at T_{n-1} .

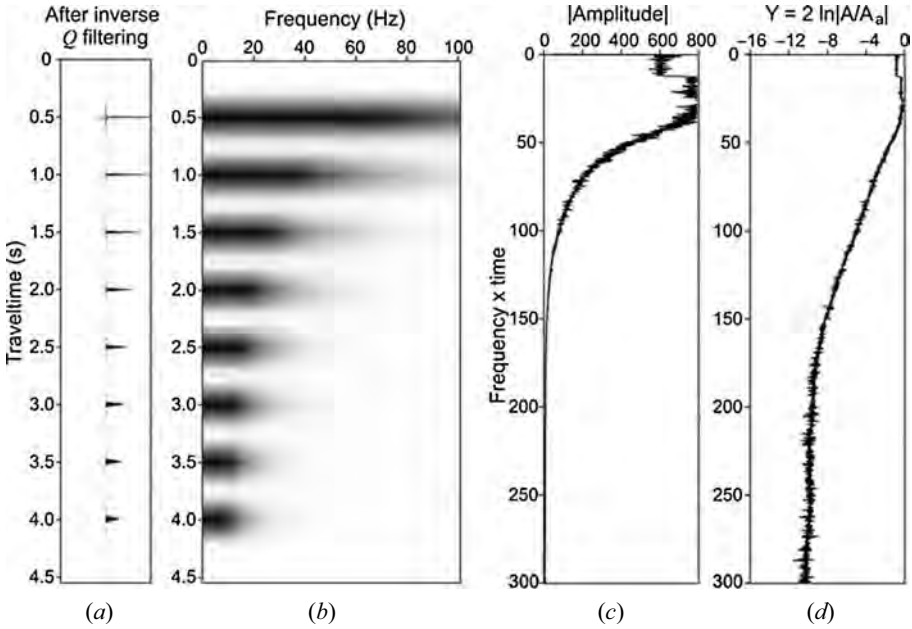


Figure 11.2 The result of inverse Q filtering, compared to the Q analysis shown in the preceding figure. (a) The synthetic seismic trace after inverse Q filtering. (b) The Gabor-transform (amplitude) spectrum, which shows the time-variant frequency content of the seismic trace after inverse Q filtering. (c) The 1-D Gabor (amplitude) spectrum with respect to the variable χ , defined as the product of frequency and time. (d) The logarithmic normalized (power) spectrum.

Amplitude $A(\tau, \omega)$ between T_{n-1} and T_n should be normalized by $\beta(\omega)$, as

$$\hat{A}(\tau, \omega) = \begin{cases} \frac{A(\tau, \omega)}{\beta(\omega)}, & \text{for } \beta(\omega) \geq \sigma, \\ 0, & \text{for } \beta(\omega) < \sigma, \end{cases} \quad (11.12)$$

before we set up a linear equation as in (11.3) with

$$y(\chi - \chi_a) = 2 \ln \left| \frac{\hat{A}(\chi)}{\hat{A}_a} \right|. \quad (11.13)$$

In expression (11.12), to stabilize the procedure, small-amplitude samples

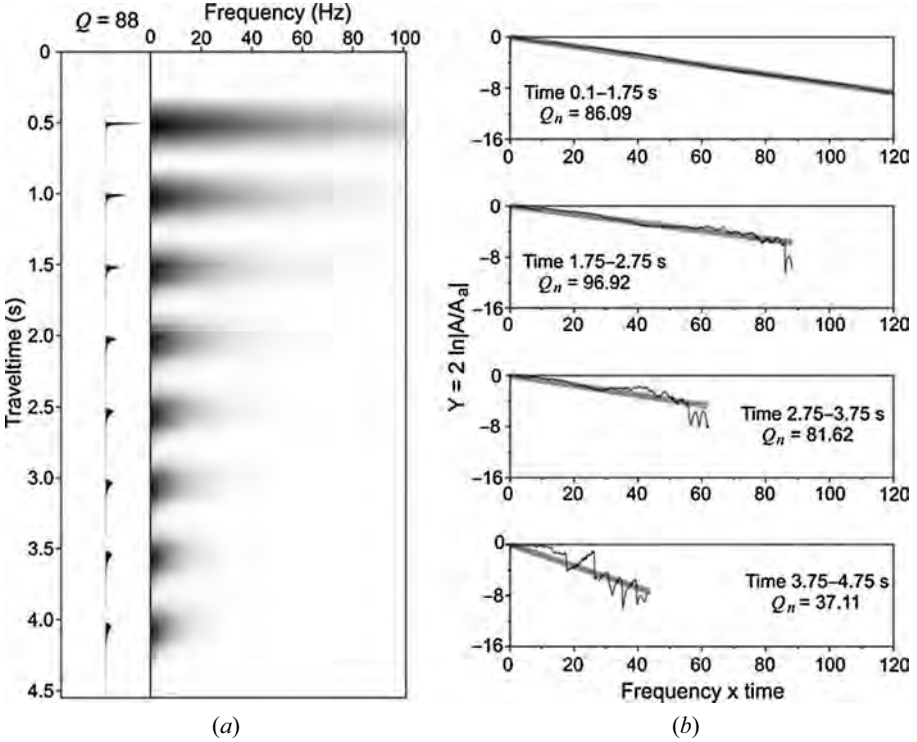


Figure 11.3 Layered- Q analysis. (a) A synthetic seismic trace with a known constant $Q = 88$ and its Gabor-transform spectrum. (b) The interval Q values estimated for different time windows.

are ignored in the Q analysis. The threshold is clearly related to the S/N ratio. In the example shown in Figure 11.3, where the seismic data set is a noise-free synthetic trace, a threshold $\sigma^2 = 10^{-5}$ (i.e. -50 dB) is used.

The numerical instability appearing in three out of four plots of panel (b) is due to the computer float precision. For a specific layer, the threshold σ is set at $\tau = 0$ (i.e. at T_{n-1}). Within the layer between T_{n-1} and T_n , amplitudes of some samples, typically at high frequencies, may be much less than σ . Amplifying these amplitude samples, as shown in expression (11.12), may cause errors in the Q analysis.

11.1.3 Average- Q analysis

Average- Q analysis, depicted in Figure 11.4 and described in this subsection, will be more robust than the previous, layered- Q analysis method.

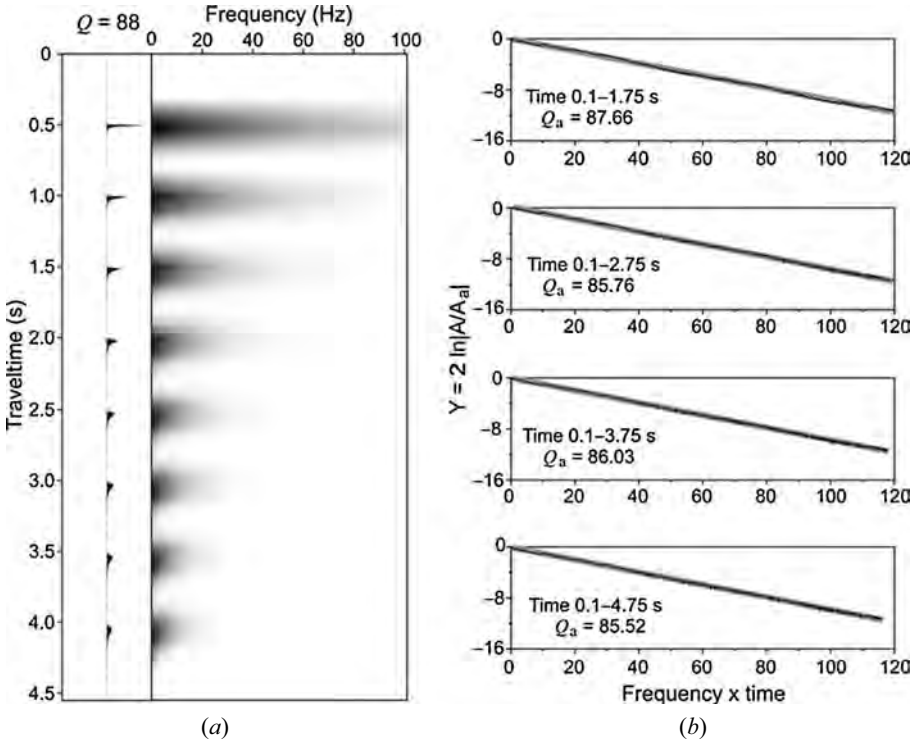


Figure 11.4 Average- Q analysis based on amplitude attenuation. (a) A synthetic seismic trace and its Gabor-transform spectrum. (b) The average Q values estimated from different time windows between the water-bottom (0.1 s) and the time samples at 1.75, 2.75, 3.75 and 4.75 s, respectively. The converted layered- Q values are listed in Table 11.1.

At the end, the estimated average Q values can be converted to the layered Q values.

The principle of the so-called average- Q analysis is to repeat the constant Q^{-1} analysis described earlier for a series of T samples, and each time $\tau = 0$ is always set at the recording surface $T = 0$. The average $Q_a^{-1}(\tau)$ function with respect to the series τ samples can then be converted to a layered Q^{-1} function, $Q^{-1}(\tau)$. This Q analysis procedure is akin to the velocity analysis.

Note that here $Q_n^{-1}(\tau)$ is used to represent an instantaneous Q^{-1} value or a layered Q^{-1} value at any time τ , whereas $Q_a^{-1}(\tau)$ is used to represent an average Q^{-1} value between the recording surface $T = 0$ and the time $T = \tau$.

Considering the definition of the average Q values,

$$\left(\frac{1}{Q_a}\right)_{n-1} = \frac{1}{T_{n-1}} \sum_{i=1}^{n-1} \frac{\Delta T_i}{Q_i} \quad \text{and} \quad \left(\frac{1}{Q_a}\right)_n = \frac{1}{T_n} \sum_{i=1}^n \frac{\Delta T_i}{Q_i},$$

where $(1/Q_a)_{n-1}$ and $(1/Q_a)_n$ are the two average $1/Q$ values between the recording surface $T_0 = 0$ and the time level $\tau = T_{n-1}$ and time $\tau = T_n$, respectively, the interval $1/Q$ value for the n th layer is given by

$$\left(\frac{1}{Q}\right)_n = \frac{T_n/(Q_a)_n - T_{n-1}/(Q_a)_{n-1}}{T_n - T_{n-1}}. \quad (11.14)$$

Table 11.1 lists the interval Q values, converted from the average Q values estimated from Figure 11.4, and the relative errors (as percentages) with respect to the true model, which is a known constant $Q = 88$. The maximum error is 6.1% in this example.

Table 11.1 The average Q values, Q_a , estimated from Figure 11.4, and the corresponding layered Q values, Q_n . The true model is a known constant $Q = 88$.

Time (s)	Q_a	Time (s)	Q_n	Errors (%)
0.1–1.75	87.66	0.1–1.75	87.66	–0.4
0.1–2.75	85.76	1.75–2.75	82.64	–6.1
0.1–3.75	86.03	2.75–3.75	86.76	–1.4
0.1–4.75	85.52	3.75–4.75	83.68	–4.9

11.2 Q analysis based on amplitude compensation

We now introduce a much more robust method for Q analysis based on the amplitude-compensation function, instead of the attenuation measurement used in the previous section.

Once we obtain an amplitude-attenuation measurement, we can use it directly to design a gain function for compensating the amplitude spectrum.

Thus, in fact, we do not necessarily estimate the Q value explicitly, if we only consider the amplitude compensation. However, a proper inverse Q filtering includes not only amplitude compensation but also phase correction, as we have seen in previous chapters. For this purpose, an explicit Q function is required.

Once the Gabor spectrum is calculated, the Q analysis may be performed in the following steps:

- 1) evaluating the attenuation function $A(\chi)$;
- 2) smoothing and normalizing the attenuation function;
- 3) designing a data-driven gain curve;
- 4) estimating Q by fitting the gain curve with a theoretical gain function.

The $A(\chi)$ samples are smoothed by applying a (five-point) median filter, and then normalized by

$$\bar{A}(\chi) = \frac{A(\chi)}{A_a}. \quad (11.15)$$

A data-driven gain curve is then designed as

$$A_d(\chi) = \begin{cases} 1, & \text{for } \chi \leq \chi_a, \\ \frac{\bar{A}(\chi) + \sigma^2}{\bar{A}^2(\chi) + \sigma^2}, & \text{for } \chi > \chi_a, \end{cases} \quad (11.16)$$

where A_d indicates that the gain function is designed directly from ‘data’. In contrast, a theoretical gain function is expressed as (equation 7.26)

$$A(\chi, Q) = \frac{\beta(\chi, Q) + \sigma^2}{\beta^2(\chi, Q) + \sigma^2}, \quad (11.17)$$

where (equation 7.28)

$$\beta(\chi, Q) = \exp\left[-\frac{\chi}{2Q}\right]. \quad (11.18)$$

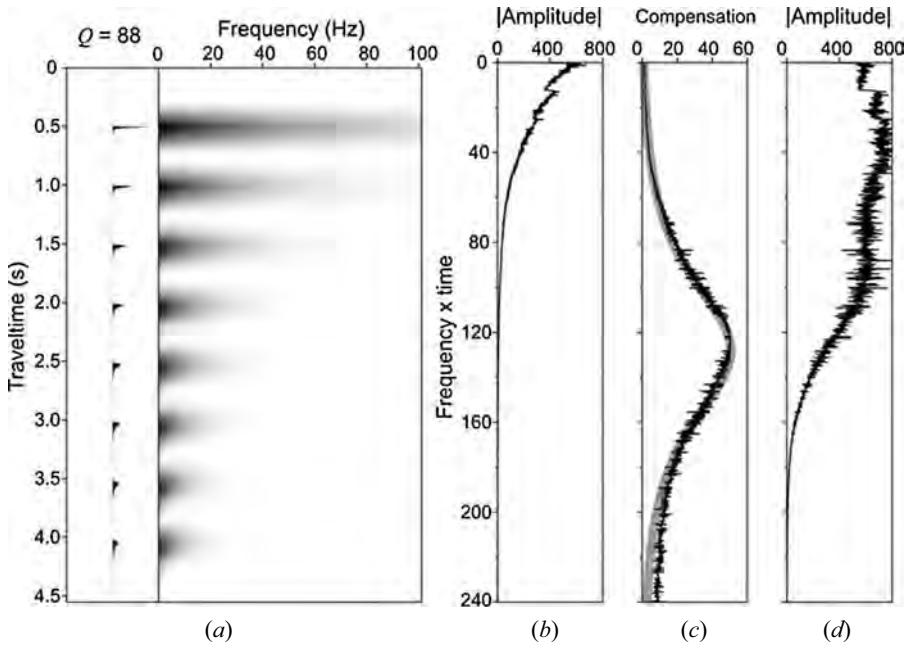


Figure 11.5 Constant- Q analysis based on amplitude compensation. (a) A synthetic seismic trace and its Gabor transform spectrum. (b) The associated amplitude-attenuation curve. (c) The amplitude-compensation curve and synthetic (grey) curve corresponding to the estimated Q value ($Q = 87.2$). (d) The amplitude spectrum after Q compensation.

Finally, Q estimation becomes a minimization problem:

$$\sum_{\chi} |A_d(\chi) - A(\chi, Q)| \rightarrow \min. \quad (11.19)$$

Here, we first mitigate the outliers using a median filter and then minimize the absolute deviation between the two gain functions, to make the minimization procedure robust in finding the Q value.

The procedure for constant- Q analysis based on the amplitude compensation is shown in Figure 11.5, in which (b) is the amplitude attenuation curve and (c) is the associated amplitude-compensation curve and the synthetic (grey) curve corresponding to the estimated Q value ($Q = 87.2$). For comparison, (d) is the amplitude spectrum after Q compensation.

The procedure for the average- Q analysis is shown in Figure 11.6, in which the left column shows the amplitude-attenuation measurement down

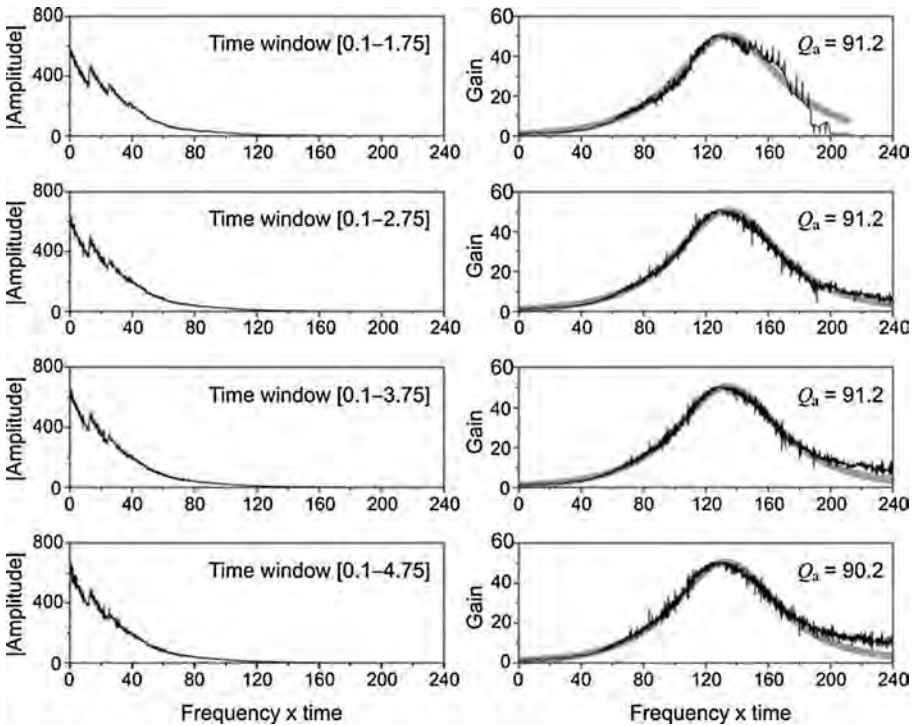


Figure 11.6 Average Q analysis based on amplitude compensation. Left column: the amplitude-attenuation curves; Right column: the amplitude-compensation curves and the synthetic gain curves (grey lines) corresponding to the estimated Q values. The four rows correspond to four different analysis windows, all of which start from the water-bottom at 0.1 s. This method is very robust and, as a consequence, the average Q values are almost equal to a constant (i.e. the interval Q value), which is close to the true constant- Q model.

to different time levels and the right column shows the associated amplitude-compensation curves and the synthetic gain curves (grey lines) corresponding to the estimated Q values. Comparing the previous Q analysis method in the last section, we can clearly see that this method, based on the compensation function, is very robust, as the numerical values of the gain function, after median filtering, are generally equal to or greater than 1.

As the average Q values are almost equal to a constant, such a constant can be considered as the interval Q value for each layer. This is close to the true constant- Q model, although the estimate ($Q = 91.2$) presents 3.6% error relative to the true model ($Q = 88$).

11.3 Correction of spherical divergence prior to *Q* analysis

Before demonstrating the *Q* analysis from real seismic data sets, we discuss now an issue regarding the spherical divergence, which is usually the major factor causing time-dependent amplitude change. The energy spreads out so that the wave decreases in strength, although the total energy in the wavefield does not change. If the medium were homogeneous, the amplitude weakening would be inversely proportional to distance. However, because velocity generally increases with depth, ray-path curvature makes the wave spread out more and thus makes the decrease in amplitude larger.

Considering the source–receiver offset y , the effect of spherical divergence on a prestack seismic trace may be expressed as (Wang, 2003b):

$$D \approx \frac{v_0}{v_{\text{rms}}^2 t(y)} \left[1 + \left(1 - \frac{v_{\text{rms}}^2}{v_0^2} \right) \left(\frac{v_0 y}{v_{\text{rms}}^2 t(y)} \right)^2 + \left(1 - \frac{v_{\text{rms}}^2}{v_0^2} \right) \left(\frac{v_0 y}{v_{\text{rms}}^2 t(y)} \right)^4 \right]^{1/2}, \quad (11.20)$$

where v_0 is the velocity at the source position, and v_{rms} is the root-mean-square (rms) velocity varying with respect to two-way time t . When the source–receiver offset $y \rightarrow 0$, this leads to Newman's (1973) well-known formula as

$$D \approx \frac{v_0}{v_{\text{rms}}^2 t}. \quad (11.21)$$

This shows that, for a normal incidence ray path through a horizontally layered model, the ray-amplitude decrease is proportional to $(v_{\text{rms}}^2 t)^{-1}$.

In the rest of this section, we consider the correction of spherical divergence on a zero-offset seismic trace (i.e. a stack section) of the *P-P* wave and *P-SV* wave. For the *P-P* wave, the correction for spherical divergence is given by

$$A^{(pp)}(t) = \frac{t v_{p,\text{rms}}^2(t)}{v_0}, \quad (11.22)$$

where $v_{p,\text{rms}}$ is the *P*-wave rms velocity which we assume here to be

$$v_{p,\text{rms}}(t) = v_0 \left(1 + \frac{1}{2} b t \right), \quad (11.23)$$

and b is the velocity gradient with respect to the one-way time (equivalently, the depth). Then equation (11.22) can be approximated as

$$A^{(pp)}(t) \approx v_0 t \left(1 + \frac{1}{2} b t \right)^2 \approx v_0 t \exp[b t]. \quad (11.24)$$

For the P - SV wave, the correction for spherical divergence is given by

$$A^{(ps)}(t) = A_{\text{down}}^{(p)}(t_p) A_{\text{up}}^{(s)}(t_s), \quad (11.25)$$

where $A_{\text{down}}^{(p)}(t_p)$ and $A_{\text{up}}^{(s)}(t_s)$ are corrections for the divergence in the downward travel path and for that in the up-going ray path, and $t = t_p + t_s$. The divergence correction of the downward P -wave travel path, based on equation (11.22), is given by (O'Brien and Lucas, 1971):

$$A_{\text{down}}^{(p)}(t_p) = \frac{t_p v_{p,\text{rms}}^2(t_p)}{2v_0}, \quad (11.26)$$

where

$$t_p = \frac{1}{1+r} t, \quad (11.27)$$

and $r = v_p/v_s$, the ratio of the P - and S -wave velocities.

For a theoretical zero-offset P - SV wave trace, the up-going SV -wave travel path is exactly the same as the downgoing P -wave travel path. Therefore, the divergence correction for the up-going SV -wave is the same as that for the downgoing P -wave. That means, whatever the wave mode is, the divergence correction for the return path of a stacked, zero-offset trace can compensate only for a fixed 6-dB loss.

Finally, the formula for the P - SV wave spherical-divergence correction is obtained as

$$A^{(ps)}(t) = \frac{t_p v_{p,\text{rms}}^2(t_p)}{v_0} = \frac{1}{1+r} \frac{t v_{p,\text{rms}}^2(\frac{1}{1+r} t)}{v_0} \approx \frac{v_0 t}{1+r} \exp\left[\frac{b}{1+r} t\right]. \quad (11.28)$$

In summary, if the formula for the *P-P* wave-divergence correction is represented in a generalized form as

$$A^{(pp)} = a t \exp[bt], \quad (11.29)$$

where *a* and *b* are two generalized coefficients, the counterpart for the *P-SV* wave divergence correction may be expressed as

$$A^{(ps)} = a' t \exp[b't], \quad (11.30)$$

where

$$a' = \frac{a}{1+r} \quad \text{and} \quad b' = \frac{b}{1+r}. \quad (11.31)$$

The velocity v_0 at the recording surface is assumed to be a constant and thus can be dropped from both the divergence-correction formulae (11.24) and (11.28). This is equivalent to scaling down the α coefficient in equations (11.29) and (11.30) simultaneously.

11.4 *Q* analyses on the *P-P* and *P-SV* wave sections

We use a pair of *P-P* and *P-SV* wave sections to demonstrate *Q* analysis (average-*Q* analysis, followed by interval *Q* calculation) on real seismic data. Figures 11.7 and 11.8 depict details for the *Q* estimation from these two sections, respectively. Figure 11.9 compares the *P-P* wave section before and after inverse *Q* filtering, whereas Figure 11.10 displays the *P-SV* wave section before and after inverse *Q* filtering.

For estimating *Q* values from seismic sections, the Gabor-transform spectra shown in Figures 11.7a and 11.8a are the average spectra over all seismic traces in the corresponding sections shown in Figures 11.9a and 11.10a, respectively. We use these Gabor-transform spectra to compute the attenuation measurements and then compensation functions with respect to the frequency-time product. We then use the compensation functions to estimate the average-*Q* values.

We conduct the average *Q* analyses at different times with an increment of 0.5 s. Figures 11.7b and 11.8b display diagnoses of the average-*Q*

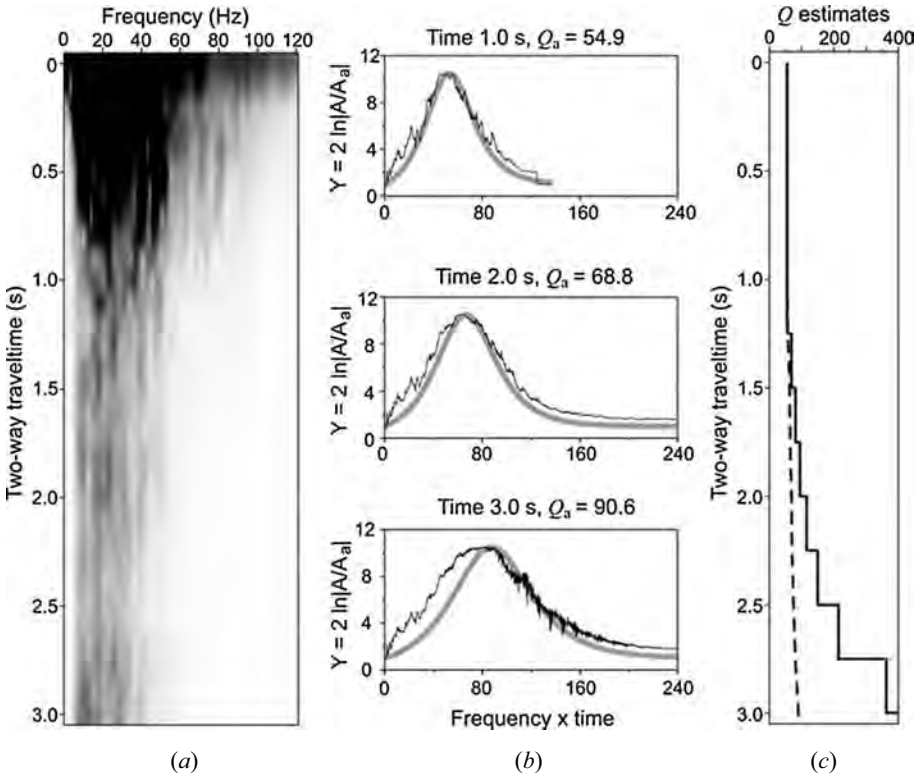


Figure 11.7 Q estimation from a P - P wave seismic section: (a) the Gabor-transform spectrum; (b) average- Q analyses at three different times; (c) estimated average- and interval- Q functions.

analyses at three different times. Figures 11.7c and 11.8c show the results of average- Q analyses (dashed lines) and the final interval Q values with a time interval of 0.25 s. As expected, the P - SV wave interval Q values are in general smaller than the P - P wave interval Q values.

Before Q analyses on the P - P wave and P - SV wave sections shown in Figures 11.9a and 11.10a respectively, these two brute stack sections have been corrected for spherical divergence effects, using the formulae (11.29) and (11.30). In the P - P wave divergence correction formula (11.29), we use $a = 1$ and $b = 0.3$. In the P - SV wave divergence-correction formula (11.30), we use $a' = 0.366$ and $b' = 0.11$. The latter is equivalent to using $r = \sqrt{3}$, the ratio of P - to S -wave velocities.

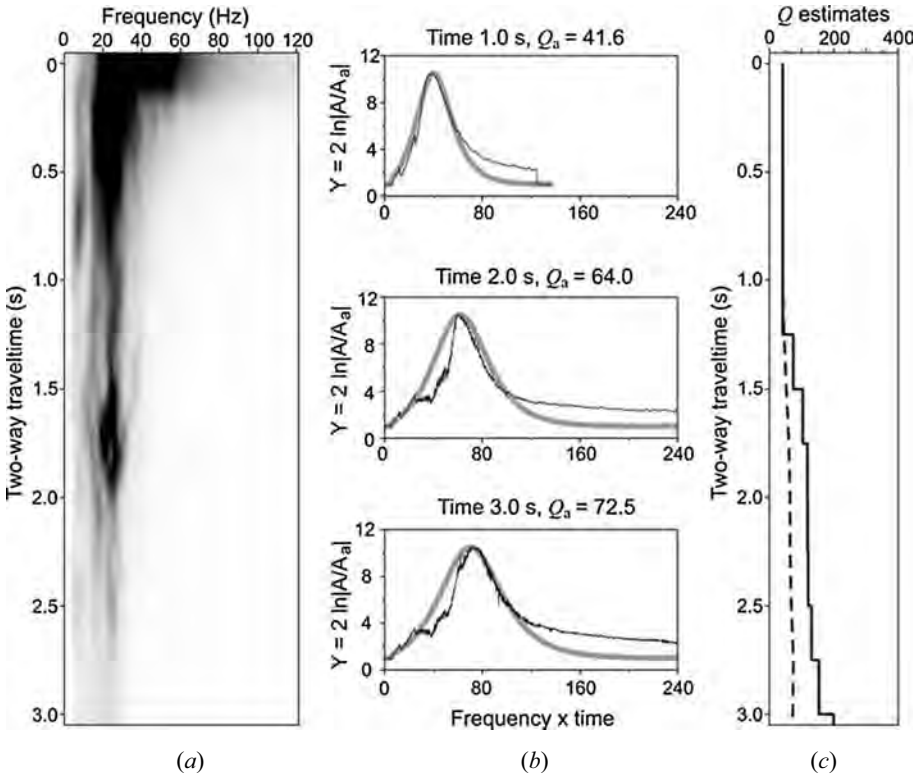


Figure 11.8 *Q* estimation from the *P-SV* wave seismic section: (a) the Gabor-transform spectrum; (b) average-*Q* analyses at three different times; (c) estimated average- and interval-*Q* functions.

The time-variant *Q* functions plotted in Figures 11.7c and 11.8c are used in designing inverse *Q* filters for *Q* effect corrections in the *P-P* and *P-SV* wave sections shown in Figures 11.9a and 11.10a, respectively. Figures 11.9b and 11.10b show the corresponding seismic sections after the application of the inverse *Q* filter. The *Q* value estimated from a reflection seismic trace reveals the anelastic properties of subsurface materials, but it can also include the attenuation that stems from elastic properties, namely from the interbed multiple reflections (O'Doherty and Anstey, 1971; Schoenberger and Levin, 1974, 1978). However, using this *Q* model to design an inverse *Q* filter and applying it to reflection seismic data, the results can show true amplitude variations of the *P-P* and *P-SV* waves, and provide reliable information for geological and lithological interpretation.

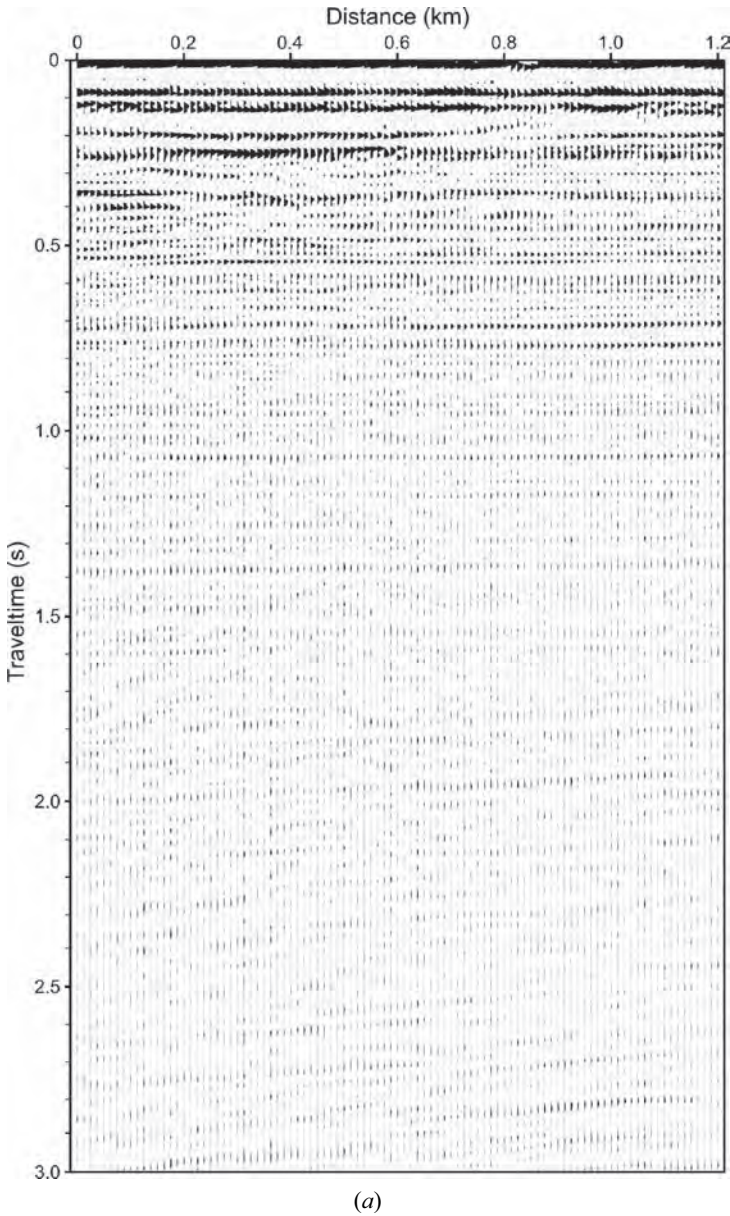


Figure 11.9 (a) A P - P wave seismic section without inverse Q filtering. It was used for Q analysis shown in Figure 11.7.

Figure 11.11 shows another application example of inverse Q filtering to a three-dimensional P - SV wave seismic data cube. The two sections are

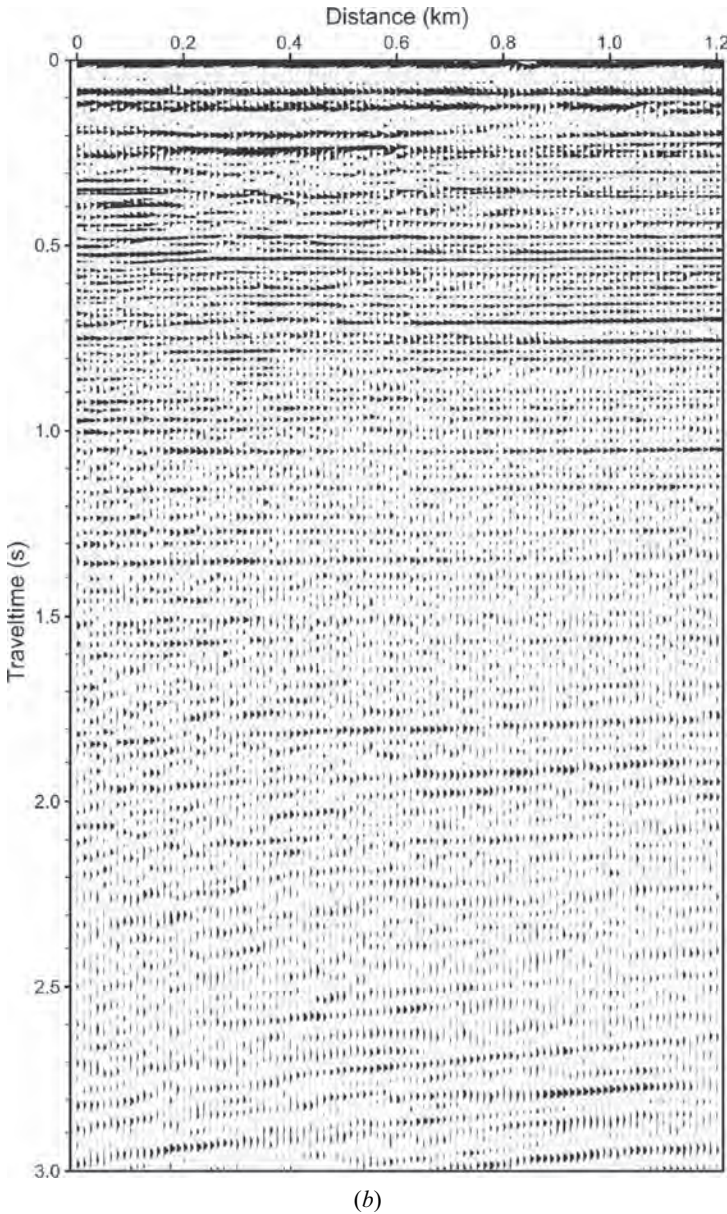


Figure 11.9 (contd) (b) The P - P wave seismic section after inverse Q filtering. The Q model was plotted in Figure 11.7c.

extracted from the data cubes before and after inverse Q filtering, respectively. After inverse Q filtering, the seismic data cube shows much

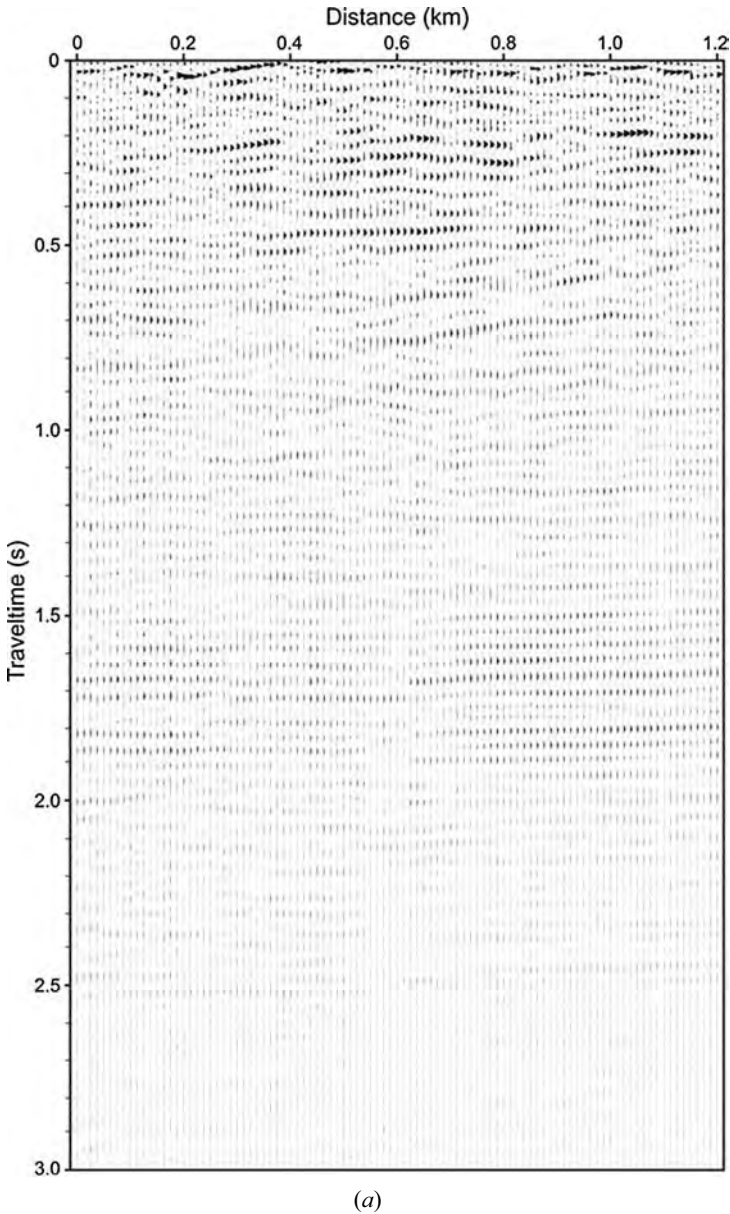
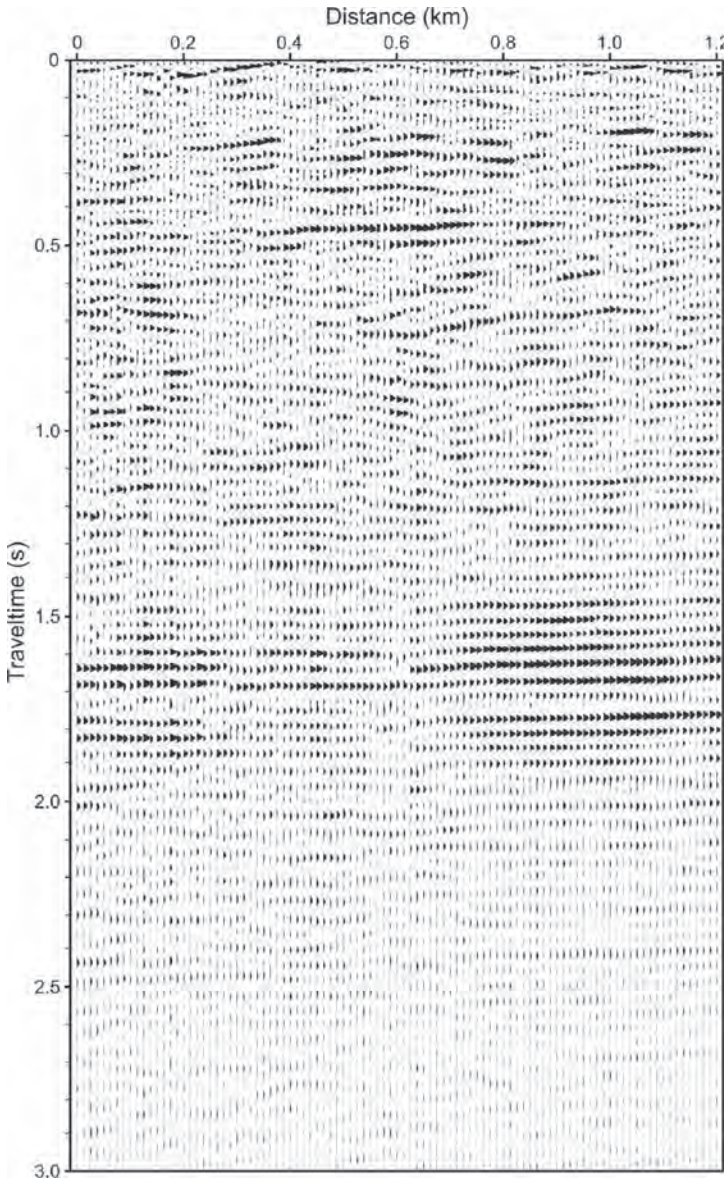


Figure 11.10 (a) A P - SV wave seismic section without inverse Q filtering. It was used for Q analysis shown in Figure 11.8.

more detailed spatial variation in P - SV wave reflection. It reveals the thickness variation of the tight-sand gas reservoir at time 2.45 s between



(b)

Figure 11.10 (contd) (b) The P - SV wave seismic section after inverse Q filtering. The Q model was plotted in Figure 11.8c.

distance 36 and 40 km. It indicates the clear existence of many small faults in different formation layers.

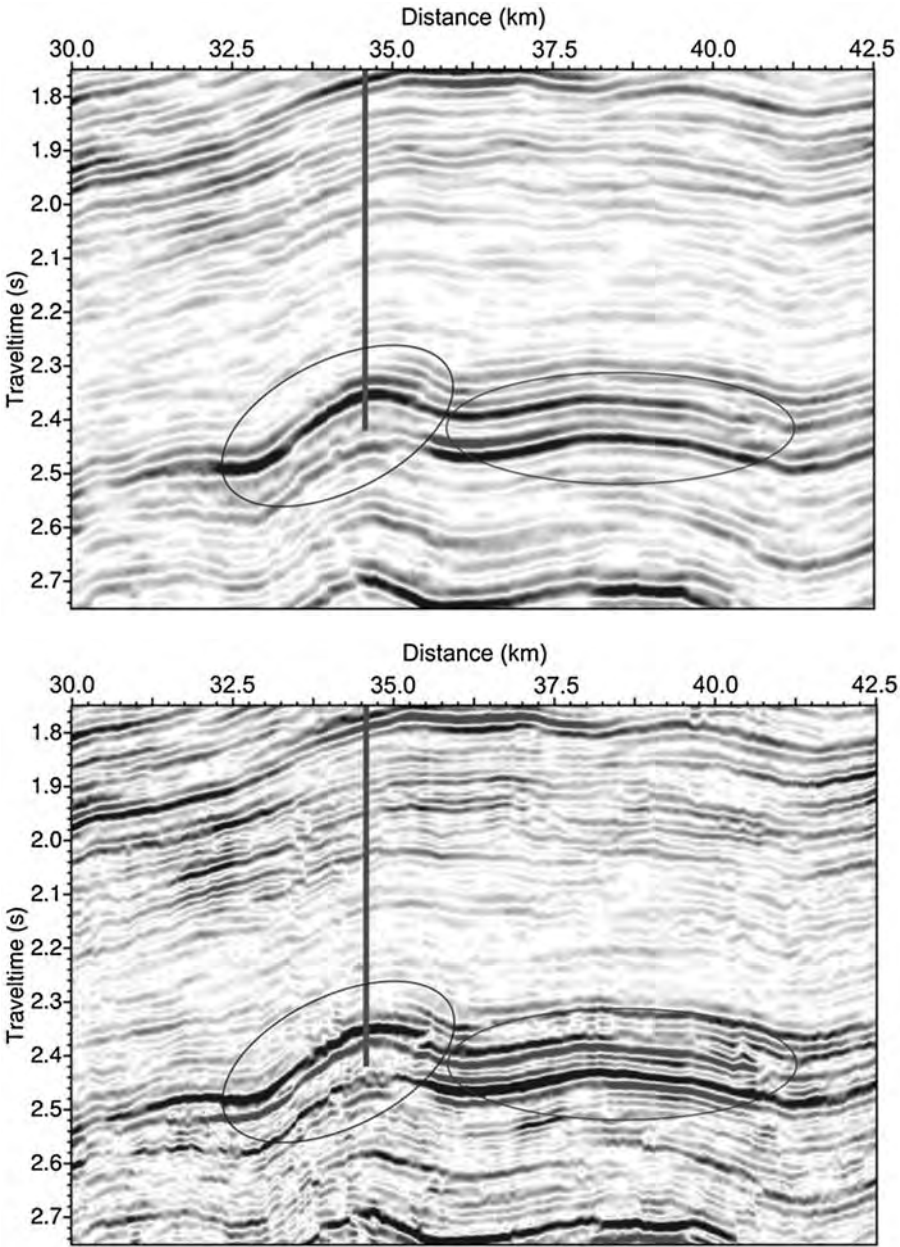


Figure 11.11 The P - SV wave seismic sections before (top) and after (bottom) inverse Q filtering. The vertical lines indicate a well location.

Chapter 12

Crosshole seismic tomography for the Q model

Abstract Seismic waveform tomography, especially with crosshole geometries, can be used to reconstruct the earth Q model with sufficient resolution. It can be implemented in the frequency domain where only distinct frequency components are used in the inversion, and, for the attenuation inversion, the real-valued velocity function is simply replaced with a complex-valued velocity function. The real-part velocity is the wave-propagation velocity we normally refer to, and the imaginary-part velocity is needed for the calculation of the attenuation factor. Because the magnitudes of these two velocity parts are significantly different, in practice they are inverted in two separate steps. That is, the waveform tomography inverts for the velocity model first, and then for the attenuation (Q^{-1}) model.

In the previous chapters, we have used vertical seismic profiling (VSP) data and surface reflection data to estimate the Q model, needed to design the inverse Q filter. In this chapter, we will use crosshole seismic data for the attenuation analysis, in which we will employ a waveform tomography technique to reconstruct the attenuation model and a velocity model as well.

Seismic waveform tomography, especially when using transmission data, is able to provide a quantitative image of physical properties in the subsurface, not only a structural image as in conventional seismic migration. It has the potential to image the velocity and attenuation fields with

significantly improved resolution, useful for time-lapse, high-resolution imaging of a reservoir. The process generally starts with an initial model and then updates it iteratively by minimizing the differences between the observed data waveforms and the theoretical data waveforms. This requires an efficient imaging tool, capable of being used on a production basis for practical problems.

For waveform inversion, the frequency-domain version enables the use of distinct frequency components and thereby reduces the quantity of data required for processing (Pratt and Worthington, 1990; Sirgue and Pratt, 2004). Although in principle all frequencies may be modelled to fit the observations (equivalent to ‘time-domain’ waveform inversion), in practice adequate reconstructions may be obtained with a reduced set of frequencies (‘frequency-domain’ waveform inversion).

In section 12.1, I will summarize the frequency-domain implementation of the waveform tomography method. As shown in Chapter 10, we can easily include the attenuation effect in the frequency-domain waveform simulation and inversion, by simply replacing the real-valued velocity with a complex-valued velocity (Song *et al.*, 1995; Hicks and Pratt, 2001). The relationship between the complex velocity and an attenuation (Q^{-1}) value is (Aki and Richards, 1980)

$$Q^{-1} = -\frac{2c_{\text{Im}}}{c_{\text{Re}}}, \quad (12.1)$$

where c_{Re} and c_{Im} are the real and imaginary parts, respectively, of the complex-valued velocity, and the real part is the wave-propagation velocity model we normally refer to in data processing.

Seismic inversion for the attenuation model (and the velocity model simultaneously) means an inversion for the complex-valued velocity model. As the real-part and imaginary-part velocities have approximately 1–2 orders of magnitude difference, their contributions to the objective function are significantly different. Thus, a two-stage strategy may be appropriate for the inversion of real, noisy data. In the first stage, we invert only for the real-part velocity model by assuming the imaginary-part velocity is zero. In the second stage, we fix the real-part velocity model as that inverted from the first stage and invert only for the imaginary-part velocity model. As shown in expression (12.1), setting the imaginary-part velocity to be zero is equivalent to assuming $Q^{-1} = 0$, and if we know the nonzero imaginary-part velocity, we can calculate the attenuation factor Q^{-1} . Therefore, this

two-stage strategy means that the first stage is a normal velocity inversion, and the second stage is actually an attenuation inversion. In sections 12.3 and 12.4, I will describe these two inversions separately.

12.1 Inverse theory for waveform tomography

In this section, I summarize the inverse theory for frequency-domain waveform tomography, for the sake of completeness. For a detailed theoretical background, readers may refer to Tarantola (1984). But for the frequency domain treatment, please see Pratt and Worthington (1990) and Pratt *et al.* (1998).

In the inverse problem, we can define the objective function as

$$J(\mathbf{m}) = \frac{1}{2} [\mathbf{P}_{\text{obs}} - \mathbf{P}(\mathbf{m})]^{\text{H}} \mathbf{C}_{\text{D}}^{-1} [\mathbf{P}_{\text{obs}} - \mathbf{P}(\mathbf{m})], \quad (12.2)$$

where \mathbf{m} is the model to invert for, $\mathbf{P}(\mathbf{m})$ is a modelled data set, \mathbf{P}_{obs} is an observed data set, the superscript $^{\text{H}}$ denotes the complex conjugate transpose and \mathbf{C}_{D} is the covariance operator in the data space with units of $(data)^2$, defining the uncertainties in the data set.

To minimize the objective function (12.2), we use a gradient method (Tarantola, 1984, 2005). The gradient direction of the data misfit, $\hat{\mathbf{g}}$, is defined by

$$\hat{\mathbf{g}} \equiv \frac{\partial J}{\partial \mathbf{m}} = -\mathbf{L}^{\text{H}} \mathbf{C}_{\text{D}}^{-1} \delta \mathbf{P} = -\mathbf{L}^{\text{H}} \delta \hat{\mathbf{P}}, \quad (12.3)$$

where \mathbf{L} is the matrix of the Fréchet derivatives of the seismic waveform $\mathbf{P}(\mathbf{m})$ with respect to the model parameters, $\delta \mathbf{P} = \mathbf{P}_{\text{obs}} - \mathbf{P}(\mathbf{m})$ is the data residual and $\delta \hat{\mathbf{P}} = \mathbf{C}_{\text{D}}^{-1} \delta \mathbf{P}$ is a weighted data residual. The model update is then given by

$$\delta \mathbf{m} = -\alpha \mathbf{C}_{\text{M}} \hat{\mathbf{g}}, \quad (12.4)$$

where \mathbf{C}_{M} is called the model covariance matrix with units of $(model\ parameter)^2$ and α is a update step length that needs to be determined.

To evaluate the gradient $\hat{\mathbf{g}}$ using equation (12.3), we need to know the Fréchet matrix \mathbf{L} , which is obtained from the following linear formula:

$$\delta \mathbf{P} = \mathbf{L} \delta \mathbf{m}. \quad (12.5)$$

This formula, relating the data perturbation $\delta\mathbf{P}$ to the model perturbation $\delta\mathbf{m}$, is the first term in a Taylor's series for $\delta\mathbf{P}$. However, the direct computation of $[\mathbf{L}]_{ij} = \partial P_i / \partial m_j$ is a formidable task when P_i are seismic waveforms. Instead, Tarantola (1984) showed that the action of matrix \mathbf{L}^H on the weighted data residual vector $\delta\hat{\mathbf{P}}$ (equation 12.3) can be computed by a series of forward modelling steps, summarized as follows.

The frequency-domain acoustic wave equation for a constant-density medium with velocity $c_0(\mathbf{r})$ is

$$\left(\nabla^2 + \frac{\omega^2}{c_0^2(\mathbf{r})} \right) P_0(\mathbf{r}) = -S(\omega) \delta(\mathbf{r} - \mathbf{r}_0), \quad (12.6)$$

where \mathbf{r} is the position vector, \mathbf{r}_0 indicates the source position, $S(\omega)$ is the source signature of frequency ω and $P_0(\mathbf{r})$ is the (pressure) wavefield of this frequency. If the velocity is perturbed by a small amount $\delta c(\mathbf{r}) \ll c_0(\mathbf{r})$, that is, $c_0(\mathbf{r}) \rightarrow c(\mathbf{r}) = c_0(\mathbf{r}) + \delta c(\mathbf{r})$, the total wavefield is then perturbed to $P_0(\mathbf{r}) \rightarrow P(\mathbf{r}) = P_0(\mathbf{r}) + \delta P(\mathbf{r})$ correspondingly. Following wave equation (12.6), δP approximately satisfies

$$\left(\frac{2\omega^2}{c_0^3(\mathbf{r})} P_0(\mathbf{r}) \right)^{-1} \left(\nabla^2 + \frac{\omega^2}{c_0^2(\mathbf{r})} \right) \delta P(\mathbf{r}) = \delta c(\mathbf{r}). \quad (12.7)$$

Considering $\delta c(\mathbf{r})$ as a series of 'virtual sources' over \mathbf{r} , the integral solution for $\delta P(\mathbf{r})$ can be expressed as

$$\left(\frac{2\omega^2}{c_0^3(\mathbf{r})} P_0(\mathbf{r}) \right)^{-1} \delta P(\mathbf{r}) = - \int_{\mathcal{M}} \delta c(\mathbf{r}') G(\mathbf{r}, \mathbf{r}') d\mathbf{r}', \quad (12.8)$$

where $G(\mathbf{r}, \mathbf{r}')$ is Green's function of the response at \mathbf{r} to a point source at \mathbf{r}' for the original velocity field and \mathcal{M} indicates the integration over the model space. Formally, Green's function satisfies (Roach, 1982)

$$\left(\nabla^2 + \frac{\omega^2}{c_0^2(\mathbf{r})} \right) G(\mathbf{r}, \mathbf{r}') = -\delta(\mathbf{r} - \mathbf{r}'). \quad (12.9)$$

Therefore, Green's function can be interpreted as an impulse response in the background medium.

Note that in the acoustic case we assume density to be constant, and define the model by the velocity field only, $\mathbf{m} \equiv \mathbf{c}$. Then, comparing equation (12.8) against the matrix-vector form of equation (12.5), we see that the Fréchet matrix is defined with element

$$L(\mathbf{r}, \mathbf{r}') = -\frac{2\omega^2}{c_0^3(\mathbf{r})} P_0(\mathbf{r}) G(\mathbf{r}, \mathbf{r}'). \quad (12.10)$$

Substituting this Fréchet kernel into equation (12.3), $\hat{\mathbf{g}} = -\mathbf{L}^H \delta \hat{\mathbf{P}}$, we obtain the gradient component

$$\hat{g}(\mathbf{r}) = \int_{\mathcal{D}} \left(\frac{2\omega^2}{c_0^3(\mathbf{r})} \right)^* P_0^*(\mathbf{r}) G^*(\mathbf{r}', \mathbf{r}) \delta \hat{P}(\mathbf{r}'), \quad (12.11)$$

where $G^*(\mathbf{r}', \mathbf{r})$ is the complex conjugate of Green's function $G(\mathbf{r}, \mathbf{r}')$. Replacing the integral over the data space, \mathcal{D} , with a summation over source and receiver pairs, denoted by s and r respectively, as the source and receiver positions are inherently discrete and finite in number, equation (12.11) becomes

$$\hat{g}(\mathbf{r}) = \left(\frac{2\omega^2}{c_0^3(\mathbf{r})} \right)^* \sum_s \sum_g P_0^*(\mathbf{r}; \mathbf{r}_s) G^*(\mathbf{r}_r, \mathbf{r}) \delta \hat{P}(\mathbf{r}_r; \mathbf{r}_s). \quad (12.12)$$

Also invoking the reciprocity of Green's function, we obtain

$$\hat{g}(\mathbf{r}) = \left(\frac{2\omega^2}{c_0^3(\mathbf{r})} \right)^* \sum_s \left(P_0^*(\mathbf{r}; \mathbf{r}_s) \sum_r G^*(\mathbf{r}, \mathbf{r}_r) \delta \hat{P}(\mathbf{r}_r; \mathbf{r}_s) \right). \quad (12.13)$$

Given a single source point \mathbf{r}_s , defining the wavefield generated by a series of virtual sources $\delta \hat{P}(\mathbf{r}_r; \mathbf{r}_s)$ as

$$P_b(\mathbf{r}; \mathbf{r}_s) = \sum_r G^*(\mathbf{r}, \mathbf{r}_r) \delta \hat{P}(\mathbf{r}_r; \mathbf{r}_s), \quad (12.14)$$

we finally obtain

$$\hat{\mathbf{g}}(\mathbf{r}) = \left(\frac{2\omega^2}{c_0^3(\mathbf{r})} \right)^* \sum_s P_0^*(\mathbf{r}; \mathbf{r}_s) P_b(\mathbf{r}; \mathbf{r}_s). \quad (12.15)$$

In equation (12.14), the conjugated Green's function $G^*(\mathbf{r}, \mathbf{r}_r)$ is the frequency-domain expression of the time reversal, and the operation $G^*(\mathbf{r}, \mathbf{r}_r) \delta \hat{\mathbf{P}}(\mathbf{r}_r; \mathbf{r}_s)$ is thus referred to as data residual backpropagation. In equation (12.15), the multiplication of the conjugated forward wavefield $P_0^*(\mathbf{r}; \mathbf{r}_s)$ and the backpropagation wavefield $P_b(\mathbf{r}; \mathbf{r}_s)$ corresponds to a zero-lag correlation in the time domain, separately for each source (Tarantola, 1984).

Note that wavefield $P_b(\mathbf{r}; \mathbf{r}_s)$ is not calculated directly from equation (12.14), but is computed using the same forward modelling scheme as used for the wave equation (12.6) with virtual sources $\delta \hat{\mathbf{P}}^*(\mathbf{r}_r; \mathbf{r}_s)$. We solve the frequency-domain wave equation (12.6) using a finite-difference scheme (Alford *et al.*, 1974; Kelly *et al.*, 1976; Virieux, 1986; Pratt, 1990, 1999; Song and Williamson, 1995; Štekl and Pratt, 1998; Min *et al.*, 2000). When considering the attenuation effect, the velocity values used in the finite-difference wave equation are complex-valued, as shown in Chapter 10.

In summary, frequency-domain waveform tomography is performed iteratively and, for each iteration, the inversion procedure may be divided into four steps:

- 1) calculating the synthetic wavefield $\mathbf{P}(\mathbf{m})$ for a given initial model, and the weighted data residual $\delta \hat{\mathbf{P}}(\mathbf{r}_r; \mathbf{r}_s)$;
- 2) backpropagating conjugated data residuals $\delta \hat{\mathbf{P}}^*(\mathbf{r}_r; \mathbf{r}_s)$ to get the conjugated wavefield $P_b^*(\mathbf{r}; \mathbf{r}_s)$ for each source;
- 3) correlating the conjugated forward wavefield $P_0^*(\mathbf{r}; \mathbf{r}_s)$ and the backpropagation wavefield $P_b(\mathbf{r}; \mathbf{r}_s)$ and finding the gradient direction $\hat{\mathbf{g}}$;
- 4) estimating the model update $\delta \mathbf{m} = -\alpha \mathbf{C}_M \hat{\mathbf{g}}$.

The optimal step length α in step 4 can be found using a linear approximation or a simple line search for a minimum of the objective function (Tarantola, 2005).

12.2 Issues in real data application

Frequency-domain waveform tomography uses distinct frequency components to adequately reconstruct either the real-valued or complex-valued subsurface velocity field. Although this makes waveform tomography a computationally tractable problem for production uses, its applicability to real seismic data, particularly in petroleum exploration and development scale, needs to be examined. Wang and Rao (2006) listed some strategies for application of the method to real data, as follows.

- 1) As real data are often band-limited with missing low frequencies, a good starting model is necessary for waveform tomography, to fill in the gap at low frequencies before the inversion of available frequencies.
- 2) In the inversion stage, a group of frequencies should be used simultaneously at each iteration, to suppress the effect of data noise in the frequency domain.
- 3) Meanwhile, a smoothness constraint on the model must be used in the inversion, to cope with the effects of data noise, uneven distribution of ray coverage and the strong sensitivities of short-wavelength model variations.

Let us consider a real example of a crosshole seismic data set, shown in Figure 12.1, acquired from two parallel boreholes 300 m apart. Due to the complexity of the local geology, the velocity variations are extreme (between 3000 and 5500 m/s), making the inversion problem highly non-linear. The penetrating rocks consist of alternating mudstone and sandstone, which are horizontally layered thin-sheet lake-environment sedimentary rocks, and igneous rock at the bottom. A string of 58 hydrophone receivers at 1.52-m spacing was placed in one borehole. Small explosive charges were fired successively in the other borehole at 0.38-m intervals. Coverage was then extended by repositioning the hydrophone string in the receiver borehole, with one receiver position overlap for tying, and repeating the shot sequence. The triggering signal for the seismograph was obtained by wrapping a wire around the end of the detonator. This opens the circuit when the shot is fired, providing an accurate time break.

Figure 12.1a displays an example common-receiver gather at 2600 m depth, with the shot depth ranging from 2497 to 2950 m. The data contain

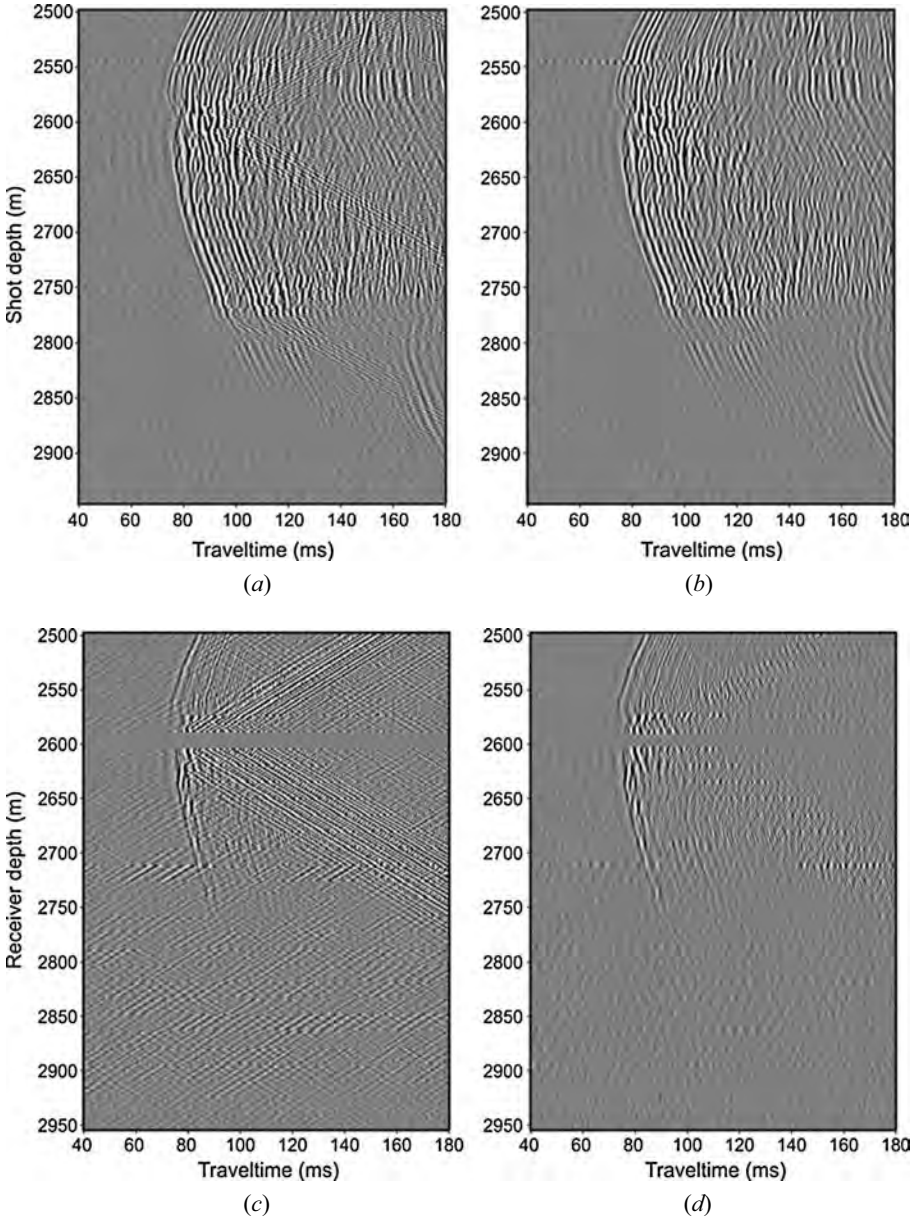


Figure 12.1 (a) An example common-receiver gather at depth 2600 m that shows weak tube waves. (b) The common-receiver gather after f - k filtering for tube-wave attenuation. (c) An example common-shot gather at depth 2600 m which evidently shows strong tube waves. (d) The shot gather after f - k filtering for tube-wave attenuation.

clear and coherent first arrivals, and the tube waves generated in the shot borehole. The tube waves appear to have a linear moveout in the common-receiver gather, with velocity of about 1460 m/s. The common-receiver gather after tube wave attenuation using an f - k filter is shown in Figure 12.1b, which also allows us to access the repeatability of the source.

The common-receiver gathers then are resorted into common-shot gathers. Figure 12.1c displays a common-shot gather at 2600 m depth, which contains much stronger tube waves. The strong tube waves are generated by the interaction of the direct body waves with discontinuities in the receiver borehole. Figure 12.1d shows the result after tube-wave attenuation using an f - k filter. In the shot gather, the receiver spacing is 1.52 m and the Nyquist wavenumber is $k_{\text{Nyq}} = 0.329 \text{ m}^{-1}$. For the tube waves with $dz/dt = 1470 \text{ m/s}$, any frequency component $f > k_{\text{Nyq}}(dz/dt) \approx 485 \text{ Hz}$ is severely aliased. Thus, we simply filter out the frequencies higher than 485 Hz. Data noise has been eliminated by a form of forward-backward linear prediction filtering in the frequency-space domain (Wang, 1999).

Figure 12.2a displays the frequency spectra of all traces within the example common-shot gather at 2600 m depth. Based on the frequency spectrum, on which there is no energy for frequency lower than 190 Hz, we choose the frequency band between 190 and 485 Hz for the inversion. Note here that we use a real-valued frequency in waveform inversion, but complex-valued velocity. When considering wave attenuation effects, one can also use a complex-valued frequency, see for example Pratt *et al.* (2005). Figure 12.2b is the source wavelet used in the waveform inversion, which is estimated directly from first arrives.

After tube-wave suppression, we apply windowing to the data to mute any energy arriving later than a few cycles following the direct arrivals (Pratt and Shipp, 1999; Pratt *et al.*, 2005). After muting, only the first arrival and transmission waveforms are in the crosshole seismic data. Windowing also serves to exclude remaining shear wave energy from the data. This preprocessing step is required primarily to precondition the data to force the inversion to fit the direct arrivals, which contain the critical information on the low and intermediate wavenumbers in the model. At a later stage, the window size can be increased in time to include more of the data.

Figure 12.3a shows an example shot gather (at depth 2758 m) after data windowing. The window length is selected to be as short as possible to enhance the signal-to-noise ratio and to eliminate shear waves, but still to include the visible diffractions and transmission associated with the direct

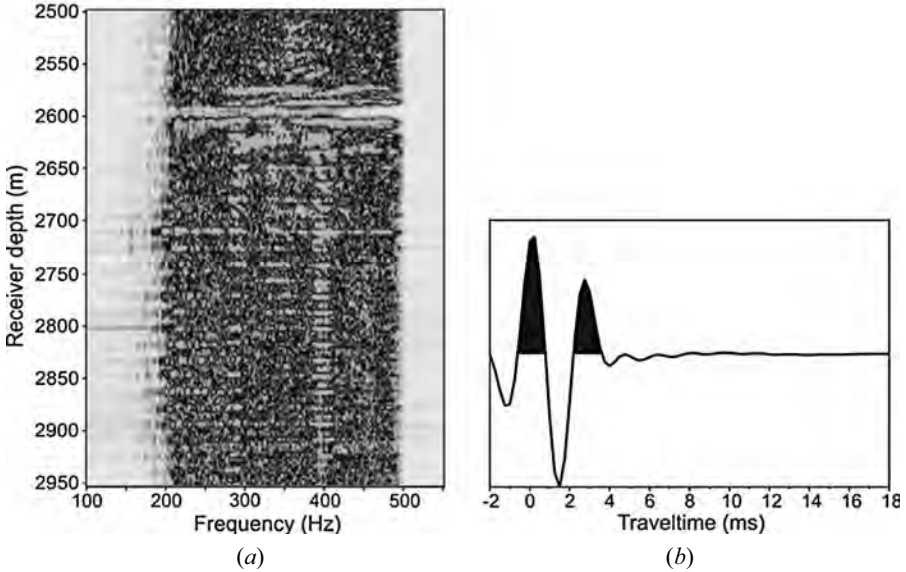


Figure 12.2 (a) The amplitude spectrum of a typical shot gather at 2600 m (Figure 12.1d). It has frequency bandwidth between 190 and 485 Hz. (b) Source wavelet estimated from real data. It is used in waveform inversion.

arrival. For comparison, Figures 12.3b and 12.3c display two modelled shot gathers generated based on tomographic inversion models. The first is a synthetic gather based on the velocity model alone, and the second based on both the velocity and attenuation models reconstructed by waveform tomography. Although a frequency-domain waveform inversion approach uses only a number of selected frequencies, the data comparison reveals that the inversion model is indeed a good representation of the subsurface earth model.

In the following inversion, we start from the lower frequencies. For low frequencies the inversion method is more tolerant of velocity errors, as these are less likely to lead to errors of more than half a cycle in the waveforms. As the inversion proceeds, we move progressively to higher frequencies.

12.3 Waveform inversion for the velocity model

For the inversion of this real data set, we make the velocity model discrete with cell size 3 m to satisfy the criterion of four cells per wavelength for the

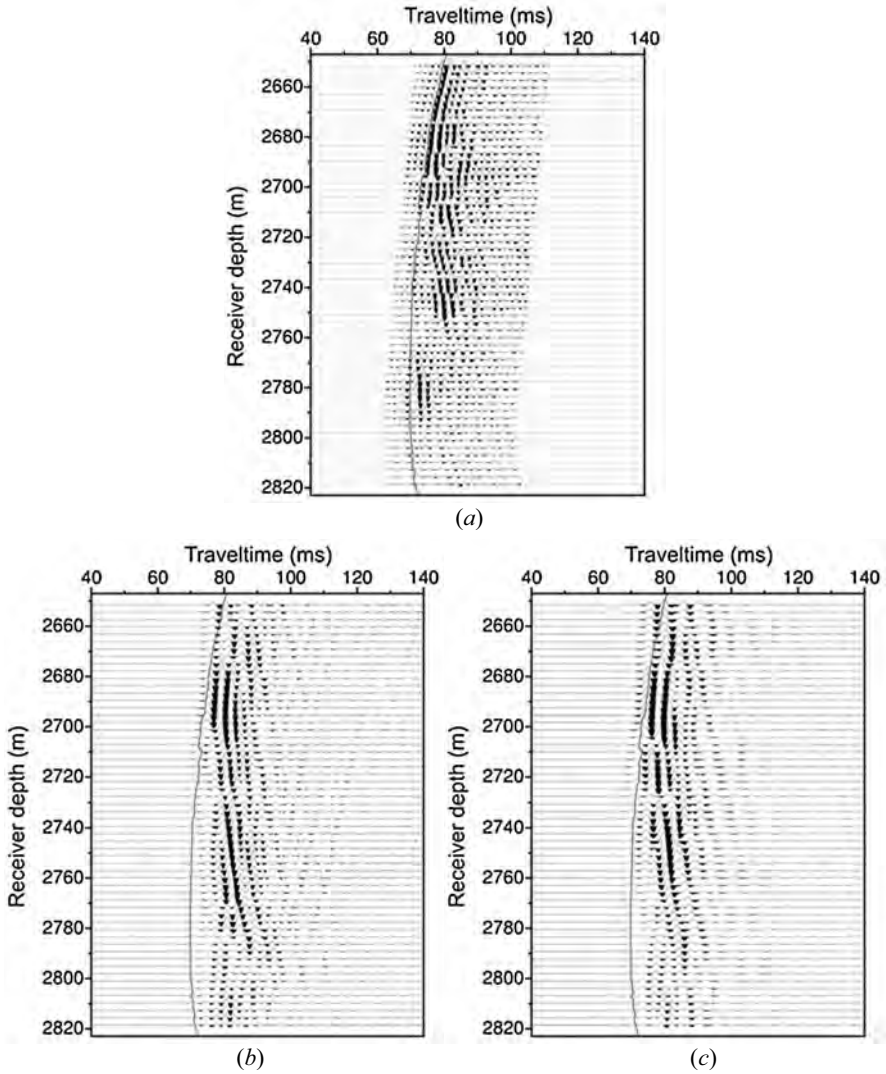


Figure 12.3 (a) An example shot gather of the real data set after data windowing. (b) Synthetic shot gather generated from the velocity model alone. (c) Synthetic shot gather generated using both the velocity and attenuation models obtained from waveform tomography. The grey curve is the time line of first arrival picked from real data.

highest frequency (485 Hz) that we use in the inversion. The depth range that we choose to invert for is from 2497 to 3022 m. Therefore, there are altogether 101 rows and 176 columns in the grid.

At the beginning of the waveform-inversion scheme, a sufficiently

accurate starting model is necessary. This model should be capable of describing the time-domain data to within a half of the dominant period, to avoid fitting the wrong cycle of the waveforms (Pratt *et al.*, 2005). The lower the frequency, the less accurate the starting model needs to be. However, all real data are band-limited, and thus a certain accuracy is required for the starting model. As we have seen from Figure 12.2, this real data set has a frequency gap between 0 and 190 Hz. This lack of low-frequency information makes the waveform inversion strongly dependent on the initial model. For the waveform tomography, we use the traveltime inversion result as an initial model and proceed with waveform inversion using the different frequencies.

Figure 12.4a displays the initial model, the result of traveltime tomography (Rao and Wang, 2005). Figure 12.4b shows the ray density, the (normalized) total length of ray segments across each single cell, a direct indicator of the confidence in the traveltime inversion solution, where a curved ray path is retraced iteratively along with velocity updating. This measurement of certainty, being proportional to the ray density, can also be used in waveform tomography to build a diagonal matrix \mathbf{C}_M^{-1} , the inverse of model covariance matrix. The latter is applied to the gradient vector $\hat{\mathbf{g}}$ before model updating (see step 3, p.214).

In waveform tomography when dealing with real data, a model smoothness constraint is a necessity. A number of real data experiments we have conducted indicate that, if we did not use a smoothness constraint in the inversion, waveform tomography did not converge at all. The primary cause is the effect of data noise, which is not necessarily white in the frequency domain. Strong outliers might have a strong and biased influence on the model update. As the frequency domain data samples are complex-valued, it is not easy to mitigate the data noise in a way similar to winnowing traveltimes and amplitudes (Wang *et al.*, 2000). In a linearized procedure of waveform tomography, if strong outliers are transferred linearly to strong model updates, it will cause the inverse problem to be unstable and divergent.

A second effect is the unevenly distributed ray density. As shown in Figure 12.4b, the ray density distribution appears to have a short-wavelength variation. An uneven distribution of ray density will cause a biased distribution of model update, as a model update is (inversely) proportional to the ray density through data residual backpropagation. When constructing the model covariance matrix \mathbf{C}_M , we can smooth the ray density distribution so as to change the weight of the model update. This approach

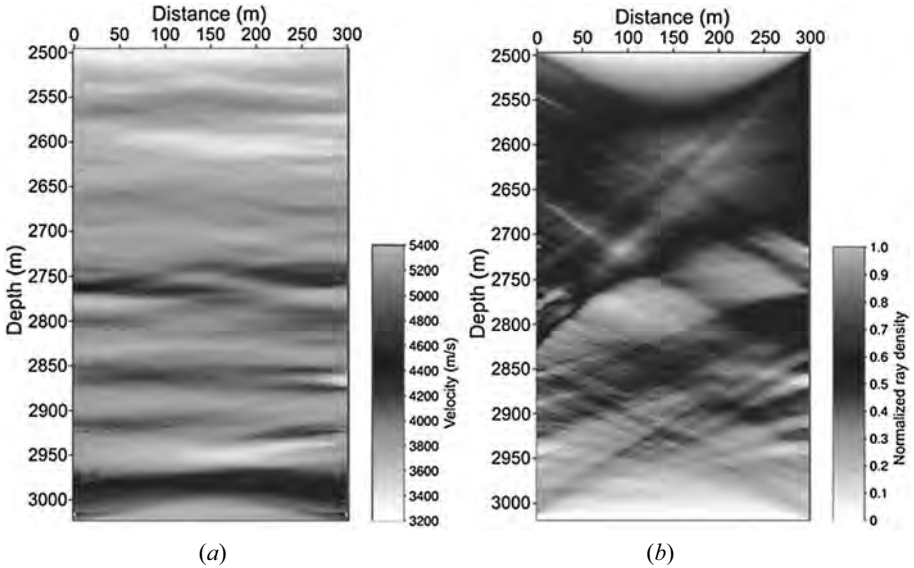


Figure 12.4 (a) The initial velocity model for waveform inversion, generated by traveltimes inversion. (b) Ray density of the real seismic data set.

might reduce the roughness of model update for any single iteration and slow down the convergence of the iterative procedure, but may not mitigate the problem in the final solution. Ray density distribution is a measurement of the illumination in the physical experiment, and thus reflects directly the resolving power distribution (Rao *et al.*, 2006).

The third effect is due to the model sensitivity. Investigation in Wang and Pratt (1997) revealed that in traveltimes inversion the long-wavelength components of the velocity field are more sensitive than shorter wavelengths, and that in amplitude inversion short-wavelength components of the velocity field are much more sensitive than long-wavelength components. Therefore, in waveform inversion where amplitude information dominates, the data residual tends to attribute to the shortest-wavelength components of the model update first (Hicks and Pratt, 2001). This is contradictory to the philosophy of iterative linear inversion. In an iterative inversion, we must get the background right first, so that linearization can be used for the inverse problem.

This analysis suggests that we could use a smooth operator of different size at each iteration, starting with a large size and then reducing the size gradually as iterations proceed. This approach is sometimes referred to as a multiscale approach. Pratt *et al.* (1998) has given a complete treatment of a

reduced parameterization approach which incorporates all possible such multi-scale approaches. It is also worthwhile to mention that Wang and Houseman (1994, 1995) used a Fourier series to parameterize the velocity model (and interface geometry) with different wavenumbers and then partitioned them into different subspaces so that they could be inverted simultaneously. In the following waveform inversion, we use a fixed 3×3 smoothing operator. That is, any model update δm_i is an average value of neighbouring nine points, centred at the i th cell, with equal weights.

To further combat the noise in real data, in the frequency-domain waveform inversion, we use a group of five neighbouring frequencies simultaneously (Pratt and Shipp, 1999; Wang and Rao, 2006). In this example, we select 60 frequencies consecutively (190, 195, 200, \dots , 485 Hz), and assign them to 12 groups with increasing frequency content. We start with the initial model generated from traveltime inversion, and invert the first frequency group (190, 195, \dots , 210 Hz) of data. Then, we switch to a higher-frequency group (215, 220, \dots , 235 Hz) of the data as the inversion progresses. The result from each lower-frequency group is used as the starting model for the inversion of the next higher-frequency group. For each group, three iterations are carried out, proceeding through all groups. For each iteration, the gradient of each frequency group is computed using all five frequencies simultaneously. Figure 12.5a shows the tomographic image after using the first frequency group (190, 195, 200, 205 and 210 Hz), and Figure 12.5b is the final result after using all 12 frequency groups consecutively.

Comparing the final result of waveform inversion (Figure 12.5b) with the traveltime inversion result (Figure 12.4a), we can see that the results of waveform inversion appear to be a significantly better representation of the geological layering than the original traveltime inversion result that is used as a starting model. The most striking features of the final waveform inversion results are high-velocity layers. At the section from 2500 to 2900 m, the layer appears laterally continuous across the section, and the vertical resolution is clearly much better. Deeper layers are discontinuous and faulted. In addition, a number of low-velocity layers are evident on the image.

12.4 Waveform tomography for the attenuation model

The magnitude of the real-part velocity is approximately 10^3 , the magnitude of Q^{-1} is just approximately 10^{-2} , thus the magnitude of the imaginary-part

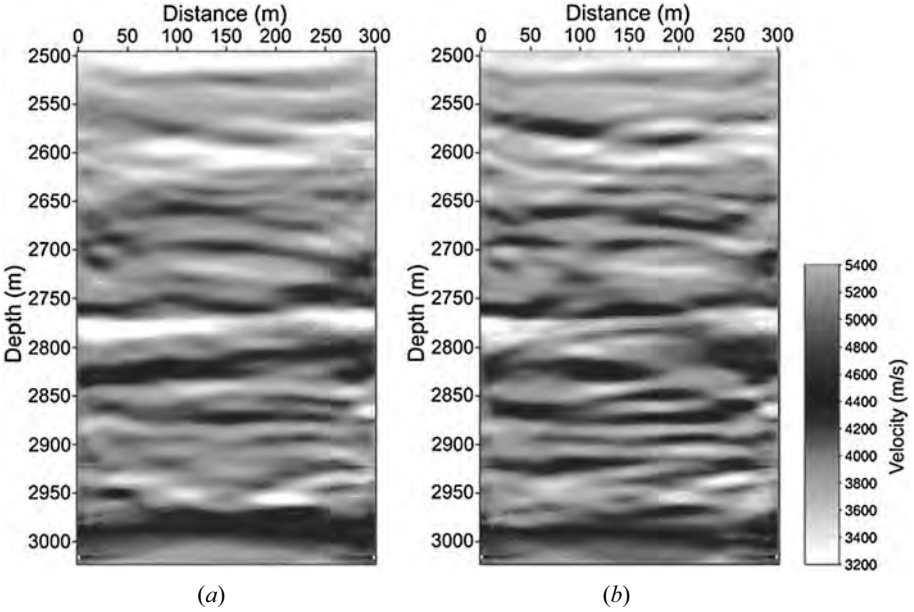


Figure 12.5 Waveform tomography for the velocity model: (a) the velocity image after using the first frequency group (190, 195, ..., 210 Hz); (b) the final inversion result after using all 12 frequency groups.

velocity is approximately 10. Therefore, their contributions to the objective function are very different. A small percentage perturbation in velocity may have equal or larger effect on the objective function than a big percentage perturbation in Q^{-1} . Therefore, we perform inversion in two stages. In the first stage, we invert only for the real-part velocity model by assuming Q^{-1} is zero. This assumption is justified as the velocity and the attenuation have five orders of magnitude difference.

In the second stage, we invert only for the imaginary-part velocity, i.e. the attenuation model, and keep the inverted real-part velocity model fixed. We use the same scheme as used in velocity inversion: each time, input a group of frequencies to the inversion; proceed the inversion gradually from low-frequency groups to high-frequency groups; also impose a 3×3 smoothness constraint on the model.

After using the first frequency group in this second stage inversion, we obtain the attenuation model shown in Figure 12.6a, which immediately reveals the strong attenuation zones. After using all the frequency groups,

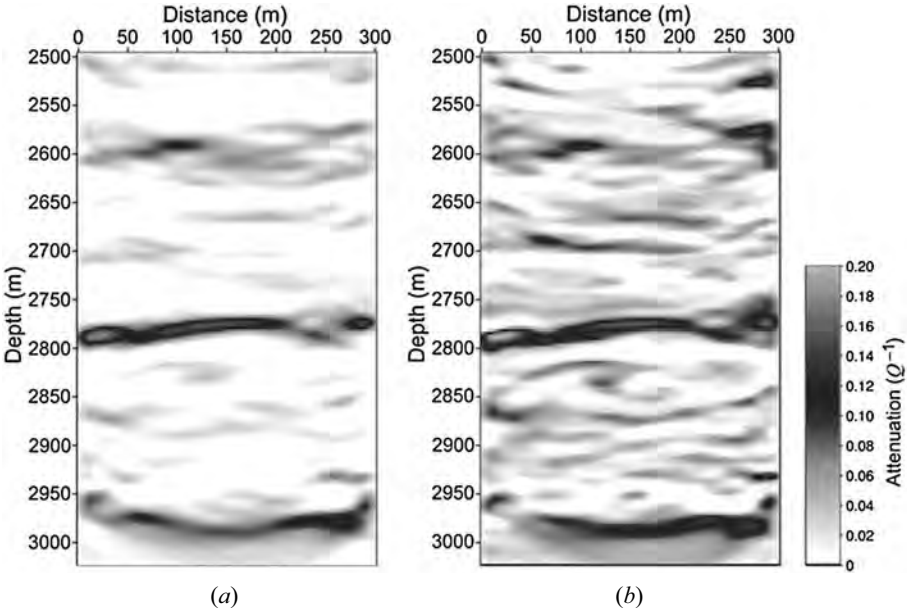


Figure 12.6 Waveform tomography for the attenuation model: (a) the attenuation image after using the first frequency group (190, 195, ..., 210 Hz); (b) the final attenuation model obtained after using all 12 frequency groups.

the reconstructed attenuation model shown in Figure 12.6b has contrary structural features, compared to the velocity model shown in Figure 12.5b. The low-velocity variations correspond to the high-attenuation zones. For example, at depth 2750–2850 m, the model shows two strips of low attenuation. These low-attenuation zones correspond to the two high-velocity layers, respectively.

As we have mentioned above, the inversion is implemented in the frequency domain. Figure 12.7a shows an example frequency slice (at 260 Hz) of the amplitudes of the real data set. Each point in the data matrix is the amplitude of a frequency component of the seismic trace associated with a source-receiver pair. Figure 12.7b displays the corresponding frequency slice of the amplitudes of a modelled data set generated from the velocity model alone (assuming $Q^{-1}=0$), and Figure 12.7c is generated from the final velocity and attenuation models, reconstructed from waveform tomography. Comparing these three frequency slices, we can see that the amplitude variation in Figure 12.7c is much closer to the amplitude

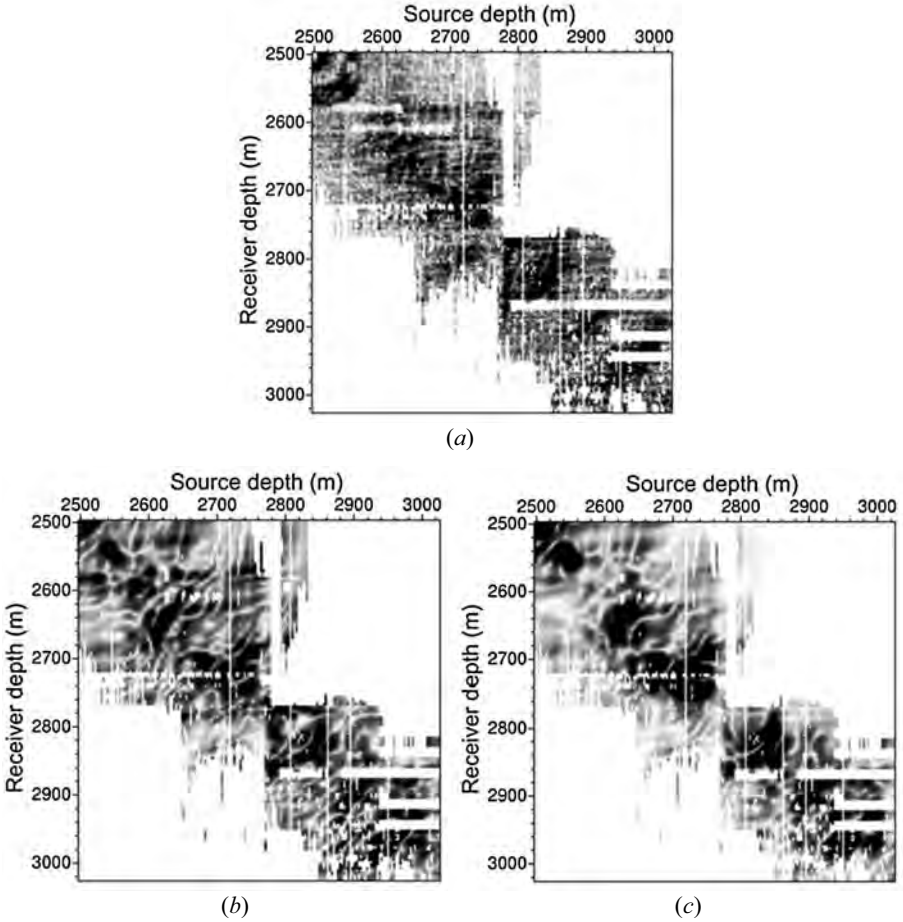


Figure 12.7 (a) An amplitude slice (at frequency 260 Hz) of the observed crosshole seismic data. (b) The amplitude slice, at the same frequency, of modelled data generated from the velocity model only. (c) The amplitude slice of modelled data generated from the final velocity and attenuation models of waveform tomography.

variation in Figure 12.7a. That is, when considering the attenuation effect on the seismic wavefield, we can have better data matching between the raw and theoretical waveforms in waveform tomography, compared with the inversion for velocity alone.

In this chapter, we have dealt with seismic inversion with crosshole recording geometry. As Chapter 9 was about reflection seismic migration with inverse Q filtering, it seems desirable to follow this with a more

expansive treatment of reflection seismic tomography incorporating Q , given the future importance of reflection seismic inversion as a likely replacement for migration. This provides me with a suggestion for the research direction; that is, reflection seismic waveform tomography in two and three dimensions.

References

- Aki K. and Richards P. G. 1980. *Quantitative Seismology*. W. H. Freeman and Co., San Fransisco.
- Aldridge D. F. 1990. The Berlage wavelet. *Geophysics* **55**, 1508–11.
- Alford R. M., Kelly K. R. and Boore D. M. 1974. Accuracy of finite-difference modelling of the acoustic wave equation. *Geophysics* **39**, 834–42.
- Aminzadeh F. and Mendel J. M. 1983. Normal-incidence layered system state-space models which include absorption effects. *Geophysics* **48**, 259–71.
- Amundsen L. and Mittet R. 1994. Estimation of phase velocities and Q -factors from zero-offset vertical seismic profile data. *Geophysics* **59**, 500–17.
- Azimi S. A., Kalinin A. V., Kalinin V. V. and Pivovarov B. L. 1968. Impulse and transient characteristics of media with linear and quadratic absorption laws. *Izvestiya - Physics of the Solid Earth* **2**, 88–93.
- Badri M. and Mooney H. M. 1987. Q measurements from compressional seismic waves in unconsolidated sediments. *Geophysics* **52**, 772–84.
- Bano M. 1996. Q -phase compensation of seismic records in the frequency domain. *Bulletin of the Seismological Society of America* **86**, 1179–86.
- Barnes A. E. 1991. Instantaneous frequency and amplitude at the envelope peak of a constant-phase wavelet. *Geophysics* **56**, 1058–60.
- Barnes A. E. 1993. Instantaneous spectral bandwidth and dominant frequency with applications to seismic reflection data. *Geophysics* **58**, 419–28.
- Bastiaans M. J. 1980. Gabor's expansion of a signal into Gaussian elementary signals. *Proceedings of the IEEE* **68**, 538–9.
- Ben-Menahem A. and Singh S. J. 1981. *Seismic Waves and Sources*. Springer-Verlag, New York.
- Bickel S. H. 1993. Similarity and the inverse Q filter: the Pareto-levy stretch. *Geophysics* **58**, 1629–33.
- Bickel S. H. and Natarajan R. R. 1985. Plane-wave Q deconvolution. *Geophysics* **50**, 1426–39.
- Bracewell R. 1965. *The Fourier Transform and Its Applications*. McGraw-Hill Book Co., New York.

- Brennan B. J. and Stacey F. D. 1977. Frequency dependence of elasticity of rock: test of seismic velocity dispersion. *Nature* **268**, 220–2.
- Carcione J. M. 2007. *Wavefields in Real Media: Wave Propagation in Anisotropic, Anelastic, Porous and Electromagnetic Media*, 2nd edn. Elsevier Science, Amsterdam.
- Carpenter E. W. 1966. Absorption of elastic waves: an operator for a constant Q mechanism. United Kingdom Atomic Energy Authority AWRE Report. Reprinted in Toksöz M. N. and Johnston D. H. (eds.), *Seismic Wave Attenuation*. Geophysics reprint series 2 (1981), pp. 418–30. Society of Exploration Geophysicists, Tulsa.
- Casula G. and Carcione J. M. 1992. Generalized mechanical model analogies of viscoelastic behaviour. *Bolletina di Geofisica Teorica ed Applicata* **34**, 235–56.
- Claerbout J. F. 1976. *Fundamentals of Geophysical Data Processing*. McGraw-Hill Book Co., New York.
- Claerbout J. F. 1985. *Imaging the Earth's Interior*. Blackwell Scientific Publications, Oxford.
- Clark R. A., Carter A. J., Nevill P. C. and Benson P. M. 2001. Attenuation measurements from surface seismic data: Azimuthal variation and time-lapse case studies. *Extended Abstracts of the 63rd Conference of European Association of Geoscientists & Engineers* L-28.
- Cole K. S. and Cole R. H. 1941. Dispersion and absorption in dielectrics, I: alternating current characteristics. *Journal of Chemical Physics* **9**, 342–51.
- Cui J. and He J. 2004. 2D seismic migration with compensation: a preliminary study. *Journal of Geophysics and Engineering* **1**, 263–7.
- Dai N. and West G. F. 1994. Inverse Q migration. *Expanded Abstracts of the 64th Annual Meeting of Society of Exploration Geophysicists*, 1418–21.
- Dasgupta R. and Clark R. A. 1998. Estimation of Q from surface seismic reflection data. *Geophysics* **63**, 2120–8.
- Dasios A., Astin T. R. and McCann C. 2001. Compressional-wave Q estimation from full-waveform sonic data. *Geophysical Prospecting* **49**, 353–73.
- Duren R. E. and Trantham E. C. 1997. Sensitivity of the dispersion correction to Q error. *Geophysics* **62**, 288–90.
- Feichtinger H. G. and Strohmer T. (eds.) 1998. *Gabor Analysis and Algorithms: Theory and Applications*. Birkhäuser Boston.
- Futterman W. I. 1962. Dispersive body waves. *Journal of Geophysical Research* **67**, 5279–91.
- Gabor D. 1946. Theory of communication. *Journal of the Institute of Electrical Engineers* **93**, 429–57.
- Ganley D. C. 1981. A method for calculating synthetic seismograms which include the effects of absorption and dispersion. *Geophysics* **46**, 1100–7.
- Gazdag J. 1978. Wave-equation migration with the phase-shift method. *Geophysics* **43**, 1342–51.
- Gazdag J. and Sguazzero P. 1984. Migration of seismic data. *Proceedings of the IEEE* **72**, 1302–15.
- Gelius L. J. 1987. Inverse Q filtering: a spectral balancing technique. *Geophysical Prospecting* **35**, 656–67.
- Gladwin M. T. and Stacey F. D. 1974. Anelastic degradation of acoustic pulses in rock. *Physics of the Earth and Planetary Interior* **8**, 332–6.
- Grossman J. P., Margrave G. F., Lamoureux M. P. and Aggarwala R. 2002. A robust algorithm for constant- Q wavelet estimation using Gabor analysis. *Expanded Abstracts of the 72nd Annual Meeting of Society of Exploration Geophysicists*, 2210–3.
- Gubbins D. 2004. *Time Series Analysis and Inverse Theory for Geophysicists*. Cambridge University Press, Cambridge.

- Guerra R. and Leaney S. 2006. $Q(z)$ model building using walkaway VSP data. *Geophysics* **71**, V127–32.
- Guo J. and Wang Y. 2004. Recovery of a target reflection underneath coal seams. *Journal of Geophysics and Engineering* **1**, 46–50.
- Hale D. 1981. An inverse- Q filter. *Stanford Exploration Project Report* **26**, 231–43.
- Hale D. 1982. Q -adaptive deconvolution. *Stanford Exploration Project Report* **30**, 133–58.
- Halpern L. and Trefethen L. N. 1988. Wide-angle one-way wave equations. *Journal of the Acoustical Society of America* **84**, 1397–404.
- Hamilton E. L. 1972. Compressional-wave attenuation in marine sediments. *Geophysics* **37**, 620–46.
- Hanyga A. and Seredyńska M. 1999a. Asymptotic ray theory in poro- and viscoelastic media. *Wave Motion* **30**, 175–95.
- Hanyga A. and Seredyńska M. 1999b. Some effects of the memory kernel singularity on wave propagation and inversion in poroelastic media, I: forward problems. *Geophysical Journal International* **137**, 319–35.
- Hargreaves N. D. 1992. Similarity and inverse Q filter: some simple algorithms for inverse Q filtering. *Geophysics* **57**, 944–7.
- Hargreaves N. D. and Calvert A. J. 1991. Inverse Q filtering by Fourier transform. *Geophysics* **56**, 519–27.
- Harris P. E., Kerner C. and White R. E. 1997. Multichannel estimation of frequency-dependent Q from VSP data. *Geophysical Prospecting* **45**, 87–109.
- Hicks G. and Pratt R. G. 2001. Reflection waveform inversion using local descent methods: estimating attenuation and velocity over a gas-sand deposit. *Geophysics* **66**, 598–612.
- Hillier K. W. 1949. A method of measuring some dynamic elastic constants and its application to the study of high polymers. *Proceedings of the Physical Society (Section B)* **62**, 701–13.
- Irving J. D. and Knight R. J. 2003. Removal of wavelet dispersion from ground-penetrating radar data. *Geophysics* **68**, 960–70.
- Jacobson R. S. 1987. An investigation into the fundamental relationship between attenuation, phase dispersion, and frequency using seismic refraction profiles over sedimentary structures. *Geophysics* **52**, 72–87.
- Johnston D. H. and Toksöz M. N. 1981. Definitions and terminology. In Toksöz M. N. and Johnston D. H. (eds.), *Seismic Wave Attenuation*. Geophysics reprint series 2 (1981), pp. 1–5. Society of Exploration Geophysicists, Tulsa.
- Jones T. D. 1986. Pore fluids and frequency-dependent wave propagation in rocks. *Geophysics* **51**, 1939–53.
- Kelly K. R., Treitel S. and Alford R. M. 1976. Synthetic seismograms: a finite difference approach. *Geophysics* **41**, 2–27.
- Kim Y.C., Gonzalez R. and Berryhill J.R. 1989. Recursive wavenumber-frequency migration. *Geophysics* **54**, 319–329.
- Kjartansson E. 1979. Constant Q wave propagation and attenuation. *Journal of Geophysical Research* **84**, 4737–48.
- Klimentos T. 1995. Attenuation of P - and S -waves as a method of distinguishing gas and condensate from oil and water. *Geophysics* **60**, 447–58.
- Kolsky H. 1953. *Stress Waves in Solids*. Clarendon Press, Oxford.
- Kolsky H. 1956. The propagation of stress pulses in viscoelastic solids. *Philosophical Magazine* **1**, 693–710.
- Kramers H. A. 1927. Le diffusion de la lumière par les atomes. *Atti del Congresso Internazionale della fisica (Como, Italy)* **2**, 545–57.

- Krönig R. 1926. On the theory of the dispersion of X -rays. *Journal of the Optical Society of America* **12**, 547–57.
- Lee M. and Suh S. 1985. Optimization of one-way equation. *Geophysics* **50**, 1634–7.
- Liu H.-P., Anderson D. L. and Kanamori H. 1976. Velocity dispersion due to anelasticity: implication for seismology and mantle composition. *Geophysical Journal of the Royal Astronomical Society* **47**, 41–58.
- Loewenthal D., Lu L., Roberson R. and Sherwood J. 1976. The wave equation applied to migration. *Geophysical Prospecting* **24**, 380–99.
- Lomnitz C. 1957. Linear dissipation in solids. *Journal of Applied Physics* **28**, 201–5.
- Margrave G. F. 1998. Theory of nonstationary linear filtering in the Fourier domain with application to time-variant filtering. *Geophysics* **63**, 244–59.
- Margrave G. F. 2001. Direct Fourier migration for vertical velocity variations. *Geophysics* **66**, 1504–14.
- Margrave G. F., Lamoureux M. P., Grossman J. P. and Iliescu V. 2002. Gabor deconvolution of seismic data for source waveform and Q correction. *Expanded Abstracts of the 72nd Annual Meeting of Society of Exploration Geophysicists*, 2190–3.
- Mason W. P. 1958. *Physical Acoustics and Properties of Solids*. Van Nostrand, Princeton, NJ.
- McCann C., Sothcott J. and Assefa S. B. 1997. Prediction of petrophysical properties from seismic quality factor measurements. In Lovell M. A. and Harvey P. K. (eds.), *Development in Petrophysics*. Geological Society Special Publication **122**, 121–30.
- McDonal F. J., Angona F. A., Mills R. L., Sengbush R. L., Van Nostrand R. G. and White J. E. 1958. Attenuation of shear and compressional waves in Pierre shale. *Geophysics* **23**, 421–39.
- Meyer O. E. 1874. Theorie der elastischen nachwirkung. *Annalen der Physik und Chemie* **1**, 108–18.
- Min D. J., Shin C., Kwon B. D. and Chung S. 2000. Improved frequency-domain elastic wave modelling using weighted-averaging difference operators. *Geophysics* **65**, 884–95.
- Mittet R., Sollie R. and Hokstad K. 1995. Prestack depth migration with compensation for absorption and dispersion. *Geophysics* **60**, 1485–94.
- Molyneux J. B. and Schmitt D. R. 1999. First-break timing: arrival onset times by direct correlation. *Geophysics* **64**, 1492–501.
- Müller G. 1983. Rheological properties and velocity dispersion of a medium with power-law dependence of Q on frequency. *Journal of Geophysics* **54**, 20–9.
- Neep J. P. 1995. Robust estimation of P -wave attenuation from full waveform array sonic data. *Journal of Seismic Exploration* **4**, 329–44.
- Neep J. P., Sams M. S., Worthington M. H. and O'Hara-Dhand K. A. 1996. Measurement of seismic attenuation from high-resolution crosshole data. *Geophysics* **61**, 1175–88.
- Newman P. 1973. Divergence effects in a layered earth. *Geophysics* **38**, 481–8.
- O'Brien P. N. S. and Lucas A. L. 1971. Velocity dispersion of seismic waves. *Geophysical Prospecting* **19**, 1–26.
- O'Doherty R. F. and Anstey N. A. 1971. Reflections on amplitudes. *Geophysical Prospecting* **19**, 430–58.
- Park J., Lindberg C. R. and Vernon F. L. 1987. Multitaper spectral analysis of high frequency seismograms. *Journal of Geophysical Research* **92**, 12 675–84.
- Peselnick L. and Outerbridge W. F. 1961. Internal friction in shear and shear modulus of Solenhofen limestone over a frequency range of 10^7 cycles per second. *Journal of Geophysical Research* **66**, 581–8.
- Peselnick L. and Zietz I. 1959. Internal friction of fine grained limestones at ultrasonic frequencies. *Geophysics* **24**, 285–96.

- Pratt R. G. 1990. Frequency domain elastic wave modelling by finite differences: a tool for crosshole seismic imaging. *Geophysics* **55**, 626–32.
- Pratt R. G. 1999. Seismic waveform inversion in the frequency domain, part 1: theory and verification in a physical scale model. *Geophysics* **64**, 888–901.
- Pratt R. G. and Shipp R. M. 1999. Seismic waveform inversion in the frequency domain, part 2: fault delineation in sediments using crosshole data. *Geophysics* **64**, 902–14.
- Pratt R. G. and Worthington M. H. 1990. Inverse theory applied to multi-source crosshole tomography I: acoustic wave-equation method. *Geophysical Prospecting* **38**, 287–310.
- Pratt R. G., Shin C. and Hicks G. J. 1998. Gauss-Newton and full Newton methods in frequency-space seismic waveform inversion. *Geophysical Journal International* **133**, 341–62.
- Pratt R. G., Hou F., Bauer K. and Weber M. 2005. Waveform tomography images of velocity and inelastic attenuation from the Mallik 2002 crosshole seismic surveys. In Dallimore S. R. and Collett T. S. (ed.), *Scientific Results from the Mallik 2002 Gas Hydrate Production Research Well Program, Mackenzie Delta, Northwest Territories, Canada*. Geological Survey of Canada Bulletin **585**.
- Pujol J. and Smithson S. 1991. Seismic wave attenuation in volcanic rocks from VSP experiments. *Geophysics* **56**, 1441–55.
- Pujol J. M., Luschen E. and Hu Y. 1998. Seismic wave attenuation in metamorphic rocks from VSP data recorded in Germany's continental super-deep borehole. *Geophysics* **63**, 354–65.
- Raikes S. A. and White R. E. 1984. Measurements of earth attenuation from downhole and surface seismic recordings. *Geophysical Prospecting* **32**, 892–919.
- Rao Y. and Wang Y. 2005. Crosshole seismic tomography: working solutions to issues in real data traveltime inversion. *Journal of Geophysics and Engineering* **2**, 139–46.
- Rao Y., Wang Y. and Morgan J. V. 2006. Crosshole seismic waveform tomography II: resolution analysis. *Geophysical Journal International* **166**, 1237–48.
- Ricker N. 1943. Further developments in the wavelet theory of seismogram structure. *Bulletin of the Seismological Society of America* **33**, 197–228.
- Ricker N. 1953. The form and laws of propagation of seismic wavelets. *Geophysics* **18**, 10–40.
- Riedel K. S. and Sidorenko A. 1995. Minimum bias multiple taper spectral estimation. *IEEE Transactions on Signal Processing* **43**, 188–95.
- Roach G. F. 1982. *Green's Functions*, 2nd edn. Cambridge University Press, Cambridge.
- Robinson J.C. 1979. A technique for the continuous representation of dispersion in seismic data. *Geophysics* **44**, 1345–51.
- Robinson J. C. 1982. Time-variable dispersion processing through the use of phased sinc functions. *Geophysics* **47**, 1106–10.
- Sams M. and Goldberg D. 1990. The validity of Q estimates from borehole data using spectral ratios. *Geophysics* **55**, 97–101.
- Sams M. S., Neep J. P., Worthington M. H. and King M. S. 1997. The measurement of velocity dispersion and frequency-dependent intrinsic attenuation in sedimentary rocks. *Geophysics* **62**, 1456–64.
- Schoenberger M. and Levin F. K. 1974. Apparent attenuation due to interbed multiples. *Geophysics* **39**, 287–91.
- Schoenberger M. and Levin F. K. 1978. Apparent attenuation due to interbed multiples, II. *Geophysics* **43**, 730–7.
- Schoepp A. R. and Margrave G. F. 1998. Improving seismic resolution with nonstationary

- deconvolution. *Expanded Abstracts of the 68th Annual Meeting of Society of Exploration Geophysicists*, 1096–9.
- Shumway G. 1960. Sound speed and absorption studies of marine sediments by a resonance method. *Geophysics* **25**, 451–67.
- Sirgue L. and Pratt R. G. 2004. Efficient waveform inversion and imaging: a strategy for selecting temporal frequencies and waveform inversion. *Geophysics* **69**, 231–48.
- Song Z. M. and Williamson P. R. 1995. Frequency-domain acoustic wave modelling and inversion of crosshole data, part I: 2.5-D modelling method. *Geophysics* **60**, 784–95.
- Song Z. M., Williamson P. R. and Pratt R. G. 1995. Frequency-domain acoustic wave modelling and inversion of crosshole data, part II: inversion method, synthetic experiments and real data results. *Geophysics* **60**, 796–809.
- Stainsby S. D. and Worthington M. H. 1985. Q estimation from vertical seismic profile data and anomalous variations in the central North Sea. *Geophysics* **50**, 615–26.
- Štekl I. and Pratt R. G. 1998. Accurate viscoelastic modelling by frequency-domain finite differences using rotated operators. *Geophysics* **63**, 1779–94.
- Stokes G. G. 1845. On the theories of internal friction of fluids in motion and of the equilibrium and motion of elastic solids. *Transactions of the Cambridge Philosophical Society* **8**, 287–305.
- Stolt R. H. 1978. Migration by Fourier transform. *Geophysics* **43**, 23–48.
- Strick E. 1967. The determination of Q , dynamic viscosity and transient creep curves from wave propagation measurements. *Geophysical Journal of the Royal Astronomical Society* **13**, 197–218.
- Strick E. 1970. A predicted pedestal effect for pulse propagation in constant- Q solids. *Geophysics* **35**, 387–403.
- Tarantola A. 1984. Inversion of seismic reflection data in the acoustic approximation. *Geophysics* **49**, 1259–66.
- Tarantola A. 2005. *Inverse Problem: Theory and Methods for Model Parameter Estimation*. Society for Industrial and Applied Maths, Philadelphia, PA.
- Thompson J. H. C. 1933. On the theory of visco-elasticity: a thermodynamical treatment of visco-elasticity, and some problems of the vibrations of visco-elastic solids. *Philosophical Transactions of the Royal Society of London (Series A)* **231**, 339–407.
- Thomson D. J. 1982. Spectrum estimation and harmonic analysis. *Proceedings of the IEEE* **70**, 1055–96.
- Thomson W. K. (Lord Kelvin) 1856. Elements of a mathematical theory of elasticity. *Philosophical Transactions of the Royal Society of London* **146**, 481–98.
- Toksöz M. N. and Johnston D. H. (eds.) 1981. *Seismic Wave Attenuation*. Geophysics reprint series 2. Society of Exploration Geophysicists, Tulsa.
- Toksöz M. N., Johnston D. H. and Timur A. 1979. Attenuation of seismic waves in dry and saturated rocks: I, laboratory measurements. *Geophysics* **44**, 681–90.
- Tonn R. 1991. The determination of the seismic quality factor Q from VSP data: a comparison of different computational methods. *Geophysical Prospecting* **39**, 1–28.
- Toverud T. and Ursin B. 2005. Comparison of seismic attenuation models using zero-offset vertical seismic profiling (VSP) data. *Geophysics* **70**, F17–25.
- Treitel S. and Robinson E. A. 1966. Seismic wave propagation in layered media in terms of communication theory. *Geophysics* **31**, 17–32.
- Trorey A. W. 1962. Theoretical seismograms with frequency and depth dependent absorption. *Geophysics* **27**, 766–85.
- Tullos F. N. and Reid A. C. 1969. Seismic attenuation of Gulf coast sediments. *Geophysics* **34**, 516–28.

- Ursin B. and Toverud T. 2002. Comparison of seismic dispersion and attenuation models. *Studia Geophysica et Geodaetica* **46**, 293–320.
- Varela C. L., Rosa A. L. R. and Ulrych T. J. 1993. Modelling of attenuation and dispersion. *Geophysics* **58**, 1167–73.
- Virieux J. 1986. *P-SV* wave-propagation in heterogeneous media: velocity-stress finite-difference method. *Geophysics* **51**, 889–901.
- Voigt W. 1892. Über innere reibung fester körper, insbesondere der metalle. *Annalen der Physik und Chemie* **47**, 671–93.
- Walden A. T. and White R. E. 1984. On errors of fit and accuracy in matching synthetic seismograms and seismic traces. *Geophysical Prospecting* **32**, 871–91.
- Walden A. T. and White R. E. 1990. Estimating the statistical bandwidth of a time series. *Biometrika* **77**, 699–707.
- Wang Y. 1999. Random noise attenuation using forward-backward linear prediction. *Journal of Seismic Exploration* **8**, 133–42.
- Wang Y. 2002. A stable and efficient approach to inverse *Q* filtering. *Geophysics* **67**, 657–63.
- Wang Y. 2003a. Quantifying the effectiveness of stabilized inverse *Q* filtering. *Geophysics* **68**, 337–45.
- Wang Y. 2003b. *Seismic Amplitude Inversion in Reflection Tomography*. Pergamon Press, Oxford.
- Wang Y. 2004a. *Q* analysis on reflection seismic data. *Geophysical Research Letters* **31**, L17606.
- Wang Y. 2004b. Multiple prediction through inversion: a fully data-driven concept for surface-related multiple attenuation. *Geophysics* **69**, 547–53.
- Wang Y. 2006. Inverse *Q* filter for seismic resolution enhancement. *Geophysics* **71**, V51–60.
- Wang Y. 2007. Multiple prediction through inversion: theoretical advancements and real data application. *Geophysics* **72**, V33–9.
- Wang Y. 2008. Inverse-*Q* filtered migration. *Geophysics* **73**, S1–6.
- Wang Y. and Guo J. 2004a. Seismic migration with inverse *Q* filtering. *Geophysical Research Letters* **31**, L21608.
- Wang Y. and Guo J. 2004b. Modified Kolsky model for seismic attenuation and dispersion. *Journal of Geophysics and Engineering* **1**, 187–96.
- Wang Y. and Houseman G. A. 1994. Inversion of reflection seismic amplitude data for interface geometry. *Geophysical Journal International* **117**, 92–110.
- Wang Y. and Houseman G. A. 1995. Tomographic inversion of reflection seismic amplitude data for velocity variation. *Geophysical Journal International* **123**, 355–72.
- Wang Y. and Pratt R. G. 1997. Sensitivities of seismic traveltimes and amplitudes in reflection tomography. *Geophysical Journal International* **131**, 618–42.
- Wang Y. and Rao Y. 2006. Crosshole seismic waveform tomography I: strategy for real data application. *Geophysical Journal International* **166**, 1224–36.
- Wang Y., White R. E. and Pratt R. G. 2000. Seismic amplitude inversion for interface geometry: practical approach for application. *Geophysical Journal International* **142**, 162–72.
- White J. E. 1965. *Seismic Waves: Radiation, Transmission and Attenuation*. McGraw-Hill Book Co., New York.
- White R. E. 1973. The estimation of signal spectra and related quantities by means of the multiple coherence function. *Geophysical Prospecting* **21**, 660–703.
- White R. E. 1980. Partial coherence matching of synthetic seismograms with seismic traces. *Geophysical Prospecting* **28**, 333–58.

- White R. E. 1984. Signal and noise estimation from seismic reflection data using spectral coherence methods. *Proceedings of the IEEE* **72**, 1340–56.
- White R. E. 1992. The accuracy of estimating Q from seismic data. *Geophysics* **57**, 1508–11.
- White R. E. and Harris P. E. 1993. *Phase and Timing Accuracy*. Research Note, Birkbeck College, University of London.
- Widess M. B. 1982. Quantifying resolving power of seismic systems. *Geophysics* **47**, 1160–73.
- Winkler K. W. 1986. Estimates of velocity dispersion between seismic and ultra sonic frequencies. *Geophysics* **51**, 183–9.
- Worthington M. H. and Hudson J. A. 2000. Fault properties from seismic Q . *Geophysical Journal International* **143**, 937–44.
- Wuenschel P. C. 1965. Dispersive body waves: an experimental study. *Geophysics* **30**, 539–57.
- Zener C. 1948. *Elasticity and Anelasticity of Metals*. University of Chicago Press, Chicago.
- Zhang J. and Wapenaar K. 2002. Wavefield extrapolation and prestack depth migration in anelastic inhomogeneous media. *Geophysical Prospecting* **50**, 629–43.

Author index

- Aki 4, 43–4, 174, 210
Aldridge 63
Alford 214
Aminzadeh 174
Amundsen 184
Anstey 203
Azimi 27, 29, 46–7
- Badri 185–6
Bano 7, 60, 107
Barnes 186
Bastiaans 120, 122
Ben-Menahem 33, 50, 54
Bickel 7, 70
Bracewell 7
Brennan 5
- Calvert 6–7, 60, 91, 100, 104, 107
Carcione 40, 52
Carpenter 7
Casula 52
Claerbout 60, 161
Clark 169, 188
Cole 34, 53
Cui 148
- Dai 148
Dasgupta 169, 188
Dasios 186
Duren 115
- Feichtinger 120
Futterman 4–5, 18–20, 41, 133, 186
- Gabor 120, 122, 188
Ganley 174
Gazdag 156, 159–60
Gelius 75
Gladwin 185
- Goldberg 186
Grossman 120
Gubbins 176
Guerra 185
Guo 20, 35, 54, 56, 148, 151, 153
- Hale 7–8, 74–5
Halpern 159
Hamilton 4
Hanyga 55
Hargreaves 6–7, 60, 91, 100, 104, 107
Harris 4, 142
He 148
Hicks 210, 221
Hillier 19
Houseman 222
Hudson 184
- Irving 95
- Jacobson 4
Johnston 4, 40
Jones 53
- Kelly 214
Kelvin 51
Kim 114
Kjartansson 27, 46, 133, 185
Klimentos 184
Knight 95
Kolsky 3, 18–9, 41, 50
Kramers 5, 18, 44
Krönig 5, 18, 44
- Leaney 185
Lee 159
Levin 203
Liu 54
Loewenthal 149

- Lomnitz 4
 Lucas 200

 Margrave 120, 152
 Mason 18, 41
 McCann 184
 McDonal 4
 Mendel 174
 Meyer 51
 Min 214
 Mittet 148, 164, 184
 Molyneux 182
 Mooney 185–6
 Müller 32, 48

 Natarajan 7, 70
 Neep 176
 Newman 199

 O'Brien 200
 O'Doherty 203
 Outerbridge 4

 Park 176–7, 180
 Peselnick 4
 Pratt 162, 174, 210–1, 214, 217, 220–2
 Pujol 169, 183

 Raikes 169, 183
 Rao 215, 220–2
 Reid 4
 Richards 4, 43–44, 174, 210
 Ricker 2–3
 Riedel 176
 Roach 212
 Robinson 6–7, 174

 Sams 5, 186
 Schmitt 182
 Schoenberger 203
 Schoepp 120
 Seredyńska 55
 Sguazzero 159–60
 Shipp 217, 222
 Shumway 4

 Sidorenko 176

 Singh 33, 50, 54
 Sirgue 210
 Smithson 183
 Song 174, 210, 214
 Stacey 5, 185
 Stainsby 169, 183
 Štekl 174, 214
 Stokes 2
 Stolt 6, 60, 100
 Strick 5, 27, 46, 133
 Strohmmer 120
 Suh 159

 Tarantola 211–2, 214
 Thompson 3
 Thomson 51, 176
 Toksöz 4, 40
 Tonn 169
 Toverud 18, 36, 40, 54–5, 174
 Trantham 115
 Trefethen 159
 Treitel 174
 Trorey 74
 Tullos 4

 Ursin 18, 36, 40, 54–5, 174

 Varela 8
 Virieux 214
 Voigt 51

 Walden 139–40
 Wang 8, 20, 35, 54, 56, 73–4, 95, 132, 136, 148, 151, 153, 176, 188, 199, 215, 217, 220–2
 Wapenaar 148
 West 148
 White 41, 139–40, 142, 169–70, 183, 186–7
 Widess 134
 Williamson 174, 214
 Winkler 5
 Worthington 169, 183–4, 210–1
 Wuenschel 5

 Zener 32, 50
 Zhang 148
 Zietz 4

Subject index

- amplitude-compensation operator 60,
86, 104, 110, 150, 157
stabilized 67, 95
- amplitude-only inverse Q filter 85–7,
107, 109–10
- attenuation coefficient 2–5, 18, 26–7,
33–5, 43, 45, 50, 53–5, 171
stabilized 158
- attenuation effect 2, 170–3
- attenuation-dispersion relation 4–5
- Azimi's second model 30–1, 47
- Azimi's third model 30–1, 47

- bandwidth 139
- bandwidth retention factor 177
- Butterworth filter 70

- Cole-Cole model 34–6, 53
- complex velocity 42, 48–9, 54–5,
170, 210
- complex wavenumber 4, 45, 61, 74
stabilized 158
- constant Q 27, 47, 188
- constant- Q inverse filter 100
- correlation coefficient 182
- covariance matrix 211
- crosshole seismic 209, 215

- dispersion 1
- dispersion quantity 6
- dispersive phase velocity 5
- dissipation 1
- dissipation factor 41, 43
- downward continuation 60, 66–7, 87,
93–4, 102, 107

- earth Q filter 5, 61, 74, 150
- elastic modulus 41, 50
- finite-difference migration 159–61
- finite-difference operator 161
- forward Q filter 93, 96, 126–7
by Gabor transform 126–8
- Fréchet derivative 211
- Fréchet matrix 211, 213
- frequency-domain waveform tomography
210–1, 214

- Gabor analysis window 123
- Gabor synthesis window 124
- Gabor transform 122–3
- gain limit 128–9, 131
- gain-limited inverse Q filter 65, 68
 γ factor 19
- general linear model 35, 54–5
- gradient method 211–214
- Green's function 212
- group velocity 61–2

- Heaviside function 123
- high-frequency moduli 51
- Hilbert transform 20, 44, 74

- imaging condition 6, 62, 103, 109,
125, 161
- inverse Gabor transform 124
- inverse Q filter 1, 2, 5, 61, 94, 103
by Gabor transform 125
for dispersion 6
- inverse Q filtered migration 147–8

- Jacobian 91–2, 104, 111

- Kelvin–Voigt viscoelastic model 51
- Kjartansson's constant- Q model 26–7, 46
- Kolsky's model 18–9, 44
- Kramers–Krönig dispersion relation 5, 20, 44
- layered inverse Q filter 113
- linear theory 5
- low-frequency moduli 51
- Marmousi velocity model 161
- migration 147–152, 156–61
 - finite-difference 159–61
 - phase-shift 149, 156
 - space-frequency domain 159–60
 - wavenumber-frequency domain 148
- modified Kolsky model 20
- modulus defect 52
- mose, units of 6
- Müller's power-law model 32, 48
- multitaper 176, 180
- objective function 211
- 1-D wave equation 156, 161
- phase velocity 5, 19–20, 27, 30–3, 35, 43, 46–47, 51, 54–5
- phase-only forward Q filter 91–3, 110
- phase-only inverse Q filter 6–7, 64, 86–7, 107, 122, 122
- phase shift migration 149, 156
- plane wave 4, 42, 188
- power-law model 27, 32, 46
- Q 2–3, 17, 40–1, 45
- Q analysis 187–8, 190, 193, 195, 201
- Q estimation 169, 174, 181, 197, 201
- Q model 18, 26, 45–8, 52–4, 56
- quality factor (Q factor) 3–4, 6, 17, 40, 45, 171, 210
- random noise attenuation 74, 132
- relaxed modulus 50, 53
- resolution enhancement 141–2
- Ricker wavelet 62
- signal-to-noise ratio 140
- similarity principle 7
- space-frequency domain migration 159–60
- spectral leakage 176
- spectral ratio method 170, 174
- spherical divergence 199–200
- stability condition 64–5
- stabilization 65, 67, 95–6, 157–8
- stabilization factor 67, 96, 128–9
- stabilized attenuation coefficient 158
- stabilized inverse Q filter 59, 66–8, 113, 132
- stabilized migration 151, 156
- standard linear solid model 32–3, 50
- Stokes wave equation 2
- stress–strain relation 41
- Strick–Azimi model 27, 46
- subspace 222
- superposition 6, 51, 152
- supersedent 147–8, 158, 161
- tomography
 - traveltime 220–1
 - waveform 211–4
- transition frequency 3
- tuning frequency 20, 22
- unrelaxed modulus 50, 53
- vertical seismic profiling (VSP) 170
- virtual source 213
- waveform tomography 209–11, 214–5
- wavenumber 4, 14, 22, 41, 45
- wavenumber-frequency domain migration 148
- Wiener criterion 43
- Zener model 32–3, 36